Geodätisch-geophysikalische Arbeiten in der Schweiz

(Fortsetzung der Publikationsreihe
«Astronomisch-geodätische Arbeiten in der Schweiz»)

herausgegeben von der

Schweizerischen Geodätischen Kommission
(Organ der Akademie der Naturwissenschaften Schweiz)

Einhundertdritter Band
Volume 103

Calibration Aspects of INS Navigation

Philipp Clausen

2019

Adresse der Schweizerischen Geodätischen Kommission:

ETH Zürich
Institut für Geodäsie und Photogrammetrie
Eidg. Technische Hochschule Zürich
8093 Zürich
Switzerland

Internet: http://www.sgc.ethz.ch

ISBN 978-3-908440-49-9

Redaktion des 103. Bandes:
Dr. P. Clausen, J. Müller-Gantenbein, Dr. Jan Skaloud, Prof. A. Geiger
Druck: Print-Atelier ADAG, Zürich

VORWORT

Ineritalsensoren kommen in verschiedenen Ausführungen, Grössen, Preisklassen und Präzisionen, welche den Markt mit Anwendungen von den hochauflösenden Gravimetern bis hin zu den Smartphones abdekt. Die Qualität dieser Sensorsignale muss durch eine Kalibration verbessert werden und dies unabhängig von der Art des Sensors oder dessen Benutzung. Dies beinhaltet auch die Restfehler, welche stochastisch Charakterisiert werden können. Diese Werte werden insbesondere in integrierten Navigationssystemen benötigt, welche unter anderem in unbemannten Fahrzeugen oder Robotern zu Land, zu Wasser und in der Luft benutzt werden. In diesem Sinn fokussiert sich die Forschung von Dr. Clausen auf zwei neue Methodologien, welche die Benutzung von MEMS Inertialsystemen qualitativ für verschiedenste Anwendungen verbessert, und dies auch für Anwendungen ausserhalb von Navigations- und Kontrollsystemen.

Zunächst schlägt der Autor eine Verfeinerung der Werkskalibrierung und deren Einsatz für kleine MEMS-IMUs mit höherer Qualität unter Laborbedingungen vor. Das Ergebnis wird in eine Reihe von Parametern aufgeteilt, die alle nachfolgenden Messungen korrigieren, während die sich eher zufällig ändernden Parameter *in situ* über ein vereinfachtes Kalibrations-Verfahren erneut bestimmt werden. Insbesondere die daraus resultierende Verbesserung der Lagegenauigkeit, die für viele UAV-Anwendungen von kurzer Dauer von entscheidender Bedeutung ist, ist herausragend. Angesichts der Tatsache, dass die Lageverbesserung proportional mit dem Quadrat der Sensorgröße zusammenhängt, ist die praktische Auswirkung von entscheidender Bedeutung, da wir auf leichten Plattformen mit derselben Instrumentierung eine erheblich höhere Genauigkeit erzielen können, was möglicherweise eine direkte Ausrichtung der optischen Sensoren ermöglicht. Dies wurde im Fall des luftgestützten Laserscannings detailliert demonstriert.

Zweitens erweitert der Autor eine hochmoderne Methode zur Charakterisierung der komplexen stochastischen Prozesse (Generalized Method of Wavelet Moments [GMWM]) auf der Grundlage der möglichen Abhängigkeit stochastischer Parameter von einer externen Variablen, die hier als ‚Kovariate' bezeichnet wird. Es ist bekannt, dass die stochastische Charakterisierung des Sensorrauschens unter äußeren Einflüssen wie Umgebungsbedingungen (z. B. Temperatur, Druck und Dynamik) variieren kann. Daher trägt das hier vorgeschlagene Verfahren diesen Einflüssen Rechnung, indem neue Funktionsbeziehungen definiert werden, deren Parameter aus den Referenzsignalen abgeleitet werden können. Diese Theorie und ihre Open-Source-Implementierungen bieten neue Einblicke in potenzielle Anwendungen außerhalb des Bereichs der Inertialsensoren, wie z. B. Oszillatoren, die von kostengünstigem Quarz bis zu anspruchsvolleren Atomuhren reichen! Obwohl in Zusammenarbeit entwickelt, hat Dr. Clausen wesentlich dazu beigetragen, die Erweiterung des GMWM-Frameworks in die Praxis umzusetzen und gleichzeitig die stochastische Prozessanalyse direkt über ein Webinterface zu ermöglichen. Daher ist es nicht verwunderlich, dass sein Beitrag auf einer IEEE-Konferenz zu diesem Thema mit einem Preis ausgezeichnet wurde.

Prof. Dr. Jan Skaloud
EPFL Lausanne
Dissertationsleiter

Prof. Dr. Alain Geiger
ETH Zürich
Präsident der SGK

PREFACE

Les capteurs inertiels peuvent se présenter sous un large éventail de déclinaisons en termes de taille, de coût, de précision, ou encore d'application. En effet, ces capteurs sont utilisés autant dans des systèmes à haute précision tel que les gravimètres que dans des systèmes embarqués à utilisation quotidienne tel que le Smartphone par exemple. Avant de pouvoir être traitées dans des systèmes intégrés tels que les systèmes de guidage, de navigation et de contrôle de véhicules autonomes, les mesures délivrées par ces capteurs doivent être corrigées par des techniques de calibration, et les erreurs résiduelles qui en découlent caractérisées stochastiquement. À cet égard, les recherches du Dr. Clausen portent sur deux nouvelles méthodologies qui améliorent qualitativement l'emploi des capteurs inertiels MEMS pour un vaste domaine d'applications, même au-delà du domaine de la navigation, du guidage et du contrôle.

En premier lieu, l'auteur propose un affinement des techniques de calibration en usine et de leur application sur des capteurs de type MEMS-IMU en laboratoire. Le résultat de cette procédure se présente sous un ensemble de paramètres qui sont appliquées aux mesures afin de les corriger. Les erreurs résiduelles, de nature plus aléatoire, sont quant à elles corrigées *in situ* via une procédure d'étalonnage simplifiée. Le travail de l'auteur démontre que la procédure proposée améliore de façon remarquable la précision de l'attitude, une donnée essentielle pour de nombreuses applications (par exemple les drones de petite taille effectuant des missions de courte durée). En effet, l'amélioration de l'attitude étant proportionnelle au carré de la taille du capteur, la signification pratique de cette amélioration pour des plateformes légères est cruciale, car tout en utilisant la même instrumentation, une précision considérablement accrue peut être obtenue. Cela offre potentiellement la possibilité de calculer directement l'orientation de capteurs optiques embarqués sur des plateformes légères, ce qui a été démontré en détail dans ce travail pour le cas du balayage laser aéroporté.

En second lieu, l'auteur élargit le développement d'une méthode de pointe pour la caractérisation de processus stochastiques complexes, la « méthode généralisée des moments d'ondelettes » (GMWM), qui est basée sur la dépendance éventuelle de paramètres stochastiques à une variable externe, appelée ici la « co-variable ». En effet, la nature stochastique du bruit affectant les signaux de capteurs peut varier en raison d'influences environnementales telles que la température, la pression et la dynamique. La méthode proposée par l'auteur tient compte de ces influences en définissant de nouvelles relations fonctionnelles, dont les paramètres peuvent être dérivés de signaux de référence. Cette méthode, implémentée et disponible dans un logiciel libre, offre de nouvelles possibilités d'applications bien au-delà de celle des capteurs inertiels, telles que la caractérisation d'oscillateurs de tout type, allant de l'oscillateur à quartz à faible coût jusqu'aux horloges atomiques les plus sophistiquées ! Bien que la recherche ait été faite en collaboration avec des partenaires, le travail du Dr. Clausen a largement contribué à la mise en pratique de l'extension de la méthode GMWM, en permettant notamment l'analyse stochastique de processus directement via une interface Web. Il n'est donc pas surprenant que sa contribution à une conférence de l'IEEE sur ce sujet ait été saluée par un prix.

Prof. Dr. Jan Skaloud
EPFL Lausanne
Directeur de thèse

Prof. Dr. Alain Geiger
ETH Zürich
Président de la CGS

FOREWORD

The inertial sensors come with broad spectra of technology, size, cost, and eventually precision that serves precise gravimeters on one side and smart-phone industry on the other. Irrespectively of the type and application, the quality of such sensors needs to be improved by calibration, and the residual errors characterized stochastically for their subsequent usage in integrated systems, such as those inside unmanned vehicles or robots operating in the air, on the surface, and below. In this respect, Dr. Clausen's research focuses on two novel methodologies that qualitatively improve the employment of MEMS inertial sensors in a large area of applications even beyond the field of navigation, guidance, and control.

First, the author proposes a refinement of factory calibration and its substitution for small MEMS-IMUs of higher quality in laboratory conditions. Its outcome is split into a set of parameters that correct all subsequent observations, whereas those of more random nature are determined *in situ* via a simplified calibration procedure. In particular, the resulting improvement in the attitude accuracy, which is a critical part for many small UAV applications of short duration, is outstanding; given that the attitude improvement is proportional to the square of the sensor size, the practical impact is crucial as it allows us to achieve considerably increased accuracy on lightweight platforms with the same instrumentation – potentially enabling direct orientation of optical sensors. This was demonstrated in details in the case of airborne laser scanning.

Second, the author expands a state-of-the-art method for the characterization of the complex stochastic processes (Generalized Method of Wavelet Moments [GMWM]) based on the possible dependency of stochastic parameters on an external variable, here called 'covariate'. Indeed, it is well known that the stochastic characterization of sensor noise may vary under external influences such as environmental conditions (e.g., temperature, pressure, and dynamics); therefore, the here proposed method takes into account these influences by defining new functional relations, whose parameters can be derived from the reference signals. This theory and its open-source implementations provide new insights into potential applications outside the field of inertial sensors, such as oscillators ranging from low-cost quartz to more sophisticated atomic clocks! Although developed in collaboration, Dr. Clausen substantially contributed to putting in practice the extension of the GMWM framework while enabling the stochastic process analysis directly through a web interface. Therefore, it comes with no surprise that his contribution at an IEEE conference on this subject was appreciated by an award.

Prof. Dr. Jan Skaloud
EPFL Lausanne
Thesis director

Prof. Dr. Alain Geiger
ETH Zürich
President of SGK

Abstract

The use of a Bayesian filter (e.g., Kalman filter) for the fusion of information from satellite positioning and inertial navigation is a common approach in many applications, where the knowledge of position, velocity, and attitude in space are of great interest. The correctness of these estimates depends on many factors, among others the quality of the sensor measurements and the errors within, which are directly reflected in the filter design. A calibration process allows compensating for deterministic influences (which in return improve for instance qualitatively the attitude initialization) and their inherent stochastic error signals required for filtering.

This thesis presents in the first part the development of methods to perform a thorough calibration of different sensors in-lab under controlled conditions and in-field for a simplified calibration with limited resources and equipment. The stochastic properties of error signals are analyzed in the second part. A novel approach called Generalized Method of Wavelet Moments (GMWM) allows investigating the error structure using wavelets, which is similar to the Allan variance. An intuitive online tool is presented, which grants simplified access to the GMWM framework that provides a consistent, identifiable, and computationally efficient estimation of stochastic model parameters. The parameters of these error models are then made dependent on an external covariate such as temperature or motion. Indeed, it is experimentally confirmed that these properties shape the stochastic behavior of the measurements and how the stochastic parameters relate functionally to the influence of the covariate. Later, such knowledge is included in the filter for the correct estimation of confidence levels.

The successful implementation of these proposed concepts is validated in a fully functional drone-system for mapping purposes. A real-time calibration scheme is applied first in-lab, later in-field to initialize the navigation processor. Apart from the benefit of achieving considerably better estimates of the attitude, and in case of satellite signal outage also of the position, the calibration allows for a simplified fusion of redundant inertial sensors. The improved performances through calibration and sensor redundancy are attractive to drone mapping applications relying on an accurate direct or integrated orientation such as lightweight airborne laser scanning systems or frame-cameras, which are utilized in the experiments.

Key words: IMU, MEMS, GNSS, INS, deterministic calibration, stochastic process, stochastic error modeling, sensor fusion, GMWM, Kalman filter, navigation

Zusammenfassung

Der Bayessche Filter (z.B. Kalman Filter) wird üblicherweise für das Zusammenführen verschiedenster Messungen benutzt. Inertialsensoren und Satelliten-basierte Messungen sind dabei die meistgebrauchten Kandidaten. Die geschätzten Grössen wie Position, Geschwindigkeit und Orientation werden für verschiedene Aufgaben im Navigationsbereich verwendet. Die Richtigkeit der Schätzung hängt sowohl von der Qualität der Messung als auch von deren Fehlerstruktur ab. Diese Struktur muss nicht nur beim Filterdesign berücksichtigt werden, sondern muss auch best möglichst von vornherein kalibriert werden.

Diese Arbeit präsentiert in einem ersten Teil die Kalibration von Sensoren unter Laborbedingungen und zeigt Methoden, wie diese Kalibration unter erschwerten realen Bedingungen ausgeführt werden kann. Die Fehlersignale der Sensoren werden dann in einem zweiten Teil durch eine Zustandsraumdarstellung repräsentiert und analysiert. Der neue Ansatz durch die sogenannte *Generalized Method of Wavelet Moments* (GMWM) erlaubt eine Analyse der Fehlerstruktur mithilfe von Wavelets (ähnlich wie die Allan Varianz). Ein online Web-Tool wird präsentiert, welches den Zugriff auf das GMWM Framework erleichtert. Diese Methode ist konsistent, identifizierbar und nicht rechenintensiv. Die Schätzung der Parameter des Fehlermodels werden dann in einem nächsten Schritt in Abhängigkeit einer externen Messung wie Temperatur oder Bewegungsdynamik gebracht. Diese beeinflussen je nach Sensortyp das Messrauschen. Verschieden Ansätze werden untersucht und deren Resultate direkt in einem Kalman Filter untergebracht.

Die erfolgreiche Umsetzung der Kalibration von deterministischen und stochastischen Fehlern wird anhand eines voll funktionsfähigen Drohnen-Systems aufgezeigt. Die Methoden zur Sensorkalibration in einer Echtzeitanwendung werden präsentiert und einem Navigationscomputer zur Verfügung gestellt. Dank der rigorosen Kalibration der Inertialsensoren verbessert sich die Navigationsautonomität, falls die Satellitenposition ausfällt. Zudem erlaubt dieser Schritt eine direkte Fusion von mehreren redundanten Sensoren. Dieser Schritt erhöht die Qualität der Positionsbestimmung, welche besonders attraktiv für z.B. luftgestützte leichtgewichtige Laserscannersysteme ist. Die Vorteile werden anhand verschiedenster Beispiele veranschaulicht.

Stichwörter: IMU, MEMS, GNSS, INS, Kalibrierung deterministischer Fehler, stochastischer Prozess, stochastische Fehlermodellierung, Sensorfusion, GMWM, Kalmanfilter, Navigation

Contents

List of Figures vii

List of Tables xiii

Conventions and Notation xx

1 Introduction 1
- 1.1 Context 1
- 1.2 Motivation 4
- 1.3 Methodology 5
- 1.4 Outline 6

I Preliminaries 9

2 Sensors for Aided Navigation 11
- 2.1 Introduction 11
- 2.2 Inertial Sensors 11
  - 2.2.1 Classification 11
  - 2.2.2 IMU Characteristics 12
- 2.3 Reference Frames 14
  - 2.3.1 Inertial Frame 14
  - 2.3.2 Earth Frame 14
  - 2.3.3 Local-Level Frame 14
  - 2.3.4 Body Frame 15
- 2.4 Strapdown Inertial Navigation 15
- 2.5 Integrated Navigation 17
  - 2.5.1 Fusion Principle 17
  - 2.5.2 Extended Kalman Filter/Smoother 18
  - 2.5.3 Redundant IMU 20
- 2.6 Aiding Sources 21
  - 2.6.1 GNSS Position and Velocity 21

2.6.2 Barometer . . . 22
2.6.3 Magnetometer . . . 25
2.6.4 Attitude Initialization . . . 26

3 Stochastic Model Identification **29**
3.1 Introduction . . . 29
3.2 Definition . . . 29
3.3 Stochastic Error Models . . . 30
3.3.1 Random Constant . . . 30
3.3.2 Quantization Noise . . . 30
3.3.3 White Noise . . . 31
3.3.4 Random Walk . . . 31
3.3.5 First-order Gauss-Markov Model . . . 32
3.3.6 Random Rate Ramp . . . 32
3.3.7 Bias Instability . . . 33
3.3.8 Example with Noise Parameters . . . 33
3.4 Definitions and Estimation Methods . . . 33
3.5 Allan Variance . . . 36
3.6 Generalized Method of Wavelet Moments . . . 37
3.6.1 Wavelet Transform . . . 38
3.6.2 Wavelet Variance . . . 38
3.6.3 WV of Stochastic Processes . . . 39
3.6.4 Parameter Estimation . . . 40
3.7 Error Analysis Example . . . 41
3.7.1 IMU Manufacture Specifications . . . 42
3.7.2 GMWM Analysis . . . 43
3.7.3 Example . . . 43

II Calibration Methodology **47**

4 Deterministic Errors **49**
4.1 Introduction . . . 49
4.2 Problem Statement . . . 49
4.3 Multi-Position Calibration . . . 52
4.3.1 Accelerometer . . . 54
4.3.2 Gyroscope . . . 59
4.3.3 Stability Over Time of Estimated Parameters . . . 63
4.4 Dynamic Calibration Scheme . . . 64
4.5 Magnetometer . . . 67

4.5.1 Problem Statement 67
4.5.2 Transformation of Ellipse to a Sphere 68
4.6 Barometer 71
4.6.1 Problem Statement 71
4.6.2 Parameter Calibration via EKF 73

5 Stochastic Parameters with Time Dependency 77
5.1 Introduction 77
5.2 Model Description 78
5.3 Dynamic GMWM Estimator 79
5.4 Temperature 81
5.5 Rotational Dynamics 86

6 Implementation 91
6.1 Introduction 91
6.2 Hardware Implementation 91
6.3 Deterministic Error Calibration In-Field 96
6.3.1 Accelerometer and Gyroscope 96
6.3.2 Magnetometers 99
6.4 Initial Attitude Determination 100
6.5 Stochastic Noise Parameter Estimation with an Online GUI 100
6.5.1 Introduction 100
6.5.2 Installation 101
6.5.3 Functionality Overview 102
6.5.4 Empirical WV and Datasheet Value 105
6.5.5 Iterative Model Identification 106
6.5.6 Estimated Parameters 106
6.5.7 Model Selection 108
6.5.8 Summary 109

III Application 111

7 Adaptive Stochastic Model 113
7.1 Background 113
7.2 Simulation Scenario 114
7.3 Discussion 115

8 Integrated Navigation 119
8.1 Introduction 119
8.2 Altitude Determination with Barometer 119

8.3 Initial Attitude Estimation 121
8.3.1 Simulated Data 122
8.3.2 GNSS/INS Prior/After Flight 124
8.3.3 Static Photogrammetry 126
8.4 Navigation during GNSS Outage 128

9 Mapping **131**
9.1 Introduction 131
9.2 Close-Range Helicopter 131
9.2.1 Setup 131
9.2.2 Attitude Quality - Continuous Reference 135
9.2.3 Attitude Quality - Photogrammetric Reference 137
9.2.4 Attitude Quality - Direct Sensor Orientation 139
9.3 Micro-UAV 141
9.3.1 Platform 141
9.3.2 Mission 141
9.3.3 Effect of Initialization 143
9.3.4 Attitude Performance 144

10 Conclusion **147**
10.1 Impact 147
10.2 Summary of Contributions 147
10.2.1 Theoretical/Conceptual Contributions 147
10.2.2 Engineering Contributions 148
10.3 Main Scientific Publications 149
10.4 Perspective 150

IV Appendix **153**

A File Formats **155**
A.1 Accepted GNSS Receiver Messages 155
A.1.1 JPS 155
A.1.2 NMEA 156

B Geckoboard **157**
B.1 Upload Specific Firmware 157
B.2 Download / Stream Data 158

C Datasheets **159**
C.1 IMAR: iIMU-FSAS 160
C.2 Northrop Grumman: LN200 161
C.3 Intersense: Navchip 163
C.4 XSENS: MTi-G 165
C.5 TE Connectivity Measurement Specialties: MS5611-01BA03 166

D GMWM Analysis **167**
D.1 ID2 - NC0 168
D.2 ID2 - NC1 170
D.3 ID2 - NC2 172
D.4 ID2 - NC3 174
D.5 ID2 - Synthetic NC 176
D.6 ID3 - NC0 178
D.7 ID3 - NC1 180
D.8 IDX - NCV2 182

E Calibration Table **185**
E.1 Base Plate 186
E.2 Base Wall 187
E.3 Transversal 188
E.4 Case Holder 189

F Rotation Table **191**
F.1 Specifications 192
F.2 Measurements 193

G Gyroscope Calibration Result **195**

Bibliography **205**

List of Figures

1.1 Input/output relation of a sensor affected by a constant offset also called bias, and a scale-factor error. 2

1.2 The filter estimates the corrections for the IMU, whenever an external aiding (e.g., the GNSS) provides a measurement update. 2

1.3 Two sensors showing different typology and amplitude of sensor noise. 3

2.1 Pictures of MEMS IMUs taken from [Analog Devices, 2018a,b; Sensonor, 2017; Colibry, 2018; Intersense, 2018] and Section C.3 13

2.2 The loosely coupled GNSS/INS integration as a possible example for the sensor fusion. Both systems work completely independently while their solutions are only fused at the end by means of a filter. Eventual feedback on the error (corrections) is directly fed back into the INS and utilized for the subsequent processes. 18

2.3 Hidden states x and observation z as a function of time k for the Markov Chain. The current state only depends on the previous state and the present measurement. 19

2.4 Principle of the synthetic IMU for the case with three individual IMUs: the measurements are projected onto a synthetic IMU. Its information is then used in the navigation processor Waegli et al. [2008]. 21

2.5 Evolution of the pressure after take-off during a typical mission with a difference in altitude of up to 200 m above ground. 23

2.6 Representation of the seven magnetic parameters provided by the WMM software knowing position and time. 26

3.1 The bottom figure shows the sum of the individual stochastic processes. 34

3.2 Analysis of two signals through the auto-correlation function. The first signal is just a Gauss-Markov (GM) process, whereas the second signal is composed of a GM and a White Noise (WN). 35

3.3 Sample plot of Allan deviation analysis. Taken directly from [IEEE, 1998]. 37

3.4 Principle application of the Maximum Overlap Discrete Wavelet Transform using shifted (and scaled) versions of the Haar Wavelet. 39

3.5 Example log-log-plot showing the influences of the different models with their shape. Red dotted: sum of theoretical noise models $\boldsymbol{\nu}(\boldsymbol{\theta})$. Multiple GM can approach the flat shape of the bias instability. 40
3.6 Comparison of the empirical WV between a navigation grade IMU and a low-cost MEMS IMU. Its shape will define the error model. 42
3.7 The implied WV is contained in the confidence interval of the empirical WV. . . 46

4.1 Aluminum support (310 mm × 220 mm × 180 mm) for the sensor board. Two independent axes (axis 1 and 2) allow for free rotation with increments of 15° (see Appendix E). 55
4.2 Side view of the IMU for the calibration procedure. A total of 12 rotations of 30° around a specific axis are presented. This sums up to a total of 36 different measurement attitudes. 56
4.3 Left: badly shaped correlation matrix for the scale-factors and the non-orthogonalities. Right: the parameters are decorrelated sufficiently due to a sufficient number of different attitude measurements. 57
4.4 Top: shows the raw data from the Inertial Measurement Unit (IMU) used for the calibration. Bottom: shows the norm of the uncalibrated data, the norm of the calibrated data, and the reference value (i.e., local gravity). 58
4.5 Evolution of the correlation matrix by reducing the parameter number. The same dataset is used as for Figure 4.3. Left: bias and non-orthogonality are estimated. Right: only bias parameters for each axis are estimated. 60
4.6 IMU installed on the one-axis high-precision rotation table (Appendix F). . . . 61
4.7 Top: measurements of the three axis for different rotation speeds and attitudes. Bottom: Zoom on the norm of the rotation rate around 300 °/s. 62
4.8 Variations of accelerometer calibration in time for the navchip x axis and its 2σ bound. 64
4.9 The 41 cm by 31 cm mount holds the IMAR and the Navchip senors. The handles allow for easy grip and save manual swinging of the setup with the power and data cables leaving the platform. 65
4.10 Top: Gyroscope measurements for each axis. First, individual axis are excited, then there is a mix of the rotation about different axis. Bottom: The accelerometer measurements are acquired by linearly shaking the setup, which is visible by the peaks. 66
4.11 Calibrated magnetometer readings are centered on a unit sphere, whereas the uncalibrated measurements are shifted and scaled. 67
4.12 Left: raw magnetometer data as ellipse and arbitrary units. Right: calibrated magnetometer data as a centered unit sphere. Data was acquired in perfect lab conditions. 70

4.13 Left: raw magnetometer data as ellipse and arbitrary units. Right: calibrated magnetometer data as a centered unit sphere. Data acquired by hand on the field. Big holes in the dataset can be seen. 70

4.14 Top: evolution of the standard deviation from the norm (equals 1) of the datapoints with a threshold set to 0.05. Bottom: evolution of the sphere coverage with a threshold of 65%. Both conditions are met around the 300th receiver packet of data. One packet consists in this case of 1 s of data. 71

4.15 The upper plot shows the absolute reference height, whereas the lower plot shows the difference in height between the reference and the converted barometric height measurements. The error grows with increasing heights. Typical values for pressure, temperature, and humidity were used for the conversion. . 72

4.16 The first plot shows the evolution of the absolute altitude. The second and third plot show the estimated parameters p_0 and k and their evolution through the GNSS code-measurements. They evolve, when the altitude is changed until they reach a plateau. The fourth plot shows firstly the difference between the barometer solution and the reference, and secondly the difference between the Global Navigation Satellite System (GNSS) code solution and the reference. The reference is the GNSS PPK solution. 75

5.1 The temperature changes smoothly from a hot state (60 °C) to a cold state (-20 °C) in roughly 3 h. 81

5.2 Left: raw data of a gyroscope and an accelerometer. Right: temperature-calibrated data where the temperature dependent bias is eliminated through splines regression. 82

5.3 The two WV overlaid noise characteristics for a hot state of 57 °C (orange) and the cold state of -19 °C (blue) with their respective confidence intervals on the z-axis accelerometer. 83

5.4 Empirical and model implied WV of the z-axis accelerometer at 20 °C mean temperature with the decomposition to AR1 and WN models. 83

5.5 Straight line (trend): estimated stochastic parameters though the *dynamic-GMWM* as a function of temperature; solid irregular line: bin-wise manually calculated parameters with confidence interval of 2σ for the process parameters WN and AR1. 85

5.6 MEMS-IMUs board mounted on the left with its power source as counterweight on the right side of the rotation table, which has a mounting plate diameter of 40 cm. 86

5.7 Acquired reference rotation rates per bin with its duration. 87

5.8 Gyroscope stochastic signature and models at minimal and maximal rotations. Top: rotational speed of 30 °/s. Middle: rotational speed of 390 °/s. Bottom: WV of slow rotation overlaid with WV of fast rotation rate. 88

5.9 Top: Empirical WV per each bin from slow (in blue) up to fast (in red) rotational speeds, which form the input to the extended GMWM framework. Bottom: predicted WV of gyroscope noise with the estimated rotational dependent stochastic model (output from the extended GMWM framework). 89

6.1 Left: model airplane in the air. Right: schematic side-view of drone with depiction of some internal components including the IMU, camera, and GNSS antenna [Rehak and Skaloud, 2015]. 92

6.2 Top-view and side-view of the payload with the camera (SODA), sensor board, and embedded computer. 93

6.3 Sensor board hosting two Navchip IMUs, a barometer, and an external magnetometer. The USB connector brings power and the connectivity to a computer for data transfer. 93

6.4 Schematics of the hardware and software implementation for the setup used in the drone application. 94

6.5 Two different phases of a typical mission. The in-lab calibration parameters are used to re-calibrate the setup just before the in-field bias calibration so that the computation of the initial attitude with calibrated data assures a certain quality. 95

6.6 Typical test site for a UAV mission. The internal μPC of the drone is connected to the GCS via the WiFi-Link and transmits information about the calibration process during handling. 96

6.7 Main GUI window on the GCS for pre-flight calibration. It displays relevant information to the user as received from the μPC. Bidirectional interaction takes place, in order to launch the calibration process and inform the user about the estimated parameters. 97

6.8 GUI on the GCS PC showing the results of the real-time calibration. Top: real-time information to the user with information about the acquired attitudes. Bottom: after the calibration, the sensor can be selected, and calibration parameters are presented. The correlation matrix of the calibration shows the calibration quality in a simplified way. Other parameters (θ and S) are displayed with zeros, as in this case the reduced multi-position-calibration scheme only estimates the current bias, whereas the non-orthogonality and scale-factor were already pre-calibrated in the lab. 98

6.9 GCS GUI in-field calibration verification: accelerometer tab providing real-time information of the sensor data. Different IMUs can be selected and individual sensor axes can be displayed alongside the mean value to visualize the calibration quality in a simplified way. 99

6.10 Overall view of the GUI with all the information as seen online. The upper part displays graphical and numerical results. The lower parts allow for data-uploading and selection, noise-modeling, and setting of options related to the computation and parameter estimation. 103

6.11 Drop-down menu for the custom dataset. The column can be chosen, the frequency can be set, and the units can be defined for the resulting plot. 104

6.12 Empirical WV representation (blue line/full-circles) for Navchip gyroscope y-axis with its CI. Datasheet specified theoretical Wavelet Variance (WV) displayed by the red line/empty-circles. 105

6.13 Evolution of iterative model identification. Noise models are added successively. 107

6.14 Summary of the parameters with their confidence interval for the last iteration shown in Table 6.1. 108

7.1 Position solutions (gray) in comparison to the reference (black). The estimated solutions shown exceed the 3σ boundary on some point of the trajectory. . . . 116

7.2 Evolution of the estimated uncertainty with different noise models programmed into the Kalman filter. The GNSS updates appear after 90 s. 116

7.3 Percentage outside 80%-bound. Top: azimuth. Bottom: north velocity. Black dashed line represents the theoretical amount of trajectories outside the bound, which would be 20%. The adaptive noise model (in green) follows this theoretical value, whereas the other two do not (hot model in red, cold model in blue). . . 118

8.1 Top: absolute altitude for different scenarios. The IMU-only solution (dotted line) diverges quickly after the GNSS outage, whereas the measurements of the barometer (dashed line) enable to bound the drift. Bottom: altitude error with confidence bound with respect to the reference. 120

8.2 The KF-predicted uncertainty in the altitude of the GNSS-IMU fusion is worse than the fusion between the IMU and the barometer. The IMU-only uncertainty grows quickly after the GNSS outage. 121

8.3 Errors in roll, pitch, and yaw based on 100 simulated accelerometer and magnetometer measurements with relation to their reference attitude. 122

8.4 Example of 2 photos taken at different attitudes from the calibration field with the visible black/white targets. 127

8.5 Error of the attitude expressed as ω, ϕ, and κ between the REQUEST algorithm and the angles provided by the photogrammetric application. 128

8.6 Top view of the trajectory part, during which a 30 s GNSS outage is simulated. . 129
8.7 Errors with relation to the reference for the IMU board. Top: planimetric error. Middle: altimetric error. Bottom: absolute velocity error. 130

9.1 Top Left: ALS installed on helicopter. Top Right: zoom on ALS system. Bottom Left: Helimap system used as reference. Bottom right: UAV "puck" scanning system with APX15. 133
9.2 Top: complete helicopter flight path (camera events represented as white triangles). Bottom: long strip area considered for the experiment (ground control points in red). 134
9.3 Differences to the AirINS in the attitude solution for the first flight line. Top: uncalibrated IMU. Middle: calibrated IMU. Bottom: fused SIMU. 136
9.4 Orientation differences between INS/GNSS derived trajectory and that resulting from the photogrammetric adjustment per photo and IMU. 138
9.5 Side-view of height profile for two slopes for the different sensor configurations (pink: not-calibrated IMU; yellow: calibrated IMU; green: SIMU; cyan: APX15; red: AirINS). 139
9.6 Height differences for the Laser data between the reference and specific sensor configurations. White patches indicate difference in height exceeding 15 cm. Top: IMU without calibration. Middle: pre-calibrated IMU. Bottom: SIMU. . . 140
9.7 Bottom and side view of the IGN camera carbon mount (length of 23 cm) together with the IMU board and the embedded computer. 142
9.8 Calibration field with the targets and UAV fuselage. 142
9.9 Test-site showing the flight path (in red) of the micro UAV with distribution of ground control points (black dots). 143
9.10 Differences between the predicted and updated roll values. Left: non-calibrated IMU exhibiting oscillations 25 min into the flight. Right: in-lab plus pre-mission calibrated IMU exploitable within minutes after take-off. 144
9.11 Orientation differences between INS/GNSS derived trajectory and that resulting from the photogrammetric adjustment for the IGN camera per photo and IMU. 145

E.1 Setup with 40 cm diameter base plate of the rotation table. 185

F.1 Rotation table with 40 cm diameter base plate. 191

G.1 Variations of 10 independent gyroscope calibration results with a 2σ bound for a typical Navchip z axis. The bias changes between 1000 °/h and 1300 °/h. The scale-factor changes between 500 ppm and 1000 ppm. The non-orthogonality changes between 0.5 mrad and 0.8 mrad. 196

List of Tables

2.1 Rough comparison (bias and price) between the different IMU-grades. 12

2.2 Comparison between small tactical grade lightweight MEMS IMU. 13

2.3 Comparison between the main properties of inertial and satellite navigation. . 22

2.4 Influence of the individual parameters on the final height using standard values and their variations. 25

3.1 Different stochastic processes with their corresponding slopes as shown in the plot of Figure 3.3 representing the Allan deviation. 37

4.1 Full calibration result for a Navchip Inertial Measurement Unit (IMU) accelerometer. The right amount and distribution of the attitudes is required to estimate the parameters. 58

4.2 Evolution of the estimated parameters for different calibration models. 59

4.3 Calibration result for a Navchip IMU gyroscope. 62

4.4 Calibration result for a gyroscope with emulated data based on typical error values. 66

5.1 Stochastic model parameters (WN, AR1) for a variable temperature estimated via the optimization. 84

5.2 Values of noise parameters. The units are expressed in the GMWM default representation of variances. The exception is the WN, where the units were converted to be easily comparable to the one from the datasheet. 87

5.3 Covariate (dynamics) dependency of stochastic parameters as estimated by the extended GMWM optimization. 90

6.1 Estimated parameters for each iteration. The upper part is dedicated to the Navchip gyroscope, whereas the bottom part shows the analysis of the Xsens sensor. The datasheet provides only the minimal information. This is properly re-scaled for the acquisition frequency of the dataset (250 Hz for the Navchip and 100 Hz for the Xsens sensors). The analysis through the online GUI (and the GMWM) allows for a refined analysis of the stochastic model. 109

7.1 Direct influence of constant gyroscope bias (8 mrad/s) and accelerometer bias (10 mg) on attitude and positon over different time periods. 114

8.1 Influence of different calibration parameters for the accelerometer (bias, scale-factor, and non-orthogonality) on the 100 simulated attitude data. 124
8.2 Influence of different calibration scenarios on the attitude determined by the REQUEST algorithm and by GNSS/INS fusion. Absolute attitude values for top: prior take-off, and bottom: after landing. 126
8.3 Comparison between the attitude provided by the photogrammetric software Pix4D and the REQUEST algorithm. 128
8.4 Error statistics for the 30 s GNSS outage for different IMU configurations. 130

9.1 Summary of the errors in the attitude from the navigation solution between our IMU with its different configurations and the reference AirINS. 135
9.2 Summary of orientation differences between INS/GNSS derived trajectory and that resulting from the photogrammetric adjustment per photo and IMU. . . . 137
9.3 Summary of the orientation differences between INS/GNSS derived trajectory and that resulting from the photogrammetric adjustment for the IGN camera. . 146

D.1 Gyroscope X-axis 168
D.2 Gyroscope Y-axis 168
D.3 Gyroscope Z-axis 168
D.4 Accelerometer X-axis 169
D.5 Accelerometer Y-axis 169
D.6 Accelerometer Z-axis 169
D.7 Gyroscope X-axis 170
D.8 Gyroscope Y-axis 170
D.9 Gyroscope Z-axis 170
D.10 Accelerometer X-axis 171
D.11 Accelerometer Y-axis 171
D.12 Accelerometer Z-axis 171
D.13 Gyroscope X-axis 172
D.14 Gyroscope Y-axis 172
D.15 Gyroscope Z-axis 172
D.16 Accelerometer X-axis 173
D.17 Accelerometer Y-axis 173
D.18 Accelerometer Z-axis 173
D.19 Gyroscope X-axis 174
D.20 Gyroscope Y-axis 174
D.21 Gyroscope Z-axis 174

D.22 Accelerometer X-axis . . . 175
D.23 Accelerometer Y-axis . . . 175
D.24 Accelerometer Z-axis . . . 175
D.25 Gyroscope X-axis . . . 176
D.26 Gyroscope Y-axis . . . 176
D.27 Gyroscope Z-axis . . . 176
D.28 Accelerometer X-axis . . . 177
D.29 Accelerometer Y-axis . . . 177
D.30 Accelerometer Z-axis . . . 177
D.31 Gyroscope X-axis . . . 178
D.32 Gyroscope Y-axis . . . 178
D.33 Gyroscope Z-axis . . . 178
D.34 Accelerometer X-axis . . . 179
D.35 Accelerometer Y-axis . . . 179
D.36 Accelerometer Z-axis . . . 179
D.37 Gyroscope X-axis . . . 180
D.38 Gyroscope Y-axis . . . 180
D.39 Gyroscope Z-axis . . . 180
D.40 Accelerometer X-axis . . . 181
D.41 Accelerometer Y-axis . . . 181
D.42 Accelerometer Z-axis . . . 181
D.43 Gyroscope X-axis . . . 182
D.44 Gyroscope Y-axis . . . 182
D.45 Gyroscope Z-axis . . . 182
D.46 Accelerometer X-axis . . . 183
D.47 Accelerometer Y-axis . . . 183
D.48 Accelerometer Z-axis . . . 183

Conventions and Notation

Notation

Typology of a Variable

s	scalar, element of a vector or a matrix
$\boldsymbol{s}$	vector
$\boldsymbol{S}$	matrix

State of a Variable

s	measured value
$\check{s}$	true value
$\mathring{s}$	approximate value
$\hat{s}$	estimated value

Abbreviation

AC	Auto-Correlation
ADC	Analog to Digital Converter
AGL	Above Ground Level
ALS	Airborne Laser Scanning
AR1	Auto-Regressive model of order one
ASCII	American Standard Code for Information Interchange
AV	Allan Variance
BI	Bias Instability
CI	Confidence Interval
CP-DGPS	Carrier Phase DGPS
DCM	Direction Cosine Matrix
DGPS	Differential GPS
DR	Drift
EKF	Extended Kalman Filter
FPGA	Field Programmable Gate Array

GALILEO	European Satellite Navigation System
GCS	Ground Control Station
GM	Gauss-Markov
GMWM	Generalized Method of Wavelet Moments
GNSS	Global Navigation Satellite System
GPS	Navstar Global Positioning System
GREIS	GNSS Receiver External Interface Specification
GUI	Graphical User Interface
IMU	Inertial Measurement Unit
INS	Inertial Navigation System
LS	Least-Squares
MEMS	Micro-Electro-Mechanical System
MLE	Maximum Likelihood Estimator
MPC	Multi-Position Calibration
NMEA	National Marine Electronics Association
PPK	Post Processed Kinematic
PPP	Precise Point Positioning
PPS	Pulse Per Second
PSD	Power Spectral Density
PVA	Position, Velocity, and Attitude
PVT	Position, Velocity, and Timing
QN	Quantization Noise
RT-PPP	Real Time PPP
RTK	Real Time Kinematic
RC	Random Constant
RW	Random Walk
RR	Random Rate
RS-232	Recommended Standard 232
SEP	Spherical Error Probable
SPP	Single Point Positioning
SV	Satellite Vehicle
SVD	Singular-Value Decomposition
SIMU	Synthetic IMU
TTL	Transistor-Transistor Logic
UART	Universally Asynchronous Receiver/Transmitter
UAV	Unmanned Aerial Vehicle

UTC	Coordinated Universal Time
VRS	Virtual Reference Station
WAAS	Wide Area Augmentation System
WMM	World Magnetic Model
WGS84	World Geodetic System 1984
WV	Wavelet Variance
WVIC	Wavelet Variance Information Criterion
WN	White Noise

1 Introduction

1.1 Context

Accelerometers and gyroscopes are inertial sensors measuring specific forces and angular rates, respectively. When spatially assembled, for instance into an orthogonal triad, they have become an essential part of a large variety of motion sensing systems. They were originally developed as the sensing components of Inertial Navigation System (INS) that are categorized according to their performance (precision) into: strategic-grade, navigation-grade, tactical-grade and low-cost [Greenspan, 1995]. An Inertial Measurement Unit (IMU) is the instrumental part of an INS, where the latter comprises also a navigation computer. In particular, the low-cost IMU enjoyed a steady boom over the last decades due to advances in the field of Micro-Electro-Mechanical System (MEMS) to become omnipresent in new domains of robotics, autonomous systems, as well as consumer electronics including smartphones, tablets, and wearable devices [Shaeffer, 2013].

Conventionally, the measurement on the x-axis l_x of an inertial sensor (accelerometer or gyroscope) can be expressed in terms of the true applied specific force f or angular velocity ω, respectively, along its sensitive axis $\check{l}_x$ and the forces or angular velocities acting along the other two other axes $\check{l}_y$ and $\check{l}_z$, respectively, by the equation [Titterton and Weston, 2004]:

$$l_x = (1 + S_x)\check{l}_x + \theta_y \check{l}_y + \theta_z \check{l}_z + b_x + \varepsilon_x, \tag{1.1}$$

where $\check{l} \in [f, \omega]$, S_x is the scale-factor error, θ_y and θ_z are the cross-axis coupling factors due to non-orthogonality of the assembly, b_x is the mean measurement bias, and ε_x is the random bias of the considered x-axis. Practical observation of scale-factor and bias is shown in Figure 1.1 as the discrepancy between the actual motion (dotted line designated as input) and the sensed data (full line designated as output). The prevailing effect (e.g., mean bias and mean slope) of these two error sources is usually deterministic and can be calibrated in

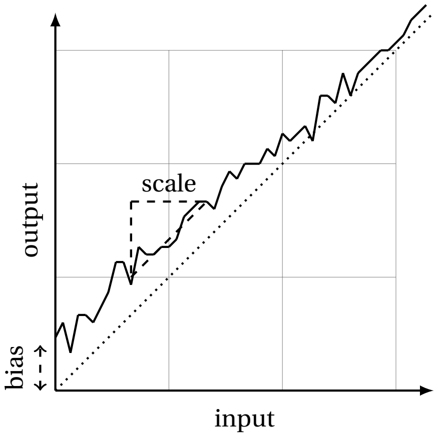

Figure 1.1: Input/output relation of a sensor affected by a constant offset also called bias, and a scale-factor error.

a laboratory using reference signals [Titterton and Weston, 2004]. Similar calibration can be completed for the different cross-coupling effects coming from the other axes of the sensor triad.

The residual, non-calibrated *random* part of b_x and ε_x is transformed by numerical processing called "strapdown inertial navigation" [Titterton and Weston, 2004] into errors in attitude, velocity, and position. Data fusion algorithms, such as the Extended Kalman Filter (EKF), mitigates the transformed effect of these errors using external aiding [Gelb and Corporation, 1994]. The basic principle of the filter is to apply the estimated errors as corrections onto the measurements as schematically depicted in Figure 1.2.

To achieve optimal estimation, the characteristics of random errors involving the inertial sensors need to be known in terms of their structure (type of random processes) as well as the value of their parameters. For instance, in state-space formulation of the sensor estimation

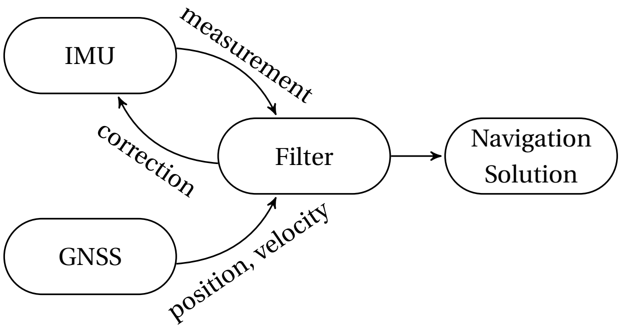

Figure 1.2: The filter estimates the corrections for the IMU, whenever an external aiding (e.g., the GNSS) provides a measurement update.

problem [Farrell and Barth, 1999], the time-correlated errors are modeled within an augmented state-vector, and their realization (actual magnitude) is observed under certain conditions and removed by a feedback mechanism. However, as the error structure of MEMS low-cost inertial sensors is inherently complex [Allen et al., 1998; Kraft et al., 1997], their representation by state-space models is less straightforward, and the determination of correct parameters becomes involved. Figure 1.3 shows an example of two MEMS sensors with each a different typology of noise, modeling of which has motivated a considerable amount of research [Nikolic et al., 2016; Xue et al., 2015; Zhang et al., 2016].

The main statistical methods employed for noise characterization in inertial sensors are: the Maximum Likelihood Estimator (MLE) [Stebler et al., 2011; Zhao et al., 2011] and the Allan Variance [El-Sheimy et al., 2008; Guerrier et al., 2016; Vaccaro and Zaki, 2012], or more recently, the Generalized Method of Wavelet Moments (GMWM) [Guerrier et al., 2013a]. The latter decomposes the observed noise (long time-series) into the wavelet variances. For a given model structure it chooses the parameters to minimize the squared distance to the wavelet variances induced by such a model. Its extension allows categorizing different model structures by considering the goodness of fit per model versus its complexity [Molinari et al., 2015]. The GMWM estimator is proven to be optimal and, in contrary to other methods, yields consistent estimates for composite stochastic processes [Guerrier et al., 2013a]. The effect of such noises is present in low-cost MEMS inertial sensors and its accurate modeling needs to be reflected in the filter design as it influences the performance of integrated navigation [Stebler et al., 2011; Guerrier et al., 2015]. Nevertheless, these designs use an important assumption that the noise parameters are stationary with respect to environmental conditions, which – as

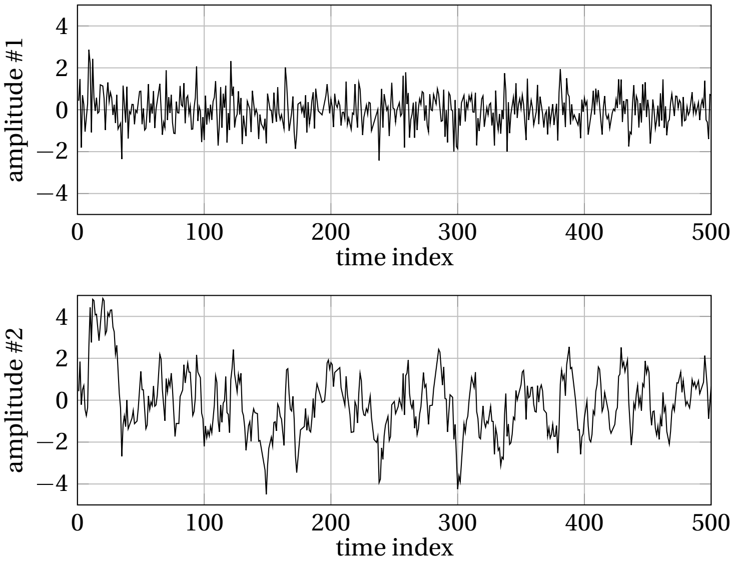

Figure 1.3: Two sensors showing different typology and amplitude of sensor noise.

will be shown in this work – is not the case. Additionally, the GMWM analysis and its derived state-space models do not consider the randomness of the mean/offsets, albeit these may have a strong or even dominant contribution in MEMS inertial sensors.

1.2 Motivation

- The factory calibration determines (and compensates for) the variation of the basic model parameters from Equation 1.1 as b_x, S_x with respect to temperature or dynamic cycling over a given period of time [Titterton and Weston, 2004]. Although these conditions are adequately addressed when dealing with the deterministic errors (i.e., the bias changes as a function of the temperature, which is taken into consideration when dealing with the sensor measurements by observing the information from a thermometer), this is unfortunately not the case for the stochastic properties of the error measurements. Indeed, the complex models underlying the stochastic errors are affected by the varying external conditions, which modify the parameter values through time. This fact has not been rigorously addressed so far. This motivates proposing an extension to the GMWM estimator to determine the variation of stochastic parameters adequately as a function of such external co-variate (be it motion dynamics, temperature, pressure, or other influences).

- Second, although the constant bias/offset in the observed signal can be easily represented by state-space augmentation, its actual estimate depends on observing conditions that are among others strongly correlated with (i) initial magnitude and associated incertitude, (ii) the goodness of initial attitude (coarse alignment), (iii) available aiding and trajectory dynamics. For these reasons, it is preferential to determine the most significant part of the bias before starting the process of navigation, especially in specific applications. One example is the autonomous navigation and sensor orientation with drones. The challenge is to use external observations to estimate/compensate the amount of the error signals as much as possible over a short observation time (around 15 min for a drone). This may be difficult with sufficient accuracy when initial discrepancies are large. The type of error as switch-on bias cannot be calibrated in the factory or the laboratory, as it changes every time the sensor is turned on/off. Thus, a pre-mission calibration is required and proposed here, for a variety of sensors.

- The position error is rapidly increasing when the external aid from the Global Navigation Satellite System (GNSS) is not available. This is, for instance, the case when the sky gets obstructed (e.g., tunnel, canyon of buildings). During this, inertial coasting through strapdown inertial navigation of the IMU is performed. If large systematic errors in the inertial readings are not mitigated, then the discrepancy from a real trajectory will proliferate in time. The forward filter is used during the processing for real-time applications. The smoothing of the trajectory improves the quality of the estimated position and attitude. Nevertheless, the initial attitude determination is of great importance for navigation. A poorly initialized attitude will take more time to be corrected, alongside the other sensor errors. Estimating initial heading with MEMS-IMU only is difficult if not impossible, reason for which the system can be equipped with other sensors, such as magnetometers. Proper attitude determination is essential in applications requiring direct sensor orientation, such as Airborne Laser Scanning (ALS). Thus, a way of estimating the initial attitude as good as possible with a limited number of sensors is proposed here.

- The packaging of such a system in small and light-weight applications is of large importance. The potential use in aerial applications for small Unmanned Aerial Vehicle (UAV) is big. The automatic navigation capabilities of UAVs over larger distances in open spaces require a firm reception of GNSS signals. This is not guaranteed in urban or natural corridors. Hence a potential flying in these regions is always risky. The concepts of ultra-safe navigation at low-cost were already introduced in other projects [Molina et al., 2011]. Losing satellite-based positioning functionality may be problematic if used in applications such as automated landing, autonomous navigation, and direct sensor orientation. For these reasons, the correct fusion of redundant, yet small sensors is also investigated.

1.3 Methodology

The aforementioned problems are divided into the following two parts:

- in-lab calibration and
- in-field calibration.

The *in-lab calibration* is composed of two elements: deterministics and stochastics. This first part is performed in the laboratory under controlled conditions and with a precise reference signal to rigorously determine the amount of the bias, non-orthogonality, and scale-factor for each sensor in the system. A calibration methodology for the different sensors is presented and evaluated.

The second component is the estimation of the stochastic error model and its parameters. These include their properties under different scenarios: without and with a changing covariate, such as temperature and motion dynamics. The specific framework for stochastic error analysis is presented.

The *in-field calibration* is composed of two parts as well, the first performed just before the mission starts (e.g., UAV take-off). This part is dedicated to the deterministic errors, that change their amount and quantity each time the system is powered on. This is the case for the IMU switch on/off bias or the biases due to environmental dependencies (e.g., magnetic perturbations depending on the location and setup).

The calibrated sensor measurements are then used to calculate the initial attitude, which is required for starting the strapdown navigation. After the bias calibration and the initial attitude estimation, the mission can begin. As the real-time navigation of the drone will be based on the in-field calibration and the result from the attitude determination, these calibration steps are executed in real-time with feedback to the user.

1.4 Outline

The content of this document is divided into three parts:

I: Preliminaries

Chapter 2 gives a small introduction to different MEMS sensors. Inertial sensors, as well as other sensor technologies, are presented together with the most recent way of their fusion: integrated inertial navigation.

Chapter 3 discusses the challenges with the identification of stochastic models. Ways to define and estimate error models are presented.

II: Calibration Methodology

Chapter 4 presents the principles and methodologies used to calibrate inertial, magnetic, and pressure sensors for their deterministic errors.

Chapter 5 expands the theory of the analysis of the wavelet variances to take into account known covariates and their influence on the stochastic properties (i.e., non-stationary stochastic models). Real models are conceived for specific sensors with covariates in temperature and rotational dynamics.

Chapter 6 describes the implementation of the algorithms for the deterministic error calibration and its usage. Then, an online web application is presented for the analysis of ”user-presented“ error-signals, which allows for a complete and thorough, yet intuitive and straightforward stochastic error calibration.

III: Application

Chapter 7 shows the impact of a covariate and its influence on the stochastic properties on the estimation of navigation parameters. This is demonstrated within a simplified (2D) simulation scenario.

Chapter 8 shows the impact of pre-flight calibration and sensor fusion on the navigation solution.

Chapter 9 analyzes the performances of the developed applications and methodologies applied on systems used for mapping purposes.

Chapter 10 presents the summary with the conclusions of the conducted research and gives the perspectives for future work.

Preliminaries Part I

2 Sensors for Aided Navigation

2.1 Introduction

This chapter first provides a brief introduction to inertial technology and shows typical characteristics of current Micro-Electro-Mechanical System (MEMS) sensors used for integrated navigation. After an introduction to reference frames, the basic principles of strapdown inertial navigation and its integration is presented. Then, typical sensors used for inertial aiding are listed.

2.2 Inertial Sensors

2.2.1 Classification

An Inertial Measurement Unit (IMU) is usually composed of a triad of accelerometers and gyroscopes. These sensors measure specific force and angular velocity respectively on three perpendicular axes. A detailed description of the IMU with its different classifications based on the overall quality of its sensors as found in [Greenspan, 1995] is synthesized in Table 2.1. Navigation- and Tactical-grade sensors have considerably better performance, meaning that they can initialize their orientation on their own (i.e., self-align) as their gyroscope biases are small enough to sense the Earth rotation. On the other end of the scale are the MEMS-IMU. They are less expensive but have more complicated noise properties, which are challenging to model and/or calibrate. This stochastic modelling will be discussed later in Chapter 3 in more detail with several examples, while calibration aspects are proposed in Chapter 4. On the other hand, MEMS devices have the largest advantage of being small and lightweight, which make them attractive for applications in small embarked systems such as drones.

Table 2.1: Rough comparison (bias and price) between the different IMU-grades.

Grade	Navigation	Tactical	Low-cost
gyroscope bias [deg/h]	$0.005 - 0.01$	$0.1 - 10$	> 100
accelerometer bias [m/s^2]	$5 \cdot 10^{-5}$	$2 - 5 \cdot 10^{-3}$	$0.05 - 0.5$
price [$]	100000	10000-1000	10-100

2.2.2 IMU Characteristics

The characterization of an IMU is not straightforward as parameters in the datasheet of the manufacturer may not be complete. A possible (non-exhaustive) list of typical specifications contain

- Input Range
- Resolution
- Misalignment
- Noise Density
- In-run Bias Stability
- Scale Factor
- Scale Factor Linearity
- Bias (switch-on repeatability over temperature or time period)
- Acceleration dependency (called g-sensitivity)
- Temperature effects
- Data latency

Other parameters may influence the output as vibrations or pressure. Table 2.2 shows a partial extraction of the datasheets of several IMU based on currently available MEMS technology of higher quality taken from [Analog Devices, 2018a,b; Sensonor, 2017; Colibry, 2018; Intersense, 2018] while details are presented in Appendix C.3.

In all the lab-equipment and other experiments, we will use the "Intersense Navchip V1" IMU, that despite being considerably older (from the year 2010) has still a comparable performance to other IMU available today.

Table 2.2: Comparison between small tactical grade lightweight MEMS IMU.

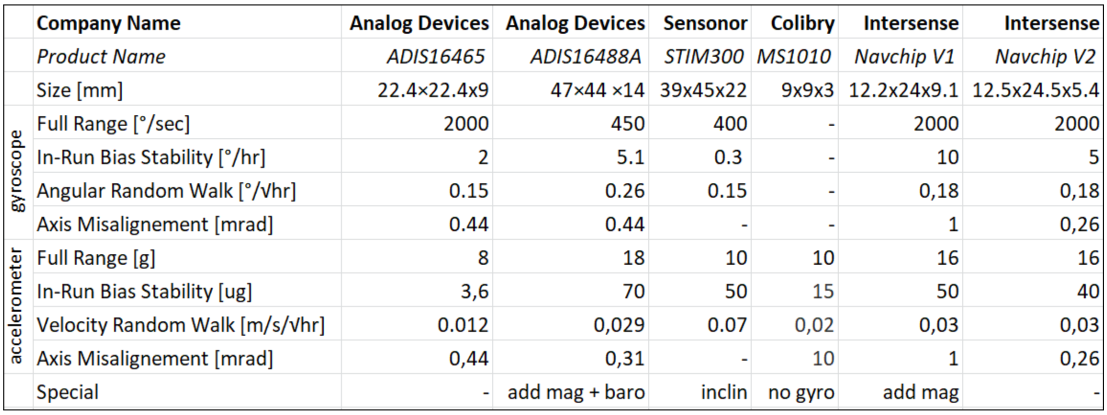

	Company Name	**Analog Devices**	**Analog Devices**	**Sensonor**	**Colibry**	**Intersense**	**Intersense**
	Product Name	*ADIS16465*	*ADIS16488A*	*STIM300*	*MS1010*	*Navchip V1*	*Navchip V2*
	Size [mm]	22.4×22.4x9	47×44 ×14	39x45x22	9x9x3	12.2x24x9.1	12.5x24.5x5.4
gyroscope	Full Range [°/sec]	2000	450	400	-	2000	2000
	In-Run Bias Stability [°/hr]	2	5.1	0.3	-	10	5
	Angular Random Walk [°/√hr]	0.15	0.26	0.15	-	0,18	0,18
	Axis Misalignement [mrad]	0.44	0.44	-	-	1	0,26
accelerometer	Full Range [g]	8	18	10	10	16	16
	In-Run Bias Stability [ug]	3,6	70	50	15	50	40
	Velocity Random Walk [m/s/√hr]	0.012	0,029	0.07	0,02	0,03	0,03
	Axis Misalignement [mrad]	0,44	0,31	-	10	1	0,26
	Special	-	add mag + baro	inclin	no gyro	add mag	-

Figure 2.1: Pictures of MEMS IMUs taken from [Analog Devices, 2018a,b; Sensonor, 2017; Colibry, 2018; Intersense, 2018] and Section C.3

2.3 Reference Frames

Different coordinate frames need to be defined within the context of inertial navigation. Some of them are briefly introduced here, where a detailed description can be found in [Stebler, 2013].

2.3.1 Inertial Frame

The inertial frame (x_i, y_i, and z_i) is a non-accelerating and non-rotating reference frame that is at rest or subject to a uniform translational motion. In such a frame, the laws of Newtonian mechanics are valid. For the purpose of navigation, an inertial frame is approximated as a celestial frame with origin at the center of mass of the Earth, such that the x_i-axis points towards the Vernal equinox and is, thus, the "spring" intersection line between the equatorial and the ecliptic plane. The z_i-axis points towards the mean celestial pole, and the y_i-axis completes the 3D right-handed Cartesian system.

2.3.2 Earth Frame

The Earth frame (x_e, y_e, and z_e) is an equatorial frame with origin at the center of mass of the Earth, such that the x_e-axis points towards the Greenwich meridian, the z_e-axis points towards the mean direction of the rotation axis of the Earth, and the y_e-axis completes the 3D right-handed Cartesian system. This frame is, therefore, an Earth Centered Earth Fixed (ECEF) frame. Examples of important realizations are the International Terrestrial Reference Frame (ITRF) and the World Geodetic System 1984 (WGS84) being the reference frame of the American Navstar Global Positioning System (GPS). Any point in this frame can be expressed either in Cartesian coordinates (x_e , y_e , z_e) or for a defined Geodetic System in ellipsoidal coordinates (ϕ, λ, h) with the latitude ϕ, the longitude λ, and the height h.

2.3.3 Local-Level Frame

The local-level frame (x_l, y_l, and z_l) is a local geodetic frame with arbitrary origin, for example a point on the Earth surface, such that the x_l-axis points to the north, the y_l-axis points to the east, and the z_l-axis points to the local nadir (down). For the purpose of navigation, the z_l direction may be considered as orthogonal to a tangent-plane of the ellipsoid at this arbitrary point. This triad of vectors constitutes the right-handed North-East-Down (NED) frame.

2.3.4 Body Frame

The body frame (x_b, y_b, and z_b) is a frame attached to the body of the vehicle. In navigation, the usual convention is to choose the forward or longitudinal direction of the vehicle for the x_b-axis, while the y_b-axis points towards the right side of the vehicle. The z_b-axis completes the triad and points downward. The rotation matrix R_l^b, transforming vectors from local-level frame to body frame, is defined as follows, where Euler angles (roll r, pitch p, and yaw y) are used as attitude parameters:

$$\boldsymbol{R}_l^b = \boldsymbol{R}_1(r)\boldsymbol{R}_2(p)\boldsymbol{R}_3(y), \tag{2.1}$$

with the individual rotational matrices defined as:

$$\begin{aligned}
\boldsymbol{R}_1(r) &= \begin{bmatrix} 1 & 0 & 0 \\ 0 & \cos(r) & \sin(r) \\ 0 & -\sin(r) & \cos(r) \end{bmatrix}, \\
\boldsymbol{R}_2(p) &= \begin{bmatrix} \cos(p) & 0 & -\sin(p) \\ 0 & 1 & 0 \\ \sin(p) & 0 & \cos(p) \end{bmatrix}, \text{ and} \\
\boldsymbol{R}_3(y) &= \begin{bmatrix} \cos(y) & \sin(y) & 0 \\ -\sin(y) & \cos(y) & 0 \\ 0 & 0 & 1 \end{bmatrix}.
\end{aligned} \tag{2.2}$$

Other sequences of Euler angles are used in photogrammetry (ω, ϕ, κ). As the parametrization of attitude by Euler angles represents a singularity (at $p = 90°$) other rotation representations can be considered such as quaternions, which are extensively discussed in [Altmann, 1986].

Although other frames related to sensors can be defined, it will be sufficient here to consider the x-axis of an accelerometer in an IMU as the one coinciding with the x-axis of the body frame.

2.4 Strapdown Inertial Navigation

An Inertial Navigation System (INS) uses the physical properties of its sensors to sense the specific force $\boldsymbol{f}^b$ acting on the body and the rotation rate $\boldsymbol{\omega}_{ib}^b$ of a body with respect to the inertial frame (non-rotating & non-accelerating) expressed in the body frame. The respective measurements are, after proper projection and correction, integrated over time.

The first-order navigation equation in the l-frame can be summarized in the following vector notation $\boldsymbol{x}$ from [Stebler, 2013]:

$$\dot{\boldsymbol{x}}^l = \begin{bmatrix} \dot{\boldsymbol{r}}_e^l \\ \dot{\boldsymbol{v}}_e^l \\ \dot{\boldsymbol{q}}_b^l \end{bmatrix} = \begin{bmatrix} \boldsymbol{D}^{-1}\boldsymbol{v}_e^l \\ \boldsymbol{R}_b^l f^b - \left(2\boldsymbol{\Omega}_{ie}^l + \boldsymbol{\Omega}_{el}^l\right)\boldsymbol{v}_e^l + \boldsymbol{g}^l \\ \frac{1}{2}\boldsymbol{q}_b^l \otimes \left[\boldsymbol{\omega}_{lb}^b\right]_q \end{bmatrix}. \tag{2.3}$$

The position is expressed with ellipsoidal coordinates in the Earth frame as $\boldsymbol{r}_e^l = [\phi, \lambda, h]^T$. The velocity is represented in the Earth frame and expressed in the NED frame as $\boldsymbol{v}_e^l = [v_N, v_E, v_D]^T$. The orientation from body frame with respect to the local frame here is represented by the quaternion $\boldsymbol{q}_b^l = [q_0, q_1, q_2, q_3]^T$.

The matrix $\boldsymbol{D}^{-1}$ is defined as

$$\boldsymbol{D}^{-1} = \begin{bmatrix} \frac{1}{R_M + h} & 0 & 0 \\ 0 & \frac{1}{(R_P + h)\cos(\phi)} & 0 \\ 0 & 0 & -1 \end{bmatrix}. \tag{2.4}$$

The meridian radius of curvature R_M is expressed as

$$R_M = \frac{a(1-e^2)}{(1-e^2\sin^2(\phi))^{3/2}}, \tag{2.5}$$

with the quantities a and e the semi-major axis and first numerical eccentricity of the reference ellipsoid, respectively.

The prime vertical radius of curvature R_P is expressed as

$$R_P = \frac{a}{(1-e^2\sin^2(\phi))^{1/2}}. \tag{2.6}$$

The rotation matrix $\boldsymbol{R}_b^l$ is a function of the quaternion $\boldsymbol{q}_b^l$ and can be computed as

$$\boldsymbol{R}_b^l = f\left(\boldsymbol{q}_b^l\right) \begin{bmatrix} q_0^2 + q_1^2 - q_2^2 - q_3^2 & 2(q_1q_2 - q_0q_3) & 2(q_1q_3 + q_0q_2) \\ 2(q_1q_2 + q_0q_3) & q_0^2 - q_1^2 + q_2^2 - q_3^2 & 2(q_2q_3 - q_0q_1) \\ 2(q_1q_3 - q_0q_2) & 2(q_2q_3 + q_0q_1) & q_0^2 - q_1^2 - q_2^2 + q_3^2 \end{bmatrix}. \tag{2.7}$$

The vector $\boldsymbol{g}^l$ represents the normal gravity vector in the ellipsoidal local frame. The vector $\boldsymbol{\omega}_{lb}^b$ is computed from

$$\boldsymbol{\omega}_{lb}^b = \boldsymbol{\omega}_{ib}^b - \left(\boldsymbol{R}_b^l\right)^T(\boldsymbol{\omega}_{ie}^l + \boldsymbol{\omega}_{el}^l), \tag{2.8}$$

where the angular velocity of the Earth frame with respect to the inertial frame expressed in the local frame is $\boldsymbol{\omega}_{ie}^{l} = [\omega_{ie}\cos\phi \;\; 0 \;\; -\omega_{ie}\sin\phi]^T$, and the angular velocity of the local frame with respect to the Earth frame expressed in the local frame is $\boldsymbol{\omega}_{el}^{l} = \left[\dot{\lambda}\cos\phi \;\; -\dot{\phi} \;\; \dot{\lambda}\sin\phi\right]^T$.

As for the notation used, the $\boldsymbol{\Omega}_{pq}^{r}$ represents a skew-symmetrix matrix associated with the vector $\boldsymbol{\omega}_{pq}^{r} = [\omega_1 \;\; \omega_2 \;\; \omega_3]$ as

$$\boldsymbol{\Omega}_{pq}^{r} = \begin{bmatrix} 0 & -\omega_3 & \omega_2 \\ \omega_3 & 0 & -\omega_1 \\ -\omega_2 & \omega_1 & 0 \end{bmatrix}, \tag{2.9}$$

and the mathematical operator $\otimes$ represents the quaternion product between two quaternions $\boldsymbol{q} = [q_0 \;\; q_1 \;\; q_2 \;\; q_3]^T$ and $\boldsymbol{p} = [p_0 \;\; p_1 \;\; p_2 \;\; p_3]^T$ expressed as

$$\boldsymbol{q} \otimes \boldsymbol{p} = \begin{bmatrix} q_0 p_0 - q_1 p_1 - q_2 p_2 - q_3 p_3 \\ q_0 p_1 + q_1 p_0 + q_2 p_3 - q_3 p_2 \\ q_0 p_2 + q_2 p_0 - q_1 p_3 + q_3 p_1 \\ q_0 p_3 + q_3 p_0 + q_1 p_2 - q_2 p_1 \end{bmatrix}. \tag{2.10}$$

Equation 2.3 is resolved by the so-called strapdown navigation algorithm for each new measurements with respect to the past solution (dead reckoning) [Stebler, 2013]. The system needs to be initialized with position, velocity, and attitude at time zero.

The navigation solution provided by the INS suffers from different kinds of errors. Firstly, initial conditions are required for the position, velocity, and attitude. Any errors in these initial conditions are propagated in time. With the help of the Global Navigation Satellite System (GNSS), the largest challenge is in the altitude initialization. Secondly, the measurements of the sensors (accelerometer and gyroscope) suffer from different types of errors (deterministic and stochastic in nature), which will, over time, accumulate as in navigational errors. Thirdly, additional errors can come from computational errors and simplifications (e.g., local frame is stationary with respect to the inertial frame, gravity models).

2.5 Integrated Navigation

2.5.1 Fusion Principle

To mitigate the influence of initialization errors as well as systematic and random errors in an inertial navigator, the IMU data are integrated with satellite positioning as well as with other aiding sensors. The most common way of integrating is the state-space approach [Gelb and Corporation, 1994], and the application of Kalman filter (real-time) and smoother (post-processing) [Titterton and Weston, 2004] introduced by Rudolf E. Kálmán in 1960. It is widely known and used in the science community ever since. Its main ability is the optimal combination of sensors of the same type (using the same physical effects for the measurements) and the fusion of sensors of different types (using different physical effects). One core assumption is the property of the signal (be it the noise or the actual measurement) of being Gaussian. This property allows to linearly combine different Gaussian measurements resulting in another Gaussian distribution. In other words, time correlated or systematic effects in observations are modeled as additional parameters in such a way that the resulting distribution is Gaussian.

The most important source of aiding is satellite positioning. Thanks to that, the drift of the INS can be suppressed/eliminated by comparing it to the GNSS, which long-term accuracy is excellent. On the other hand, the INS can bridge the intervals between subsequent GNSS solutions. Different levels of integration exist, but here the *loosely coupled* scheme is detailed. It utilizes GNSS-derived position and velocity. Their differences with relation to INS find themselves in the filter (as observations). The filter estimated corrections are injected to the INS-solution as well as other error parameters. Figure 2.2 shows a possible realization of such integration. This approach is simple, but if there is no GNSS solution (due to an insufficient number of satellites observations), then no new corrections can be computed. In this case, the INS carries on alone, or is only partially controlled (e.g., in height with barometric observations).

2.5.2 Extended Kalman Filter/Smoother

The Kalman filter shown in Figure 2.2 is used to estimate the errors in the INS-predicted trajectory as well as in the sensors. The parameters of its state vector δx can be comprised of the position error δr, the speed error δv, the attitude error $\delta\phi$. They represent the system states.

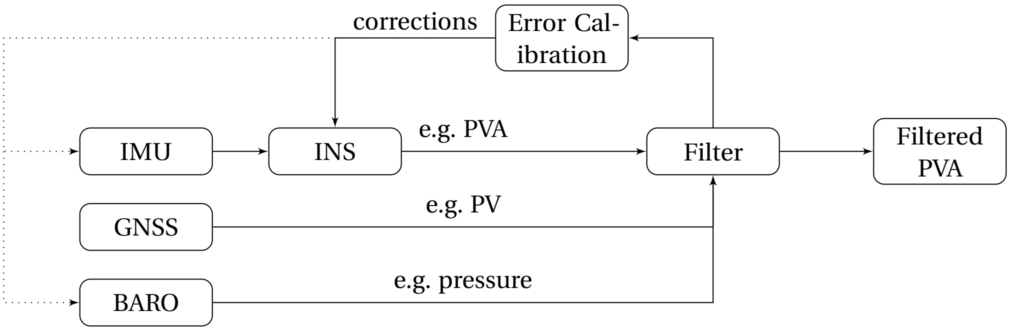

Figure 2.2: The loosely coupled GNSS/INS integration as a possible example for the sensor fusion. Both systems work completely independently while their solutions are only fused at the end by means of a filter. Eventual feedback on the error (corrections) is directly fed back into the INS and utilized for the subsequent processes.

The accelerometer error δe_a and the errors in the gyroscope δe_g represent the augmented states, showing the error states. They incorporate a certain number of time-correlated errors in accelerometers and gyroscopes. Their implementation depends on the design criteria. The following shows an example of a possible state-vector, where an additional error state for the barometer bias was added:

$$\delta x = [\underbrace{\delta r \;\; \delta v \;\; \delta\phi}_{\text{system states}} \;\; \underbrace{\delta e_a \;\; \delta e_g \;\; \delta e_b}_{\text{error states}}]^\top \tag{2.11}$$

The Kalman filter is an iterative procedure, where update and prediction in the time k take turns. The future state x_{k+1} only depends on the current state x_k as well as the new measurement z_{k+1} (property of a Markov Chain). This property is very interesting for numerical evaluation in terms of computational resources. Figure 2.3 gives a simple overview of this process. The time relation between the states x is not necessarily linear. This fact can be circumvented by linearising the equations (e.g., Equation 2.3 possibly extended by auxiliary states) around the current estimate, while applying the estimated state-vector for correcting the trajectory as well as to time-correlated sensor errors. This gives rise to the *Extended Kalman Filter* (EKF). The filter for discrete times is expressed as

$$\begin{aligned} \boldsymbol{x}_k &= \boldsymbol{f}(\boldsymbol{x}_{k-1}, \boldsymbol{u}_{k-1}) + \boldsymbol{\Gamma}_{k-1}\boldsymbol{w}_{k-1} \\ \boldsymbol{z}_k &= \boldsymbol{h}(\boldsymbol{x}_k) + \boldsymbol{v}_{k-1} \end{aligned} \tag{2.12}$$

where $\boldsymbol{f}$ is the function relating the state of the previous step the to the current step and $\boldsymbol{h}$ relates the observations to the current states. The vectors $\boldsymbol{w}_k$ and $\boldsymbol{v}_k$ are zero-mean Gaussian white noise vectors. Their covariance matrices are represented by $\boldsymbol{Q}_k$ and $\boldsymbol{R}_k$ respectively. $\boldsymbol{\Gamma}_{k-1}$ represent the coupling between the state and defined white noise vectors.

The predicted state $\boldsymbol{x}_k^-$ can be calculated and the covariance matrix $\boldsymbol{P}_k^-$ is computed using the transition matrix $\boldsymbol{\Phi}_{k-1}$ using:

$$\begin{aligned} \boldsymbol{x}_k^- &= \boldsymbol{f}(\boldsymbol{x}_{k-1}^+, \boldsymbol{u}_{k-1}), \\ \boldsymbol{P}_k^- &= \boldsymbol{\Phi}_{k-1}\boldsymbol{P}_{k-1}^+\boldsymbol{\Phi}_{k-1}^T + \boldsymbol{\Gamma}_{k-1}\boldsymbol{Q}_{k-1}\boldsymbol{\Gamma}_{k-1}^T, \end{aligned} \tag{2.13}$$

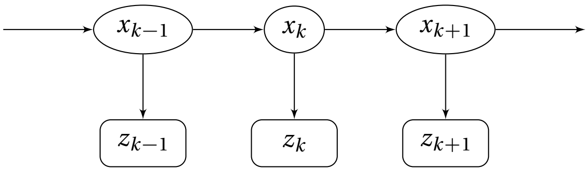

Figure 2.3: Hidden states x and observation z as a function of time k for the Markov Chain. The current state only depends on the previous state and the present measurement.

where $\boldsymbol{\Phi}_{k-1} = \frac{\partial \boldsymbol{f}(\boldsymbol{x}_{k-1}^{+}, \boldsymbol{u}_{k-1})}{\partial \boldsymbol{x}}$. With measurement $\boldsymbol{z}_k$ and its covariance matrix $\boldsymbol{R}_k$ the Kalman gain $\boldsymbol{K}_k$,the updated state vector $\boldsymbol{x}_k^{+}$, and its updated covariance matrix $\boldsymbol{P}_k^{+}$ can be computed as:

$$\begin{aligned}
\boldsymbol{K}_k &= \boldsymbol{P}_k^{-} \boldsymbol{H}_k^{T} (\boldsymbol{H}_k \boldsymbol{P}_k^{-} \boldsymbol{H}_k^{T} + \boldsymbol{R}_k)^{-1}, \\
\boldsymbol{P}_k^{+} &= (\boldsymbol{I} - \boldsymbol{K}_k \boldsymbol{H}_k) \boldsymbol{P}_k^{-}, \\
\boldsymbol{x}_k^{+} &= \boldsymbol{x}_k^{-} + \boldsymbol{K}_k (\boldsymbol{z}_k - \boldsymbol{h}(\boldsymbol{x}_k^{-})),
\end{aligned} \tag{2.14}$$

with $\boldsymbol{H}_k = \frac{\partial \boldsymbol{h}_k(\boldsymbol{x}_{k-1}^{+})}{\partial \boldsymbol{x}}$.

In general, the linearisation applies to the state transition model as well as the observation models. The crucial part for the filter is the proper initialization as well as the correct choice of the stochastic models which reflect the underlying certitude in modeling and observations.

The navigation solution can be smoothed in post-processing. This is achieved by combining the forward filtered solution with the backward direction in a "fixed-interval-smoother" [Wägli, 2009]. Another option is to smooth the data only in one single direction (forward or backward) by means of the "Rauch-Tung-Striebel" algorithm [Gelb and Corporation, 1994].

2.5.3 Redundant IMU

The concept of redundant IMUs is highlighted by [Wägli et al., 2010] for MEMS sensors and further investigated by [Stebler, 2013]. Apart from the possible detection of faulty observation, the sensor noise level can be estimated in a redundant-IMU configuration and its effect on navigation mitigated. Multiple IMUs can be combined together by different means. The simplest one is the so-called Synthetic IMU (SIMU): in this technique, the individual sensors are projected onto a "virtual" IMU with defined axes (see Figure 2.4). The merged data is only now introduced into the navigation processor. Hence one can replace a simple IMU by such synthetic IMU in the strapdown navigation (see Figure 2.2) with minimal adaptions. Another advantage is that defective sensors/axes can be identified and then excluded (if enough redundancy is available) prior to its utilization. However, errors in the individual sensors cannot be corrected Only the merged system is subject to corrections. Hence, this approach is applicable when the largest part of the systematic errors es removed by calibration (as presented in Chapter 4).

Averaging the sensor-readings (i.e., each axis of the sensors has the same weight) is simple. Nevertheless, giving different weights (i.e., as opposed to equal weights) to the individual sensor readings proves advantageous, when not every sensor has the same level of noise. However, it may be, that one sensor is defective and a simple averaging of all the data will lead to a large discrepancy. Different approaches (e.g., ARMA-GARCH and Markovian Regime-

Switching) to weigh the individual sensor-readings were proposed in detail in [Stebler, 2013]. These algorithms are applicable especially if the noise levels of the different sensors change significantly over time.

2.6 Aiding Sources

2.6.1 GNSS Position and Velocity

The GNSS is an absolute positioning system meaning that the Position, Velocity, and Timing (PVT) are provided with respect to the Earth. These are available when signals from a minimum of four satellites are tracked. Nowadays, there exist several systems. Each of them is controlled by a different entity. They are interoperable on some frequencies. Hence combination of them results in better coverage due to a higher number of tracked satellites. The GPS (U.S.), GLONASS (Russia) are fully functional systems while COMPAS (China) and the GALILEO (Europe) are being deployed. The observations and derived PVT from a receiver are provided usually with an update rate of around 1 Hz - 10 Hz. While some receivers have output rates of up to 100 Hz, nevertheless these are strongly correlated in time.

The dependency of a direct line of sight to the satellites brings this system to its limits when navigating through natural or urban corridors when obstructions cover a big part of the sky. There a position fix is not always possible under all circumstances while its quality varies according to the observed constellation. The systems are designed to provide positioning in the *meter*-level. In optimal conditions when ionospheric corrections are applied, *sub*-meter or *cm*-level positioning is possible but requires special setup such as multi-frequency (and multi-constellation) receivers operating in carrier-phase differential mode. This setup usually consists of a base-station on the ground, which data/corrections are then combined with the rover data either in real-time called Real Time Kinematic (RTK), or post-processing called Post

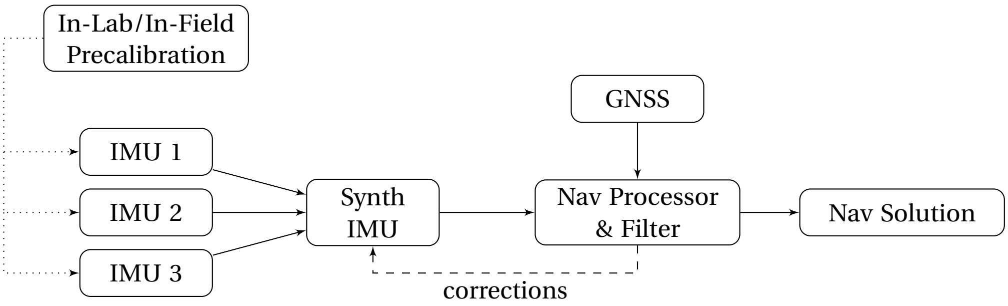

Figure 2.4: Principle of the synthetic IMU for the case with three individual IMUs: the measurements are projected onto a synthetic IMU. Its information is then used in the navigation processor Waegli et al. [2008].

Table 2.3: Comparison between the main properties of inertial and satellite navigation.

Property	INS	GNSS
Information	relative to start-point	absolute on Earth
Data Rate [Hz]	100 to few 1000	< 10
Accuracy	short term	long term
Availability	always	limited
Operation modes	strapdown, gimbalded	SPP, differential, RTK, PPP, single vs. multiple frequency and constellation
Weakness	sensor-errors, gravity field	signal reception, quality, attitude determination

Processed Kinematic (PPK). Although receiver-to-satellite ranges, range-rates, and carrier-phase observations can be used for inertial aiding [Wägli, 2009] with certain advantages [Farrell, 2001]. This work will consider the direct usage of GNSS derived PVT.

The presented properties of the GNSS are complementary to the properties of the IMU, which make them ideal candidates for combining their individual advantages. The significant disadvantage of the IMU is the long-term-instability, which is caused by the accumulation of sensor errors. Some of them can be eliminated by calibration, but remaining errors have a random character that can not be compensated apriori. In contrast, GNSS provides absolute positioning. A resumé of integrating inertial and satellite positioning is given in the Table 2.3.

2.6.2 Barometer

The barometer is a device which measures the pressure of a medium. The daily unit used in the weather forecast is hPa or bar, where 1 hPa is equivalent to 1 mbar. The pressure in the atmosphere is inversely proportional to the height above the surface. A modeled relation between the pressure p and the height h ranging from sea-level to several km above the surface of the earth can be found in [Atmosphere, 1962].

The barometer with its pressure measurement and the subsequent altitude calculations can be used for different applications. [Parviainen et al., 2011] uses the measurement changes in a relative way to estimate the road grade in combination with the accelerometer. [Zhang et al., 2012] improves the vertical GNSS solution with the barometer measurements while estimating the errors in the barometer first in an external filter. This augmented solution is then used in the navigation with improved confidence on the vertical axis. [Bevermeier et al., 2010] calibrates the barometer outputs with a topographic map, which is available at certain waypoints. After the successful calibration, the data is fused with the GNSS and the IMU. [Jonghyuk and Sukkarieh, 2003] does not calibrate the parameters of the barometer directly but rather does propose to model the measurement outputs with a first-order Gauss-Markov process. In Section 4.6 we describe a more rigorous approach of barometer-data usage within an INS based integration. For that, we need to specify first the observation equations and related parameters.

A typical evolution of pressure sensed by a barometer on a drone at two different flying heights is shown in Figure 2.5. The drone reaches the flight heights after several minutes of climbing. After completing a mapping mission, the drone comes back to the same place for landing.

The height can be derived from such pressure readings with several assumptions that are generally valid when flying close to the ground (<200 m above ground). The hydrostatic equation, assuming the atmosphere is static with relation to the Earth, states, that small changes in pressure dp depend on the density of the air ρ, the gravity g, and the slight change in the altitude dh:

$$dp = -\rho g dh. \tag{2.15}$$

Strictly speaking, the air density, as well as the gravity, are depending on the altitude too, but for applications using MEMS sensors and close to ground operations (e.g., small Unmanned Aerial Vehicle (UAV)) this dependency can be ignored or accounted for by simpler models [Atmosphere, 1962].

The air density ρ can be expressed using the equation of a perfect gas, which our atmosphere

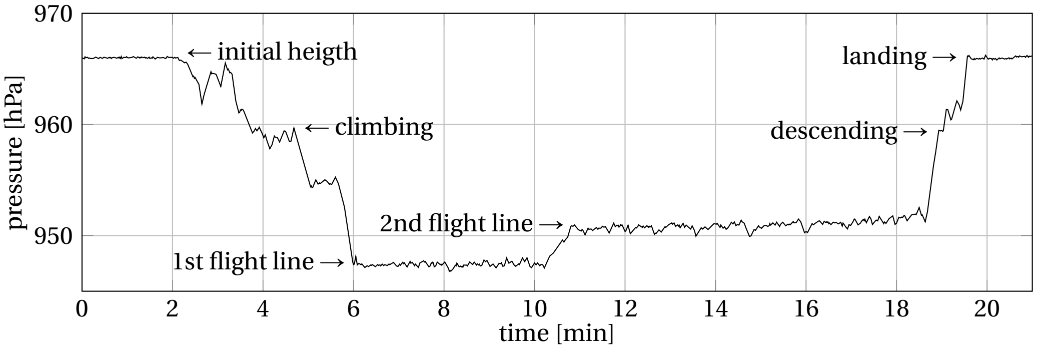

Figure 2.5: Evolution of the pressure after take-off during a typical mission with a difference in altitude of up to 200 m above ground.

is modeled after:

$$\rho = \frac{pM}{RT}, \tag{2.16}$$

where M is the molar mass of the air expressed in mol, R is the gas constant with a value of $8.3144598\,\mathrm{J\,mol^{-1}\,K^{-1}}$, and T is the temperature expressed in K. Substituting Equation 2.16 into Equation 2.15 yields after rearranging:

$$\frac{1}{p}dp = -\frac{Mg}{RT}dh. \tag{2.17}$$

An assumption is made, that the atmosphere is isothermic (i.e., its temperature is constant over the integrated altitudes). Indeed, for the drone flight <200 m above the ground, the thermal gradient over this region is negligible. Integrating Equation 2.17 on the left and right side from the initial altitude h_0 to some arbitrary altitude h_i gives:

$$\ln\left(\frac{p_i}{p_0}\right) = -\frac{Mg}{RT}(h_i - h_0), \tag{2.18}$$

where p_0 denotes the pressure at the initial altitude and p_i represents the pressure at the arbitrary altitude. By rearranging the terms, the equation expresses the altitude of a point h_i, if the temperature T, the initial altitude h_0, the pressure at the starting point p_0 and the pressure on the height of interest p_i are known:

$$h_i = h_0 - \frac{RT}{Mg}\ln\left(\frac{p_i}{p_0}\right). \tag{2.19}$$

The molar mass M of the air depends on the humidity. If water vapor is present, the molar mass will decrease (i.e., $M_{\text{humide}} < M_{\text{dry}}$). To get a precise altitude, the molar mass of the air has to be known accurately enough. Here again, we use the assumption, that this value changes only slowly in time and that it stays constant locally and temporally, as for most drone-operations. A similar problem exists with the pressure p_0 at the reference altitude h_0. Instead of tracking it continuously, we assume that the local pressure stays constant during the duration of the experiment (usually <1 h).

The influence of the parameters on the final height is resumed in Table 2.4. Standard pressure is chosen for the reference pressure p_0, whereas the pressure p_i was selected in such a manner to represent a height difference of roughly 200 m. The individual influences with their variations show that a precise knowledge of the pressure p_0 and p_i are crucial to the final altitude computation, as their influence is strong. In addition, the knowledge on the humidity of the air to correctly define the molar mass of the humid air is important too. These parameters influence the final altitude by several meters.

Table 2.4: Influence of the individual parameters on the final height using standard values and their variations.

Parameter	Unit	Typical value	Variation	Height influence
T	K	293.15	± 1 K	± 0.61 m
p_i	hPa	950	± 1 hPa	± 9.03 m
p_0	hPa	970	± 1 hPa	± 8.83 m
M	kg/mol	0.029	± 0.001 kg/mol	± 6.17 m

2.6.3 Magnetometer

The Earth's magnetic field is produced by several sources. One of the contributors is the Earth's liquid iron outer core that is in constant movement. Other materials like for instance magnetic minerals in the crust contribute to the magnetic field as well. The direction of this field can be sensed by a magnetometer with relation to the magnetic north that generally does not coincide with the geographic north.

The World Magnetic Model (WMM) provides the direction of this magnetic field given a specific location and a defined time. In the absence of local perturbation or other external influences such as ionospheric changes, and for latitudes $<75°$ the estimated accuracy of the WMM is $<0.5°$. The knowledge of the time is used as an input to the WMM, as the magnetic field evolves in direction and intensity over time. Due to this, the model has to be adapted after a few years, so such prediction is valid. The currently adopted model is called "WMM2015" and is valid until the year 2020. [Chulliat et al., 2015b] describe the usage of the model and explain its validity from a depth of 1 km under the Earth to several km above the surface of the Earth.

The implementation of the WMM via the freely accessible library [Chulliat et al., 2015a] provides seven elements per position as shown in Figure 2.6. These magnetic field elements are expressed in nT (nano Tesla). As example, the typical field strength measured in the Lausanne area is about 47 000 nT. The northerly intensity X, the easterly intensity Y, and the vertical intensity Z are orthogonal vectors. The vertical intensity is measured positively downwards with respect to the WGS84 ellipsoid, while the X intensity is in the direction of geographic north. The remaining parameters are the horizontal intensity H with its declination angle D, which is measured clockwise positively from the geographical north. The total intensity F with its inclination angle I is measured positively downward from the horizontal plane. The elements X, Y, and Z can be determined from F, I, and D and vice-versa. Note that although the orientation with relation to North is a prime interest when employing a three-axes magnetometer for navigation, the realization of the horizontal projection often requires accelerometers (e.g., IMU).

The magnetometer will sense in addition to the Earth's magnetic field other magnetic disturbances. These disturbances can come from other magnetic sources placed nearby. When these are constant per operating environment (electronic devices or specific location), then their effect can be possibly accounted for and removed by calibration (see Chapter 4).

2.6.4 Attitude Initialization

As mentioned before, the IMU measurements are integrated over time, but the initial conditions at time stamp t_0 need to be known. The initial position of the system is for instance provided by a GNSS receiver. The velocity can also be provided by the GNSS receiver or set to zero when the vehicle or the platform with the IMU is not moving with respect to the Earth surface. This is the moment where the initial attitude is computed. The accelerometers can be used to compute roll and pitch in the leveling procedure. With that, the gyroscope output is used to calculate the heading, as long as it "senses" the Earth rotation. Such static coarse alignment uses the measurements directly from the body frame and tries to relate them via the rotation matrix to the local frame. The procedure can be expressed by the projection of two vectors, which reference is known. The gravity vector expressed in the local-frame $\boldsymbol{g}^l$ and the Earth rotation in relation to the inertial-frame i expressed in the local-frame $\boldsymbol{\omega}^l_{ie}$ (which is a function of the position on the Earth) are related through the following equation:

$$\begin{bmatrix} -\boldsymbol{f}^b & \boldsymbol{\omega}^b_{ib} & -\boldsymbol{f}^b \times \boldsymbol{\omega}^b_{ib} \end{bmatrix} = \boldsymbol{R}^b_l \begin{bmatrix} \boldsymbol{g}^l & \boldsymbol{\omega}^l_{ie} & \boldsymbol{g}^l \times \boldsymbol{\omega}^l_{ie} \end{bmatrix}. \tag{2.20}$$

This equation is rearranged in a way to directly compute the attitude matrix as

$$\boldsymbol{R}^b_l = \begin{bmatrix} -\boldsymbol{f}^b & \boldsymbol{\omega}^b_{ib} & -\boldsymbol{f}^b \times \boldsymbol{\omega}^b_{ib} \end{bmatrix} \begin{bmatrix} \boldsymbol{g}^l & \boldsymbol{\omega}^l_{ie} & \boldsymbol{g}^l \times \boldsymbol{\omega}^l_{ie} \end{bmatrix}^{-1}. \tag{2.21}$$

The measurements can be averaged over several seconds to decrease the noise of the measurements. A problem arises when the matrix is non-invertible. This is, for instance, the case when

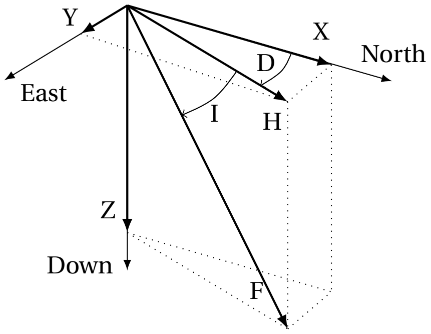

Figure 2.6: Representation of the seven magnetic parameters provided by the WMM software knowing position and time.

one of the vectors is close to zero. The detection of the Earth's rotation is for MEMS gyroscope challenging due to the increased noise level and because the rotation rate is a weak signal. In such a case one can use the magnetometer measurements instead of the gyroscope measurements as presented in [Wägli, 2009]. The representation is similar and uses the magnetometer measurements from the sensor in the body-frame $\boldsymbol{m}^b$ as well as the reference local magnetic field $\boldsymbol{m}^l$, which is provided by the WMM as explained in Subsection 2.6.3:

$$\begin{bmatrix} -\boldsymbol{f}^b & \boldsymbol{m}^b & -\boldsymbol{f}^b \times \boldsymbol{m}^b \end{bmatrix} = \boldsymbol{R}_l^b \begin{bmatrix} \boldsymbol{g}^l & \boldsymbol{m}^l & \boldsymbol{g}^l \times \boldsymbol{m}^l \end{bmatrix}. \tag{2.22}$$

Another possibility with optimal estimation is to define the attitude from vector observations as first evoked in [Wahba, 1965] and known as Whaba's Problem. The goal is to find the orthogonal 3x3 matrix $\boldsymbol{R}_l^b$ that minimizes the function L expressed as

$$L(\boldsymbol{R}_l^b) = \frac{1}{2}\sum_i w_i(\boldsymbol{l}_i^b - \boldsymbol{R}_l^b \boldsymbol{l}_i^l), \tag{2.23}$$

where $\boldsymbol{i}$ represents the number of measurement vectors (e.g., magnetometer, and accelerometer, and their cross-product means $i = 3$), $\boldsymbol{l}_i^l$ represents the measurements in the l-frame, $\boldsymbol{l}_i^b$ are the measurements in the b-frame with the corresponding weights on the measurement w_i. One possible solution to this problem was proposed by [Y. Bar-Itzhack, 1996] using the quaternion $\boldsymbol{q}_l^b$ parametrization:

$$L(\boldsymbol{q}_l^b) = \frac{1}{2}\sum_i w_i(\boldsymbol{l}_i^b - \boldsymbol{R}_l^b \left(\boldsymbol{q}_l^b\right) \boldsymbol{l}_i^l). \tag{2.24}$$

Such a quaternion estimation algorithm (QUEST) and its recursive version (REQUEST) can be used, to estimate the rotation, even when the attitude between the different static measurements changes. The information of the gyroscopes is then used to project the new attitudes from one measurement position to the next [Choukroun et al., 2004]. A profound comparison of the different algorithms of attitude determination and their usage (e.g., advantages and disadvantages) can be found in [Markley, 1998].

We will later use the QUEST algorithm with the pre-calibrated signals of the accelerometers and magnetometers to initialize the strapdown navigation with our redundant IMUs.

3 Stochastic Model Identification

3.1 Introduction

This chapter provides an introduction to the problem of stochastic model identification. Parameters of stochastic error models, which are a fundamental part of integrated inertial navigation are determined here. In fact, after calibration of deterministic errors [IEEE, 2011], the random stochastic characterization need to be incorporated inside the navigation filter. This is done in a rigorous way, by identifying the stochastic model structure, determining its parameters and express them as an augmented part of the state-space model.

In a first part of this chapter, a set of basic stochastic error models is recalled to the reader following [Gelb and Corporation, 1994; Hamilton, 1994]. Then a quick overview to estimate the parameters of these models is presented. More detailed description is given for the Generalized Method of Wavelet Moments (GMWM) [Guerrier et al., 2013a], as this approach is used in this research to first identify the stochastic properties of sensors. Later this approach is extended to account for the evolution of stochastic parameters with changing environmental conditions. In the last part of this chapter, the stochastic properties of inertial sensor employed in this research are analyzed, and guidelines are given when proceeding with its stochastic sensor calibration.

3.2 Definition

Let t denote the time and $X(\cdot)$ a real function. The stochastic process for each index t with $X(t)$ can be defined. For time $t \subseteq \mathbb{R}$ the function $X(t)$ is a continuous time stochastic process. If the time can be indexed by the variable k as t_k with $k \in \mathbb{Z}$, then the function becomes a discrete time stochastic process with notation X_k.

3.3 Stochastic Error Models

A short overview of the most common stochastic error models is presented. Most of them can be expressed as state-space models, which is essential for their use in state-space estimators, such as Kalman filters.

3.3.1 Random Constant

The continuous time equation of the Random Constant (RC) process is

$$\dot{X}(t) = 0, \tag{3.1}$$

with an initial value defined at time t_0 as

$$X(t_0) = X_0. \tag{3.2}$$

This equation represents a random value, which is constant during the whole process. The discrete time stochastic process can be written as

$$X_{k+1} = X_k, \tag{3.3}$$

with the initial value X_0 following a Gaussian distribution with mean value and variance defined in $\mathcal{N}(\mu_{X_0}, \sigma_{RC}^2)$. Specific sensor characteristics like the tun-on turn-off bias (i.e., the bias changes whenever the device is powered on) can be modelled with this random constant process.

3.3.2 Quantization Noise

The name quantization noise used in this document here is also known as white phase modulation noise, which is due to the time quantization of the signal and its resolution [W. Allan, 2016]. It has not to be confused with the bit quantization resulting from quantization in the analog-to-digital conversion, which will result in the quantization of the information [Han and Wang, 2011; Titterton and Weston, 2004]. The continuous time equation for the Quantization Noise (QN) process is given as

$$\dot{X} = Q \cdot \sqrt{\Delta t} \cdot \dot{U}(t), \tag{3.4}$$

where Δt represents the sampling period and $U(t)$ is a uniformly distributed random number. The discrete-time stochastic process can be written as

$$\begin{aligned} X_{k+1} &= \sqrt{Q} \cdot (U_{k+1} - U_k) \\ U_k &= \sqrt{12} \cdot \tilde{U}_k, \end{aligned} \tag{3.5}$$

where $\tilde{U}_k$ is a uniformly distributed number defined in the range $[0, 1]$.

3.3.3 White Noise

The continuous White Noise (WN) process is a stationary process and is described as

$$X(t) = W(t). \tag{3.6}$$

The process $W(t)$ follows a Gaussian distribution. The discrete-time process is written as

$$X_k = W_k, \tag{3.7}$$

with W_k defined as a zero-mean Gaussian distribution $\mathcal{N}(0, \sigma^2_{WN})$.

3.3.4 Random Walk

The continuous-time process of the Random Walk (RW) is expressed as

$$\dot{X}(t) = W(t), \tag{3.8}$$

stating that the time-derivative of the process is a WN process. With the initial condition $X(t_0) = X_0$ the integrated process is written as

$$X(t) = \int_{t_0}^{t} W(t') dt'. \tag{3.9}$$

The discrete-time sequence can be expressed as

$$X_{k+1} = X_k + W_k, \tag{3.10}$$

where W_k follows a zero-mean Gaussian distribution $\mathcal{N}(0, \sigma^2_{RW})$ as well.

3.3.5 First-order Gauss-Markov Model

The continuous-time exponentially time correlated Gauss-Markov (GM) process can be written as

$$\dot{X}(t) = -\beta X(t) + W(t), \tag{3.11}$$

where the correlation time $1/\beta$ expresses how past measurements influence the current measurements. The discrete-time sequence is written as

$$X_{k+1} = e^{-\beta \Delta t} X_k + W_k, \tag{3.12}$$

where Δt represents the time between samples. The variance of this process is σ_{GM}^2 and can be used to generate the driving noise W_k following $\mathcal{N}(0, \sigma_{GM}^2(1 - e^{-2\beta \Delta t}))$. If β is large, the correlation time will be short, and thus the process will approach that of a WN. On the other hand, if β is small, the process is highly correlated in time, and it will be similar to RW. The Auto-Regressive model of order one (AR1) is another way to describe this process. It is a re-parametrisation of Equation 3.12 as

$$X_{k+1} = \phi X_k + W_k, \tag{3.13}$$

with $\phi = e^{-\beta \Delta t}$.

3.3.6 Random Rate Ramp

The Random Rate (RR) process is a linearly growing function X_1 with a constant specific slope of X_2. It is expressed as

$$\begin{aligned} \dot{X}_1(t) &= X(2) \\ \dot{X}_2(t) &= 0. \end{aligned} \tag{3.14}$$

The discrete-time sequence can be written as

$$X_{k+1} = X_k + c_{RR} \cdot \Delta t, \tag{3.15}$$

with c_{RR} denoting the slope of the process following a Gaussian distribution $\mathcal{N}(\mu_{RR}, \sigma_{RR}^2)$, which can be interpreted as a continuous drift in a certain direction (i.e., positive or negative).

3.3.7 Bias Instability

This Bias Instability (BI) is also known as 'flicker noise' or as '1/f noise' has a strong dependency on the frequency, hence the name. In a sensor, small bias fluctuations of the signal can be modeled by this process. One possible way to generate the discrete-time sequence is as

$$X_{k+1} = \begin{cases} W_{k+1}, & \text{if}\,\mathrm{mod}(t_{k_1}, T_{BI}) = 0 \\ X_k, & \text{otherwise.} \end{cases} \tag{3.16}$$

The parameter T_{BI} expresses the period of the fluctuations and W_k follows $\mathcal{N}(0, \sigma^2_{BI}))$.

3.3.8 Example with Noise Parameters

A subset of the stochastic error models presented in the previous section is visualized here as an example on Figure 3.1. The values for the model parameters are chosen in a way to reflect the different contributions of each model visually. The following quantities are used:

- WN with model parameter $\sigma^2_{WN} = 1$,
- RW with model parameter $\sigma^2_{RW} = 8.1 \cdot 10^{-5}$,
- GM with model parameter $\sigma^2_{GM} = 2.5 \cdot 10^{-3}$ and correlation time $1/\beta = 300$, and
- RR with model parameter $c_{RR} = 2 \cdot 10^{-5}$.

In this example, no units are used and the correlation time is expressed in number of samples. This is equivalent to an acquisition frequency of 1 Hz. Each process individually has its own characteristics, but the mix of several of these processes makes it difficult to distinguish visually which stochastic processes are present and which are not (see bottom plot of Figure 3.1). Once the stochastic models are defined, the next question is how to reverse the process and determine the parameters quantitatively from the combined error signal. The following sections will review some common methods employed for the noise model estimation and its parameters.

3.4 Definitions and Estimation Methods

The process sequence X_k with $k \in \mathbb{Z}$ is generated by the parameter vector $\boldsymbol{\theta}$. It can include a multitude of the sequences presented in the previous section. These represent the error components of the sensors (i.e., $\Delta \boldsymbol{f}^b$ for the accelerometers and $\Delta \boldsymbol{\omega}^b_{ib}$ for the gyroscopes). The goal is firstly to define the stochastic error model, and in a second step to estimate this parameter vector. This information is then used in the navigation Kalman filter/smoother.

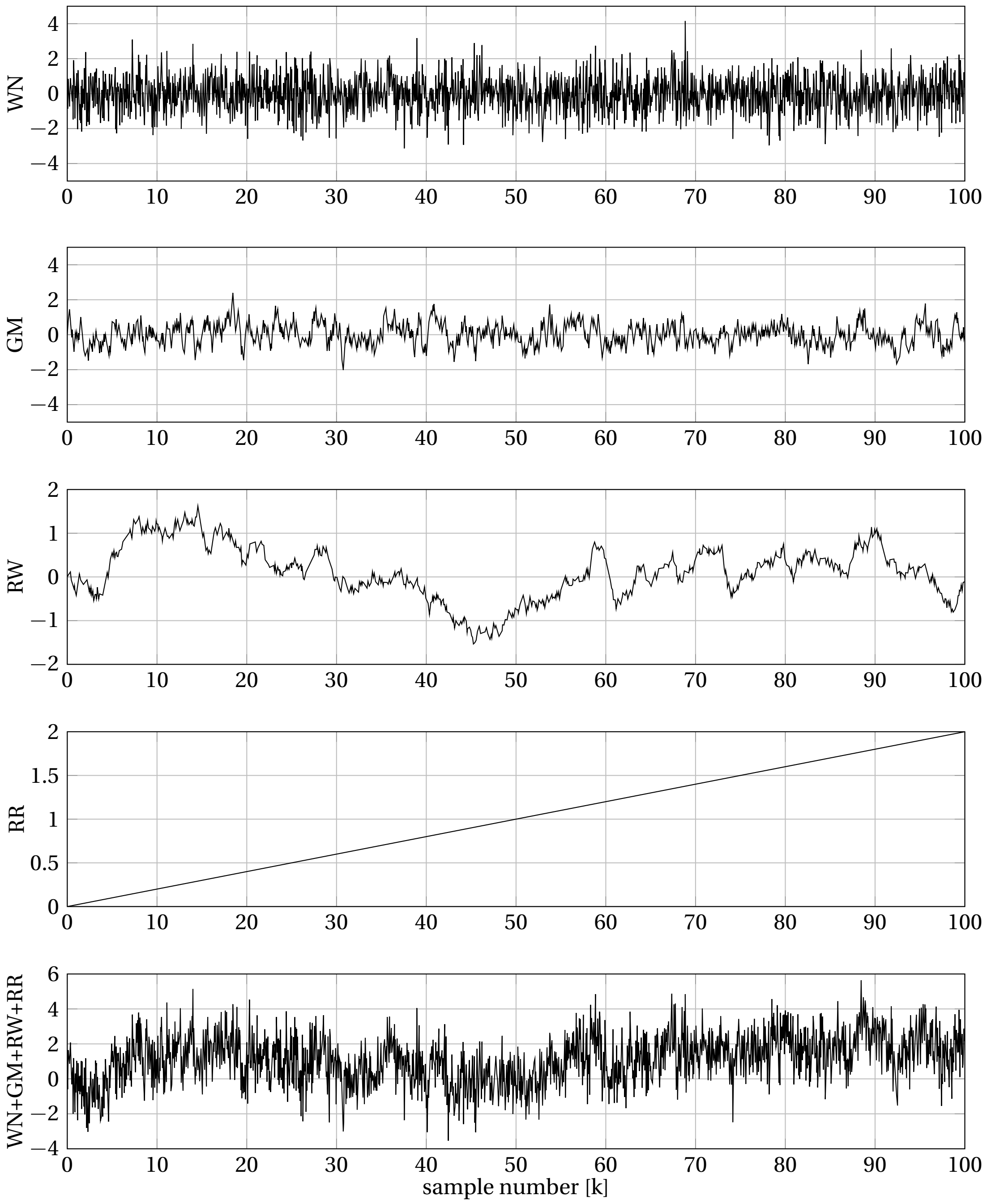

Figure 3.1: The bottom figure shows the sum of the individual stochastic processes.

The Auto-Correlation (AC) function or the Power Spectral Density (PSD) can be used to characterize some properties of the signals [Brown and Hwang, 2011]. The analysis of the signal through the AC can reveal the presence of correlated noise. The example shown in Figure 3.2 depicts a situation, where two different signals are compared. The first signal consist only of a GM process with a correlation time $1/\beta = 300$. The resulting normalized AC sequence can be used to estimate the correlation time from the plot $\hat{\beta} = 1/301$, which corresponds to the theoretical one of $\beta = 1/300$. In this simple case, the analysis through the AC function is usable.

The problem arises when multiple stochastic signals are superimposed. The second example on the Figure 3.2 shows a signal composed of a WN and a GM with the same properties as in the first case. The analysis through the AC function does not provide any usable information concerning the parameters of two composite processes. The only information it provides is that there may be a mix of several models and that they are somehow superimposed.

The analysis through the PSD is also possible and is used for different kind of sensors [IEEE, 2011]. The result is represented in a log-log plot, where the frequency is represented on the x-axis, and the power of the PSD is on the y-axis. Periodic signals are easily identifiable. In fact, commonly used noise-processes can be identified and quantified by linear regression on parts of the PSD curve. The relatively easily identifiable processes include the RW, BI, WN, and QN.

Like for the analysis through the AC, the identification is simple but is limited to a certain set of processes. However, the estimation of parameters for a sum of several similar processes is difficult (i.e., the parameters of a sum of multiple GM processes cannot be estimated) to achieve reliably with the PSD analysis.

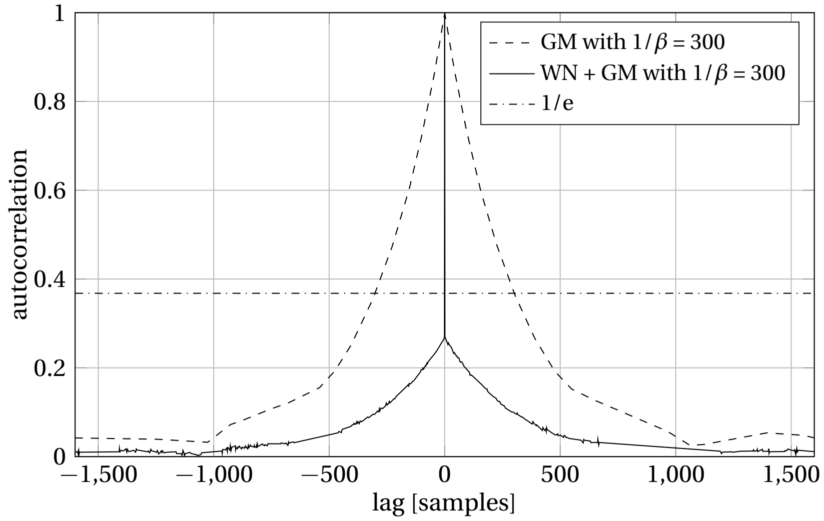

Figure 3.2: Analysis of two signals through the auto-correlation function. The first signal is just a GM process, whereas the second signal is composed of a GM and a WN.

3.5 Allan Variance

The Allan Variance (AV) was originally introduced by David Allan to analyze the stability of oscillators [Allan, 1966]. The variability of the stability of clocks is analysed in detail in [Lesage and Audoin, 1973; Allan and Barnes, 1981], whereas an intuitive example is provided in [Allan, 1987]. The basic principle is explained here. The sample average of τ consecutive observations from a realization X_k at position k is

$$\bar{X}_k(\tau) = \frac{1}{\tau}\sum_{j=0}^{\tau-1} X_{k-j}. \tag{3.17}$$

Then the AV $\sigma^2_{\bar{X}}(\tau)$ is defined as the expectation of the squared differences between the $\bar{X}_k(\tau)$ as

$$\sigma^2_{\bar{X}}(\tau) = \frac{1}{2}\mathbb{E}\left[\left(\bar{X}_k(\tau) - \bar{X}_{k-\tau}(\tau)\right)^2\right]. \tag{3.18}$$

One of the estimators for this quantity was proposed in [Greenhall, 1991] and can be written as:

$$\hat{\sigma}^2_{\bar{X}}(\tau) = \frac{1}{2(N-2\tau+1)}\sum_{k=2\tau}^{N}\left(\bar{X}_k(\tau) - \bar{X}_{k-\tau}(\tau)\right)^s, \tag{3.19}$$

where N denotes the number of samples.

The analysis of error signals of for instance an Inertial Measurement Unit (IMU) through this AV is employed by many researchers [Guerrier, 2009; Haiying, 2004; El-Sheimy et al., 2008; Strus, 2007; Xing and Gebre-Egziabher, 2008; Yuan et al., 2016]. In addition, this procedure is a recognized method to analyze the random processes in datastructures [IEEE, 1998]. Figure 3.3 shows a snippet from this document showing the individual contributions of the stochastic error models on the Allan deviation.

Nevertheless, the work in [Guerrier et al., 2013b] has shown that the estimator of noise parameters via regression analysis of the AV is an inconsistent estimator when a multitude of stochastic processes are present at the same time in the signal. This estimator converges for a big dataset to the parameter value only if there is one single error model. When a mix of processes is present, the estimator will be biased.

Table 3.1: Different stochastic processes with their corresponding slopes as shown in the plot of Figure 3.3 representing the Allan deviation.

Process Name	Parameters	Slope
QN	Q	-1
WN	σ^2_{WN}	-0.5
BI	T_{BI}, σ^2_{BI}	0
GM	β, σ^2_{GM}	$[-0.5, 0.5]$
RW	σ^2_{RW}	0.5
RR	c_{RR}	1

3.6 Generalized Method of Wavelet Moments

The previously mentioned methods for stochastic parameter estimation suffer from various limitations going from numerical instability, computational inefficiency to statistical inconsistency. For this reason, a recently proposed approach has been used to build a new computational platform for sensor calibration which makes use of the quantity called Wavelet Variance (WV) to deliver an estimation framework with the name GMWM [Guerrier et al., 2013a]. This method not only allows to estimate the parameters of considerably complex stochastic process models, but allows to do so in a numerically stable, computationally efficient, and statistically consistent manner. It can be employed on a personal computer using the open-source statistical environment `R` with the `gmwm` package programmed in `C++` [Balamuta et al., 2016b].

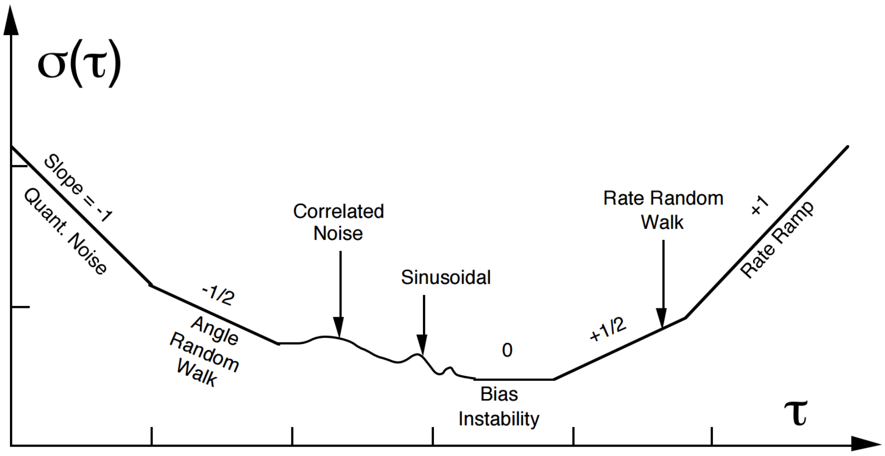

Figure 3.3: Sample plot of Allan deviation analysis. Taken directly from [IEEE, 1998].

3.6.1 Wavelet Transform

A time-series can be analyzed via wavelets (in a similar way as a the Fourier analysis). The wavelet-series represents the time-series by a certain orthonormal set of wavelets, which are a basis. The wavelet can be shifted in position (along the dataset) and scaled to create a whole family of wavelets issued from a mother wavelet. In this case, the wavelet coefficients are issued from a modified discrete wavelet transform [Percival and Walden, 2000].

In general terms, to obtain this quantity, any observed signal (in our case the observed error-signal) is transformed into a weighted-average over different *scales* of observations (i.e., the averages are applied to a certain number of observations at a time). We refer to these scales with the letter j, where $j \in [1, \log_2(T) - 1]$ with T denoting the total number of data points. The wavelet coefficient $h_{j,l}$ used for filtering the data have the following properties:

$$\sum_{l=0}^{L_j-1} h_{j,l} = 0, \quad \sum_{l=0}^{L_1-1} h_{1,l}^2 = \frac{1}{2}, \text{ and } \sum_{l=-\infty}^{\infty} h_{1,l} h_{1,l+2m} = 0, \tag{3.20}$$

where $m \in \mathbb{N}^+$, $L_j = (2^j - 1)(L_1 - 1) + 1$ is the length of the filter at level j and L_1 is the length of the first level filter $h_{1,l}$. Then, the wavelet coefficients $W_{j,t}$ are defined as

$$W_{j,t} = \sum_{l=0}^{L_j-1} h_{j,l} X_{t-l}. \tag{3.21}$$

The wavelet coefficients can be applied in different ways, but the most useful (in the present context) is the Maximum Overlap Discrete Wavelet Transform [Percival, 1995]. Its simplified usage on a dataset is depicted in Figure 3.4, where the Haar wavelet is applied to the signal of interest, by firstly shifting it through all the samples. This process is then repeated with the scaled version of the Haar filter until the WV for all the scales is computed.

3.6.2 Wavelet Variance

Once the wavelet coefficients $W_{j,t}$ are calculated, then the Wavelet Variance is defined as the variance of these wavelet coefficients at level j

$$\nu_j^2 = \text{Var}[W_{j,t}]. \tag{3.22}$$

When using the Haar Wavelet filter $h_{j,l}$ [Percival and Guttorp, 1994], then the WV has an exact relationship to the AV, which is expressed as

$$\nu_j^2 = 2\text{AV}_j. \tag{3.23}$$

An unbiased estimator for the WV issued from a certain wavelet transformation is given by the maximum overlap discrete wavelet transform estimator directly calculated with the formula [Percival, 1995]

$$\hat{\nu}_j^2 = \frac{1}{M_j} \sum_{t=L_j}^{T} W_{j,t}^2, \tag{3.24}$$

where $M_j = T - L_j + 1$ is the number of weighted-averages, formally called wavelet coefficients and denoted as $W_{j,t}$, issued from the scale of decomposition j. Supposing we have J scales (or levels) then we can define the vector of empirical WV as

$$\hat{\boldsymbol{\nu}} = [\hat{\nu}_j^2]_{j=1,\dots,J}. \tag{3.25}$$

3.6.3 WV of Stochastic Processes

The first step in modeling the stochastic behavior of the errors is in identifying the type of stochastic model that can best describe them. These can be done by inspecting the log-log

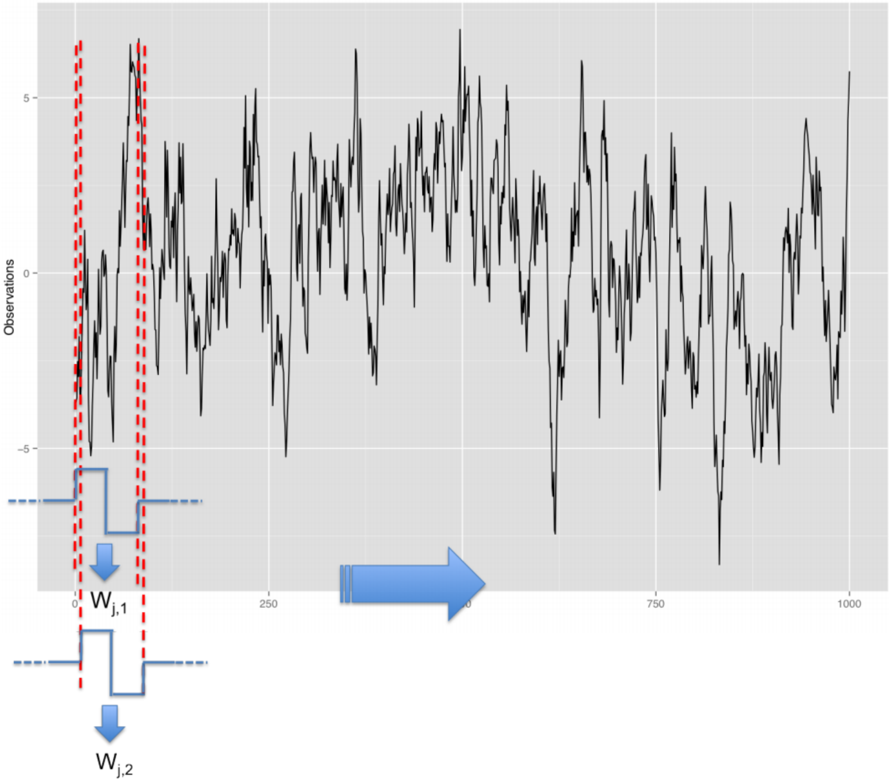

Figure 3.4: Principle application of the Maximum Overlap Discrete Wavelet Transform using shifted (and scaled) versions of the Haar Wavelet.

plot of the WV. As it is a scaled version of the AV, which is also commonly represented through a log-log-plot. Figure 3.5 visualizes some of these models (their sum is represented with a red-dotted line), which are also listed in Table 3.1. This plot shows that it is relatively simple to detect and associate one type of model at a separate part of the scale, but when several models are overlapping at the same scales, then their identification becomes more problematic, and the correct estimation of their parameters becomes challenging for traditional estimators such as the regression in the AV or the maximum-likelihood-estimator [Guerrier et al., 2016]. Going back to Table 3.1, it collects a broad set of models that the GMWM estimator can deal with and, in particular, the second column shows the set of parameters that we are interested in estimating (i.e., the values that in some way explain the behavior of the measurements) that we generally denote as $\boldsymbol{\theta}$.

Once a model is identified by the user, it is possible to obtain a known form for the WV (called theoretical WV) which depends on these parameters $\boldsymbol{\theta}$ and which will be denoted as:

$$\nu_j^2(\boldsymbol{\theta}) = \text{Var}[W_{j,t}(\boldsymbol{\theta})], \tag{3.26}$$

where $W_{j,t}(\boldsymbol{\theta})$ represents the wavelet coefficients issued from the j^{th} scale of the wavelet decomposition which are a function of the parameter vector $\boldsymbol{\theta}$ and $\text{Var}[\cdot]$ represents the variance operator (for more details see [Zhang, 2008] where a similar notion is discussed for the AV). With this in mind, given a certain model (identified by the user) and its parameter values, it is therefore possible to obtain the theoretical WV $\nu_j^2(\boldsymbol{\theta})$. However, in reality the parameter vector $\boldsymbol{\theta}$ is (obviously) unknown and the only quantity that can be observed is the estimated (empirical) WV $\hat{\boldsymbol{\nu}}$ which should be *close* to the vector of theoretical model-based WV denoted as $\boldsymbol{\nu}(\boldsymbol{\theta}) = [\nu_j^2(\boldsymbol{\theta})]_{j=1,\dots,J}$, whose parameters are yet to be estimated and unknown.

3.6.4 Parameter Estimation

Given that the empirical WV and the model implied WV should be in some sense close to each other, the GMWM estimator attempts to inverse the mapping between the WV and the model

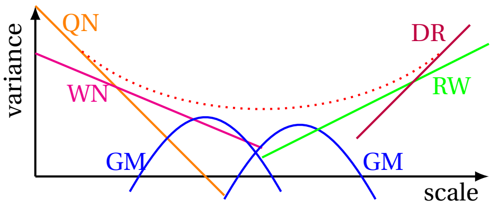

Figure 3.5: Example log-log-plot showing the influences of the different models with their shape. Red dotted: sum of theoretical noise models $\boldsymbol{\nu}(\boldsymbol{\theta})$. Multiple GM can approach the flat shape of the bias instability.

parameters $\boldsymbol{\theta}$ by finding the solution to the following minimization problem:

$$\hat{\boldsymbol{\theta}} = \underset{\boldsymbol{\theta} \in \boldsymbol{\Theta}}{\text{argmin}} \left(\hat{\boldsymbol{v}} - \boldsymbol{v}(\boldsymbol{\theta})\right)^T \boldsymbol{\Omega} \left(\hat{\boldsymbol{v}} - \boldsymbol{v}(\boldsymbol{\theta})\right), \tag{3.27}$$

where $\boldsymbol{\Omega}$ is a positive-definite weighting matrix chosen in an appropriate manner [Guerrier et al., 2013a]. Hence, the GMWM tries to find the values of $\boldsymbol{\theta}$ that allow the theoretical WV (defined by the model structure selected by the user) to be close to the empirical (observed) WV in a weighted least-squares manner. The statistical properties of the GMWM estimator $\hat{\boldsymbol{\theta}}$ have been proven to show that the estimator is consistent and asymptotically normally distributed [Guerrier et al., 2013a].

Using the properties of the estimator, the GMWM framework allows to deliver a series of handy tools for the sensor calibration procedure [Guerrier et al., 2015; Guerrier and Molinari, 2016; Molinari, 2016]:

1. a large variety of noise-models mentioned in Table 3.1 can be combined to deliver the needed complex models;
2. a so-called robust version of the GMWM allows to perform the same procedure also when the observed data is affected by disturbances that could otherwise negatively impact the analysis and estimation;
3. confidence intervals for the estimated parameters which provide a range of values within which there is a high probability of finding the true parameter $\boldsymbol{\theta}$ of interest;
4. a goodness-of-fit test that allows determining if the estimated model well describes the observed errors;
5. the Wavelet Variance Information Criterion (WVIC), which allows to classify different models and determine which model is the best in terms of prediction;
6. an automatic model selection procedure based on the WVIC.

The proper knowledge of the stochastic properties for the implementation of the navigation filter improves the quality of the navigation solution [Stebler et al., 2014].

3.7 Error Analysis Example

This section briefly shows an analysis of stochastic errors in inertial sensors through the GMWM framework, so the reader becomes familiar with the interpretations of plots and the notation used in this document when comparing the empirical WV of two different sensors.

The first sensor is the navigation grade IMU LN200 [Appendix C.2] and the second sensor is the Micro-Electro-Mechanical System (MEMS) IMU Navchip [Appendix C.3]. The error signal of the gyroscopes is considered here. The data is acquired under constant environmental conditions with the sensor at rest. A constant offset in the signal is removed automatically by the GMWM framework prior to analysis. This constant offset can, for instance, be the Earth's rotation rate sensed by the gyroscope (if it is not buried in the noise), or it can be the signal picked up by an accelerometer, that corresponds to the projection of gravity and/or mean bias of the sensor. Usually, the first couple of minutes of the sensor readings are discarded, before the temperature of the sensor stabilizes. The applied model for the stochastic noise parameters depends on the overall shape of the empirical WV. The error model of a low-cost MEMS IMU tends to be more complicated than the one found on a high-end IMU (see Figure 3.6).

3.7.1 IMU Manufacture Specifications

Random Noise

One of the first quantities the datasheet of an IMU usually mentions is the *noise density*. It is usually expressed as a PSD value relating a certain noise quantity to the frequency. Typical units used for the accelerometers are $\mu g/\sqrt{\mathrm{Hz}}$ and $m/s/\sqrt{h}$ for the quantity called *velocity random walk*. The gyroscope noise is often characterized by the units $°/s/\sqrt{\mathrm{Hz}}$ for the PSD, or the $°/\sqrt{h}$ for the so called *angular random walk*. These characteristics are equivalent up to a certain conversion factor.

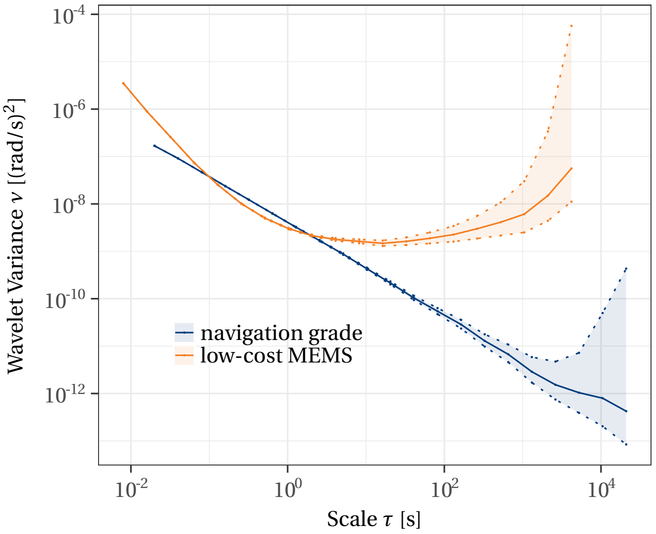

Figure 3.6: Comparison of the empirical WV between a navigation grade IMU and a low-cost MEMS IMU. Its shape will define the error model.

In-run Bias
A second value often found in datasheets of MEMS-IMU is the *in-run bias stability*. This value reflects the flat part following the region dominated by a WN. This flat region cannot directly be expressed through a state-space error model but it can be approximated by a sum of multiple GM processes (see Figure 3.5). This value can be for instance expressed as mg for the accelerometers and it can be expressed in $^\circ/\mathrm{h}$ for the gyroscope.

Random Bias
The turn-on stability of the instrument mean offset is the so-called random bias. This characteristic is usually present in the manufacturer datasheet only for more precise inertial sensors (e.g., tactical and navigational grade) yet absent in low-cost MEMS-IMUs. This offset is substantial and can not be identified by the GMWM framework, as the mean signal is removed prior to wavelet analysis. It needs to be dealt with separately either in pre-calibration (in-lab and prior-mission) as will be explained in Chapter 4, and its residual part with state-space modeling.

Bias Repeatability
This parameter describes how consistent the random bias is, and how much it evolves over time and/or temperature range.

3.7.2 GMWM Analysis

The results from the GMWM estimation follow a unit, range, or convention that depends on the input. In fact, the data is considered as is (i.e., as samples). Internally, the GMWM framework and its optimization process handle all the computations in a unit-independent manner. The only parameter the user can adapt is the frequency of the data. The default frequency is set to 1 Hz. Wrong specification of this variable will lead to false units in the estimated parameters. If the data is for instance entered with the units [rad/s], then the estimated parameters, which are mostly variances, would be expressed in the dedicated unit as $[(\mathrm{rad/s})^2]$. One exception is the correlation time $1/\beta$ of the GM process, which is expressed as a function of the sampling time expressed in [s]. The value of the sampling time is important to note, as the conversion between the AR1 and the GM model parameters relies on this quantity. This is shown in the next section, where with an example.

3.7.3 Example

We analyze the variations in a static dataset of approximately 2 h acquired for the Navchip IMU. The first 15 min are not considered for thermal reasons. The rest of the data has a length of 1800000 samples and has an acquisition frequency of 250 Hz. The following "R" code is used to read the binary data and to investigate the error structure of the signal. This example data is encoded with seven double-values, as `NAVCHIP_FLT` was chosen as parameter for the data-type. The first double-value represents the data timestamp with the unit [s]. Three double-values for the three gyroscope axes are followed by another three double-values for the three accelerometer axes. The unit used for the raw gyroscope measurements is [arcsec], whereas the unit used for the raw accelerometer measurements is [mm/s]. Internal conversion, through the acquisition frequency, results in the usual units [rad/s] and [m/s^2] respectively.

```
# load library and data
library(gmwm)
data_object <- read.imu(file = "data.imu", type = "NAVCHIP_FLT")
imu_object <- imu(data_object, gyros = 1, freq = 250)

# plot WV
plot(wvar.imu(imu_object))
```

By analyzing the shape of the empirical WV in Figure 3.7 (blue dots) and comparing it to Figure 3.5 several process models can be visually identified:

- due to the steep negative slope in the small scales the QN model is selected,
- due to the less-steep negative slope in the small to middle scales the WN model is selected,
- due to the long flat part in the middle spanning over multiple scales several GM models are selected, and
- due to the slightly positive slope in the late scale the RW model is selected.

The combination of these models is then chosen and the gmwm-package will estimate the model parameters when applying the following code snippet:

```
# define model
gyro_model <- 3*GM() + QN() + WN() + RW()

# estimate and plot model parameters
imu_gmwm <- gmwm(gyro_model, imu_object, robust = FALSE, freq = 250)
plot(imu_gmwm)

# print parameters to terminal
summary(imu_gmwm, inference = TRUE)
```

A possible result printed in the terminal can look like this, with the first column denoting the model parameter name, the second column denoting the estimated parameter value, the third with the fourth column denoting the upper and lower confidence interval, and the fifth column denoting the standard error:

```
# terminal output
Model Information:
               Estimates       CI Low      CI High            SE
BETA        2.327144e-02 2.327144e-02 2.327144e-02 9.114528e-15
SIGMA2_GM   5.910478e-09 3.909285e-09 7.911671e-09 2.264824e-13
BETA        2.983416e-01 2.983416e-01 2.983416e-01 6.888085e-15
SIGMA2_GM   4.523155e-09 4.037374e-09 5.008937e-09 7.040430e-13
BETA        4.173938e+00 4.173938e+00 4.173938e+00 3.522668e-15
SIGMA2_GM   6.211927e-09 5.957557e-09 6.466296e-09 5.078587e-12
QN          2.188529e-06 2.184493e-06 2.192565e-06 2.453735e-09
WN          3.777401e-07 3.750446e-07 3.804356e-07 1.638753e-09
RW          3.756467e-13 2.359102e-13 5.153832e-13 8.495378e-14
```

The different GM are printed in the same order as they are labeled in the legend of Figure 3.7 (i.e., from large scales to small scales). They sum up and approach the flat part in the middle to large scales. The chosen model is contained in the confidence interval of the estimated WV. For using the estimated parameters in a Kalman filter/smoother or for comparison with the datasheet of the manufacturer, these parameters may need to be re-scaled, e.g., from the provided *variance* units into PSD values:

- The Navchip datasheet states a typical noise density for the WN component of the gyroscope of $11\,°/\mathrm{h}/\sqrt{\mathrm{Hz}}$.
- The conversion from the GMWM raw-units $[(\mathrm{rad/s})^2]$ to the required datasheet-units by using the acquisition frequency is done by converting the estimated WN value from the terminal output as $\sqrt{3.777401e-7}/\pi\cdot 180\cdot 3600/\sqrt{250}$, which results in $8\,°/\mathrm{h}/\sqrt{\mathrm{Hz}}$.
- In case the GM-model is used in the estimation framework, then the first parameter from the result is the inverse of the correlation time, also known as `BETA`, which has the units [1/s]. It is only correct if the frequency of the dataset was included correctly from the beginning. The parameter `SIGMA2_GM` follows the same notation as the `WN` parameters, i.e., this parameter is a variance and needs conversion to the specific unit as was done for the `WN`-parameter.
- If the AR1-model is used in the estimation framework, then the parameters provided are `AR1` and `SIGMA2`. They are a reparametrization of the GM-model, as explained in the previous section. The in the framework included function `ar1_to_gm(theta, freq)` can be used to easily convert the parameters, in which `theta` represents the two parameters of the AR1-model, and `freq` is the frequency of the dataset.

- The parameter `RW` is a variance value as well. Thus it can be converted into the appropriate units following the same convention as the `WN` value.

The WN-values from the estimation framework and the datasheet correspond well to each other. In fact, the datasheet is slightly pessimistic concerning these values, to stay on the save sides, as these can vary per sensor as well as to account for the fact that the level of WN may be higher at higher instrument temperature as discussed in Chapter 5. Nevertheless, each sensor has to be calibrated individually for the error model and their parameters in order to correctly represent the state-space error model, which is required for the subsequent sensor fusion.

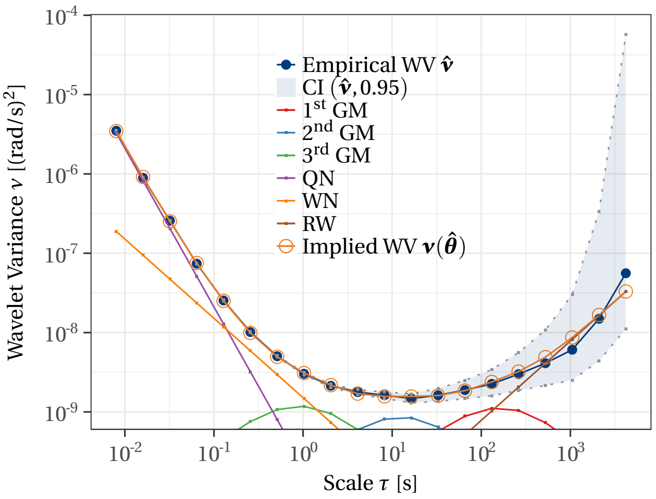

Figure 3.7: The implied WV is contained in the confidence interval of the empirical WV.

Calibration Methodology Part II

4 Deterministic Errors

4.1 Introduction

This chapter provides information about the calibration of the deterministic errors. The calibration details for the accelerometer, gyroscope, magnetometer, and the barometer are presented. Nevertheless, these principles are applicable to other types and classes of sensors. Whereas the calibration procedure is explained in detail, the results of the influence of the proper calibration on the navigation solution is visualized by examples in Chapter 8 and Chapter 9.

4.2 Problem Statement

Before the measurements of the Inertial Measurement Unit (IMU) are fed to the Inertial Navigation System (INS), the deterministic errors are evaluated. These can include the random bias $\boldsymbol{b}$, the scale-factor $\boldsymbol{S}$, and the non-orthogonality $\boldsymbol{\theta}$. The stochastic influences on the measurements $\boldsymbol{\varepsilon}$ are explained in detail in Chapter 3 and Chapter 5. One way to express the uncalibrated accelerometer or gyroscope readings $\boldsymbol{l}$ is

$$\boldsymbol{l} = \check{\boldsymbol{l}} + \boldsymbol{S} \cdot \check{\boldsymbol{l}} + \boldsymbol{\theta} \cdot \check{\boldsymbol{l}} + \boldsymbol{b} + \boldsymbol{\varepsilon}, \tag{4.1}$$

where $\check{\boldsymbol{l}}$ represents the true specific force or the rotation rate vector. The scale-factor can for instance also be included with a quadratic influence on the input. Other influences such as acceleration/gravity dependency can be added to this model. The scale-factor and the non-orthogonality can be rearranged into one single matrix R_S as:

$$\boldsymbol{l} = R_S \cdot \check{\boldsymbol{l}} + \boldsymbol{b} + \boldsymbol{\varepsilon}, \tag{4.2}$$

where the diagonal elements of the 3×3 matrix R_S represent the scale-factors and the off-diagonal elements are the misalignment between the axes:

$$R_S = \begin{bmatrix} s_{xx} & \theta_{xy} & \theta_{xz} \\ \theta_{yx} & s_{yy} & \theta_{yz} \\ \theta_{zx} & \theta_{zy} & s_{zz} \end{bmatrix}. \tag{4.3}$$

The vector $\boldsymbol{b}$ represents the long-term stable bias, which can be precalibrated (in-lab and in-field prior to mission take-off). The last part is represented through the vector $\boldsymbol{\varepsilon}$. It can be split into two parts:

- short term correlated errors such as Auto-Regressive model of order one (AR1) and
- White Noise (WN).

These quantities need to be estimated for a proper representation of the signals prior usage.

In the calibration procedure, the sensor output $\boldsymbol{l}$ is compared to a reference signal $\check{\boldsymbol{l}}$ and the discrepancies are split into the influences of the deterministic errors by the estimation algorithm. If performed in controlled conditions in a laboratory, an expensive equipment is used to align the IMU to a specific reference. The six-position calibration is widely used and can calibrate for the bias and the scale-factor of the sensitive axes [Titterton and Weston, 2004]. This axis is usually aligned vertically. This static procedure takes advantage of the knowledge of the local gravity to determine the accelerometer biases. In a similar way it takes an advantage of the Earth's rotation rate which is projected on to the vertical axis for a given latitude φ for determining the gyroscope biases. The rotation rate of the Earth expressed in the l-frame $\boldsymbol{\omega}_{ie}^{l}$ is obtained by projecting the true rotation rate of the earth on to the local frame by using the latitude φ from the current position:

$$\boldsymbol{\omega}_{ie}^{l} = \begin{bmatrix} \omega_{ie}\cos\varphi \\ 0 \\ -\omega_{ie}\sin\varphi \end{bmatrix}. \tag{4.4}$$

The bias b of the vertical sensitive axis (accelerometer as well as gyroscope) is then estimated by taking measurements with the axis pointing upwards l_{up} and another measurement with the axis pointing downwards l_{down} [Aggarwal et al., 2008] and combining the measurements as

$$b = \frac{l_{up} + l_{down}}{2}. \tag{4.5}$$

The scale-factor s can be retrieved with the knowledge of a reference signal r (either local gravity, Earth's rotation rate) and both positive and negative measurements [Aggarwal et al., 2008] by

$$s = \frac{l_{up} - l_{down} - 2r}{2r}. \tag{4.6}$$

However, this type of calibration with two measurements does not take into account the non-orthogonality elements. Also, it assumes that the sensors sensitive axis is aligned with the reference signal, realization of which is difficult. These problems can be circumvented by using multiple measurements in different directions and by estimating the unknown parameters via e.g., a Least-Squares (LS) approach. Denoting the measurement from one attitude as $[l_x, l_y, l_z]^T$, the n observations at different orientation are assembled in a measurement vector $\boldsymbol{l}$ with size $3n \times 1$, the n reference signals for each axis r are assembled in a $3n \times 12$ matrix $\boldsymbol{A}$, and the vector of the unknown parameters (i.e., scale-factor, non-orthogonality, and bias) is represented in the vector $\boldsymbol{x}$ as:

$$\boldsymbol{l} = \boldsymbol{A} \cdot \boldsymbol{x}$$

$$\begin{bmatrix} l_{x1} \\ l_{y1} \\ l_{z1} \\ l_{x2} \\ l_{y2} \\ l_{z2} \\ \vdots \\ l_{xn} \\ l_{yn} \\ l_{zn} \end{bmatrix} = \begin{bmatrix} r_{x1} & r_{y1} & r_{z1} & 1 & 0 & 0 & 0 & 0 & 0 & 0 & 0 & 0 \\ 0 & 0 & 0 & 0 & r_{x1} & r_{y1} & r_{z1} & 1 & 0 & 0 & 0 & 0 \\ 0 & 0 & 0 & 0 & 0 & 0 & 0 & 0 & r_{x1} & r_{y1} & r_{z1} & 1 \\ r_{x2} & r_{y2} & r_{z2} & 1 & 0 & 0 & 0 & 0 & 0 & 0 & 0 & 0 \\ 0 & 0 & 0 & 0 & r_{x2} & r_{y2} & r_{z2} & 1 & 0 & 0 & 0 & 0 \\ 0 & 0 & 0 & 0 & 0 & 0 & 0 & 0 & r_{x2} & r_{y2} & r_{z2} & 1 \\ \vdots & \vdots & \vdots & \vdots & \vdots & \vdots & \vdots & \vdots & \vdots & \vdots & \vdots & \vdots \\ r_{xn} & r_{yn} & r_{zn} & 1 & 0 & 0 & 0 & 0 & 0 & 0 & 0 & 0 \\ 0 & 0 & 0 & 0 & r_{xn} & r_{yn} & r_{zn} & 1 & 0 & 0 & 0 & 0 \\ 0 & 0 & 0 & 0 & 0 & 0 & 0 & 0 & r_{xn} & r_{yn} & r_{zn} & 1 \end{bmatrix} \cdot \begin{bmatrix} s_{xx} \\ \theta_{xy} \\ \theta_{xz} \\ b_x \\ \theta_{yx} \\ s_{yy} \\ \theta_{yz} \\ b_y \\ \theta_{zx} \\ \theta_{zy} \\ s_{zz} \\ b_z \end{bmatrix} \tag{4.7}$$

The parameters $\hat{\boldsymbol{x}}$ are then estimated in the LS sense by using:

$$\hat{\boldsymbol{x}} = \left(\boldsymbol{A}^T \boldsymbol{A}\right)^{-1} \boldsymbol{A}^T \boldsymbol{l} \tag{4.8}$$

This procedure appears simple and effective, however its practical realization is difficult. The complexity in this procedure is manifold. Firstly, in order to compare the measurements of a sensor axis to a reference, they need to be perfectly aligned. Any misalignment is projected back to a faulty calibration. Secondly, the reference signal from the Earth's rotation is weak (small) and therefore can not be used to calibrate the low-cost Micro-Electro-Mechanical System (MEMS) gyroscopes, with an increased noise. This calibration hence requires a reference signal of higher amplitude, as the one provided by a rotation table. This makes the calibration procedure not usable in the field. On the other hand, Earth's gravity is sufficient to calibrate the accelerometers.

4.3 Multi-Position Calibration

In order to circumvent the disadvantages presented in the previous section, [Syed et al., 2007] proposes a different scheme. The measurements from the x-axis of the IMU l_x are considered to be only influenced by a scale factor S_x. Moreover, the measurements on the y-axis l_y are influenced by the y-axis scale-factor S_y and its misalignment with respect to the x-axis θ_{yz}. The measurements of the z-axis l_z are influenced by the z-axis scale-factor S_z, the misalignment to the x-axis θ_{zy} as well as the misalignment to the y-axis θ_{zx}. In addition, a bias value for each axis is defined with b_x, b_y, and b_z. This can be put in an equation as:

$$\begin{bmatrix} l_x \\ l_y \\ l_z \end{bmatrix} = \begin{bmatrix} 1+S_x & 0 & 0 \\ -\theta_{yz} & 1+S_y & 0 \\ \theta_{zy} & -\theta_{zx} & 1+S_z \end{bmatrix} \cdot \begin{bmatrix} \check{l}_x \\ \check{l}_y \\ \check{l}_z \end{bmatrix} + \begin{bmatrix} b_x \\ b_y \\ b_z \end{bmatrix}, \tag{4.9}$$

where the quantities $\check{l}_x$, $\check{l}_y$, and $\check{l}_z$ denote the true acceleration or rotation rate for each axis and can be extracted as:

$$\begin{aligned} \check{l}_x &= \frac{l_x - b_x}{1+S_x} \\ \check{l}_y &= \frac{l_y - b_y + \theta_{yz}\dfrac{l_x - b_x}{1+S_x}}{1+S_y} \\ \check{l}_z &= \frac{l_z - b_z - \theta_{zy}\dfrac{l_x - b_x}{1+S_x} + \theta_{zx}\dfrac{l_y - b_y + \theta_{yz}\dfrac{l_x - b_x}{1+S_x}}{1+S_y}}{1+S_z} \end{aligned} \tag{4.10}$$

The reference local gravity $\boldsymbol{g}$ or the reference Earth's rotation rate $\boldsymbol{\omega}_{ie}$ is used to impose a condition on the norm on the accelerometers or the gyroscopes readings:

$$\begin{aligned} f_{acc} &= \check{l}_x^2 + \check{l}_y^2 + \check{l}_z^2 - \|\boldsymbol{g}\|^2 = 0 \\ f_{gyr} &= \check{l}_x^2 + \check{l}_y^2 + \check{l}_z^2 - \|\boldsymbol{\omega_{ie}}\|^2 = 0 \end{aligned} \tag{4.11}$$

The combination of the previous two equations results in the calibration model f with the observations $\boldsymbol{l}$, the residuals $\boldsymbol{v}$, and the parameters (bias, scale-factor, and non-orthogonality) assembled in the vector $\boldsymbol{x}$

$$f\left(\boldsymbol{l}-\boldsymbol{v},\boldsymbol{x}\right)=0. \tag{4.12}$$

The linearization of Equation 4.12 around the initial parameter $\mathring{\boldsymbol{x}}$ with its incremental parameter vector $\boldsymbol{\delta x}$ gives:

$$\begin{array}{llllll} f\left(\boldsymbol{l}-\boldsymbol{v},\mathring{\boldsymbol{x}}+\boldsymbol{\delta x}\right)=0 & & & & & \\ f(\boldsymbol{l},\mathring{\boldsymbol{x}}) & -\left.\dfrac{\partial f(\boldsymbol{l},\boldsymbol{x})}{\partial \boldsymbol{l}}\right|_{\boldsymbol{l},\mathring{\boldsymbol{x}}} & \cdot\boldsymbol{v} & +\left.\dfrac{\partial f(\boldsymbol{l},\boldsymbol{x})}{\partial \boldsymbol{x}}\right|_{\boldsymbol{l},\mathring{\boldsymbol{x}}} & \cdot\delta\boldsymbol{x}=0 \\ \boldsymbol{w} & -\boldsymbol{B} & \cdot\boldsymbol{v} & +\boldsymbol{A} & \cdot\delta\boldsymbol{x}=0 \end{array} \tag{4.13}$$

This functional relationship is called *Gauss-Helmert model* [Merminod, Septembre, 2018] with the two design matrices $\boldsymbol{A}$ and $\boldsymbol{B}$. $\boldsymbol{w}$ represents the misclosure vector, components of which are depending on the measurements $\boldsymbol{l}$ and the first guess of the parameter vector. The goal is to satisfy the following relation in a LS adjustment:

$$\boldsymbol{B}\boldsymbol{v}-\boldsymbol{A}\delta\boldsymbol{x}-\boldsymbol{w}=0 \tag{4.14}$$

The parameter vector $\hat{\boldsymbol{x}}$ is calculated, by incrementally adding the estimated correction vector $\delta\hat{\boldsymbol{x}}$ to the initial estimate $\mathring{\boldsymbol{x}}$ as

$$\hat{\boldsymbol{x}}=\mathring{\boldsymbol{x}}+\delta\hat{\boldsymbol{x}}, \tag{4.15}$$

where the correction vector is calculated as

$$\delta\hat{\boldsymbol{x}}=-\boldsymbol{N}^{-1}\boldsymbol{A}^{T}\boldsymbol{C}^{-1}\boldsymbol{w}, \tag{4.16}$$

with

$$\boldsymbol{C}=\boldsymbol{B}\boldsymbol{P}^{-1}\boldsymbol{B}^{T}, \tag{4.17}$$

and normal matrix as

$$\boldsymbol{N}=\boldsymbol{A}^{T}\boldsymbol{C}^{-1}\boldsymbol{A}. \tag{4.18}$$

The matrix $\boldsymbol{P}$ is the weight given to the measurements. The standard deviation σ for the different observations is considered constantly and equal for each axis and can be taken from the datasheet (noise levels):

$$\boldsymbol{P}=\frac{1}{\sigma^{2}}\boldsymbol{I}_{3n\times 3n}, \tag{4.19}$$

where n represents the number of readings taken at different attitudes. As observations are averaged, their Power Spectral Density (PSD) noise level theoretically decreases with $\sqrt{n}$. The cofactor matrix $\boldsymbol{Q_{xx}}$ of the unknown parameters is useful to establish the correlation matrix between these parameters and is obtained from

$$\boldsymbol{Q_{xx}} = \boldsymbol{N}^{-1}. \tag{4.20}$$

The vector of residuals is estimated from

$$\hat{\boldsymbol{e}} = \boldsymbol{P}^{-1}\boldsymbol{B}^T\boldsymbol{C}^{-1}(\boldsymbol{A}\delta\hat{\boldsymbol{x}} + \boldsymbol{w}). \tag{4.21}$$

The estimated variance for each parameter component $\hat{\boldsymbol{\sigma}}_x^2$ is based on the estimated a posteriori variance:

$$\hat{\boldsymbol{\sigma}}_x^2 = \hat{\boldsymbol{e}}^T\boldsymbol{P}\hat{\boldsymbol{e}}, \tag{4.22}$$

from the dispersion matrix $\boldsymbol{D}$, which gives the uncertainty on the estimated parameter vector $\hat{\boldsymbol{x}}$ as

$$\boldsymbol{D} = \hat{\boldsymbol{\sigma}}_x^2\boldsymbol{Q_{xx}}. \tag{4.23}$$

4.3.1 Accelerometer

The local gravity $\boldsymbol{g}$ serves as a reference for the calibration of the accelerometers, when the IMU is in a fixed position and thus not experiencing other external forces. By orienting the sensor into different attitudes, the signal strength per axis varies accordingly, which allows to decouple the parameters.

In order to facilitate the task of acquiring data, a specific support was created (see Figure 4.1). It is composed of an aluminum body with 2 independent turnable axes. The increments for a fixed rotation is set to 15° per step. Note that the use of the multi-position-calibration scheme does not require perfect alignment between the IMU and this support, nor the exact change in orientation. Thus, the angular increments are only approximate and their perfect knowledge is not needed for the calibration procedure. For the same reason, the table on which the device is mounted, does not need to be perfectly leveled either.

The order in which the readings from different attitudes are recorded does not matter, however, their distribution is important. The following procedure is proposed that assures that the measurements from each axis can be put in relation with at least one other axis:

(1) set the x-y-plane approximately horizontal with the z-axis pointing upwards,

(2) average a measurement for 30 s,

(3) rotate the IMU by 30° along the y-axis and take another measurement,

(4) repeat the rotations and measurements along the y-axis until 360° are reached,

(5) rotate the IMU by 30° along the x-axis and take another measurement,

(6) repeat the measurements at 30° steps along the x-axis until 360° are reached,

(7) rotate the IMU such that the y-z-plane is horizontal with the x-axis pointing upwards,

(8) rotate the IMU by 30° along the z-axis and take another measurement,

(9) repeat the measurements at 30° steps along the z-axis until 360° are reached.

This procedure for the rotation around the different axis is visualized in Figure 4.2. Here again, a perfect alignment is not necessary, as only the norm of the measurements is needed for the calibration.

If several intermediate attitudes are missed, the multi-position-calibration will not be able to decorrelate the different parameters to be estimated. In this case, the correlation matrix is badly shaped. This is shown in the left part of Figure 4.3, where the three biases b_x, b_y, and b_z are sufficiently decorellated from the other parameters, whereas the scale-factors and the non-orthogonalities remain correlated. Only the full set of the different attitudes leads

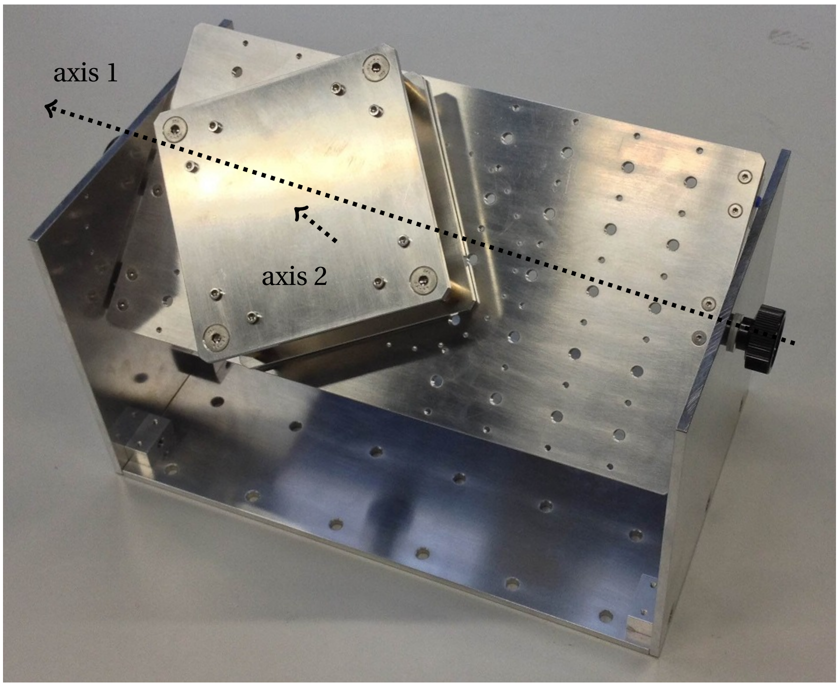

Figure 4.1: Aluminum support (310 mm × 220 mm × 180 mm) for the sensor board. Two independent axes (axis 1 and 2) allow for free rotation with increments of 15° (see Appendix E).

to sufficient decorrelation of the parameters. This scenario is represented in the right part of Figure 4.3.

A typical dataset with the raw measurements is shown in Figure 4.4. The calibration procedure can be followed step-by-step. One can see how the x-axis was almost leveled and how the

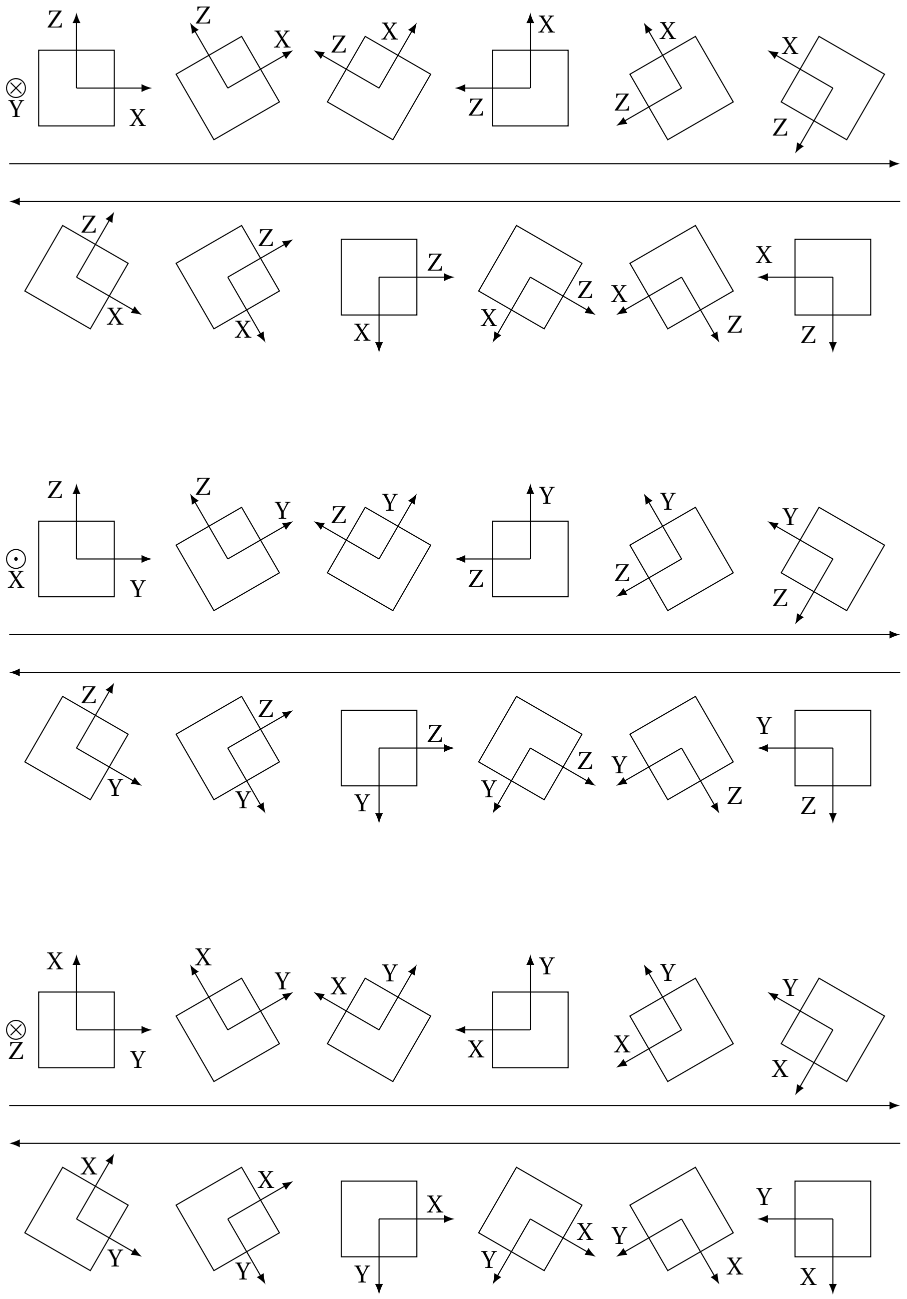
Z
⊗
Y
X
Z
X
Z
X
X
Z
X
Z
X
Z
Z
X
Z
X
Z
X
X
Z
X
Z
X
X
Z
X
Z
Z
Z
⊙
X
Y
Z
Y
Z
Y
Y
Z
Y
Z
Y
Z
Z
Y
Z
Y
Z
Y
Y
Z
Y
Z
Y
Y
Z
Y
Z
Z
X
⊗
Z
Y
X
Y
X
Y
Y
X
Y
X
Y
X
X
Y
X
Y
X
Y
Y
X
Y
X
Y
Y
X
Y
X
X

Figure 4.2: Side view of the IMU for the calibration procedure. A total of 12 rotations of 30° around a specific axis are presented. This sums up to a total of 36 different measurement attitudes.

rotation was executed around this axis, as the y and the z-axis undergo a full rotation and hence sense the local gravity once in a positive sense, and once in a negative sens. The subsequent rotations around the y-axis as well as the z-axis are nicely visible too. The norm of the acquired signal is shown in the bottom part of Figure 4.4. The deviations from the local gravity are significant and easily visible for the non-calibrated signal. The different changes in the norm of the signal are a function of the attitudes, as every axis contributes with its own properties (i.e., bias, scale-factor and non-orthogonality).

The calibration results for one IMU are shown in Table 4.1. The results from bad (insufficient) configuration are associated with a correlation matrix as the one shown in the left Figure 4.3, whereas the good calibration results are associated to the case, where the correlation matrix is almost the identity matrix (e.g., Figure 4.3 right).

If not enough different attitudes are available, the algorithm will have difficulties to correctly estimate the parameters. In other words, accumulating more measurements of the same attitude does not lead to a better parameter estimation. One option to circumvent this problem, is to decrease the number of unknowns (i.e., the number parameters to estimate). This is applicable if some set of parameters is constant in time (e.g., non-orthogonalies or possibly also scale-factors) and therefore is determined once for all (e.g., in lab), while others change per switch-on (e.g., biases). Indeed, such an approach will be adopted later for the Unmanned Aerial Vehicle (UAV) pre-flight calibration. Then, instead of estimating the full set, one can choose to calibrate a subset of the parameters. Although the number of measurements stays the same, the decreased complexity of the matrices $\boldsymbol{A}$ and $\boldsymbol{B}$ in the calibration model allows to estimate the reduced parameter vector from less variations of attitude. We will

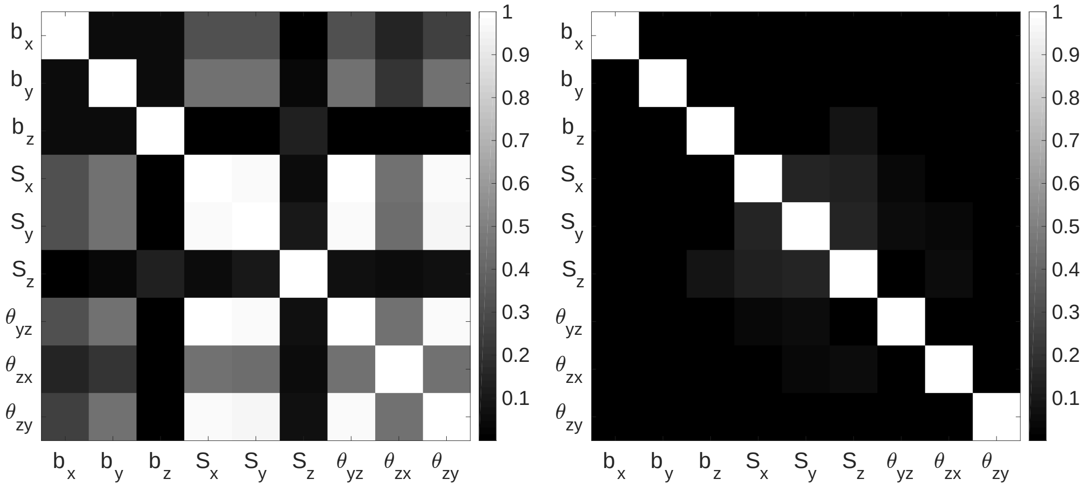

Figure 4.3: Left: badly shaped correlation matrix for the scale-factors and the non-orthogonalities. Right: the parameters are decorrelated sufficiently due to a sufficient number of different attitude measurements.

Table 4.1: Full calibration result for a Navchip IMU accelerometer. The right amount and distribution of the attitudes is required to estimate the parameters.

	insufficient configuration		optimal configuration	
parameter	value	std	value	std
b_x [m/s^2]	-5.91e-2	9.70e-5	-6.52e-2	1.43e-4
b_y [m/s^2]	2.08e-1	1.26e-4	2.12e-1	1.36e-4
b_z [m/s^2]	-3.58e-2	5.00e-5	-2.92e-2	1.58e-4
S_x [-]	2.36e-3	1.83e-4	-3.45e-4	1.73e-5
S_y [-]	-2.02e-3	8.37e-5	-3.21e-4	1.60e-5
S_z [-]	-1.18e-3	5.97e-6	-1.22e-3	1.94e-5
θ_{yz} [rad]	4.54e-2	2.20e-3	-7.05e-4	4.05e-5
θ_{zx} [rad]	-1.52e-5	2.10e-5	-3.70e-4	4.36e-5
θ_{zy} [rad]	6.40e-4	7.16e-5	-9.04e-4	4.11e-5

distinguish between these three calibration cases:

(a) the full model consists of all 9 parameters: bias, scale-factor, and non-orthogonality for

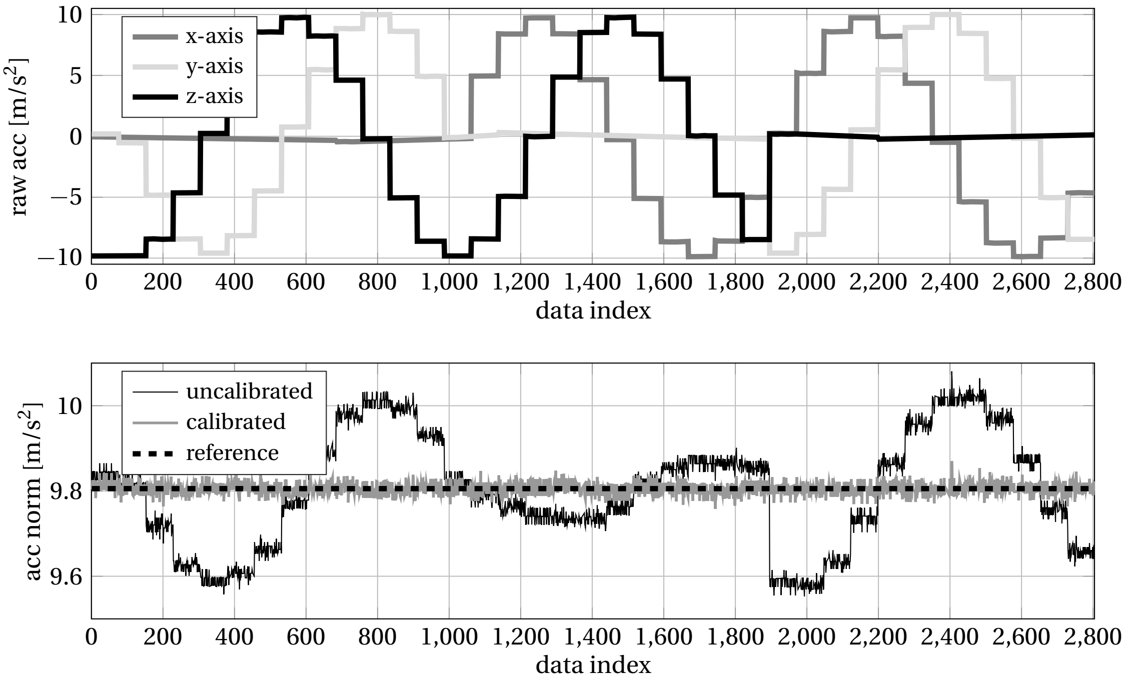

Figure 4.4: Top: shows the raw data from the IMU used for the calibration. Bottom: shows the norm of the uncalibrated data, the norm of the calibrated data, and the reference value (i.e., local gravity).

Table 4.2: Evolution of the estimated parameters for different calibration models.

	full model		reduced model		minimal model	
parameter	value	std	value	std	value	std
b_x [m/s^2]	-5.91e-2	9.70e-5	-5.87e-2	1.03e-4	-5.81e-2	9.98e-5
b_y [m/s^2]	2.08e-1	1.26e-4	2.09e-1	1.27e-4	2.09e-1	1.27e-4
b_z [m/s^2]	-3.58e-2	5.00e-5	-3.41e-2	5.62e-5	-3.41e-2	5.62e-5
S_x [-]	2.36e-3	1.83e-4	-	-	-	-
S_y [-]	-2.02e-3	8.37e-5	-	-	-	-
S_z [-]	-1.18e-3	5.97e-6	-	-	-	-
θ_{yz} [rad]	4.54e-2	2.20e-3	6.33e-3	2.23e-4	-	-
θ_{zx} [rad]	-1.52e-5	2.10e-5	1.35e-4	2.13e-5	-	-
θ_{zy} [rad]	6.40e-4	7.16e-5	-3.12e-4	1.91e-5	-	-

each axis;

(b) the reduced model consists of 6 parameters: bias and non-orthogonality for each axis;

(c) the minimal model consists of 3 parameters: only the bias for each axis.

According to the needs, the two design matrix $\boldsymbol{A}$ and $\boldsymbol{B}$ are adapted to the new calibration model. The result of the estimated parameters is shown in Table 4.2 with their respective correlation matrix in Figure 4.5. By reducing the model, the errors or mismatches are distributed on the retained parameters. The estimation will find the optimal solution in the sense of LS.

4.3.2 Gyroscope

When the IMU is stationary, the gyroscope senses only the rotation rate of the Earth and this value can be used as the reference. As with the accelerometers, different orientations of the gyroscope sensitive axis with relation to the local level frame lead to different amounts of the Earth's rotation rate sensed. The problem with this approach is twofold. First, the excitation of the gyroscopes is limited to the very weak Earth rotation rate. This compared to the rotational dynamics of a vehicle or a drone (i.e., rotation rates of several degrees per second) is insignificant. Hence, in order to correctly estimate the scale-factor parameters, a significantly stronger signal is required. Secondly, the amount of noise present in sensors of lower quality (i.e., consumer MEMS sensors) is likely to be too high to distinguish between the reference signal and noise, as the Earth's rotation is buried in the latter.

A stronger reference signal can be obtained by using a rotation table as that shown in Figure 4.6. This one-axis table is capable to change orientation with a precision of 1 arcsec (0.000 28°) and a set angular speed with precision better than 0.00004% of its value up to a rotation rate of 360 °/s (see Appendix F). The rotation table has a 40 cm large plate, on which equipment can be mounted. It posses a mechanism with which data and power can be transported from the rotating table to the static base. By this means, power up to 24 V and 1 A can be supplied to the equipment if necessary.

For our case, the IMU mount from Figure 4.1 is directly fixed on this rotation table. The interface is compatible to either hold an external battery, or to be supplied via the base of the rotation table. Figure 4.6 shows the final setup with the protective cage around it. The gyroscopes are excited with different rotation rates. Here, the rates of 3 °/s, 30 °/s, and 300 °/s are chosen. The different axis are exited, by turning the mounted IMU in different orientations with relation to the calibration table. As each axis is completely flipped during the calibration procedure, there is no need to set negative reference rotation rates.

As opposed to the calibration for the accelerometers (i.e., only one single acceleration value), the calibration of the gyroscopes is possible with a multitude of reference rotation rates. This allows to relax the number of different attitudes and thus the required number of different excitations on each axis. As with the case of the accelerometer calibration, the absolute orientations do not have to be precisely set, as the calibration input is the absolute rotation value of the reference signal (i.e. speed of the rotation table). The following procedure is considered for the gyroscope calibration by notating arbitrary the 6 faces of the IMU by letters A through F and the 8 corners of the IMU by the letters A' through H':

(1) point the first face A upwards,

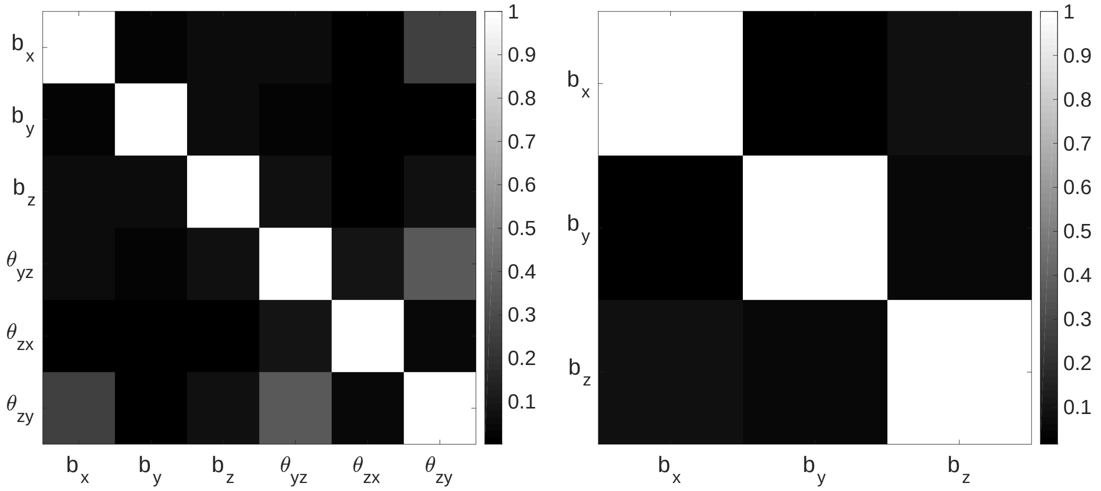

Figure 4.5: Evolution of the correlation matrix by reducing the parameter number. The same dataset is used as for Figure 4.3. Left: bias and non-orthogonality are estimated. Right: only bias parameters for each axis are estimated.

(2) set the rotation speed to 3 °/s and measure for 10 s,

(3) set the rotation speed to 30 °/s and measure for 10 s,

(4) set the rotation speed to 300 °/s and measure for 10 s,

(5) repeat points (1) though (4) for the remaining faces B, C, D, E, and F, by pointing them upwards as well one after the other,

(6) point the first corner A' upwards, such that the 3 faces emerging into corner A' represent a pyramidal shape,

(7) set the rotation speed to 3 °/s and measure for 10 s,

(8) set the rotation speed to 30 °/s and measure for 10 s,

(9) set the rotation speed to 300 °/s and measure for 10 s,

(10) repeat points (6) though (9) for the remaining corners B', C', D', E', F', G' and H' by pointing them upwards one after the other.

A typical dataset of 42 measurements (14 different spacial orientations with each three different rotation speeds) for the in-lab gyroscope calibration is represented in Figure 4.7. The lower

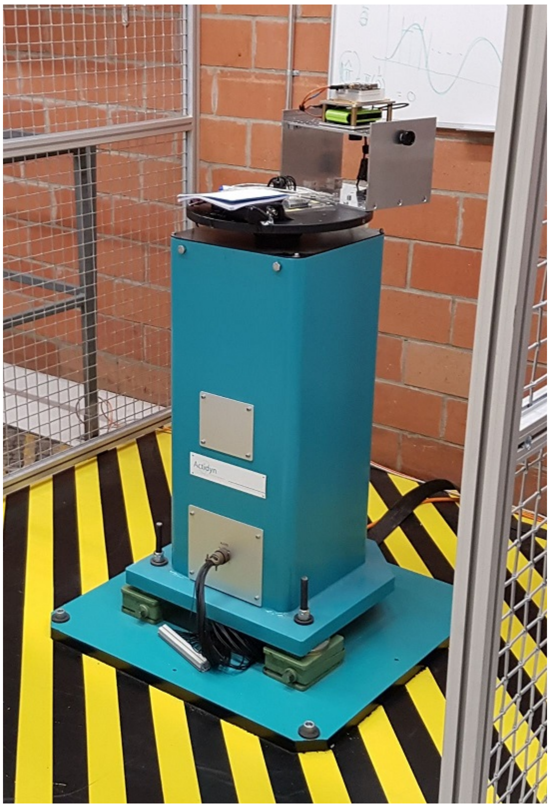

Figure 4.6: IMU installed on the one-axis high-precision rotation table (Appendix F).

Table 4.3: Calibration result for a Navchip IMU gyroscope.

parameter	value	std
b_x [rad/s]	-1.09e-4	5.05e-5
b_y [rad/s]	3.25e-3	5.19e-5
b_z [rad/s]	3.28e-5	3.94e-5
S_x [-]	-7.84e-4	2.27e-5
S_y [-]	-2.97e-3	2.40e-5
S_z [-]	-7.31e-5	1.71e-5
θ_{yz} [rad]	1.85e-3	4.55e-5
θ_{zx} [rad]	-1.63e-3	3.26e-5
θ_{zy} [rad]	1.49e-3	3.26e-5

part of this figure shows a zoom on the peak values of 300 °/s. There is clearly a difference between the measured norm and the reference signal. This calibration procedure decorrelates the estimated parameters sufficiently. As with the case of the accelerometers, the order of the measurements is not important. The value of the estimated parameters for the dataset shown in Figure 4.7 is presented in Table 4.3.

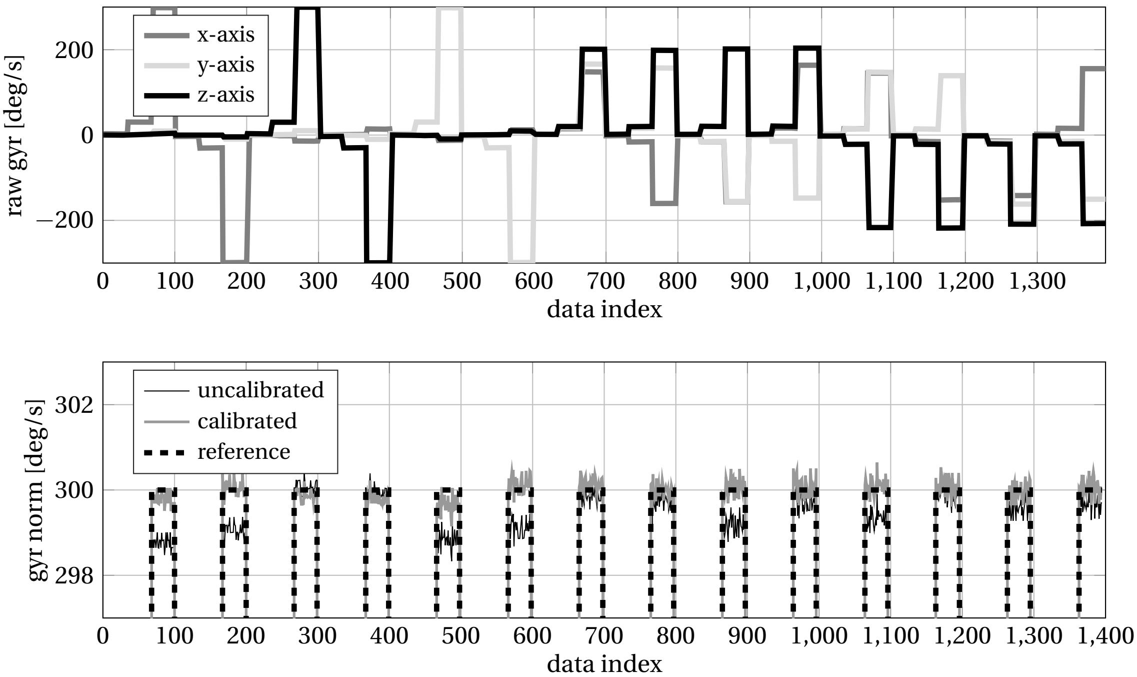

Figure 4.7: Top: measurements of the three axis for different rotation speeds and attitudes. Bottom: Zoom on the norm of the rotation rate around 300 °/s.

4.3.3 Stability Over Time of Estimated Parameters

The stability of the estimated parameters between independent measurements is analyzed on ten full calibration datasets. The measurements are all collected under the same conditions. The datasets 1 through 6 were acquired on the first day, whereas the datasets 7 through 10 were acquired on the second day. The 10 estimated parameter sets for one axis of the accelerometer are presented in Figure 4.8. The amount of the bias changes between the two days, whereas the observed variations in the scale-factor and the non-orthogonality terms corresponds to their 2σ confidence interval. A similar pattern is observed for the different axis of the accelerometer and the gyroscope.

Therefore, scale-factor and the non-orthogonality present some stability over the time. Apart from the temperature change, the mechanical mounting inside the housing of the IMU will have an influence especially on the alignment between the axis. This alignment (compensated via the three non-orthogonality parameters between the axis) can be considered as time invariant. The same is considered for the scale-factor. Hence, 6 parameters can be considered as constants for a specific IMU and its axis. As the switch-on-switch-off-bias is the part that evolves the most over different datasets it is recommended to be re-calibrated every time the sensor is switched on.

The estimation of the full model (accelerometers or the gyroscopes) requires a considerable amount of attitudes and external equipment. However, if only a subset of the calibration parameters is to be estimated, then the amount of orientations is lower to be practicable in the field. Hence, precalibrating the IMU for the scale-factors and the non-orthogonalities leaves the three biases, which can be estimated (as the minimal calibration model) with only 6 different attitudes. This presents a huge advantage practically, as this calibration procedure can be used in the field with small UAV, without special equipment.

The same procedure may be considered for the gyroscopes. The gyroscope triad is precalibrated for all 9 parameters while the 3 biases are considered time-varying. If low-cost MEMS sensors with a bias stability $>20\,^\circ/\mathrm{h}$ are used, then the Earth's rotation rate can not be sensed. For sensors considered here, the in-run bias stability is specified as $18\,^\circ/\mathrm{h}$, while the switch-on bias is at a level of hundred $^\circ/\mathrm{h}$ or larger. In such case taking the mean-offset from the zero as the bias replaces the calibration. This idea is further explained with it's implementation in the software in Chapter 6 and a typical full calibration result is shown in Appendix G again with its 2σ bound representing the uncertainty.

4.4 Dynamic Calibration Scheme

The disadvantage with the previously described calibration procedure for the gyroscope is its dependency on a high-precision calibration table to generate the reference signal. Another possibility to obtain a reference signal for the gyroscope calibration is to use another IMU. In fact, any (more) precise IMU than the one that needs calibration can be used. Figure 4.9 shows

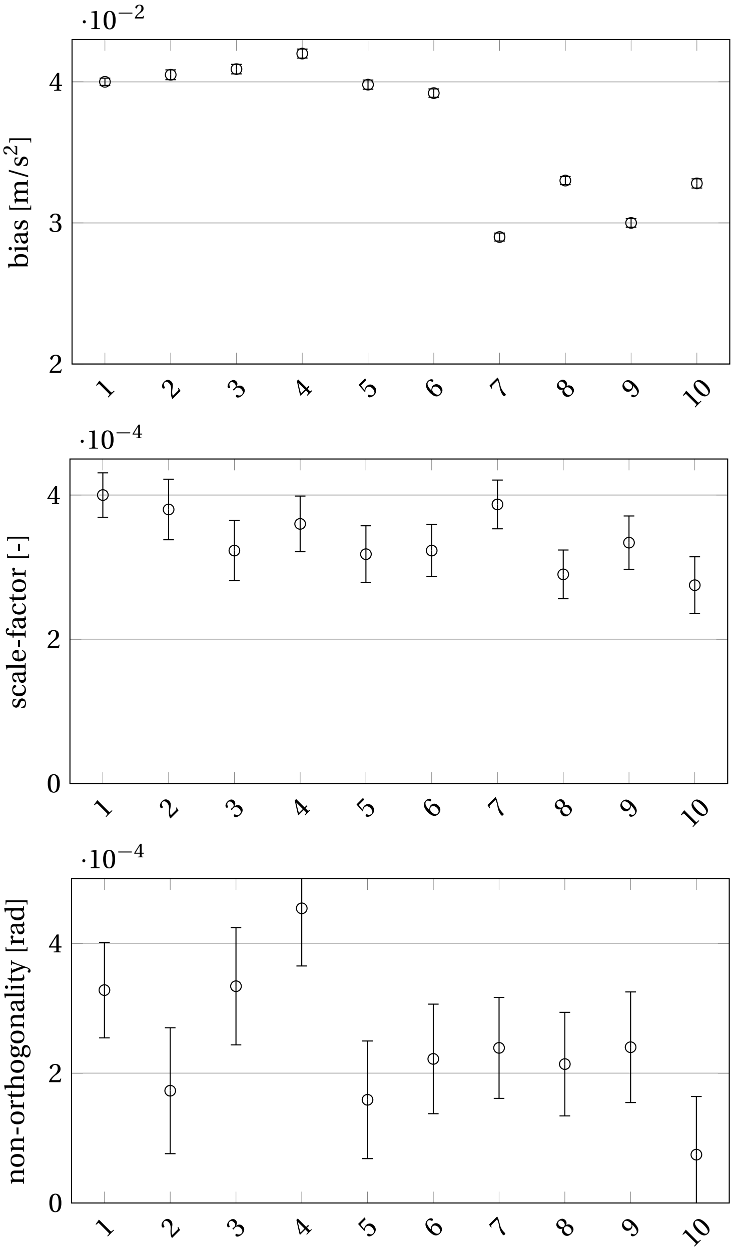

Figure 4.8: Variations of accelerometer calibration in time for the navchip x axis and its 2σ bound.

a setup, where a tactical grade IMU (IMAR-FSAS see C.1) is rigidly connected to the MEMS IMU (Navchip). This setup allows to rotate both IMUs in a same way. The rigid construction allows for a correct measurement of the rotation rate, as long as the acquired observations are referred to the same time. Both IMUs should have also same or similar sampling rate, that is sufficient for the induced rotations (up to 200 °/s).

The principle for this calibration procedure follows a similar idea as with the rotation table: the norm of the reference IMU gyroscope readings is used as the condition in the Gauss-Helmert model. However, instead of having only a couple of different reference values (i.e., 3 °/s, 30 °/s, and 300 °/s) at a limited number of attitudes, a whole vector with a discrete set of norms is generated. The dataset is acquired by swinging first the IMUs around each axis individually, then around a combination of several axis. A typical signal set acquired by the IMU is represented in Figure 4.10.

The calibration is only as good as the reference IMU. If the reference signal is biased, this error will be projected on to the supposedly calibrated IMU. The procedure itself is tested here with a emulated dataset. The dataset takes the raw measurements of the swinging IMAR and adds on it the 9 parameters, which are to be estimated. In addition, a white noise component of 0.001 rad/s amplitude is added to all the axis. This is done to simulate a lower grade IMU, which has increased stochastic noise properties. Indeed, this noise level is a typical value for the Navchip IMU, which can also be found in Section C.3. The result of the calibration

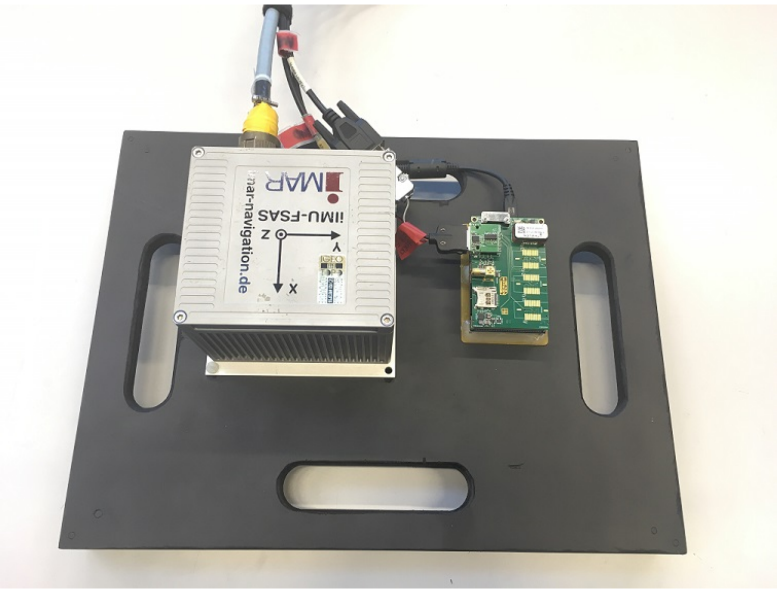

Figure 4.9: The 41 cm by 31 cm mount holds the IMAR and the Navchip senors. The handles allow for easy grip and save manual swinging of the setup with the power and data cables leaving the platform.

Table 4.4: Calibration result for a gyroscope with emulated data based on typical error values.

parameter	simulated value	estimated value	estimated std
b_x [rad/s]	-3.60e-4	-3.28e-4	1.99e-5
b_y [rad/s]	1.96e-3	1.95e-3	2.03e-5
b_z [rad/s]	-2.45e-4	-2.56e-4	1.89e-5
S_x [-]	-3.02e-3	-3.02e-3	1.36e-5
S_y [-]	-3.19e-3	-3.18e-3	1.31e-5
S_z [-]	3.57e-4	3.69e-4	1.25e-5
θ_{yz} [rad]	1.58e-4	1.23e-4	1.96e-5
θ_{zx} [rad]	-1.27e-3	-1.29e-3	1.75e-5
θ_{zy} [rad]	1.34e-3	1.32e-3	1.77e-5

considering the full model is summarized in Table 4.4. It shows, how the parameters can be correctly recovered and how this system can be used to calibrate an IMU without the need of the rotation table.

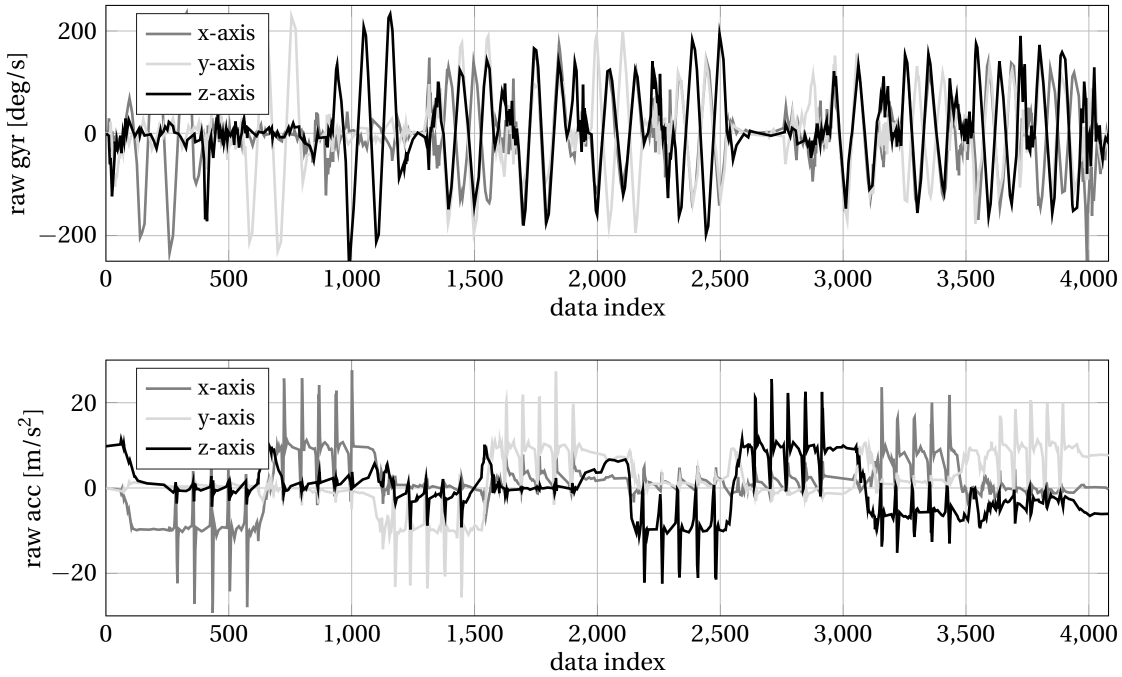

Figure 4.10: Top: Gyroscope measurements for each axis. First, individual axis are excited, then there is a mix of the rotation about different axis. Bottom: The accelerometer measurements are acquired by linearly shaking the setup, which is visible by the peaks.

4.5 Magnetometer

4.5.1 Problem Statement

An ideal magnetometer measures the strength of the total magnetic field and its direction $\check{\boldsymbol{m}}$. The magnetic field of the Earth is subject to distortions due to many sources. The hard iron bias expressed by the 3×1 vector $\boldsymbol{b}_h$ is due to a nearby magnetic source (e.g., UAV motor magnets). It shifts the magnetometer measurement by a constant amount in one direction. In contrast, the soft iron distortion, expressed by the 3×3 matrix $\boldsymbol{R}_s$, affects the measurements irregularly depending on the orientation of the sensor. This kind of distortion is due to ferromagnetic materials and their interaction with the magnetic field. Sensor axis non-orthogonality $\boldsymbol{N}$, scale-factors $\boldsymbol{S}$, and sensor offsets $\boldsymbol{b}_o$ can be considered too. An example is shown in Figure 4.11, where the unit sphere at the centre represents the calibrated readings, while the spheroid results from the combined effect of the previously mentioned influences as

$$\boldsymbol{m} = \boldsymbol{R}_s \cdot \boldsymbol{S} \cdot \boldsymbol{N}(\check{\boldsymbol{m}} + \boldsymbol{b}_h) + \boldsymbol{b}_o + \boldsymbol{\varepsilon}, \tag{4.24}$$

with $\boldsymbol{\varepsilon}$ representing a Gaussian white noise $\mathcal{N}(0,\sigma^2)$. A translation by $\boldsymbol{b}$ plus a total transformation by the 3×3 matrix $\boldsymbol{R}$ describes this shifted ellipsoid as:

$$\boldsymbol{m} = \boldsymbol{R} \cdot \check{\boldsymbol{m}} + \boldsymbol{b} + \boldsymbol{\varepsilon}. \tag{4.25}$$

The transformation matrix and bias are combined as:

$$\begin{aligned} \boldsymbol{R} &= \boldsymbol{R}_s \cdot \boldsymbol{S} \cdot \boldsymbol{N} \\ \boldsymbol{b} &= \boldsymbol{R}_s \cdot \boldsymbol{S} \cdot \boldsymbol{N} \cdot \boldsymbol{b}_h + \boldsymbol{b}_o. \end{aligned} \tag{4.26}$$

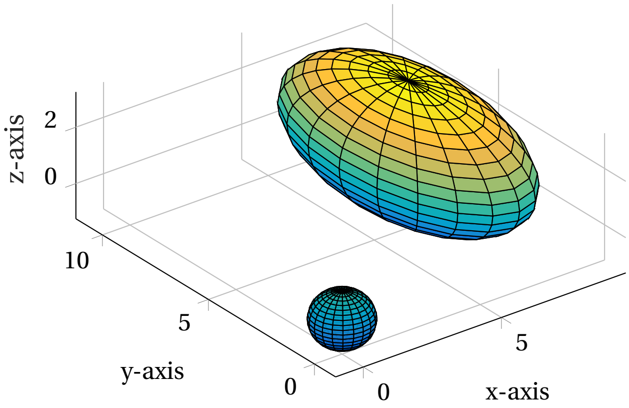

Figure 4.11: Calibrated magnetometer readings are centered on a unit sphere, whereas the uncalibrated measurements are shifted and scaled.

The calibration of the magnetometer in its environment can be achieved by different means. One example is the so called compass swinging explained by [Bowditch, 1984] and [Gebre-Egziabher et al., 2006]. Here, only the horizontal component of the Earth's magnetic field is considered. The heading with respect to the magnetic north is measured. This value is then directly compared to a reference. Several measurements are taken by swinging the magnetometer through different headings and a correction is determined by means of the reference. The drawbacks of this method are twofold. First, the error corrections of the heading depend on the total magnetic field, which is a function of a location. So the calibration has to be redone when moving. The other drawback consists of the need to level the magnetometer prior calibration and this is done through extra sensors such as an accelerometer.

Another approach focuses on the minimization of the difference between the magnitude of the observed magnetic field and the magnitude of the local Earth magnetic field via a Maximum Likelihood Estimator (MLE) [Alonso and Shuster, 2003]. It was shown that such "scalar value approach" is highly dependent on the initial values and can converge to wrong parameters. The utilization of the vector measurements is some what better, yet still sensitive to the goodness of the initialization [Wu and Shi, 2015; Vasconcelos et al., 2011]. Those approaches try to best fit the measurements to the ellipsoid. [Kok et al., 2012] goes one step further and calibrates the alignment between the magnetometer and the IMU at the same time, by taking the accelerometer measurements into account.

Another approach consists of fitting the measurements not via the MLE but geometrically, for instance utilizing Singular-Value Decomposition (SVD) and the properties that relay a sphere to the ellipse [Renaudin et al., 2010; Vasconcelos et al., 2011]. Such method is adapted as follows.

4.5.2 Transformation of Ellipse to a Sphere

The goal of calibration is to invert the Equation 4.25 to recover the ideal measurements $\check{\boldsymbol{m}}$, which are represented by a centered sphere with a radius of the intensity of the magnetic field:

$$\check{\boldsymbol{m}} = \boldsymbol{R}^{-1}(\boldsymbol{m} - \boldsymbol{b}). \tag{4.27}$$

The LS approach is used here. For this, the 3-axis ellipsoid is expressed in its quadratic form:

$$ax^2 + by^2 + cz^2 + 2dxy + 2exz + 2fyz + 2gx + 2hy + 2iz = 1. \tag{4.28}$$

The parameters $\hat{\boldsymbol{x}} = [a, b, c, d, e, f, g, h, i]^T$ are estimated from the ith sensor readings x_i, y_i, and z_i. The system with the N measurements, the design matrix $\boldsymbol{H}$, the residual $\boldsymbol{v}$, and the parameters in $\boldsymbol{x}$ are written as

$$\boldsymbol{z} - \boldsymbol{v} = \boldsymbol{H} \cdot \boldsymbol{x}$$

$$\begin{bmatrix} 1 \\ 1 \\ \vdots \\ 1 \end{bmatrix} - \begin{bmatrix} v_1 \\ v_2 \\ \vdots \\ v_N \end{bmatrix} = \begin{bmatrix} x_1^2 & y_1^2 & z_1^2 & 2x_1y_1 & 2x_1z_1 & 2y_1z_1 & 2x_1 & 2y_1 & 2z_1 \\ x_2^2 & y_2^2 & z_2^2 & 2x_2y_2 & 2x_2z_2 & 2y_2z_2 & 2x_2 & 2y_2 & 2z_2 \\ \vdots & \vdots & \vdots & \vdots & \vdots & \vdots & \vdots & \vdots & \vdots \\ x_N^2 & y_N^2 & z_N^2 & 2x_Ny_N & 2x_Nz_N & 2y_Nz_N & 2x_N & 2y_N & 2z_N \end{bmatrix} \cdot \begin{bmatrix} a \\ b \\ c \\ d \\ e \\ f \\ g \\ h \\ i \end{bmatrix}. \tag{4.29}$$

With the same weight for all the measurements the solution to the LS problem is

$$\hat{\boldsymbol{x}} = \left(\boldsymbol{H}^T \mathbf{H}\right)^{-1} \mathbf{H}^T \mathbf{z}. \tag{4.30}$$

The parameters in $\hat{\boldsymbol{x}}$ are then used to recompute the matrix $\boldsymbol{R}$, respectively the inverse $\boldsymbol{R}^{-1}$ and the translation vector $\boldsymbol{b}$ of the ellipsoid as in Equation 4.27 [Vasconcelos et al., 2011]. A typical result is shown in Figure 4.12. The uncalibrated magnetometer dataset is composed of full revolutions of the sensor around all its axes. A complete ellipse can be described and the parameters can be estimated. A rotation and translation leads then to the centered unit sphere.

This full dataset represents an optimal acquisition from the laboratory. In reality, this calibration will be performed on the field, on the location where the sensor will be used. A real-time implementation is required for the usage with a feedback mentioning a complete calibration. A typical in-field calibration is represented in Figure 4.13, where the distribution of the data points does not follow patterns around the sphere. They are more randomly clustered, as the calibration is done by hand without an apriori any indicator for completeness.

In fact, the problem comes from the quadratic form of equation 4.28, which is used to describe the ellipsoid. Under certain circumstances, the same equation is used to describe other surfaces, such as hyperboloids or paraboloids. If the parameter determination is done in real-time, with pieces of data coming in periodically, attention has to be paid not to converge too early to a local optimum, which could correspond to another quadratic surface (i.e., not the ellipsoid).

To avoid such situation, two indicators are employed. The first indicator represents the data coverage of the sphere. In fact, the total surface of the sphere is divided into 100 equally distributed small surface areas. If a measurement falls into the area delimited by such a bin, then this bin will be assumed as *complete*. The only data considered are the data from different bins acquired during movement. This lightens the computation while improving the observability of the parameter vector $\hat{\boldsymbol{x}}$. The nearby mounted IMU is used to distinguish between the moving and the static states with some empirical threshold on the IMU data. The acquisition goes on as long as the minimum number of required bins is not filled.

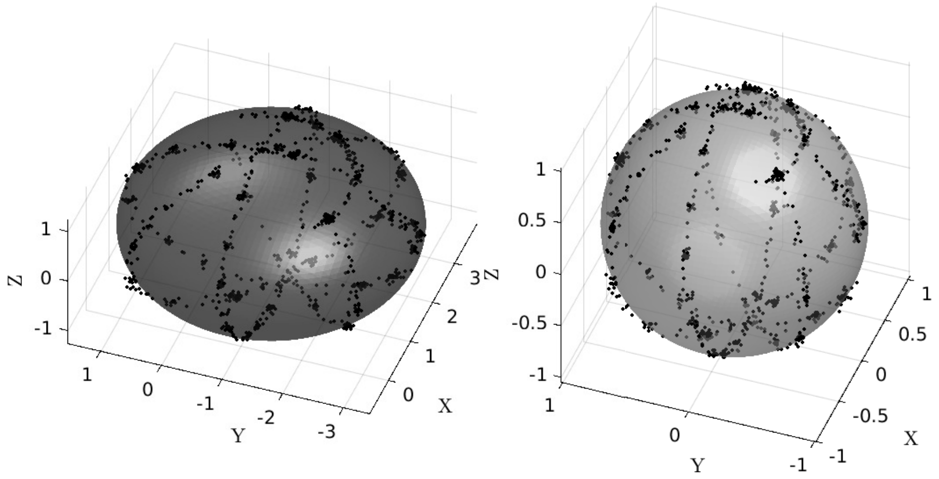

Figure 4.12: Left: raw magnetometer data as ellipse and arbitrary units. Right: calibrated magnetometer data as a centered unit sphere. Data was acquired in perfect lab conditions.

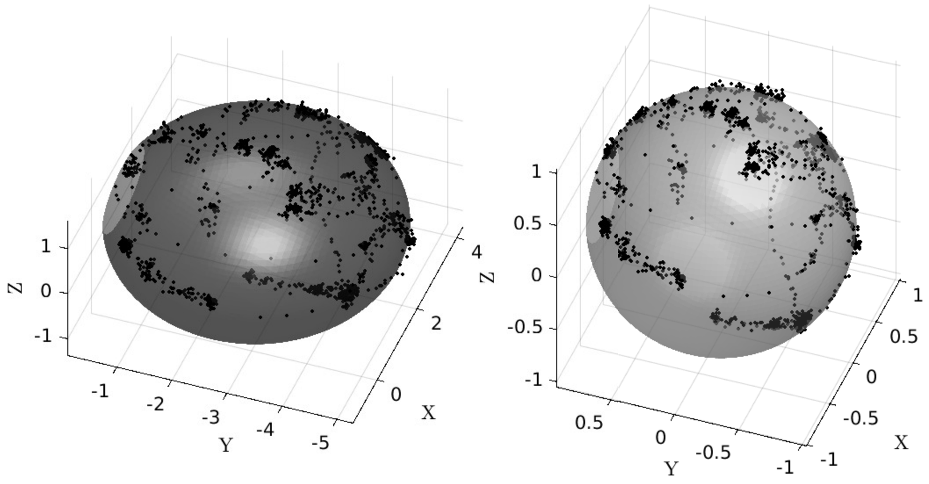

Figure 4.13: Left: raw magnetometer data as ellipse and arbitrary units. Right: calibrated magnetometer data as a centered unit sphere. Data acquired by hand on the field. Big holes in the dataset can be seen.

The second indicator is the variation of the norm of the calibrated data that should lie around the value of the radius of the sphere, which equals the value one. This distribution is an indicator of how close the mapped data are to the sphere. These two indicators and their evolution of a dataset acquired in-field conditions is shown in Figure 4.14. In fact, the first estimation of the parameters is carried out after 30 packets, where one packet corresponds to one second of data acquired at 125 Hz. Subsequent estimations are executed every 10 packets. This procedure is repeated until both criteria are met. The sphere coverage threshold is set to 65% whereas the threshold for the standard deviation from the norm is set to 0.05. Both indicators highly depend on the distribution of the data. Several jumps in these indicators can be observed when the estimation leads to a new set of parameters for the sphere.

4.6 Barometer

4.6.1 Problem Statement

The Equation 2.19shows the basic relations to calculate the height difference δH from observing the pressures p_0 and p_i, with the molar mass M, and the temperature T provided by a model. Figure 4.15 shows so determined barometric differences in altitude during a UAV flight together with the differences to the reference. Humid air is assumed. As seen in the bottom of the figure, the barometric solution drifts away with relation to the reference provided by the Global Navigation Satellite System (GNSS) carrier-phase differential height, which grows with

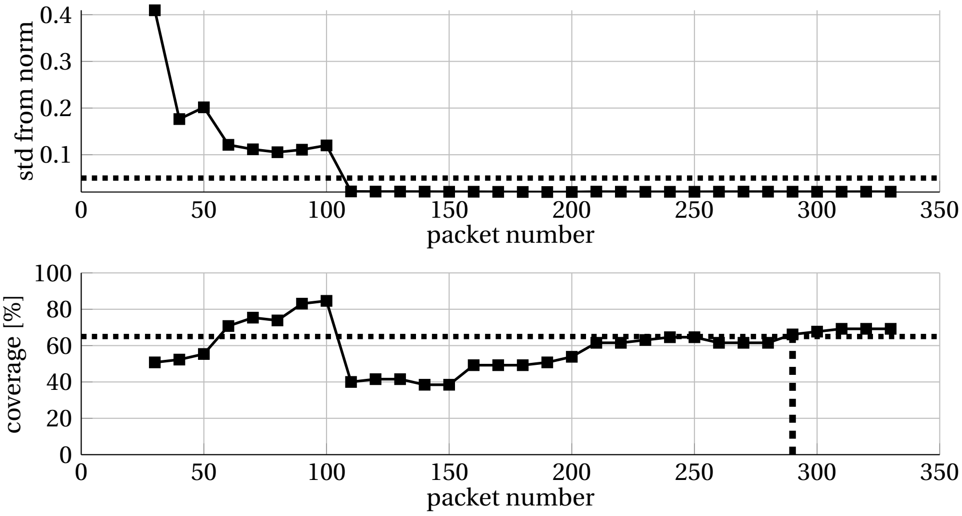

Figure 4.14: Top: evolution of the standard deviation from the norm (equals 1) of the datapoints with a threshold set to 0.05. Bottom: evolution of the sphere coverage with a threshold of 65%. Both conditions are met around the 300th receiver packet of data. One packet consists in this case of 1 s of data.

increasing height.

The reasons for the increasing drifts are mainly twofold:

1. Wrong guess (model) of the molar mass of the humid air,
2. Imprecise measurements of the temperature and the pressure due to the hardware limitations.

The barometer used in the setup is a small MEMS device as explained in Appendix C.5. Although the sensor provides temperature and pressure measurements, however the fact that it is mounted inside the bay of the UAV drone does not reflect the temperature of the air. During the preparation on the ground before takeoff, all the sensors are running and producing heat, the temperature T rises by more than 10 °C above the ambient air temperature. The direct usage of the temperature measurement from the sensor is thus not reliable and without compensation introduces errors of several meters.

Similar problems exist with the pressure data. In fact, the provided pressure data is internally compensated by the measured temperature. In other words, wrong measurement of the temperature leads to a wrong internal scaling of the the pressure. This is problematic, as the reference pressure p_0 comes directly from the barometer, as additional equipment to measure this quantity is unavailable.

After take-off, air is pushed by the engine through holes in the fuselage of the drone to cool the engine controller and indirectly also the additional hardware. Due to this airflow, the

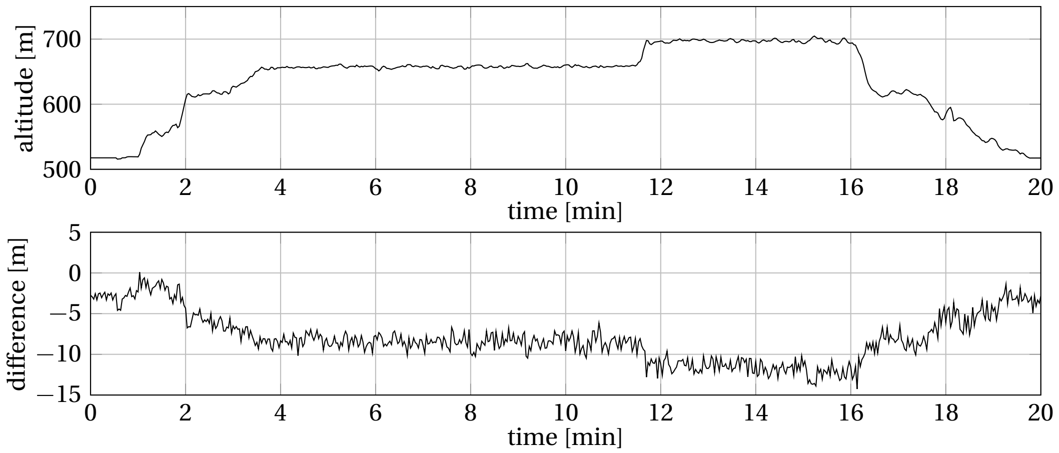

Figure 4.15: The upper plot shows the absolute reference height, whereas the lower plot shows the difference in height between the reference and the converted barometric height measurements. The error grows with increasing heights. Typical values for pressure, temperature, and humidity were used for the conversion.

measured temperature inside the drone approaches the external ambient air temperature 0and thus the pressure readings p_i are correctly scaled. Such 'stabilization' occurs within minutes after take-off.

The exact molar mass M of the air is also unknown, as no additional equipment is available to observe this quantity directly and reliably on the field. The humidity in the air influences the modeled value and thus the height estimation via the Equation 2.19 by several meters (see Table 2.4).

4.6.2 Parameter Calibration via EKF

Instead of relying in these wrongly measured parameters p_0 and T as well as the immeasurable parameter M, an o-line calibration of these quantities is proposed, employing the initial height measurement h_0 and the subsequent height measurements during the flight h_i from the GNSS-receiver. The ratio of the temperate and the molar mass is combined in a single new parameter $k = M/T$.

The parameters to be estimated are assembled in an augmented state vector:

$$\boldsymbol{x} = [\Delta h \quad k \quad p_0]^T, \tag{4.31}$$

noting that Δh is already a part of the usual state vector. The height h_{INS} is traditionally calculated from the INS or some other dynamic model. The measurement update is usually expressed as

$$z = h(x) + v. \tag{4.32}$$

Linearisation around the current state $\tilde{x}$ and rearranging results in the KF observation

$$z - h(\tilde{x}) = \left[\frac{\partial h}{\partial x}\right]_{\tilde{x}} \Delta x + v. \tag{4.33}$$

If a GNSS measurement h_{GNSS} is available, then a KF-observation can directly be calculated as

$$z_{GNSS} = h_{GNSS} - h_{INS}, \tag{4.34}$$

with the measurement matrix $H_{GNSS} = [1 \quad 0 \quad 0]$. If a barometer measurement p_{baro} is available, then the KF-observation is rewritten as

$$z_{baro} = p_{baro} - p_{INS}, \tag{4.35}$$

where p_{INS} is the pressure and expressed as a function of the to be estimated parameters p_0 and k, the calculated height h_{INS} as well as the other quantities h_0, R, and g, which are fixed and known. They are related via

$$p_{INS} = p_0 \exp\left(\frac{-kg}{R}(h_{INS} - h_0)\right). \tag{4.36}$$

The measurement matrix is computed from $H_{baro} = [\frac{\partial p_{INS}}{\partial h_{INS}} \quad \frac{\partial p_{INS}}{\partial k} \quad \frac{\partial p_{INS}}{\partial p_0}]$ with

$$\begin{aligned} \frac{\partial p_{INS}}{\partial h_{INS}} &= \frac{-kg}{R} \cdot p_{INS} \\ \frac{\partial p_{INS}}{\partial k} &= \frac{-g}{R}(h_{INS} - h_0) \cdot p_{INS} \\ \frac{\partial p_{INS}}{\partial p_0} &= \frac{p_{INS}}{p_0} \end{aligned} \tag{4.37}$$

Current estimates are used to calculated the H matrix whenever updates are available. The process models are incorporated with $\dot{c} = 0$, meaning that this parameter does not change in time (i.e., the humidity and the temperature does not change, which is reasonable for UAV applications with a typical duration of 20 min). The initial quantity can be calculated from standard atmospheric values such as $c(0) = \frac{M}{T}$.

The process model for the reference pressure is stated as $\dot{p_0} = 0$. Here again, the change in time is negligible, as the pressure is assumed constant for the short time of the UAV mission. It is initialized by simply taking the first pressure reading from the barometer $p_0(0) = p_{baro}(0)$.

The Figure 4.16 shows the results of the continuous estimation of the two parameters. The drone flies at roughly 200 m height. The parameters p_0 and k are estimated during the climbing and stabilize once the drone remains at the same altitude (i.e., additional measurements do not change the estimation of the parameters).

The newly calculated parameters of the state vector $\hat{\boldsymbol{x}}$ serve as values in the conversion from pressure to altitude, until a next set is estimated. The longer the flight is, the smaller the error becomes. The GNSS code measurements are noisy and have an offset compared to the Post Processed Kinematic (PPK) solution, which is smooth. The barometer is able to compensate such noise and bridge the outages in GNSS signal reception practically with very high accuracy ($<$1 m).

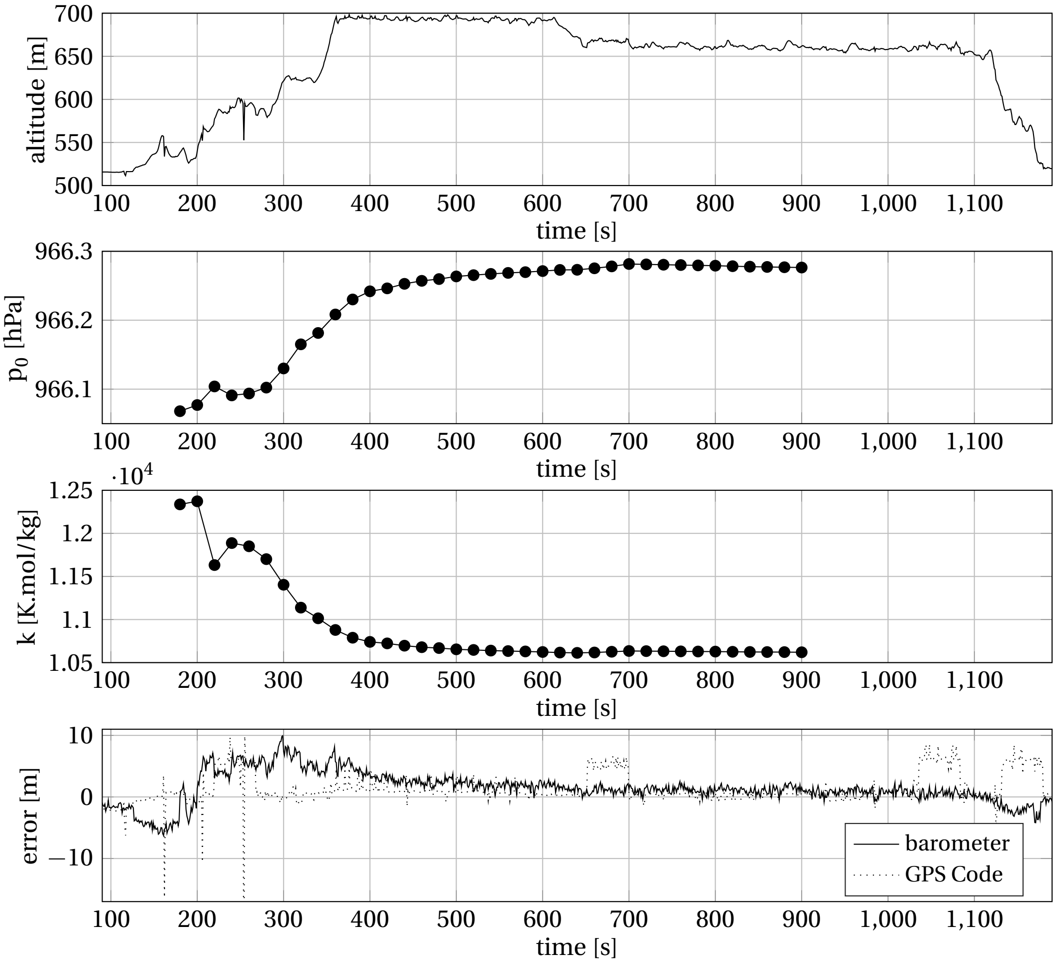

Figure 4.16: The first plot shows the evolution of the absolute altitude. The second and third plot show the estimated parameters p_0 and k and their evolution through the GNSS code-measurements. They evolve, when the altitude is changed until they reach a plateau. The fourth plot shows firstly the difference between the barometer solution and the reference, and secondly the difference between the GNSS code solution and the reference. The reference is the GNSS PPK solution.

5 Stochastic Parameters with Time Dependency

5.1 Introduction

The factory calibration determines (and compensates for) the variation of basic model parameters as bias b or scale-factor S with respect to temperature or dynamic cycling over a given period of time [Titterton and Weston, 2004]. Although these conditions are adequately addressed when dealing with the deterministic errors (i.e., the bias changes as a function of the temperature, which is taken into consideration when dealing with the sensor measurements), this is unfortunately not the case for the stochastic properties of the error measurements. Indeed, the complex models underlying the stochastic errors are affected by the varying external conditions which modify the parameter values of the error state-space model through time. This fact has not been rigorously addressed so far. This motivates proposing an extension to the Generalized Method of Wavelet Moments (GMWM) estimator to determine the variation of stochastic parameters adequately as a function of such external co-variate (e.g., temperature, pressure).

This chapter will in a first part refresh the stochastic parameters and the GMWM estimator, to pass on to the extension, which takes into account an external co-variate. The mathematical properties of the estimator are briefly presented. The mathematical proof is being edited and will be submitted in spring 2019[1]. Part of this chapter is based on this manuscript in preparation. Two case-studies are considered. In the first case, we analyze the evolution of the stochastic properties as a function of the temperature. This is realized by placing the sensor on a flat surface inside a thermal chamber temperature of which is modified over a long period of time. The variations of the sensor signal output are studied (after subtracting its mean) as a function of the temperature.

---

[1] Estimation of Inertial Sensor Stochastic Characteristics under Varying Environmental Conditions, IEEE Transactions on Signal Processing

In the second case, we analyze the evolution of the stochastic properties of a sensor subject to motion dynamics. There, the sensor is placed on a high precision rotation table and spun at different rotational speeds. Then, variations from the reference are studied as a function of turn-rate.

The information from the stochastic calibration of the sensors is fed directly to the Kalman filter, which will allow for an optimized solution in the sense of uncertainty (i.e., not too optimistic and not too pessimistic). We will demonstrate the impact of covariate-dependent stochastic models (and their omission) on the estimation of trajectory parameters in the later Chapter 7.

5.2 Model Description

The determined parameters of the stochastic noise of a sensor evolve in time due to external/environmental influences, they do not necessarily correspond to those found in the controlled environment, which is provided by a datasheet. An influence can be the temperature or the physical motion of the device. Other influences such as pressure, or humidity are possible too and depend on the typology of the sensor used. Although part of these conditions is adequately addressed when dealing with the deterministic errors (e.g., a sensor in a heating chamber observes a constant signal and the temperature-dependent deterministic calibration model then forces the signal back to such a constant), this is unfortunately not the case for the stochastic characterization.

We let $(Y_t, X_t : t \geqslant 1)$ denote the real-valued bi-variate stochastic process we wish to study with t the indexed time-stamps defined in $[1, T]$. The processes (Y_t) and (X_t) correspond, respectively, to the process of interest (e.g., signal of an inertial sensor) and an explanatory covariate (e.g., temperature); they are referred to as the *signal* and the *covariate* from hereafter. The covariate is believed to have an “impact” on the signal, it is formalized by the following regression model

$$Y_t = f(X_t) + Z_t, \quad t = 1, \ldots, T, \tag{5.1}$$

where the error process Z_t (the *error* from hereafter) is a zero-mean process, i.e. $\mathbb{E}[Z_t|X_t] = 0$, and f is an unknown real-valued smooth function (see [Hastie and Tibshirani, 1990]). More specifically, the error is modelled as a finite sum of independent latent processes. Attention is restricted to error processes that have the following form

$$Z_t = W_t + Q_t + \sum_{i=1}^{d} A_{t,i}, \quad d < \infty, \tag{5.2}$$

where W_t is a white noise process (WN), Q_t is a quantization noise process (QN), and A_t represents a first order auto-regressive process (AR1). In the context of inertial sensor calibration, each of these latent processes has a physical meaning [Titterton and Weston, 2004]. Although the same model is sometimes considered in various applications (see for example the model considered in [Nikolic et al., 2016]), there are a variety of latent models that are preferred to characterize the stochastic error of inertial sensors so that these have a state-space representation.

5.3 Dynamic GMWM Estimator

Until now, the dataset was constructed from signal variations in static conditions, where the sensor was placed at rest, and the measurements are taken for several hours. Hence, an entire dataset would be used for a GMWM analysis by subtracting its mean. For a situation when such conditions are no longer valid (e.g., leap-change in temperature or several different rotation speeds) we define a total of K different bins k in the dataset with each a different constant covariate c_k. Different latent stochastic processes used for each bin k are defined as:

- White Noise (WN):

$$\begin{aligned}\sigma^2_{WN,k} &= f_1(\varsigma_1, \varsigma_2, c_k)\\ &= \exp(\varsigma_1 + \varsigma_2 \cdot c_k)\end{aligned} \tag{5.3}$$

- Quantization Noise (QN):

$$\begin{aligned}\sigma^2_{QN,k} &= f_2(\kappa_1, \kappa_2, c_k)\\ &= \exp(\kappa_1 + \kappa_2 \cdot c_k)\end{aligned} \tag{5.4}$$

- Auto-Regressive model of order one (AR1):

$$\begin{aligned}\phi_{AR1,k} &= f_3(\varphi_1, \varphi_2, c_k)\\ &= \tanh(\varphi_1 + \varphi_2 \cdot c_k)\end{aligned} \tag{5.5}$$

$$\begin{aligned}\sigma^2_{AR1,k} &= f_4(\upsilon_1, \upsilon_2, c_k)\\ &= \exp(\upsilon_1 + \upsilon_2 \cdot c_k)\end{aligned} \tag{5.6}$$

The functions $f_{1,2,3,4}$ are mapping functions that incorporate the covariate dependence of the stochastic process. The choice to connect the noise parameters and the covariate c_k via an exp-function can be translated to a kind of linear relation on the log-log plot. This mapping function can also be chosen differently. The choice for the tanh-function in Equation 5.5 is related to the fact that the parameter ϕ from the AR1 process has a definition domain between -1 and 1. Hence, other functions fulfilling this requirement could be used as a mapping function as well.

With these definitions we write, the new extended parameter vector $\boldsymbol{\theta}$ taking into account WN, QN, and AR1 to:

$$\boldsymbol{\theta}_E = \left[\varsigma_1 \ \varsigma_2 \ \kappa_1 \ \kappa_2 \ \varphi_1 \ \varphi_2 \ \upsilon_1 \ \upsilon_2\right]^T \tag{5.7}$$

Here again, the empirical Wavelet Variance (WV) $\hat{\boldsymbol{v}}_k$ over the K different bins have to match with the theoretical WV $\boldsymbol{v}(\boldsymbol{\theta}, c_k)$ of these bins, which is now a function of the measured covariate c_k. The estimator $\hat{\boldsymbol{\theta}}$ is thus minimizing the following objective function, which is a modified version of the GMWM estimator:

$$\hat{\boldsymbol{\theta}} = \underset{\boldsymbol{\theta}\in\boldsymbol{\Theta}}{\operatorname{argmin}} \frac{1}{K} \sum_{k=1}^{K} \left\| \hat{\boldsymbol{v}}_k - \boldsymbol{v}(\boldsymbol{\theta}, c_k) \right\|^2_{\hat{\boldsymbol{\Omega}}_k}, \tag{5.8}$$

where $\hat{\boldsymbol{\Omega}}_k$ is a weighting matrix of the k^{th} bin. The formal discussion and the different proofs of the estimator properties will be addressed in detail in the mentioned upcoming manuscript. The proofs include the following properties:

- Identifiable: stating that if the result of one set of parameters leads to the same result as another set of parameters, then these parameters have to be the same:

  $$\boldsymbol{v}(\boldsymbol{\theta}_1) = \boldsymbol{v}(\boldsymbol{\theta}_2) \quad \text{iff} \quad \boldsymbol{\theta}_1 = \boldsymbol{\theta}_2. \tag{5.9}$$

- Consistent: the estimator $\hat{\boldsymbol{\theta}}$ is said to be consistent if it converges in probability and with growing dataset size to the true $\boldsymbol{\theta}_0$:

  $$\hat{\boldsymbol{\theta}} \xrightarrow{\text{p}} \boldsymbol{\theta}_0. \tag{5.10}$$

- Asymptotically normal: stating that the distribution converges to a normal distribution with growing dataset size :

  $$\sqrt{T}\left(\hat{\boldsymbol{\theta}} - \boldsymbol{\theta}_0\right) \xrightarrow[T\to\infty]{\text{p}} \mathcal{N}\left(\boldsymbol{0}, \boldsymbol{\Sigma}\right). \tag{5.11}$$

5.4 Temperature

This first case study will show how the *dynamic-GMWM* performs on a real dataset. The chosen data was acquired from a non-moving Inertial Measurement Unit (IMU) placed in a cooling/heating chamber[2]. Hence, the signal-change corresponds to errors, which nature has deterministic and stochastic dependence on a (continuous) change of the temperature. The temperature X_t is observed and recorded at time t with an acquisition rate of 1 Hz. This information is used in a first step to compensate for the bias variation $f(X_t)$ (according to Equation 5.1). The determination of this function and its parameters is considered as the deterministic sensor calibration for the temperature induced bias. Such a calibration step is necessary, as pure raw data is recorded (i.e., no data calibration was performed beforehand).

The IMU sensor was installed in a closed heating/cooling unit. The temperature in this chamber was set in a way that the starting temperature was 60 °C. The room was then cooled down to -20 °C over a time-span of roughly 3 h (see Figure 5.1). The change of the temperature is neither linear nor step-wise, but it is smooth and continuous.

The static data acquired during the temperate change consists of the three axes of a gyroscope and the three axes of an accelerometer (an IMU-sensor-triad). The transition from a hot state to a cold state, which corresponds to the temperature-changes is shown Figure 5.2 together with the sensor uncompensated and not pre-calibrated raw-data. One can directly see two things. First, the values of the mean signals change considerably in time with the change of the temperature. Over the 80 °C temperature range the gyroscope bias evolves by more than 8 mrad/s whereas the accelerometer bias evolves by more than 0.1 m/s^2. Secondly, the apparent change of the noise characteristics (quantity and amplitude) is visible in the left part of Figure 5.2. The change in the noise-characteristics is clear from the shown amplitude.

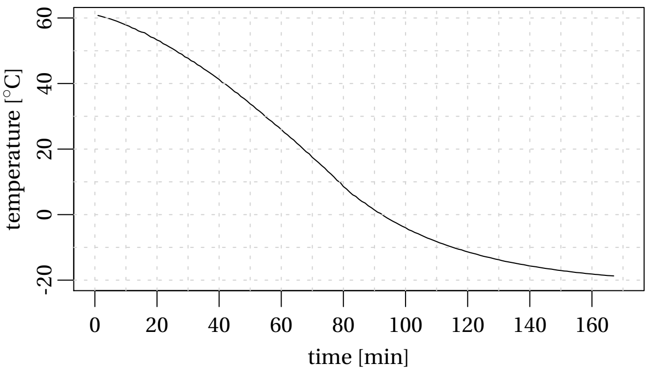

Figure 5.1: The temperature changes smoothly from a hot state (60 °C) to a cold state (-20 °C) in roughly 3 h.

---

[2] automotive grade IMU, data courtesy of Applanix

In order to compensate for the influence $f(X_t)$ of the temperature on the mean error-signals (Equation 5.1), we employ a spline regression by taking as inputs the observed raw data signal Y_t and the measured temperature X_t. Then we apply the fitted spline to the dataset in order to compensate for the temperature change. This brings the mean error-signal back to zero. Depending on the typology of the influence, it is possible to choose a simpler linear or quadratic model to account for the temperature influence. The right part of Figure 5.2 shows the resulting signal for a gyroscope as well as an accelerometer after application of the spline regression. From now on we are working only on such residual signal Z_t as introduced in Equation 5.1 and further expanded in Equation 5.2. The analysis of such signal will be used in the following for determining the noise characteristics as a function of the temperature.

Figure 5.3 shows the analysis WV plot of the residual z-axis accelerometer error signals for two different temperatures. A total of 200'000 samples from the beginning and another 200'000 samples from the end of the dataset are considered. The mean temperature of the first sub-sample is 57 °C whereas the second sub-sample has a mean temperature of around -19 °C. The change of the noise characteristics is clearly visible in the first scales, which are determined with the highest confidence. The WV at larger scales are determined with lower confidence. Nevertheless, they continue to depict the general tendency of the change.

The applied model for the GMWM analysis is a sum of one AR1 plus a WN process. The combination of these two noise-typologies becomes apparent when looking at the Figure 5.4. It

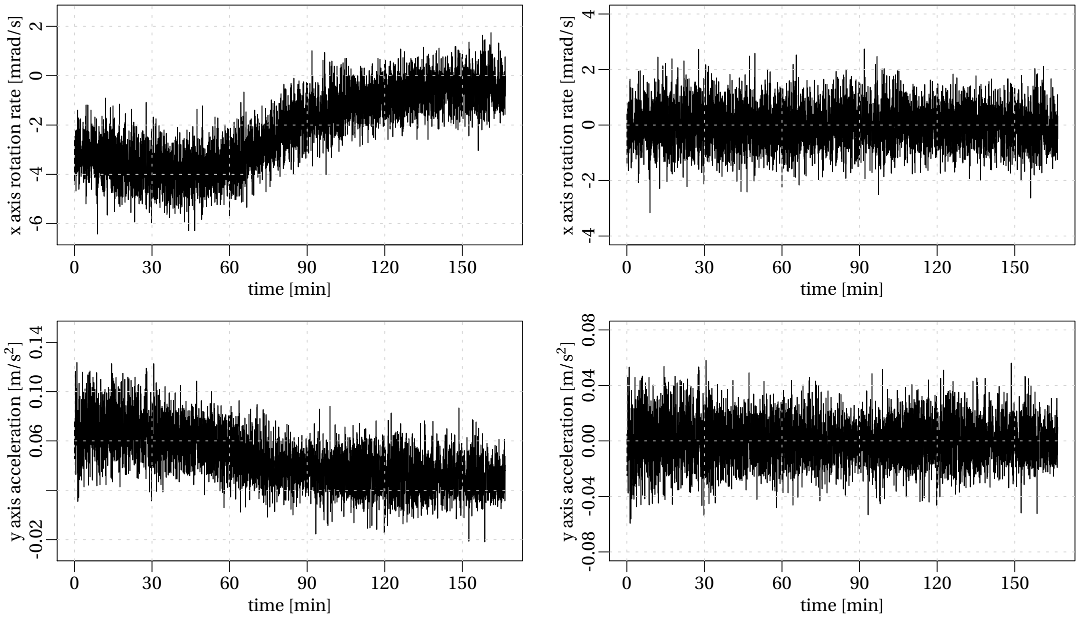

Figure 5.2: Left: raw data of a gyroscope and an accelerometer. Right: temperature-calibrated data where the temperature dependent bias is eliminated through splines regression.

shows the two model parameters which are determined by the GMWM and their combination (final implied model) for a moderate temperature of 20 °C.

The optimization process according to the objective function Equation 5.8 is supplied with derivatives of the defined model, parameters, and the initial values deducted from the border conditions of the data at hot and cold temperatures. The found parameters after the optimization procedure are summarized in Table 5.1.

These estimated noise parameters are plotted in Figure 5.5 against the individual (manual) bin-

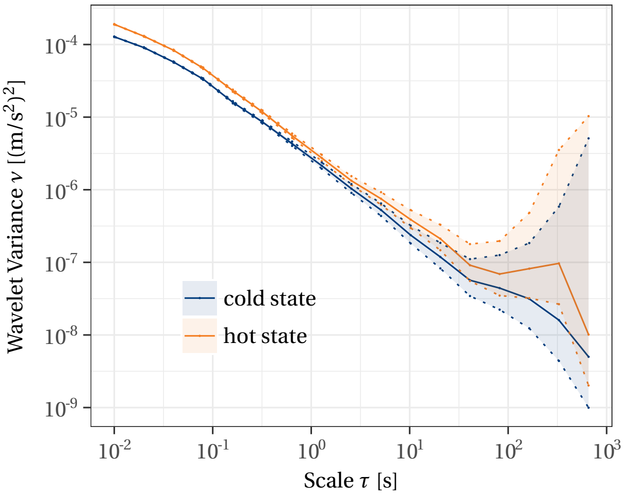

Figure 5.3: The two WV overlaid noise characteristics for a hot state of 57 °C (orange) and the cold state of −19 °C (blue) with their respective confidence intervals on the z-axis accelerometer.

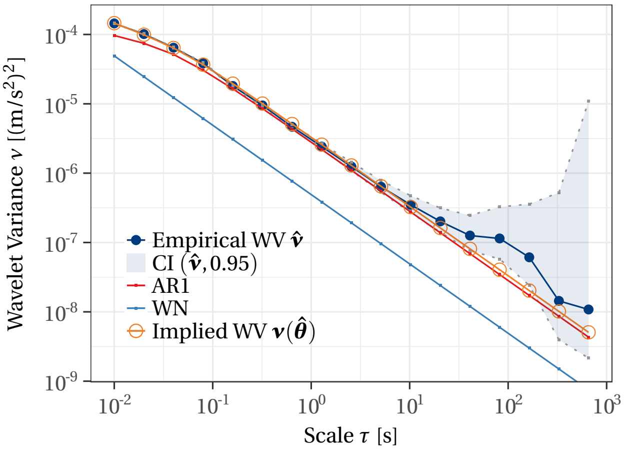

Figure 5.4: Empirical and model implied WV of the z-axis accelerometer at 20 °C mean temperature with the decomposition to AR1 and WN models.

Table 5.1: Stochastic model parameters (WN, AR1) for a variable temperature estimated via the optimization.

WN		AR1			
ς_1	ς_2	φ_1	φ_2	ϵ_1	ϵ_2
-11.68	6.71e-3	0.32	-2.53e-5	-9.21	3.88e-3

wise estimation of the very same model. The separately "per bin" estimated parameters follow the global temperature dependent stochastic model nicely and stay within its confidence interval (2σ). The optimization through the "dynamic GMWM" took a couple of seconds to execute, whereas the bin-wise computation was long and took almost 1 h on the very same computer to terminate.

As can be seen on Figure 5.5, the model parameters vary abruptly on the boundaries of the data (i.e., at very hot temperature) and follow less the general estimated trend. Hence, using these extreme boundary conditions for the initialization of the searched parameters could lead to different results (i.e., local minimum). Moreover, the length of the used bins can be modified/adapted as a function of the available data (e.g., slowly changing temperature over time allows for longer bins, which leads to higher confidence of determined parameters.

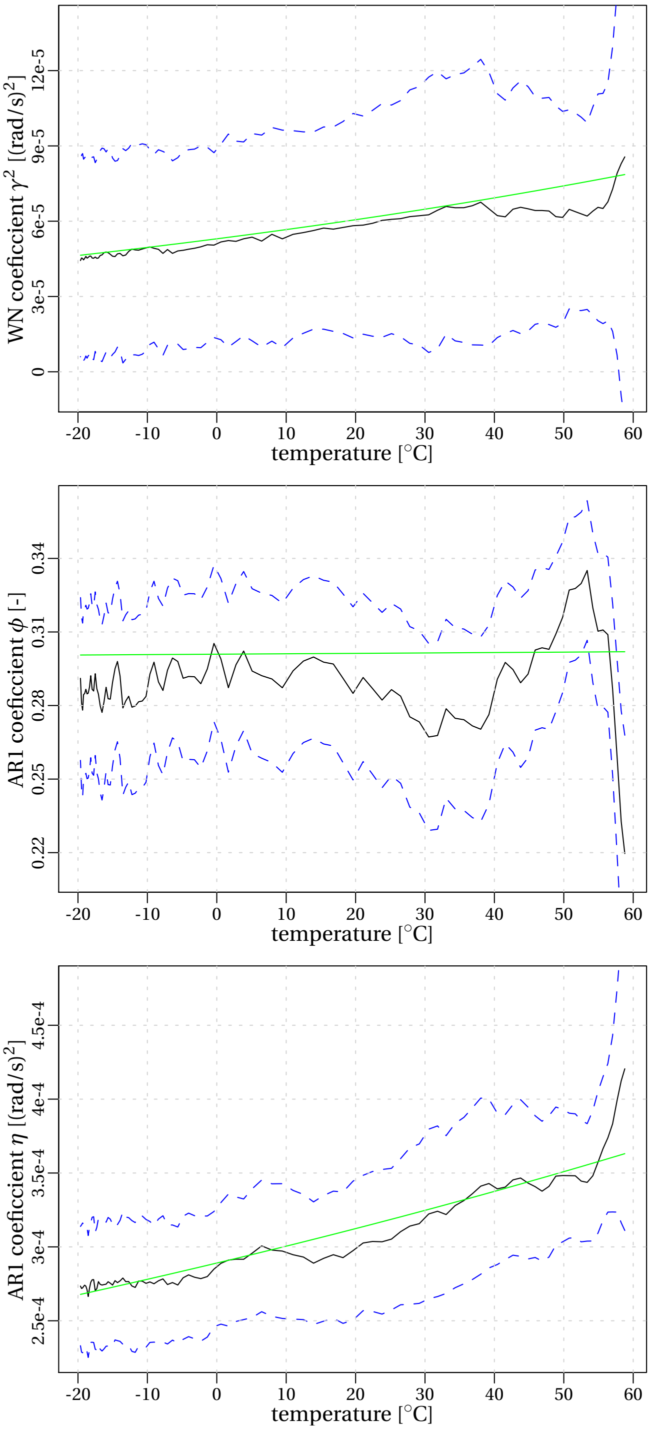

Figure 5.5: Straight line (trend): estimated stochastic parameters though the *dynamic-GMWM* as a function of temperature; solid irregular line: bin-wise manually calculated parameters with confidence interval of 2σ for the process parameters WN and AR1.

5.5 Rotational Dynamics

The sensor used in this second experiment is the Micro-Electro-Mechanical System (MEMS)-IMU with an angular random walk of $0.18\,{}^\circ/\sqrt{\mathrm{h}}$ and an in-run bias instability of $10\,{}^\circ/\mathrm{h}$, which is presented in Appendix C.3. The sensor board was mounted on a high-precision single-axis rotation table from Actidyn (Figure 5.6). This rotation table is capable of orienting the mounted equipment in any given direction from its origin with a precision of $\sim$0.0003°. The rate precision is 0.000 04 % of rate value, which is sufficient to precisely command all rotational speed up to $1000\,{}^\circ/\mathrm{s}$ (see Appendix F). As explained before, a good WV analysis requires a high number of samples ($\gtrsim 10^6$). This table rotation speeds are stable. Thus a sufficient amount of data can be gathered for the WV of each bin. The commanded values of rotation speeds serve as a reference observable c_k for the gyroscope, which sensitive axis is parallel to that of the rotation table.

A dataset was collected containing a total of $K = 13$ bins at rotation rates ranging from $30\,{}^\circ/\mathrm{s}$ up to $390\,{}^\circ/\mathrm{s}$ with an equal spacing of $30\,{}^\circ/\mathrm{s}$ (see Figure 5.7). Each bin k has a length of 40 min with the IMU running at an acquisition frequency of 500 Hz. This amounts to a total of 15.6 millions data samples per one axis of the gyroscope.

A preliminary analysis is performed at the two extreme points $k = 1$ where the rotation

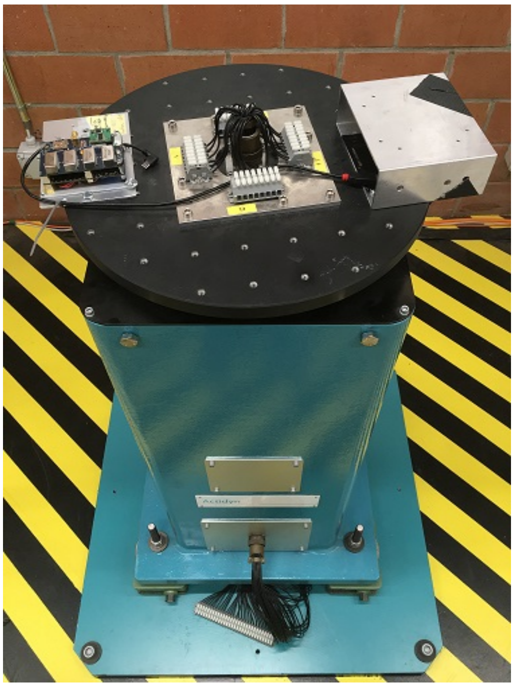

Figure 5.6: MEMS-IMUs board mounted on the left with its power source as counterweight on the right side of the rotation table, which has a mounting plate diameter of 40 cm.

Table 5.2: Values of noise parameters. The units are expressed in the GMWM default representation of variances. The exception is the WN, where the units were converted to be easily comparable to the one from the datasheet.

Process	Parameter	Unit	Datasheet	rotation rate 30 °/s	rotation rate 390 °/s
WN	σ^2_{WN}	$°/\sqrt{\text{h}}$	0.18	0.146	0.439
QN	σ^2_{QN}	$(\text{rad/s})^2$	-	9.756e-06	2.220e-16
AR1#1	ϕ_{AR1}	-	-	0.9998091	0.9999607
	σ^2_{AR1}	$(\text{rad/s})^2$		3.751e-12	2.923e-12
AR1#2	ϕ_{AR1}	-	-	0.9939760	0.9996113
	σ^2_{AR1}	$(\text{rad/s})^2$		1.107e-10	9.573e-12

rate is 30 °/s and at $k = 13$ with a rotation rate of 390 °/s. The WV is calculated from the rotational error sequence and a suitable stochastic model is chosen. The model parameters are estimated by the GMWM estimator. The top plot in Figure 5.8 shows how well the model fits at low rotational speeds 30 °/s composed of WN, QN, and two AR1 processes within the confidence interval of the WV, noting that the uncertainty of the latter grows with larger scales.

The WV signature is significantly different for the rotational speed of 390 °/s (middle plot of Figure 5.8). The GMWM optimization is fed with the same model as for the 30 °/s rotation speed. Nevertheless, the QN is completely absent as the slope of the WV at small scales now resembles that of a WN. Hence, the WN process changed its strength while the value of parameters for two AR1 processes (see Figure 5.8) moved slightly as well.

The bottom plot of Figure 5.8 illustrates both situations in a common perspective. The change of the noise characteristic is visible, especially the absence of the QN on the orange plot (faster rotation), respectively its change to WN. Table 5.2 resumes the found parameters by the GMWM framework for these two rotational speeds. Each model is mentioned together with that specified on the factory datasheet.

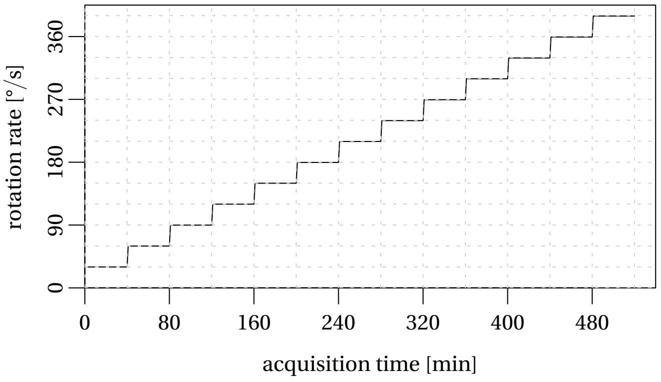

Figure 5.7: Acquired reference rotation rates per bin with its duration.

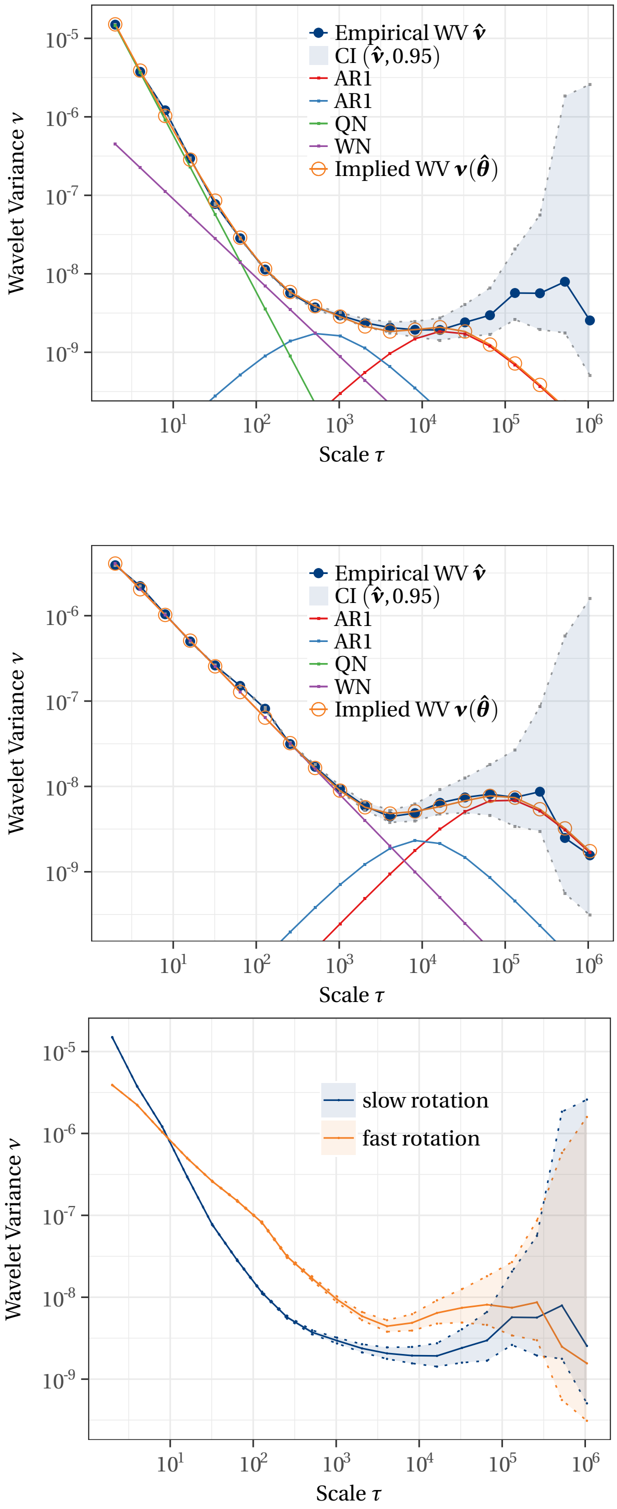

Figure 5.8: Gyroscope stochastic signature and models at minimal and maximal rotations. Top: rotational speed of 30 °/s. Middle: rotational speed of 390 °/s. Bottom: WV of slow rotation overlaid with WV of fast rotation rate.

As can be seen from Table 5.2 and Figure 5.8, the stochastic parameters evolve considerably with the dynamics, fact of which motivates the application of the "dynamic GMWM" estimator from Equation 5.8 using the noise functional dependencies described in Equation 5.3 through - Equation 5.6. This expanded GMWM estimation is then applied to the data using all bins. The individual WV per bin are visualized in the top plot of Figure 5.9. The result of the optimization provides the desired relation that is depicted in the bottom plot of Figure 5.9, where the stochastic noise parameters are predicted as a function of dynamics. The transition from a mix of the QN and WN processes at low rotational speeds to a state that is mostly dominated by WN is depicted in Figure 5.9 as a color-transition from blue (slow rotational speed) to red (fast rotational speed). The stochastic noise parameters found by the extended GMWM framework

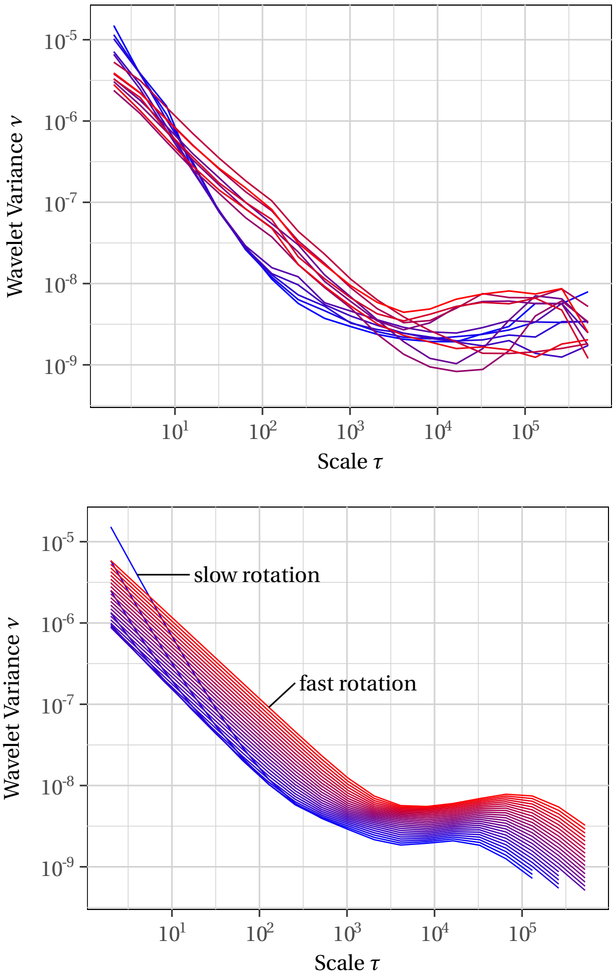

Figure 5.9: Top: Empirical WV per each bin from slow (in blue) up to fast (in red) rotational speeds, which form the input to the extended GMWM framework. Bottom: predicted WV of gyroscope noise with the estimated rotational dependent stochastic model (output from the extended GMWM framework).

Table 5.3: Covariate (dynamics) dependency of stochastic parameters as estimated by the extended GMWM optimization.

Noise Acronym	Parameters	Value
WN	ς_1	-14.0893
	ς_2	0.4014
QN	κ_1	-11.2795
	κ_2	-3.9025
AR1#1	φ_1	4.5624
	φ_2	0.1260
	υ_1	-26.2883
	υ_2	-0.0398
AR1#2	φ_1	2.7867
	φ_2	0.2186
	υ_1	-22.7203
	υ_2	-0.3902

are summarized in Table 5.3. These values can be employed in the functional relations from Equation 5.3 through - Equation 5.6 to update the stochastic properties in the Kalman Filter according to the actual dynamics.

6 Implementation

6.1 Introduction

This chapter describes the implementation of the proposed software and hardware solutions related to stochastic and deterministic calibration of inertial sensors. These include in the first part the software for the deterministic error calibration before a mission and its interaction with a navigation filter in real-time. Prior to that, the hardware implementation of the whole system is presented with all sensors and data flows on a small Unmanned Aerial Vehicle (UAV) platform. In the second part, the stochastic parameter identification and estimation are presented, with its web Graphical User Interface (GUI) in a free online implementation.

6.2 Hardware Implementation

The laboratory posses a multitude of drones for different purposes. Although the developed navigation payload can be carried on several of these drones, it will be presented in relation to the model airplane called `TOPOplane` (see Figure 6.1 [Rehak and Skaloud, 2015]). It has a size of 1630 mm by 1700 mm and its overall weight at full capacity is 2.8 kg. This airframe has a typical endurance of 40 min with a payload of 600 g. The flying speed is around 15 m/s and the stabilization and way-point trajectory following are handled by a pixhawk autopilot [Pixhawk, 2018].

A second airframe was developed in 2017 and a new payload in 2018. The heart of this payload is composed of a rigid box which holds the sensor board with redundant Inertial Measurement Unit (IMU), the camera, and the embedded computer (see Figure 6.2). This box is fixed in the bay of the airplane and is removable. It is made of machined carbon plates in an assembly that reduces the weight while preserving rigidity. The rigidity of this box is of importance for photogrammetric applications, where the measurements of the IMU have to be put in relation with the information from the camera. The relative orientation between these two sensors (IMU and camera) should stay as constant as possible, to correctly relate the attitude provided by the IMU to the photos for the direct or integrated orientation of the latter.

The sensor board with the redundant IMUs consists of two layers. A Field Programmable Gate Array (FPGA) is implemented on the bottom part of the sensor board, which handles the data acquisition, time synchronization, and power distribution [Kluter, 2012]. A specific software runs on this FPGA, which configures the different sensors and serves the data through the USB port upon request to the host computer. The upper board is composed of a multitude of sensors. Up to four IMUs, five magnetometers, and a barometer can be hosted. In fact, the *Navchip* sensor includes one IMU plus one 3-axis magnetometer in the same enclosure. In addition, an external magnetometer is installed next to it. This amounts to a total of five magnetometers. Figure 6.3 gives an overview of the components and their assembly.

This sensor board is also equipped with serial and digital inputs. Its serial connection accepts any information sent either via the RS-232 or the TTL protocol at a typical rate of 9600 baud. It is connected to the Global Navigation Satellite System (GNSS) receiver and records any messages such as Position, Velocity, and Timing (PVT). This information is later used for the fusion with IMU data. The digital input serves for synchronization. In fact, the GNSS receiver outputs a Pulse Per Second (PPS) signal, which is used for precise timekeeping. This pulse consists of a sharply rising and falling signal and is forwarded to the IMU for aligning its sampling. The signal is also received by the sensor board to synchronize all other sensor measurements to the common GNSS time.

The embedded computer (AAEON UP Board on the newest payload of Figure 6.2) is equipped with a 64-bit Intel Atom processor with 4 cores and runs a 64-bit version of Linux [UP board, 2018]. It has sufficient computation capacity for all data handling and processing. Smaller and lighter embedded computers (such as a Raspberry Pi Zero [Raspberry Pi, 2018]) are also

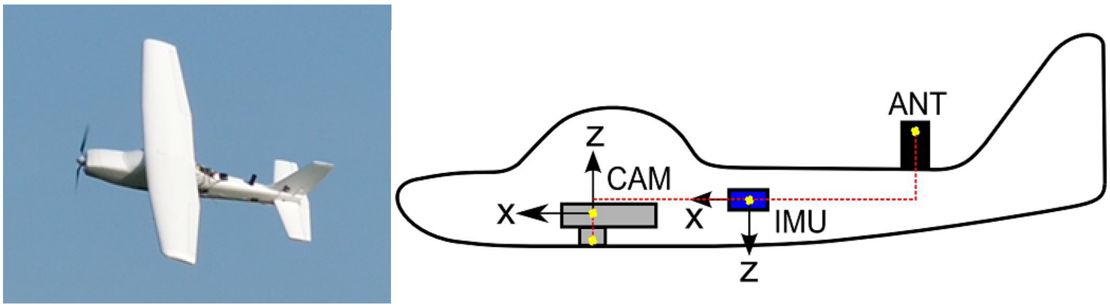

Figure 6.1: Left: model airplane in the air. Right: schematic side-view of drone with depiction of some internal components including the IMU, camera, and GNSS antenna [Rehak and Skaloud, 2015].

used in other setups, where the camera weight is greater. This trade-off comes with lower

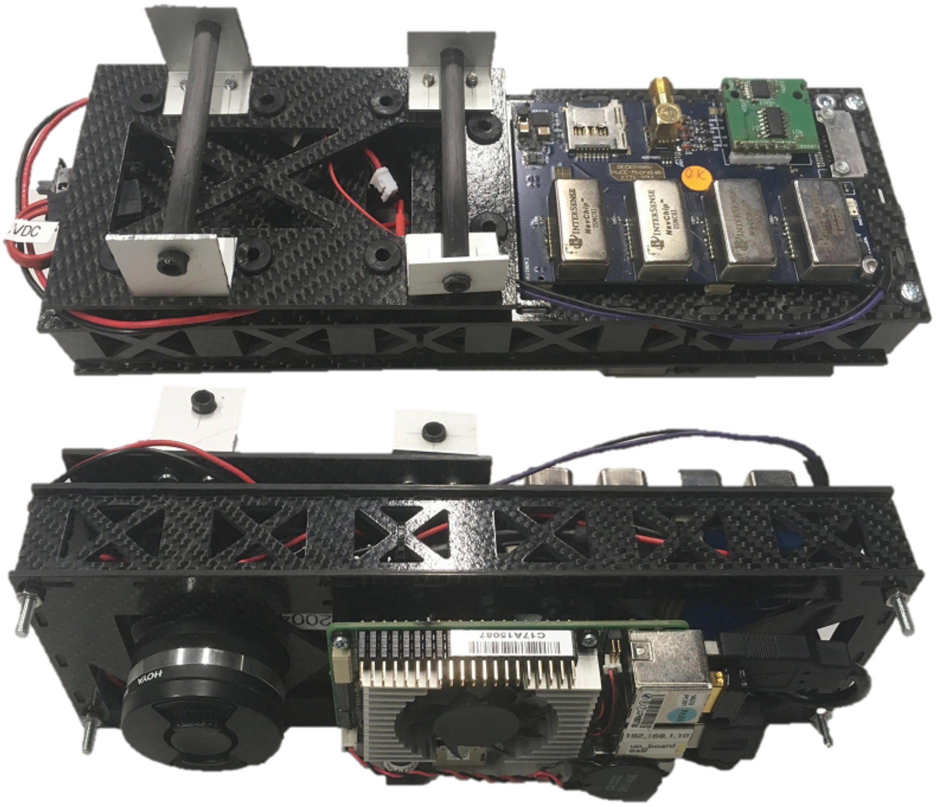

Figure 6.2: Top-view and side-view of the payload with the camera (SODA), sensor board, and embedded computer.

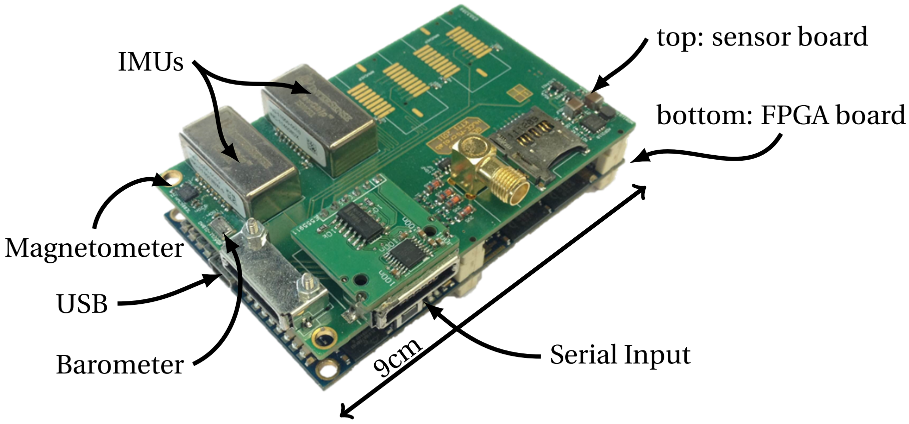
IMUs
top: sensor board
bottom: FPGA board
Magnetometer
USB
Barometer
9cm
Serial Input

Figure 6.3: Sensor board hosting two Navchip IMUs, a barometer, and an external magnetometer. The USB connector brings power and the connectivity to a computer for data transfer.

computational capacity in data serving, real-time in-field calibration (see Section 6.3), and integrated inertial navigation, including its initialization (see Section 6.4) and possibly also the piloting of the camera.

Although the software on the embedded computer does all such calculations, these can be controlled by a remote PC. Different solutions were implemented to ease the interface between the computer on the ground and the embedded computer within the drone. Typically, results and messages from the computation (i.e., completion of deterministic calibration and its quality) are displayed on the ground computer so the user can take appropriate action. The working principles are explained in details in the next sections.

The integration between the main hardware components and the information flow is depicted schematically in Figure 6.4 and explained as:

- **GNSS-receiver:** mounted in the airplane body and provides PVT data, that is sent to the autopilot as well as to the FPGA board, where it is stored and forwarded to the embedded PC. In addition, certain events, such as 'taking a picture', are time-tagged directly by the receiver and are transmitted as EV-messages.
- **FPGA board:** is equipped with different sensors. Each IMU provides measurements of rotation rates (ω) and accelerations (f) at a maximum of 1000 Hz[1]. The magnetometer provides the information on the magnetic fields (m) at a frequency of 250 Hz. The barometer measurements include the pressure (p) as well as the temperature (T) at 10 Hz. The board takes care of gathering data from all sensors (including the messages from the GNSS receiver) and making them available for further use through the USB connector.

---

[1] with more than 2 IMUs on board, the maximum sampling is limited to 500 Hz

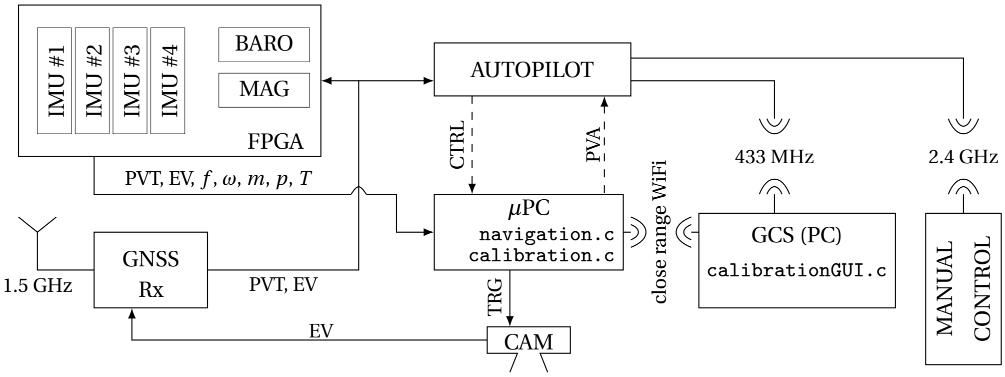

Figure 6.4: Schematics of the hardware and software implementation for the setup used in the drone application.

- **Manual Control:** allows to switch between different flight modes, including manual or assisted piloting via the remote control during take-off, landing, or emergency situations.
- **Autopilot:** receives PVT data from the GNSS receiver, and possibly also a complete navigation solution from the embedded μPC. It can also forward information or commands issued from the Ground Control Station (GCS) to the μPC, or initiate camera exposures.
- **GCS PC:** receives telemetry data, plans and monitors the mission including the possibility of switching between flight modes. Other instances provide a user interface to display information and results from the calibration. If the drone is close, the latter communication goes through a local WiFi connection. Otherwise, a 433 MHz radio connection is used.
- **μPC:** downloads the data from the FPGA board. This raw binary data is then extracted and put in a format, which is expected by the navigation computer. A part of it is also sent to the GCS PC, where it is displayed to the user in a GUI in the pre-calibration phase of the mission or later within a mission for real-time navigation. This embedded PC pilots also the presented camera.
- **Camera:** physically connected to μPC that commands its operation. It sends to the GNSS receiver a pulse at each exposure to time-tag the acquired photos.

The usage of the different programs running on the μPC and the GCS PC is explained in detail in Figure 6.5 concerning the different phases of the mission. In the first step (I), the sensors such as accelerometer, gyroscope, and magnetometer are calibrated in-field. The newly estimated parameters are then directly applied to the sensor readings. With the corrected sensor measurements, the initial attitude of the platform is calculated in the second step (II), to initiate (together with the GNSS provided position and velocity) the strapdown navigation.

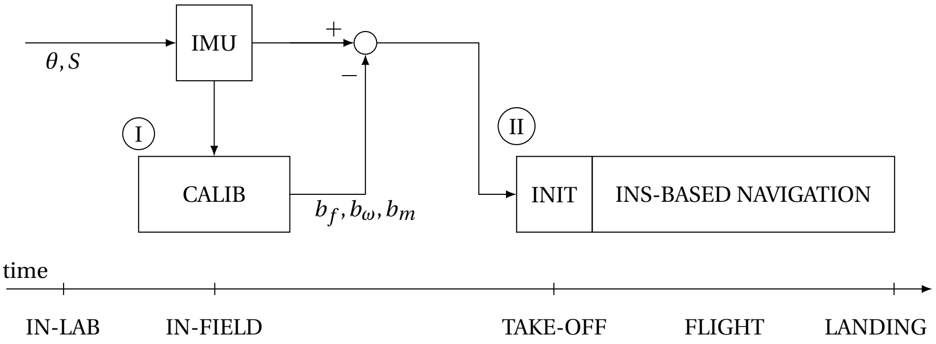

Figure 6.5: Two different phases of a typical mission. The in-lab calibration parameters are used to re-calibrate the setup just before the in-field bias calibration so that the computation of the initial attitude with calibrated data assures a certain quality.

6.3 Deterministic Error Calibration In-Field

6.3.1 Accelerometer and Gyroscope

Figure 6.6 shows a typical in-field calibration setup with the drone. The embedded μPC is connected to the GCS PC via a WiFi-Router and transmits information and status messages. The plane is placed securely and firmly on a support at different orientations for the calibration procedure.

The main window of the calibration GUI executed on the GCS PC is shown in Figure 6.7. It informs the user about the states of the sensors:

- GPS-time and other information provided by the GNSS (e.g., leap seconds, number of satellites),
- calibration status for the accelerometers, gyroscopes, and magnetometers,
- sensor frequency and total amount of data downloaded,
- information provided by the thermometer and barometer,
- tab with related information on the sensor readings, and
- buttons to launch processes such as ’Calibrate’ and ’Initial Position’.

Theoretically, a full calibration of the 9 error parameters of the accelerometers is possible

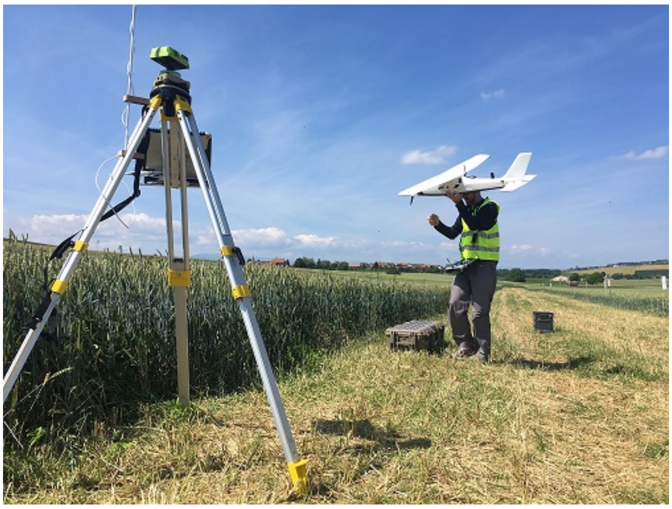

Figure 6.6: Typical test site for a UAV mission. The internal μPC of the drone is connected to the GCS via the WiFi-Link and transmits information about the calibration process during handling.

in the field, as the reference signal (Earth's gravity) is available. Nevertheless, the procedure with the many (> 20) positions distributed over all possible attitudes is not practical in the field, when the sensor board is installed inside the drone bay. An unstable surface, possible wind, and constraints on the different attitudes due to wings and antennas do not allow for a long static measurement, which is required to correctly estimate the non-orthogonality θ and the scale-factor error S. On the other hand, these parameters can be pre-calibrated in the laboratory, and only random biases need to be determined in the field. For these practical reasons, a reduced multi-position-calibration procedure is utilized, which requires a minimal of 6 positions and estimates the bias of the accelerometers in real-time. As seen in the previous chapters, their change is significant and needs to be calibrated every time the sensor is turned on/off. Since the non-orthogonality θ and scale-factor errors S are known for each axis and sensor from the lab-calibration, they are already applied to the raw data prior to all other calibration.

The situation for the gyroscopes is different, as no strong reference signal is available in the field (i.e., the signal of the Earth's rotation is buried within the noise of the employed sensors). Hence, the only field calibration that will be applied to the gyroscopes is subtracting the mean measurements taken over a short times span of typical 10 s while the plane is still on the ground. As it is the case for the accelerometers, this procedure is fused with the in-lab calibrated θ and S.

Figure 6.8 depicts a typical synthesis of the in-field calibration displayed on the GCS PC.

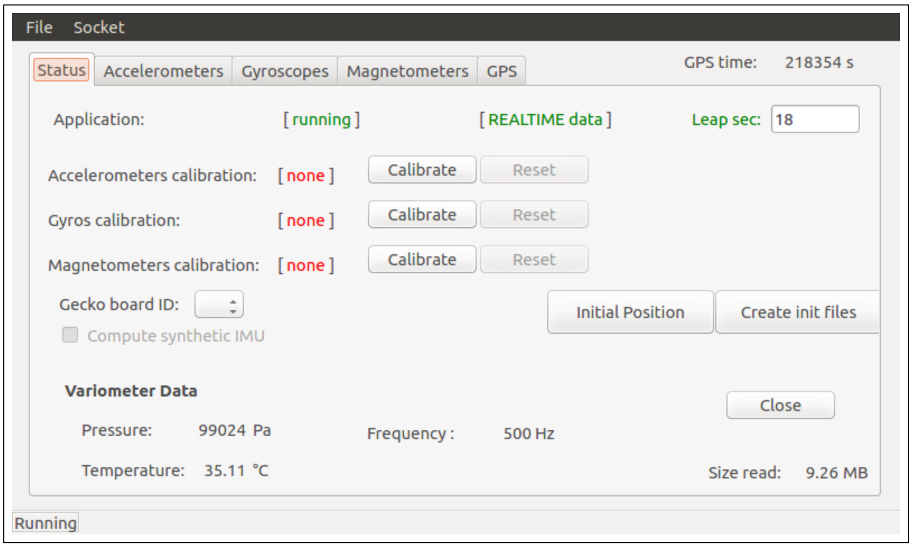

GPS time: 218354 s

Application: [running] [REALTIME data] Leap sec: 18

Accelerometers calibration: [none]

Gyros calibration: [none]

Magnetometers calibration: [none]

Gecko board ID:

Variometer Data

Pressure: 99024 Pa

Frequency : 500 Hz

Temperature: 35.11 °C

Size read: 9.26 MB

Running

Figure 6.7: Main GUI window on the GCS for pre-flight calibration. It displays relevant information to the user as received from the μPC. Bidirectional interaction takes place, in order to launch the calibration process and inform the user about the estimated parameters.

During the calibration, the static data acquired at different attitudes is shown as a progress bar. The change of attitude is recognized automatically. Only attitude changes with a minimum angular distance of 20° between them are accepted by the algorithm. The GUI informs the user about the acceptability of chosen attitudes. Once enough data is acquired, the parameter estimation is launched. Depending on the μPC used, the estimation process for all the IMUs

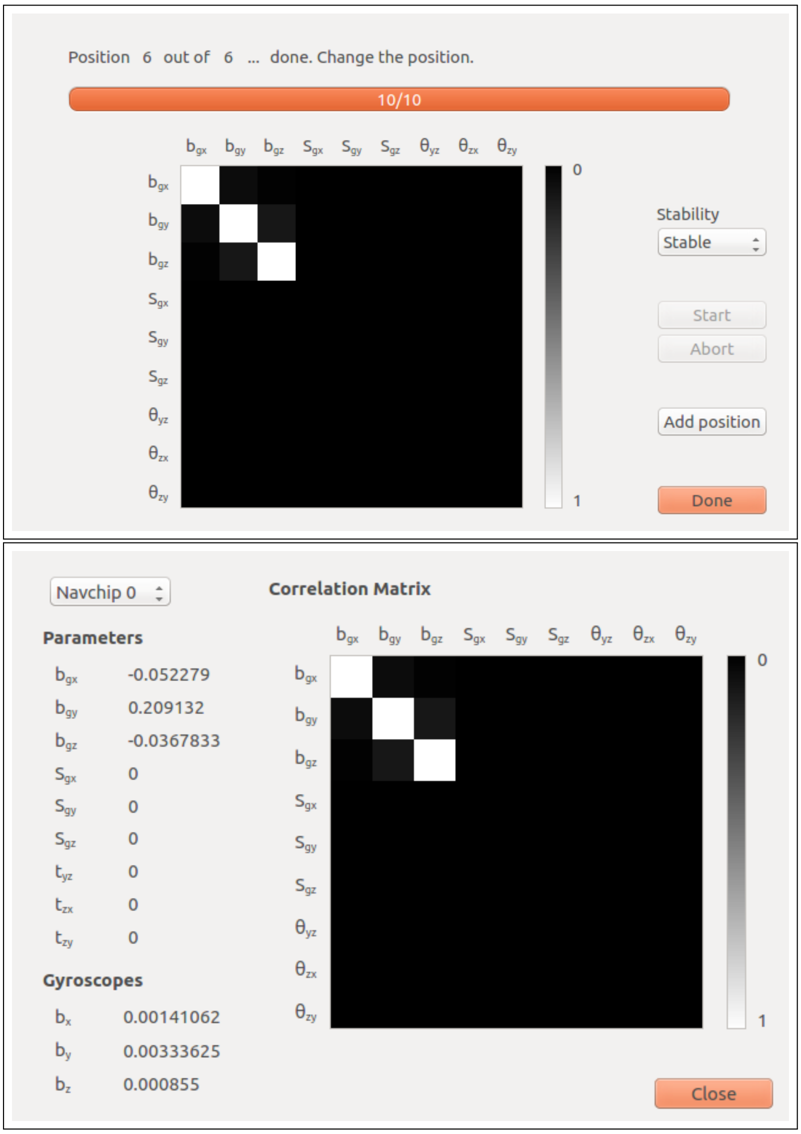
Position 6 out of 6 ... done. Change the position.

10/10

Stability: Stable

Navchip 0

Parameters

b_{gx}	-0.052279
b_{gy}	0.209132
b_{gz}	-0.0367833
S_{gx}	0
S_{gy}	0
S_{gz}	0
t_{yz}	0
t_{zx}	0
t_{zy}	0

Gyroscopes

b_x	0.00141062
b_y	0.00333625
b_z	0.000855

Figure 6.8: GUI on the GCS PC showing the results of the real-time calibration. Top: real-time information to the user with information about the acquired attitudes. Bottom: after the calibration, the sensor can be selected, and calibration parameters are presented. The correlation matrix of the calibration shows the calibration quality in a simplified way. Other parameters (θ and S) are displayed with zeros, as in this case the reduced multi-position-calibration scheme only estimates the current bias, whereas the non-orthogonality and scale-factor were already pre-calibrated in the lab.

is executed in a couple of seconds. The estimated parameters are displayed alongside their matrix of correlation. This serves as a tool to verify the quality of the in-field calibration. If necessary, the procedure can be re-initialized for all or some of the sensors. The parameters not subjected to the estimation process are represented as zeros and their corresponding places in the correlation matrix is blackened.

As shown in Figure 6.9, the accelerometer and gyroscope tabs also show the current sensor readings. In order to reduce the load on the data transfer and the GUI update rate, 1 s-packages are created of all the sensors (i.e., mean of data over 1 s) when transmitted to the GCS. The actual application of the calibration result can be verified, by plotting the norm of the signal and turning the sensor in different attitudes. Figure 6.9 shows an example of how much the norm of the sensor reading changes for the accelerometer after calibration. A similar procedure can be applied to the magnetometers and gyroscopes.

6.3.2 Magnetometers

The magnetometers need to be calibrated for each take-off, as environmental conditions may change locally. The user has to watch the defined criteria (percentage on sphere coverage and norm/standard-deviation of sphere radius), which were introduced in Chapter 4 and has to keep on rotating the sensor until completion. A recommended way to achieve proper calibration is following this procedure:

- point the x-axis upwards,

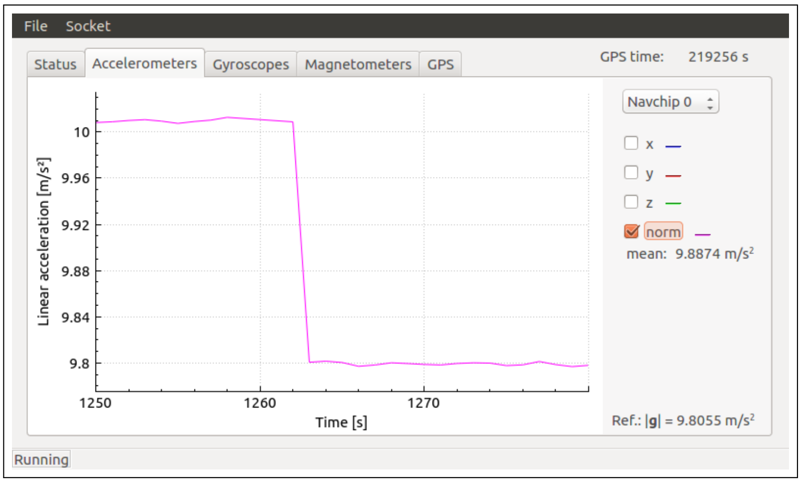

GPS time: 219256 s

Navchip 0

☐ x

☐ y

☐ z

☑ norm

mean: 9.8874 m/s²

Ref.: |**g**| = 9.8055 m/s²

Running

Figure 6.9: GCS GUI in-field calibration verification: accelerometer tab providing real-time information of the sensor data. Different IMUs can be selected and individual sensor axes can be displayed alongside the mean value to visualize the calibration quality in a simplified way.

- rotate around the x-axis two times,
- point the y-axis upwards,
- rotate around the y-axis two times,
- point the z-axis upwards,
- rotate around the z-axis two times,
- point the z-axis downwards, and
- do precession-like movements around this axis to complete the calibration.

The calibration for each magnetometer is then directly applied to the raw sensor readings. As the calibration depends on the environment, the best location is to perform the calibration next to the launch position with all the in-board electronics turned on, by avoiding the possible influence of the car, other metal objects, and the PC.

6.4 Initial Attitude Determination

The initial attitude is determined after a full calibration of the sensors (accelerometers, gyroscopes, and magnetometers) by the procedure described in Section 6.3 once the GNSS position fix is available. The calculations for the initial attitude of the drone for the subsequent navigation process is launched via the GUI. Ideally, the drone is placed on the ground next to the launch position. When pressed, the button `Initial Position` executes automatically two tasks. The first task stores the current position of the drone, which is provided by the GNSS-receiver, while its velocity is set to zero. The second task that is launched in parallel is the initial attitude determination via the accelerometers and the magnetometers through the QUEST algorithm described in Chapter 4.

If the desired position and attitude of the drone before launch are adequate, then the button `Create init files` in the GUI can be pushed. This process will initiate all the necessary parameters for the integrated navigation based on the results of the calibration and the attitude initialization.

6.5 Stochastic Noise Parameter Estimation with an Online GUI

6.5.1 Introduction

The stochastic noise calibration can be accessed on the following link: https://github.com/SMAC-Group/gui4gmwm. It is called *gui4gmwm* and uses the principles and extension to the theory shown in Chapter 3. The server implementation of the freely available *gmwm*-package in the programming language *R* [R Core Team, 2016; Balamuta et al., 2016a] with an online GUI makes it easy to use. It surpasses the hurdle for a user of installing, understanding, and modifying the specific programming language. It provides practitioners a readily-available tool to perform sensor calibration in the sense of estimating the stochastic parameters of an error signal. This can be performed without the knowledge of different functions and their influence on the result.

This motivated the development of this web implementation, where the user can access a limited yet important amount of the *gmwm*-R-package functions in a simplified and a comprehensive way via an online tool. This latter is programmed through `shiny`, a web application framework for `R` [Chang et al., 2017]. The parameters of stochastic time-series can be estimated either from provided test-datasets, or custom data can be uploaded and analyzed. The best model is then automatically suggested via the Wavelet Variance Information Criterion (WVIC), described in Chapter 3.

This section presents in the first part an overview of the GUI. In a second part, a dataset is analyzed via the Wavelet Variance (WV), and the noise model is identified within an iterative process. We describe more details about the usage in [Clausen et al., 2018b] and [Clausen et al., 2018a].

6.5.2 Installation

The GUI is not only available on a particular server, but can also be installed offline on the personal computer. The following lines of code allow its installation on a system running a recent version of R through Rstudio while including the installation of all necessary packages from GitHub and its dependencies:

```
# Install dependencies
devtools::install_github("SMAC–Group/gmwm")
devtools::install_github("SMAC–Group/imudata")
install.packages(c("scales", "reshape", "shiny", "shinydashboard", "leaflet"))
# Install the GUI package from GitHub
devtools::install_github("SMAC–Group/gui4gmwm")
```

After the installation, the program can be run by loading the gui4gmwm-package and launching the application through the terminal in R:

```
library(gui4gmwm)
runApp("gui4gmwm")
```

The functionality of the online interface equals to the offline version. However, the offline version can be adapted and changed by the user. The implementation is done through the Shiny-application in Rstudio [RStudio Inc., 2017].

6.5.3 Functionality Overview

After the startup, the main application window is presented as in Figure 6.10. This window is divided into four parts. The first part is located in the upper half and displays graphical and numerical results of the calculations (dashed box in Figure 6.10). Graphical results (in the tab called `Selected Sensor`) represent the analysis of the WV on a log-log plot, whereas the numerical results (shown in the tab called `Summary`) represent the estimated parameters of the defined model for the time-series. The tab called `Help` provides more information and a link to a webpage, where a detailed description about this GUI can be found.

The second part is situated on the left-hand side of the lower half of the window (dotted box in Figure 6.10). This part is used for the selection of the dataset containing the error measurements. Different datasets are included by default in the package and serve as an example to learn about the features of the platform. This is emphasized by the default checkbox named `from library`. A predefined set of IMUs and their different sensor axes (e.g., accelerometer, gyroscope) can be chosen. The data included in the software are error measurements from different kinds of sensors ranging from low-cost Micro-Electro-Mechanical System (MEMS)-IMUs to navigational-grade high-end IMUs. The data consists of static measurements of the two types of sensors (gyroscopes and accelerometers), where each consist of three axes. The lengths of the error measurements vary between datasets. In general, these should be taken over a period of at least 30 min at relatively high frequency. Also, the longer the dataset, the more reliable the estimation is achieved (i.e., confidence is improved), but there is no imposed minimal length of the dataset. The mean value of the dataset is irrelevant for the calculations as it is removed automatically.

A custom dataset can be uploaded by choosing the checkbox `custom`. A drop-down menu unfolds like shown in Figure 6.11 and a dataset can be uploaded. It must have a column-wise arranged text format with comma-separated values. The data is directly read and interpreted with a default sampling frequency of 1 Hz as indicated in the GUI. The data provided is neither interpreted nor converted; it is used as provided. The following example shows a snippet from a dataset containing six columns of data:

```
0.53766714,0.51975577,1.46454965,1.46454965,2.52197255,2.52197255
1.83388501,2.01266500,2.92617312,2.92836720,6.77272314,6.77491722
-2.25884686,0.24339694,3.60153901,3.60811577,1.58608908,1.59266584
0.86217332,1.99341731,3.29950158,3.31147061,6.15509221,6.16706124
0.31876524,2.84457976,5.22828018,5.24518630,8.39162517,8.40853129
```

The maximum file size for the custom dataset on the online version is 100 MB, whereas there is no limitation for the offline version. This is due to the long processing time on the currently available server. If needed, the sampling frequency can be set, the units can be defined, and the column number to be interpreted can be selected through a slider according to the dataset and the number of available columns. Attention needs to be paid to a sufficient number of decimal values. The plot of the empirical WV $\hat{\boldsymbol{\nu}}$ of the selected data is calculated when the button `Plot WV` is clicked. The result is shown on the log-log plot as a blue line with its 95% confidence interval in a light blue color.

The third part is situated in the center of the lower half of the window (dash-dotted box in Figure 6.10). In this section, the user can choose a subset of the available models. These

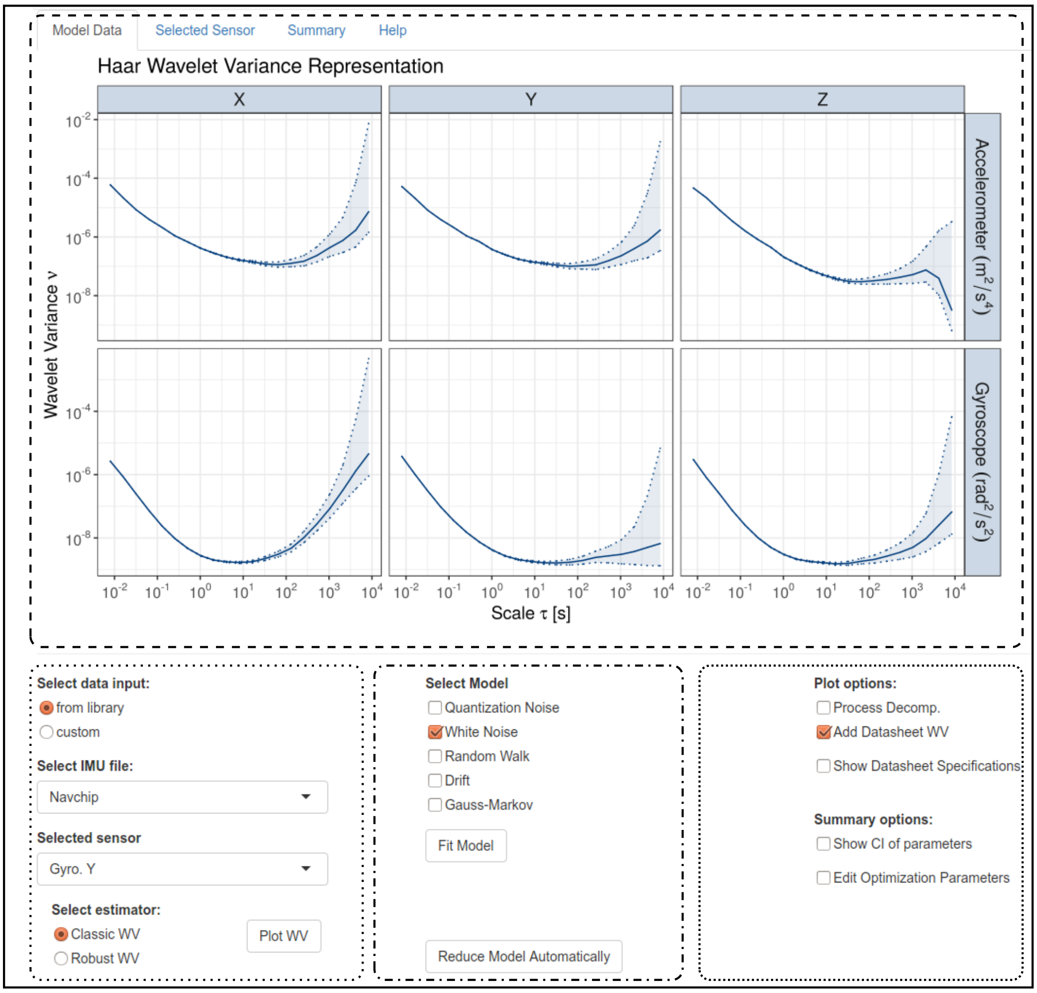
Model Data
Selected Sensor
Summary
Help
Haar Wavelet Variance Representation
X
Y
Z
Accelerometer (m²/s⁴)
Gyroscope (rad²/s²)
Wavelet Variance ν
Scale τ [s]
10^-2
10^-4
10^-6
10^-8
10^-2 10^-1 10^0 10^1 10^2 10^3 10^4
Plot WV
Fit Model
Reduce Model Automatically

Select data input:
● from library
○ custom

Select IMU file: Navchip

Selected sensor: Gyro. Y

Select estimator:
● Classic WV
○ Robust WV

Select Model
☐ Quantization Noise
☑ White Noise
☐ Random Walk
☐ Drift
☐ Gauss-Markov

Plot options:
☐ Process Decomp.
☑ Add Datasheet WV
☐ Show Datasheet Specifications

Summary options:
☐ Show CI of parameters
☐ Edit Optimization Parameters

Figure 6.10: Overall view of the GUI with all the information as seen online. The upper part displays graphical and numerical results. The lower parts allow for data-uploading and selection, noise-modeling, and setting of options related to the computation and parameter estimation.

include Quantization Noise (QN), White Noise (WN), Random Walk (RW), Drift (DR), and multiple Gauss-Markov (GM) processes through a slider, selection of which ranges from one to five models. The button `Fit Model` launches the estimation of the parameters defined by the selected model. Clicking the button `Reduce Model Automatically` will perform the same task, but it will check each possible model permutation and combination. If n represents the number of selected models, then the total number of possible noise model combinations that is checked is $2^n - 1$. According to the number of models selected, this procedure can take a long time to execute. The best model is evaluated and selected via the WVIC. Its fit is then presented visually, and the values of its parameters are shown in the `Summary` tab.

The fourth part is situated on the right side of the lower half of the window (dotted box in Figure 6.10) and includes several options. The first set concern the plotting of the results:

- `Process Decomp.`: The result of the parameter estimation is the implied WV, which will be displayed in orange color. If the user wants to observe the individual contributions of the noise parameters to the overall model, then this checkbox can be activated. The different model's contributions are shown with different colors.
- `Add Datasheet WV`: This option overlays the plot with the WV according to the manufacturer's datasheet of the selected sensor from the library onto the plot with a red color. If a custom sensor is used, the parameters of the QN, WN, RW, DR, and one GM can be specified. In addition, as most of the datasheets lack the information on the specific parameters of a GM process, the Bias Instability (BI) can be set with its cut-off frequency.

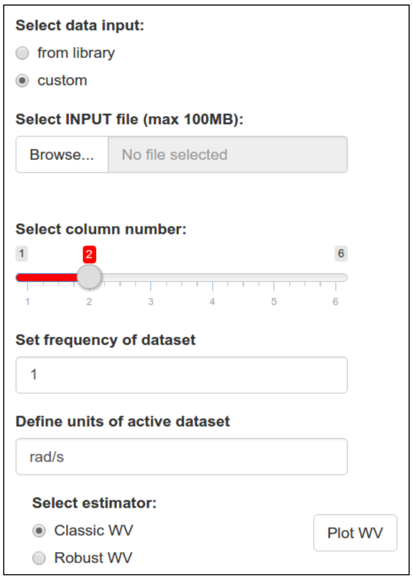

Select data input:

○ from library

● custom

Select INPUT file (max 100MB):

Browse... No file selected

Select column number: 2

Set frequency of dataset

1

Define units of active dataset

rad/s

Select estimator:

● Classic WV

○ Robust WV

Figure 6.11: Drop-down menu for the custom dataset. The column can be chosen, the frequency can be set, and the units can be defined for the resulting plot.

The second set of options concern the computation and the results shown in the `Summary` tab:

- `Show CI parameters`: By default, this option is turned off, as the estimation of the confidence intervals takes more time to execute. It calculates the confidence intervals of the estimated parameters which are displayed in the summary tab. This is not to be confused with the confidence intervals of the empirical WV, which is always plotted.

- `Edit Optimization Parameters`: Here, some options for the optimization procedure can be set to adapt the optimization process, such as the seed number for the randomness and repeatability of the results.

- `Information Window`: Whenever the server or a local computer is processing data, some information is shown in this window, and the user is informed which calculations are executed. The information includes messages such as `Generating summary with Confidence Intervals...` or `Calculating empirical WV...`.

6.5.4 Empirical WV and Datasheet Value

Once the data source is selected (library or custom), the datasheet values are overlaid by activating the checkbox `Add Datasheet WV` in the fourth part of the GUI. A click on the button `Plot WV` launches the calculations of the empirical WV $\hat{\boldsymbol{\nu}}$ and if necessary, also the theoretical WV based on the datasheet parameters. An example is shown in Figure 6.12 and is placed in the upper half of the actual GUI. Information about the dataset is directly integrated onto the figure title, such as type and name of the sensor, duration, and sampling frequency.

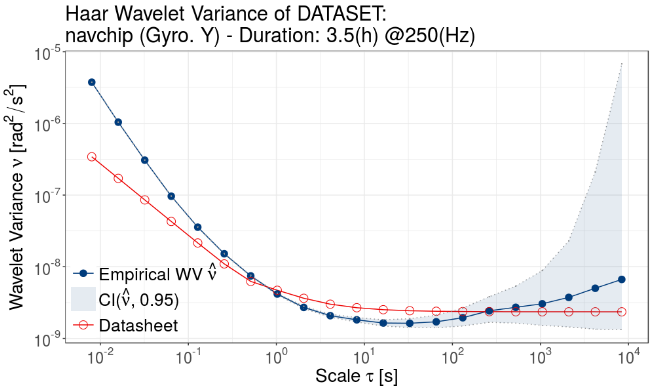

Figure 6.12: Empirical WV representation (blue line/full-circles) for Navchip gyroscope y-axis with its CI. Datasheet specified theoretical WV displayed by the red line/empty-circles.

6.5.5 Iterative Model Identification

The log-log plot of the WV is useful to understand what kind of models underlie the provided error signal. An example of how this plot is useful in this sense is given in Figure 3.5, where the shape of the WV curve over several scales may indicate the presence or absence of certain stochastic models. If we compare the latter plot with the one given in Figure 6.12 we arrive quickly to a suggestion that the signal is likely composed at least of a QN, WN and several GM process models.

In order to find out which combination of the models appears to fit the best, we select the desired models by clicking the checkboxes in the middle part of the GUI and then press the `Fit Model` button to start the parameter estimation. The estimated composite model comprising QN + WN noise (error) is shown in the top part of Figure 6.13 as orange line of its implied WV.

Given the fact that the chosen model (orange line) does not entirely lie within the confidence intervals of the empirical WV (blue line), we decide to add an additional GM process, to improve the fit on the middle and larger scales between the empirical and the theoretical WV. The result is plotted in the center of Figure 6.13, where we see that the model appears to fit better the empirical WV.

Although adding a GM process model improves the fit visually and decreases the objective function value around the middle scales, there still persists a small difference at some bigger scales. Thus, we can add more GM processes to the model and continue the iterative model selection. The final solution is presented in the bottom of Figure 6.13, which shows an overall (almost) perfect match between the empirical and the model-implied WV. However, such good agreement may be considered excessive given the size of the confidence intervals at the last few larger scales. In any case, it is appropriate that the final chosen model lies within the confidence interval of the empirical WV (blue color). In this case, we can stop the iterative model identification (which can also result in a set of different models) and go to the next step to extract the parameters of these models.

6.5.6 Estimated Parameters

Once the model is defined, and the parameters are estimated, we can retrieve their values with the level of confidence by clicking in the upper part on the tab called `Summary`. The parameters will appear for each underlying model together with the value of the objective function, which gives an overall indication of how well the fitted model describes the empirical WV (see Figure 6.14). The smaller the objective function value, the better the fit to the observed signal. In addition, the confidence interval with upper and lower bounds for each parameter value is provided.

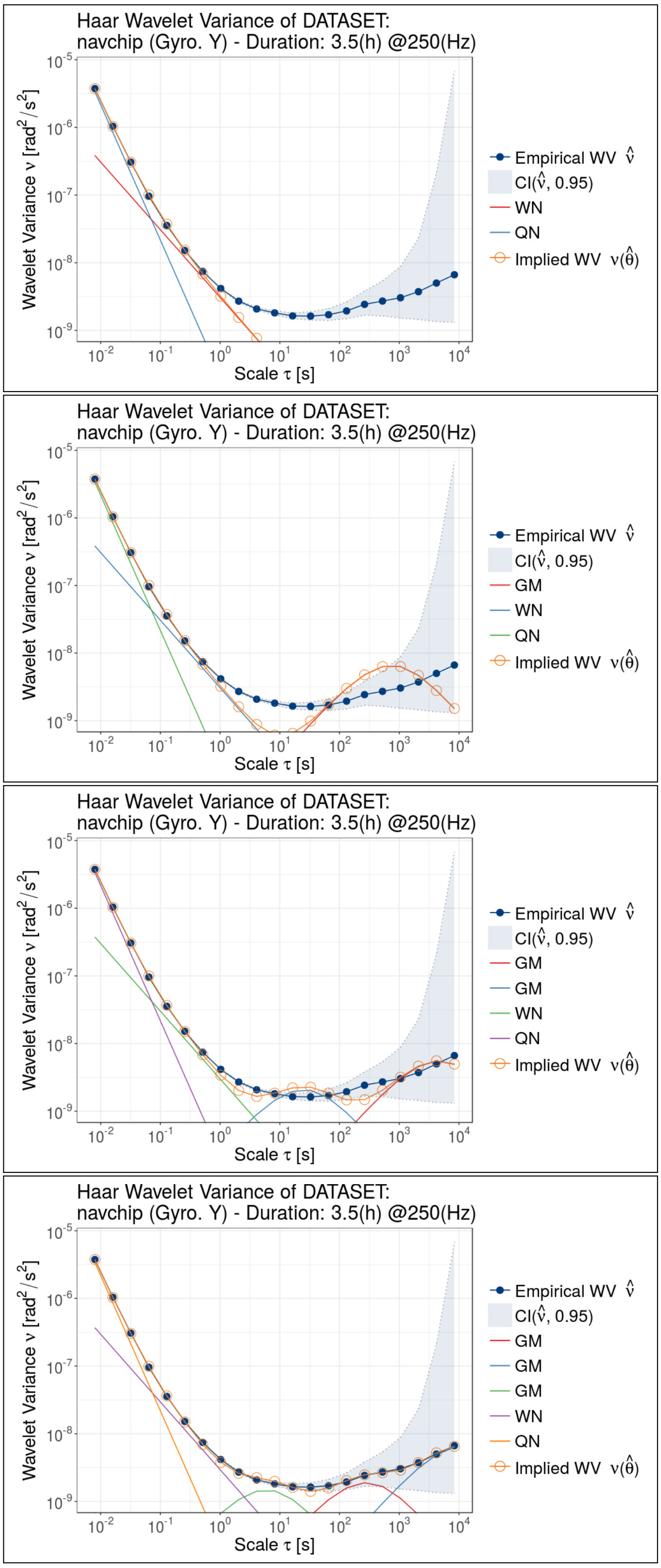

Figure 6.13: Evolution of iterative model identification. Noise models are added successively.

Table 6.1 presents an example of the estimated parameter values for the gyroscopes from Navchip and MTi-G IMU. It can be seen how parameter values change depending on the underlying models in the estimation. In each case, the Generalized Method of Wavelet Moments (GMWM) matched the empirical and the theoretical WV (implied by the fitted model) as best as possible. It can be seen that the estimated amplitude of the WN corresponds well to the values in the datasheet (first line in Table 6.1 for each sensor) of the Navchip; while it differs by one order of magnitude for the MTi-G. There is also a significant difference in the typology of noises, i.e., the MTi-G does, for instance, not contain a QN. Of course, the parameters provided by the datasheet are general across a product line of many sensors; however, a detailed analysis of each individual sensor axis refines the modeling. The parameters may differ between the IMUs of the same type and even with the sensor axis of the same IMU.

6.5.7 Model Selection

Once a set of models has been identified as possible candidates to describe the stochastic error signal, the WVIC criterion can be used to select which of these models appears to better predict the WV of future replicates of this error signal while preventing overfitting. Although the platform allows computing this criterion for each individual model, it is its comparison to other models that helps to understand a reasonably low WVIC value. To do so, the GUI provides the function `Reduce Model Automatically`, in which it is possible to define an overall *most complex* model which includes all other models. This function evaluates all possible combinations of the stochastic models automatically and ranks their fit in terms of the WVIC directly in the GUI with its parameters in the summary tab. With this additional information coming from the automated model selection process, it is, therefore, possible to make a final decision on which model to use within the navigation filter, together with the knowledge of its parameters.

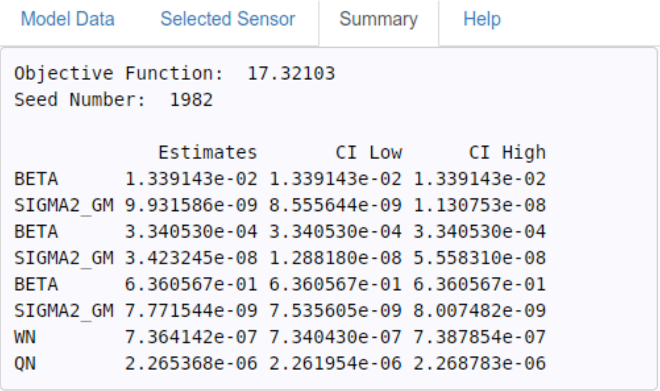

```
Objective Function:  17.32103
Seed Number:  1982

             Estimates       CI Low      CI High
BETA      1.339143e-02 1.339143e-02 1.339143e-02
SIGMA2_GM 9.931586e-09 8.555644e-09 1.130753e-08
BETA      3.340530e-04 3.340530e-04 3.340530e-04
SIGMA2_GM 3.423245e-08 1.288180e-08 5.558310e-08
BETA      6.360567e-01 6.360567e-01 6.360567e-01
SIGMA2_GM 7.771544e-09 7.535605e-09 8.007482e-09
WN        7.364142e-07 7.340430e-07 7.387854e-07
QN        2.265368e-06 2.261954e-06 2.268783e-06
```

Figure 6.14: Summary of the parameters with their confidence interval for the last iteration shown in Table 6.1.

Table 6.1: Estimated parameters for each iteration. The upper part is dedicated to the Navchip gyroscope, whereas the bottom part shows the analysis of the Xsens sensor. The datasheet provides only the minimal information. This is properly re-scaled for the acquisition frequency of the dataset (250 Hz for the Navchip and 100 Hz for the Xsens sensors). The analysis through the online GUI (and the GMWM) allows for a refined analysis of the stochastic model.

		WN	QN	GM #1	GM #2	GM #3	Objective Function
	units	$(\text{rad/s})^2$	$(\text{rad/s})^2$	$(1/\text{s})$ $(\text{rad/s})^2$	$(1/\text{s})$ $(\text{rad/s})^2$	$(1/\text{s})$ $(\text{rad/s})^2$	(-)
Navchip Gyroscope Y	datasheet	6.85e-7	-	5.00e-1 2.35e-9	-	-	-
	iteration (a)	7.69e-7	2.25e-6	-	-	-	192
	iteration (b)	7.66e-7	2.25e-6	5.05e-3 3.45e-8	-	-	151
	iteration (c)	7.52e-7	2.26e-6	8.13e-4 2.91e-8	1.49e-1 1.10e-8	-	53
	iteration (d)	7.36e-7	2.27e-6	1.34e-2 9.93e-9	3.34e-4 3.42e-8	6.36e-1 7.77e-9	17
MTi-G Gyroscope Y	datasheet	7.62e-5	-	2.50e-2 9.40e-9	-	-	-
	iteration (a)	4.72e-5	-	-	-	-	456
	iteration (b)	3.50e-6	-	2.04e+2 4.54e-5	-	-	12
	iteration (c)	2.65e-6		1.51e-3 2.98e-7	2.06e+2 4.62e-5	-	8
	iteration (d)	2.03-6	-	6.10e-2 1.15e-7	9.43e-4 2.04e-7	2.08e+2 4.68e-5	2

6.5.8 Summary

Given the rigor and the capacity of the GMWM method to separate composed stochastic processes and estimate its parameters, the developed software interface is envisaging extensions for including the new developments of this methodology. Indeed, the main updates will include the implementation and visualization of additional and more complex stochastic signals where, for example, the model parameters may vary over time as a function of known external factors. For the moment this is possible - as shown in Chapter 5 - only within the R-environment through the updated R-package. Nevertheless, even at this current stage, we believe that the presented platform allows engineers to easily perform calibration tasks which were originally extremely complex to carry out. It does so by new avenues to a more straightforward tackling of problems that can refine the calibration of inertial sensors. Moreover, it must be stated that the presented methodology that underlies the IMU stochastic calibration is completely general and can be used for all kinds of analyses dealing with other types of sensors or time-dependent random data.

Application Part III

7 Adaptive Stochastic Model

7.1 Background

The use of covariate dependent stochastic models, parameters of which are estimated with the *dynamic-GMWM*, is employed in INS-based navigation filtering within a simplified simulated scenario. The Inertial Measurement Unit (IMU)-measurements are fused with other sensor information (e.g., Global Navigation Satellite System (GNSS) position and velocity, barometer, odometer) to correct the IMU trajectory that is due to initialization as well as systematic and random errors in inertial sensors. The time-correlated errors are part of the augmented state vector, the value of it is estimated and fed back (i.e., subtracted) from inertial observations prior to strapdown navigation.

If the calibration by an external aid is missing, the errors of the IMU will accumulate while propagating from the measurements to the navigation solution. In a simplified way: a systematic error in the acceleration will become a linearly growing error in velocity, and due to the two integrations in the computation, this will become a quadratically increasing error in position. A similar dependence applies to the gyroscopes which are measuring rotation rates and in the end affect the orientation. Without correction, the navigation solution drifts depending on the quality of the measurements and magnitude of initialization errors.

As a manner to take into account the errors of the inertial measurements and their accumulation during fusion with other observations, the Kalman filter computes the uncertainty value of the states such as position, velocity, and orientation. The knowledge of the underlying noise model and its parameters (i.e., quantity) allows the filter to predict the encountered dynamics accordingly. Generally, the uncertainty of trajectory (navigation) states will grow as long as there are no external updates available. Apart from the actual trajectory, this growth is directly related to the noise parameters specified in the filter.

Table 7.1: Direct influence of constant gyroscope bias (8 mrad/s) and accelerometer bias (10 mg) on attitude and positon over different time periods.

time [s]	attitude error [°]	speed error [m/s]	position error [m]
20	9	2	20
40	18	4	80
60	27	6	180
120	55	12	720

For instance, if the White Noise (WN) value of the sensor errors in the Kalman filter is set too low (although the measurements posses a higher WN value), then the uncertainty on the filtered states will grow not fast enough, and thus the predicted quality of the navigation solution will be too optimistic. On the other hand, if the WN value in the Kalman filter is set too high (although the measurements posses a lower WN value), then the uncertainty of the filtered states will grow unnecessarily fast, and thus the predicted uncertainty of the navigation solution will be too pessimistic. Both scenarios (pessimistic and optimistic) are undesired with relation to sensor fusion (e.g., rejection/acceptation of observations and their effect on the estimated trajectory as well as auxiliary states such as sensor biases). To stay on the save side, and thus pessimistic, a higher WN parameter value is usually chosen manually on a case-by-case selection.

7.2 Simulation Scenario

A sensor may undergo large temperature changes, which affect the sensor readings (e.g., the sensor in a vehicle is turned on and warms up, later cools down with an airflow. The analysis in the previous Chapter 5 showed that the temperature has a non-negligible effect on the sensor readings in both the deterministic and stochastic part of the signal. Of course, if the deterministic part is not correctly accounted for, the integration of included errors will systematically and directly influence the position and attitude of the navigation solution. This is briefly shown in Table 7.1, where the bias on the accelerometers and gyroscopes influence the position and the orientation respectively.

The influence of the stochastic part of the signal is more difficult to demonstrate, and that is why the following simulation scenario is considered here:

- A vehicle is moving on a 2D circular trajectory. A local frame is considered as an inertial frame, where gravity is omitted.
- The vehicle is initialized at the East/North coordinates (0,100) m with an East/North ve-

locity of (3.49,0) m/s. Then the trajectory is estimated via strapdown inertial navigation around a circle with a radius $r = 100\,\mathrm{m}$ at a constant velocity.

- Upon reaching the point (0,-100) m (i.e., after 90 s) the GNSS position updates are used at 1 Hz and the vehicle completes one turn of the circle after another 90 s (i.e., after a total of 180 s).

The IMU mounted on the car senses the rotation rate via the z-gyroscope ω_z (mounted perpendicular to the 2D trajectory) and the acceleration via the x-y accelerometers $a_{x/y}$ (x-axis pointing in the direction of movement around the circle, whereas the y-axis is perpendicular and points to the center of the trajectory). The nominal reference signals are:

$$\begin{aligned}
&\omega_z = \frac{2\pi}{180}\ \mathrm{rad/s},\\
&a_x = 0,\\
&a_y = r\omega_z^2 = 0.122\ \mathrm{m/s^2}.
\end{aligned}$$

These signals (accelerometer and gyroscope) are corrupted only with a WN process to simplify the example. The strength of the simulated WN grows linearly from the beginning of the track (sensor is cold) to the end (sensor warms up). The Kalman filter fuses the inertial trajectory with GNSS positions, while using noise models at three different scenarios:

1. Kalman filter with a constant low WN value corresponding to sensor state/temperature at the beginning of the track;
2. Kalman filter with a constant high WN value corresponding to sensor error values at the end of the track;
3. Kalman filter with temperature-corresponding (i.e., covariate updated) WN value that represents the true modeled noise parameter.

7.3 Discussion

Figure 7.1 shows Monte-Carlo realizations. A total of 1000 trajectories (i.e., realizations of WN sequences) are considered. Depending on the actual error accumulation, the position deviates at time $t = 90$ s up to 30 m from the reference trajectory. Then the position error is bounded at the moment the GNSS position measurements are used.

The quality of the estimated trajectory is given by the P-matrix of the filtered states containing variance on its diagonal. As long as there are no external updates, this uncertainty will grow. Figure 7.2 shows the different growth rates of such uncertainty (in terms of σ) on the orientation and the velocity for different cases of the WN-values. If falsely a high value of WN is used in the filter, then the uncertainty grows unnecessarily fast. However, this case stays on the "save side" of the sensor fusion.

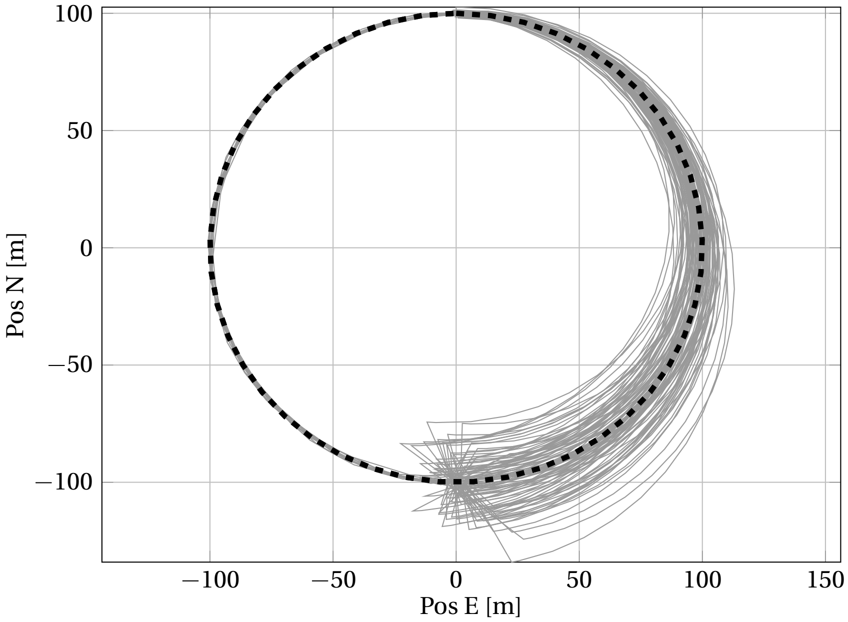

Figure 7.1: Position solutions (gray) in comparison to the reference (black). The estimated solutions shown exceed the 3σ boundary on some point of the trajectory.

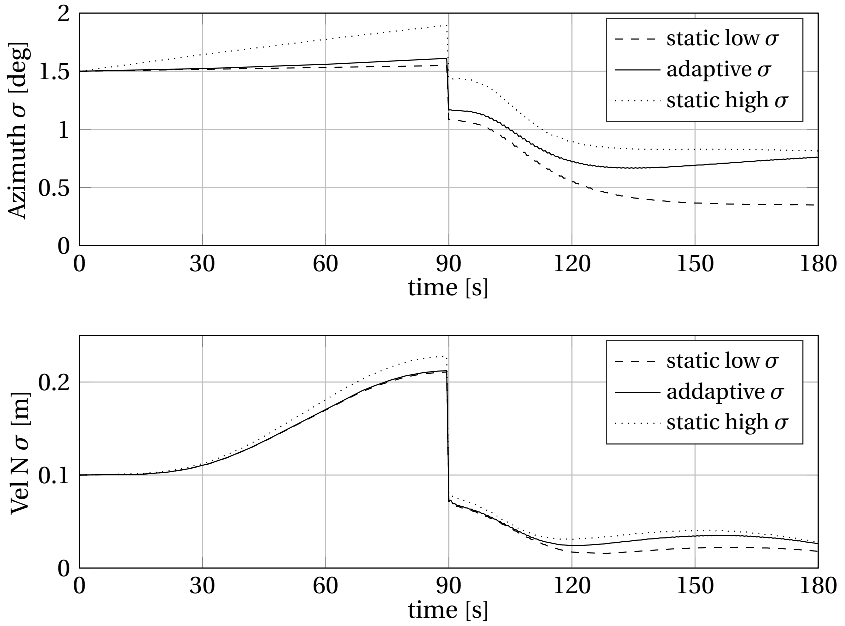

Figure 7.2: Evolution of the estimated uncertainty with different noise models programmed into the Kalman filter. The GNSS updates appear after 90 s.

On the other hand, if a too optimistic value of WN is set in the filter (i.e., a falsely too low value), the result will be overconfident, and correct updates may get rejected. This is not only sub-optimal but dangerous. Using the dynamically adapted value of the WN in the filter, the reality is correctly represented in the filter and the filtered solution is optimal, and the predicted confidence adequate.

Figure 7.3 visualizes the advantages when using the covariate (temperature) adapted stochastic models within a Kalman filter. For each time stamp along the trajectory, the distribution of the 1000 computed navigation solutions is compared to the reference. This empirical deviation is set in relation to the predicted uncertainties of the navigation states and the three defined noise models (i.e., static low, static high, covariate-adaptive). The 80% confidence interval is chosen here as an example. In theory, this interval puts 80% of the trajectories inside the 1.28σ-bound and 20% of the trajectories beyond this 1.28σ threshold. The distribution of the trajectories with the static low noise model (blue) deviates quickly from the reference 80% bound. The same can be said about the distribution of the trajectories with the static hot noise level (red). Only the distribution of the trajectories generated through adaptive filtering of the noise model (green) allows following the reference distribution correctly. This is necessary to correctly/optimally estimate the states and their confidence.

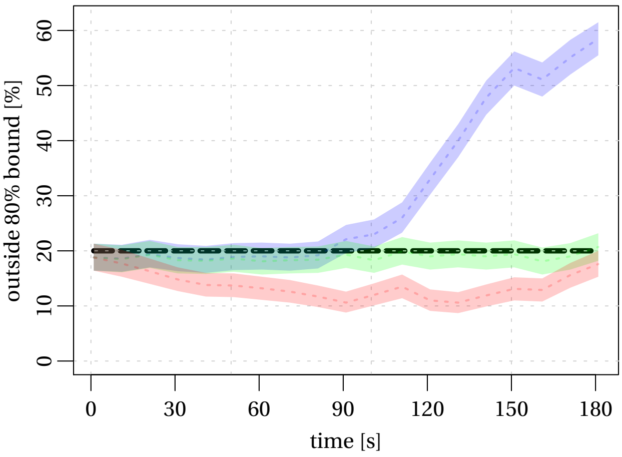

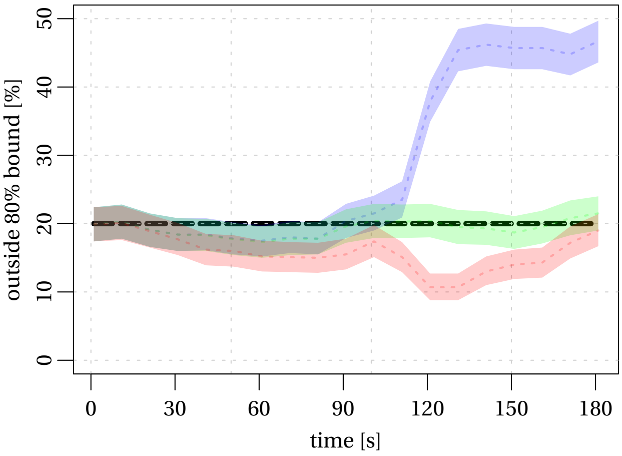

Figure 7.3: Percentage outside 80%-bound. Top: azimuth. Bottom: north velocity. Black dashed line represents the theoretical amount of trajectories outside the bound, which would be 20%. The adaptive noise model (in green) follows this theoretical value, whereas the other two do not (hot model in red, cold model in blue).

8 Integrated Navigation

8.1 Introduction

This chapter shows the application of different calibration schemes discussed in Chapter 4 and the fusion of the accelerometer, magnetometer, and the barometer in relation to airborne missions, where the derived attitude and altitude is compared to a reference. The sensors in question are mounted inside a Unmanned Aerial Vehicle (UAV), which has interesting properties: on the one hand, the light nature of the UAV allows for easy deployment and usage for a multitude of applications, on the other hand, as the payload is limited, a reference high-grade Inertial Measurement Unit (IMU) cannot be mounted inside. Other means to obtain a reference are therefore explored.

The equipment used in relation with the UAV and its experiments were presented in Chapter 6. It consists of the IMU board. The subsequent sections show its applications for the altitude determination in the absence of a Global Navigation Satellite System (GNSS)-signal and the attitude initialization with simulated and real data. In the last section, a navigation solution is considered, where multiple IMUs are fused into one single synthetic IMU.

8.2 Altitude Determination with Barometer

The performance of barometer calibration and height determination Above Ground Level (AGL) is investigated as follows: the IMU and the GNSS observations are fused until time stamp 400 s after the micro-UAV take-off. At this moment, a GNSS outage occurs (artificially) for the rest of the flight. This can be due to a bad satellite constellation, as the drone flies in a narrow valley, due to electromagnetic interference, or a GNSS malfunctioning. Also, the cause could be due to a large banking angle of the drone, as the GNSS antenna is directional and a too steep banking angle will cause the GNSS-receiver to lose visibility to some of the satellites.

A first solution consists of the IMU standalone navigation from this point on. As such, the navigation solution diverges quickly with an unbound error on the vertical axis (as well as on the horizontal plane). The absolute navigation solution in the altitude for this scenario is shown with a dotted line in the top part of Figure 8.1. The error in the altitude reaches more than 30 m after 2 min of the outage, a fact of which compromises safe navigation close to the ground.

The second solution consists of considering additional pressure measurements p_i provided by the barometer once the outage occurs at time-stamp 400 s. The barometer observations are present from the beginning. Hence the parameters (p_0 and k) are calibrated with the method explained in Section 4.6 thanks to the GNSS observations directly from the start on. These additional pressure observations are able to stabilize the navigation solution in the vertical channel from the time index 400 s to GNSS like quality. This is shown in the top part of Figure 8.1 as a dashed line.

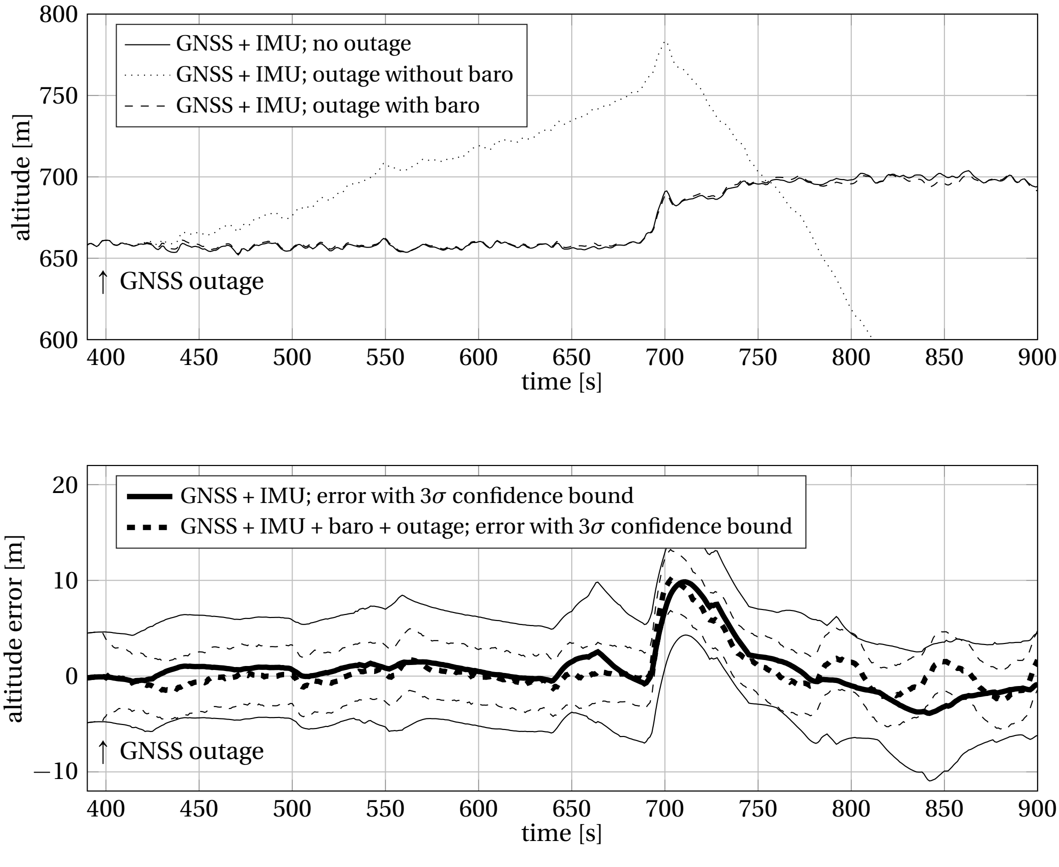

Figure 8.1: Top: absolute altitude for different scenarios. The IMU-only solution (dotted line) diverges quickly after the GNSS outage, whereas the measurements of the barometer (dashed line) enable to bound the drift. Bottom: altitude error with confidence bound with respect to the reference.

The lower part of Figure 8.1 shows the error with relation to the reference for the normal case (no outage) and the case with the outage but with the use of barometer measurements. As can be seen, the barometer aiding in height surpasses in quality what a multi-frequency GNSS receiver used in a stand-alone mode could provide. This is further highlighted in Figure 8.2, showing the 1σ confidence interval only.

On the one hand, it shows how fast the navigation solution based only on the IMU measurements diverges (dotted line). The 1σ confidence interval reaches 2 min after the GNSS outage a value of 25 m. This value continues increasing continuously to several hundreds of meters afterward. On the other hand, the navigation solution (dashed line) is more precise directly with the barometer (mean $\sigma = 1\text{m}$), than it would be with the GNSS measurements (mean $\sigma = 1.8\text{m}$) provided by the receiver (full line). This is due to the fact that the GNSS height determination with code measurements has a worse precision in the vertical axis than a fully calibrated and sensitive barometer.

8.3 Initial Attitude Estimation

The goal here is to investigate how well the REQUEST algorithm estimates the initial attitude (with roll, pitch, and yaw parametrization), by using three different approaches while verifying its performances in different situations. The first approach uses simulated measurements to compute the attitude, on which several combinations of accelerometer errors are introduced. The second approach compares the estimated attitude from the REQUEST to the estimated attitude computed via a GNSS/Inertial Navigation System (INS) fusion from a real dataset (smoothed solution before and after the mission, which represent take-off and landing). The third approach uses a photogrammetric approach that verifies the quality of the attitude initialization.

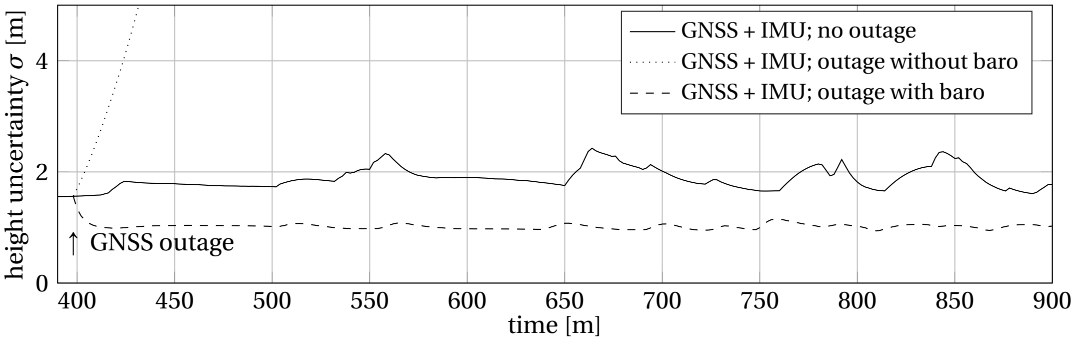

Figure 8.2: The KF-predicted uncertainty in the altitude of the GNSS-IMU fusion is worse than the fusion between the IMU and the barometer. The IMU-only uncertainty grows quickly after the GNSS outage.

8.3.1 Simulated Data

A total of 100 different attitudes are created with simulated measurements for the accelerometers and the magnetometers. The angle for roll is confined to ±180°, pitch is limited to ±90°, and yaw is defined in ±180°. The perfect sensor readings from accelerometers and magnetometers are overlaid with simulated white noise. The REQUEST algorithm is then used to determine the attitude of the sensor platform as explained in Subsection 2.6.4. This scenario represents the error-free case, which was used to determine the correct implementation of the algorithm. The estimated results in roll, pitch, and yaw are directly compared to the reference attitudes, which were used to generate the measurements in the first place (see Figure 8.3).

In the next step, the impact of a correct accelerometer calibration is investigated (whereas a correct magnetometer calibration is discussed in the following subsection). The attitude determination quality is compared to different scenarios, where parameters such as scale-factor S, non-orthogonality θ, and bias b are added. Typical values for the accelerometer error parameters found in the datasheet C.3 are used here to simulate an eventual impact. The following parameters are used:

- bias with $b = [25 \ \ -25 \ \ 25]^T$ mg;
- scale-factor error with $S = [0.2 \ \ -0.2 \ \ 0.2]^T$ %;

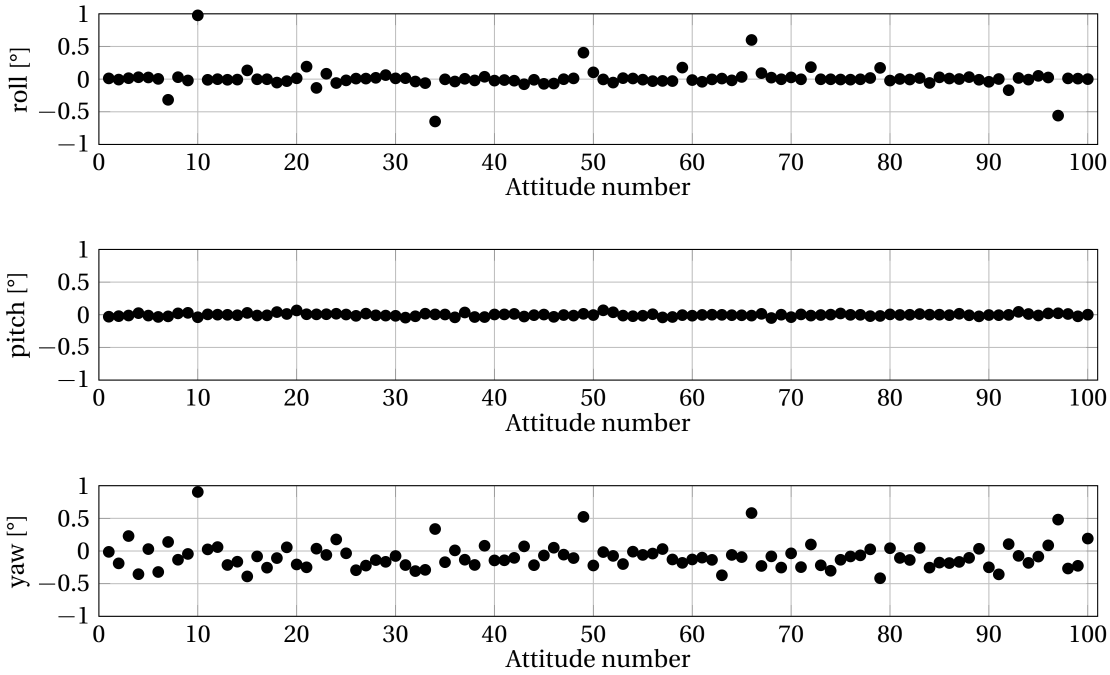

Figure 8.3: Errors in roll, pitch, and yaw based on 100 simulated accelerometer and magnetometer measurements with relation to their reference attitude.

- non-orthogonality with $\theta = [4 \ \ -4 \ \ 4]^T$ mrad.

These parameters are employed to falsify the true accelerometer data $\check{l}$ as:

$$l = A \cdot \check{l} + b, \tag{8.1}$$

with

$$A = \begin{bmatrix} 1+S(1) & 0 & 0 \\ \theta(1) & 1+S(2) & 0 \\ \theta(2) & \theta(3) & 1+S(3) \end{bmatrix} \quad \text{and} \quad b = \begin{bmatrix} b(1) \\ b(2) \\ b(3) \end{bmatrix}. \tag{8.2}$$

The error-free attitude determination is compared to the cases, where the data is corrupted with

1. only the bias parameter b (equivalent to the in-lab pre-calibration of S and θ),
2. only the scale-factor parameter S,
3. only the non-orthogonality parameter θ,
4. a mix of the non-orthogonality θ and scale-factor S parameters (equivalent to pre-calibration of only b),
5. the full set of the parameters (equivalent to no pre-calibration).

The mean errors in roll, pitch, and yaw including the standard-deviation as well as the maximum error are assembled in Table 8.1 for all the previously defined scenarios 1 through 5 as well as the error-free case. The usage of error-free measurements and the correct estimation of the attitude angles show that the implementation is done in the right way. In fact, the REQUEST-algorithm is implemented in the calibration GUI functionality presented in Chapter 6.

If no pre-calibration is performed and the data is taken as such (see scenario 5), then the attitude determination is not usable, as it can vary in the attitude values by several ten degrees. The distribution of the errors can be decreased by pre-calibrating the sensor readings for scale-factor and non-orthogonality (see scenario 1), where only the bias of the accelerometer is influencing the attitude determination. Mean errors and the distribution are decreased, but the distribution is still one order of magnitude higher than is required. A full calibration is necessary, as the bias component represents by far the most significant influence.

Table 8.1: Influence of different calibration parameters for the accelerometer (bias, scale-factor, and non-orthogonality) on the 100 simulated attitude data.

influence scenario	difference	roll [°]	pitch [°]	yaw [°]
error free	mean	0.009	-0.002	-0.079
	std	0.162	0.022	0.204
	max	0.976	0.068	0.904
1) only b	mean	-0.071	-0.668	-1.274
	std	12.395	0.819	12.681
	max	84.615	2.285	56.362
2) only S	mean	0.014	-0.004	-0.056
	std	0.182	0.044	0.234
	max	1.020	0.117	0.946
3) only θ	mean	0.118	-0.001	-0.043
	std	1.172	0.132	1.199
	max	5.345	0.332	5.276
4) θ and S	mean	0.124	-0.003	-0.020
	std	1.172	0.139	1.195
	max	5.383	0.345	5.312
5) θ and S and b	mean	-0.072	-0.666	-1.388
	std	12.959	0.831	13.285
	max	89.337	2.208	56.886

The scenarios 2 through 4 show the influence of the scale-factor and non-orthogonality and their impact on the attitude determination. Especially scenario 4 shows a case, where the bias is calibrated with the latter two left aside. The impact is small (std of 1° with a max error of 5°) compared to the bias influence, but for a complete calibration, it has to be taken into account and to as.

8.3.2 GNSS/INS Prior/After Flight

A flight mission with our UAV was performed to acquire a real dataset usable in this part of the experiment. The flight duration was around 20 min. This allows, among others, for proper mitigation of errors due to attitude initialization with GNSS/INS fusion, especially at the terminal phase of the mission and thanks to smoothing, also at the start. This trajectory/attitude serves here as a reference, to which the algorithms are compared to.

The typical flight mission foresees a certain period before the take-off, where the accelerometers, gyroscopes, and the magnetometers are calibrated. Like mentioned in earlier sections, the accelerometers are calibrated via the multi-position-calibration scheme explained in Section 4.3 and the magnetometers are calibrated (i.e., ellipsoid to sphere transformation) by the procedure explained in Subsection 2.6.3. After the calibration, just before take-off, the UAV is set on the ground, and the attitude determination algorithm REQUEST is performed to calculate the initial attitude of the UAV (and its sensor board mounted inside the payload bay). The same procedure (e.g., calibration of accelerometers and magnetometer and subsequent attitude determination) is performed again at the end of the mission just after landing. The accelerometers may have changed their bias and thus need a re-calibration. The same problem exists for the magnetometers, where the landing spot may influence the magnetic field. It will affect the shape of the correctly calibrated sphere based on the magnetometer data from another location, as it is a function of the local magnetic field.

In order to asses the impact of the pre-calibration of the accelerometers and the magnetometers on the attitude determination, several calibration scenarios are considered here, which can all be compared to the GNSS/INS reference:

1. all the sensors are fully calibrated,
2. the accelerometer is not calibrated, whereas the magnetometer is,
3. the magnetometer is only partially calibrated, but the accelerometer is corrected, and
4. the magnetometer is not calibrated, whereas the accelerometer is.

Table 8.2 resumes the results of these defined scenarios. First of all, the reference GNSS/INS absolute attitude can be compared to the case, where all the sensors are correctly and fully calibrated. This corresponds to scenario 1. The roll and pitch attitude correspond to each other and the yaw-value, with a difference to the reference of 1°, is usable for the initialization of the navigation in the case of prior take-off and after the landing.

If the magnetometer is only partially calibrated (sphere parameter estimation based on an ellipse with 30% coverage, instead of the 70%), then the attitudes do not correspond to the reference values. This is shown in scenario 3. The same can be said, when the sensors are not calibrated at all (i.e., scenario 4). Especially the values in the yaw-component are significantly different from the reference. Thus, a partial magnetometer calibration is not sufficient. As much as possible of the magnetometer-sphere has to be covered, by swinging the sensors/UAV through all the different orientations, to map the local magnetic field.

Table 8.2: Influence of different calibration scenarios on the attitude determined by the REQUEST algorithm and by GNSS/INS fusion. Absolute attitude values for top: prior take-off, and bottom: after landing.

	scenario	roll [°]	pitch [°]	yaw [°]
prior take-off	GNSS/INS	2.36	-0.46	15.51
	1) all calibrated	2.16	-0.40	16.59
	2) no accelerometer calibration	1.86	-0.48	16.10
	3) partial magnetometer calibration	1.70	-1.05	33.38
	4) magnetometer not calibrated	11.45	-15.35	-30.62
after landing	GNSS/INS	12.45	1.39	75.04
	1) all calibrated	11.40	1.35	76.34
	2) accelerometer not calibrated	11.25	1.17	76.61
	3) magnetometer partially calibrated	7.29	0.78	83.53
	4) magnetometer not calibrated	11.13	2.00	-17.25

8.3.3 Static Photogrammetry

More measurements are required for statistical evaluation of the attitude initialization quality. For this, another approach is pursued. Our plane (with the integrated camera and IMU board) is fixed on a tripod at large bending angle and photos are taken at different places with some variation in their rotation.

The method of the photogrammetric bundle adjustment (with ground control points) is employed to provide the absolute attitude reference [Pix4D, 2018]. This process requires to identify points/features on the photos, which are then directly referenced to the same points in the other photos, if present. If some points in the picture are known in the real world, then their projection on the pictures can be directly related to the camera orientation. Indeed, the camera needs calibration too, which is not further elaborated here.

The lab has access to such a calibration field (see Figure 8.4) with numerous signalized targets of known coordinates placed in different positions throughout this camera calibration field. The experiment was conducted in this environment that is challenging for magnetometers due to its proximity to steel-reinforced concrete or other steel structures.

The attitude parametrization used in the photogrammetry (angles ω, ϕ, and κ) differs from the notation used in this document and other navigational literature. Hence, the results from the REQUEST algorithm need to be converted for comparison reasons to this specific photogrammetric notation [Baumker and Heimes, 2002].

The sensors need calibration prior to attitude determination. Hence, the accelerometers are again calibrated as shown via the multi-position calibration scheme in Section 4.3. The calibration scheme for the magnetometers is used as well, which was presented in Subsection 2.6.3. In fact, the static positions are used for the accelerometer calibration, whereas the movement between the static positions is used for the magnetometer calibration (i.e., in order to fill the bins of the magnetometer calibration sphere and to obtain an ideal minimal coverage of 70%).

After the conversion to the photogrammetric notation, the Figure 8.5 shows the difference between the reference (i.e., from the employed photogrammetric Pix4D software) and the REQUEST algorithm. The results are resumed in Table 8.3. The standard deviation calculated from the attitude errors lies between 2° to 3°. This should be sufficient for starting the "fine-alignment"/refining via the Kalman filter filtering.

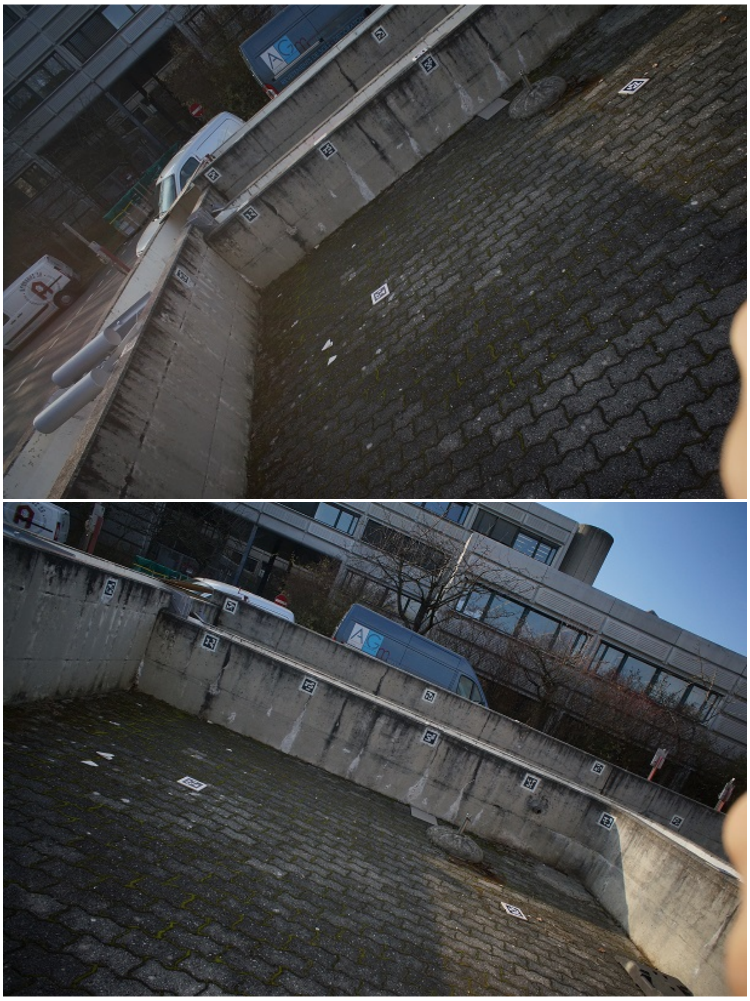

Figure 8.4: Example of 2 photos taken at different attitudes from the calibration field with the visible black/white targets.

Table 8.3: Comparison between the attitude provided by the photogrammetric software Pix4D and the REQUEST algorithm.

quantity	ω [°]	ϕ [°]	κ [°]
mean error	-0.28	0.08	1.53
std error	2.50	2.09	3.00
max error	4.66	4.37	6.92

The relatively higher differences in the results compared to the simulation or to the GNSS/INS fusion can be explained by the location of the experiment. In fact, the calibration of the accelerometers does not depend on the physical location. This changes drastically for the magnetometers. Concrete structures and metal bars embedded in the concrete supporting the targets as well as in the buildings surrounding the calibration field influence the local magnetic field. Knowing the algorithm delivers such results in this environment, it is completely usable in the application fulfilling the need to initialize the navigation filter in an outdoor scenario.

8.4 Navigation during GNSS Outage

The real-time strapdown inertial navigation/integration originally developed for PC-platforms [Skaloud et al., 2010] was adapted for the developed sensor board and an embedded computer.

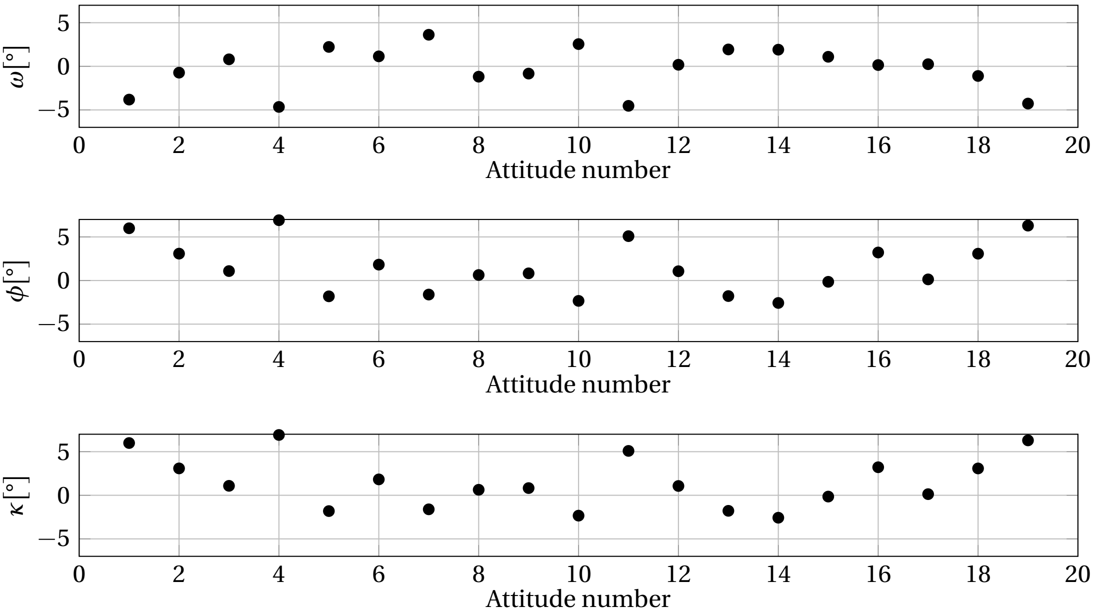

Figure 8.5: Error of the attitude expressed as ω, ϕ, and κ between the REQUEST algorithm and the angles provided by the photogrammetric application.

The stochastic parameters per each IMU and each sensor axis were adequately estimated via the GMWMW framework (see Appendix D for complete stochastic modeling results of the sensors). The sensors consist of the four individual IMUs mounted on our IMU-board and the fused (with equal weights) synthetic version which we call SIMU.

A total of five navigation computers (data coming from precalibrated IMU1, IMU2, IMU3, IMU4, and SIMU) can be run simultaneously on the embedded computer in parallel if needed, which will provide the navigation solution. A typical scenario is chosen for a micro UAV flight. A GNSS outage of 30 s is simulated on the recorded data, to force the navigation solution to be solely dependent on strapdown navigation. The trajectory in question is a U-turn and is depicted in Figure 8.6.

Table 8.4 resumes the navigation errors for the position and the velocity, which are also visualized in Figure 8.7 with more details. The fused SIMU has overall a less bad navigation solution than the individual IMUs. The planimetric error, as well as the velocity error, can be cut in half, depending on which IMU it is compared to. In any case, the SIMU performs best in this shown example. The added "autonomy" allows for a save usage in case a problem (e.g., GNSS outage) occurs.

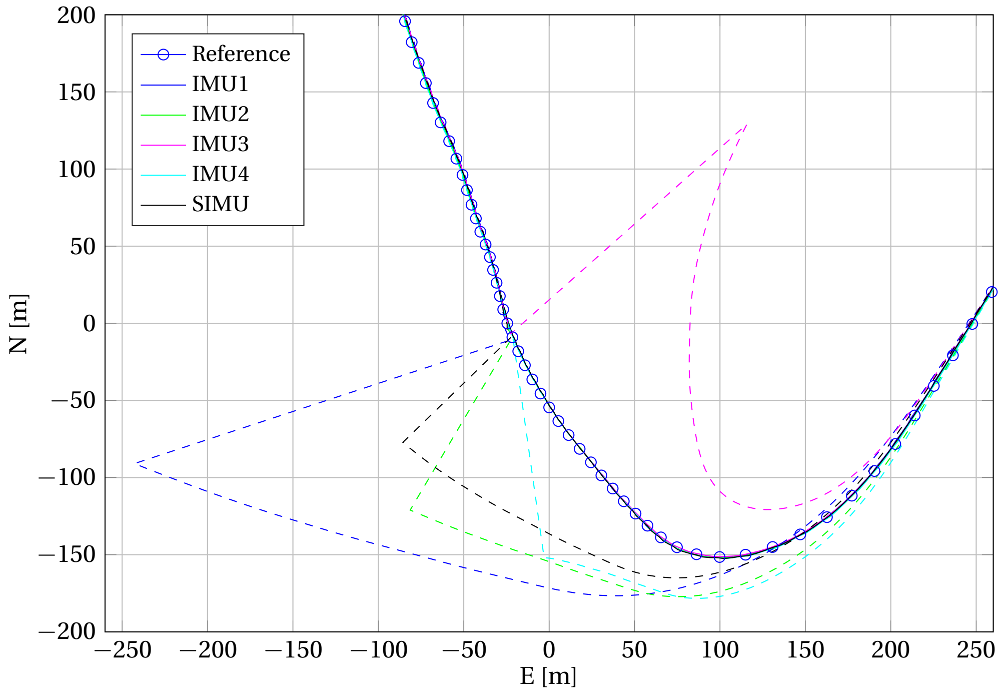

Figure 8.6: Top view of the trajectory part, during which a 30 s GNSS outage is simulated.

Table 8.4: Error statistics for the 30 s GNSS outage for different IMU configurations.

maximum error	IMU1	IMU2	IMU3	IMU4	SIMU
planimetric [m]	236.79	126.29	195.37	142.30	93.55
altimetric [m]	3.86	10.59	28.39	15.62	5.46
absolute velocity [m/s]	14.33	7.19	13.69	9.24	4.90

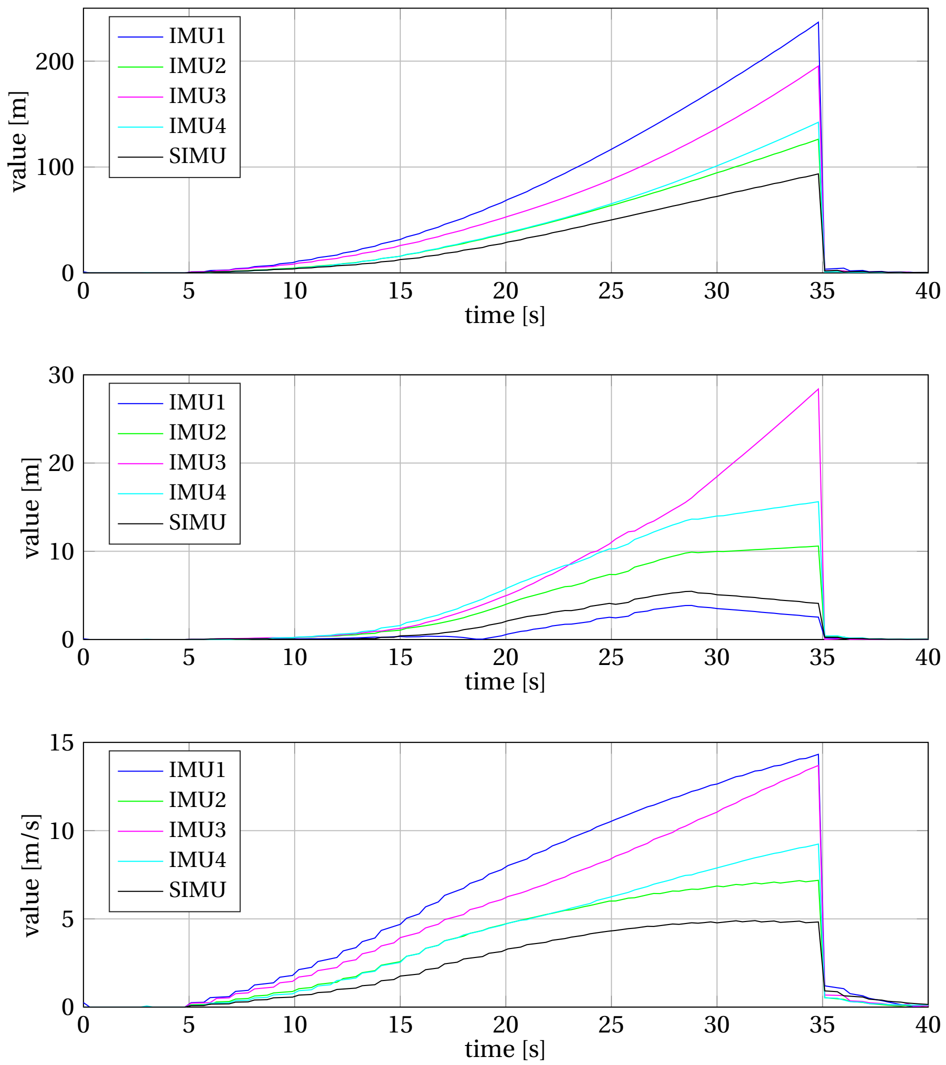

Figure 8.7: Errors with relation to the reference for the IMU board. Top: planimetric error. Middle: altimetric error. Bottom: absolute velocity error.

9 Mapping

9.1 Introduction

This chapter shows the benefit when using the proposed calibration and data fusion methods. The first section applies this method to direct orientation of an Airborne Laser Scanning (ALS) system. This particular setup is described with a brief overview of the reference sensors and testing area. Then, the performance of our sensor board is analyzed. It demonstrates the possible benefits when using a system composed of multiple Micro-Electro-Mechanical System (MEMS) Inertial Measurement Unit (IMU), which were all correctly calibrated.

The second section applies the presented calibration methods to mapping with a micro Unmanned Aerial Vehicle (UAV). Again, the setup and the mapping missions are described, and the impact of the precalibration on the performance of the attitude determination is shown.

9.2 Close-Range Helicopter

9.2.1 Setup

To benefit from a continuous orientation reference while investigating the ALS performance, our MEMS IMU board is rigidly mounted on a state-of-the-art airborne mapping system on board a helicopter. Principally, the ALS system is composed of several elements:

- laser scanning unit: it sends a laser pulse, detects the reflected beam from a surface, and measures the time between sending and receiving;
- geo-referencing system: this system provides position and attitude in order to relate the information from the laser scanner to the world. It is composed of an Inertial Navigation

System (INS) and a Global Navigation Satellite System (GNSS) receiver;

- dedicated software: to synchronize the measurements and treat the data in real-time and/or post-processing:
- frame camera: takes photos to increase the palette of derived mapping products.

The density (in terms of cm per pixel, or number of laser points per area) of the generated maps depends on the equipment used, which is directly related to the scanning height Above Ground Level (AGL), the velocity, and the update rate of the system and its sensors. This depends on the application and the requirements needed for the final mapping product. An overview of the technology, as well as the different applications and hardware can be found in [Baltsavias, 1999; Schär, 2010].

The ALS system from the Lausanne based company Helimap is used here in this experiment [Helimap System SA, 2018]. Our sensor board with the redundant MEMS-IMU system is mounted rigidly to a whole acquisition apparatus (as mentioned before), and it is partly composed of:

- Laserscanner Riegl VQ480U [Riegl, 2015],
- PhaseOne frame digcam (IXAR180, 42 mm lens, 80Mpx, pixel size 5.2 µm) [PhaseOne, 2014],
- IXblue AIRINS navigation grade IMU (gyro bias 0.008 °/h) [Ixblue, 2015], and
- Javad GNSS dual constellation and dual frequency receiver.

These devices are providing the reference measurements and reference solutions both in the air and in the ground. They usually are side mounted on a helicopter, as depicted in Figure 9.1 and the mission is flown at a speed of 10-15 m/s - that is similar to that of a fixed-wing micro UAV. In the described experiment the system is augmented not only by our redundant IMU board but also by a lighter and smaller data acquisition unit that is supposed to be carried by a drone. This 2.7 kg integrated package is equipped with a set of sensors:

- Laserscanner velodyne Puck LITE [Velodyne Lidar, 2018],
- Camera Sony (A6000, 16 mm lens, 24Mpx, pixel size 3.9 µm)[Sony, 2018],
- small GNSS-IMU integrated solution APX-15[Trimble, 2016]

For further analysis and the simplicity of the description, our Navchip MEMS IMU will be simply referred to as *IMU*. The first two setups concern the experiment, where this IMU is either calibrated (in-lab and just before the flight) or uncalibrated. The third setup is the fusion of the four side-by-side mounted and calibrated IMUs to form one Synthetic IMU (SIMU).

The flight line considered for the photogrammetric reference consists of a 1.5 km straight line (forward-backward), which was flown in the vicinity of Romanel-sur-Morges next to Lausanne (see Figure 9.2). Different ground control points are implemented in the region, to have a reference to compare the results to. Around 90 photos are taken just in this area. The flight duration of this particular flight line is 300 s, whereas the whole mission (start to landing) was almost one hour long.

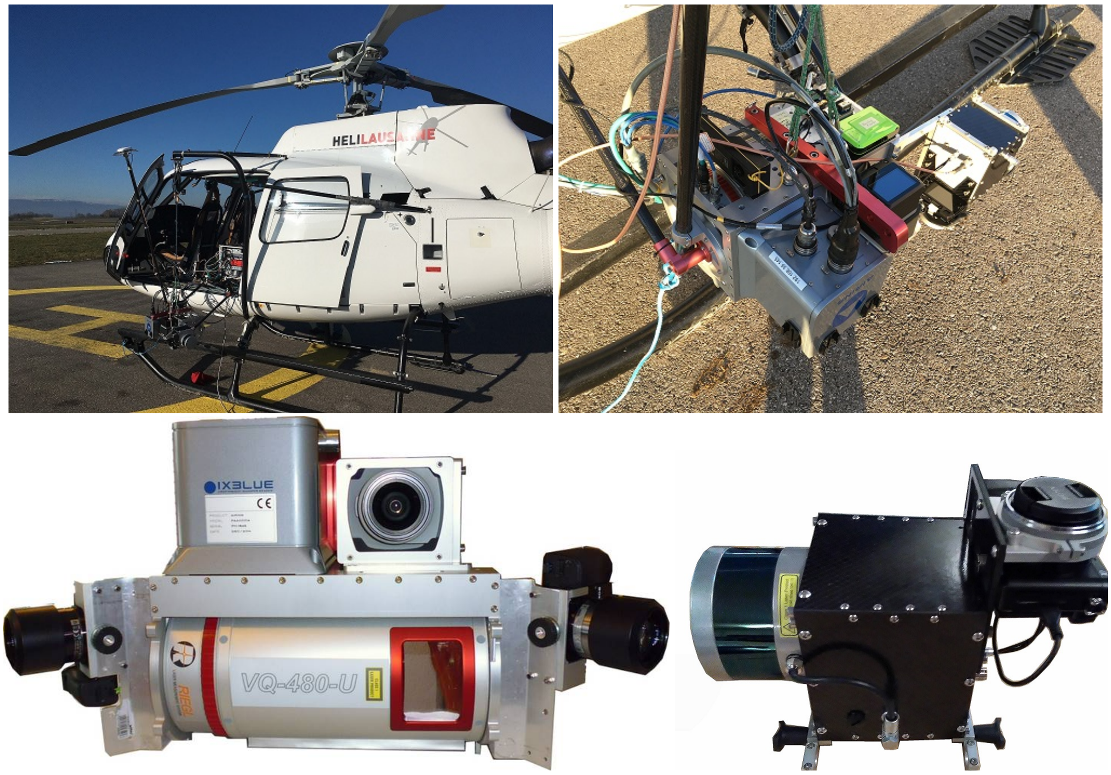

Figure 9.1: Top Left: ALS installed on helicopter. Top Right: zoom on ALS system. Bottom Left: Helimap system used as reference. Bottom right: UAV "puck" scanning system with APX15.

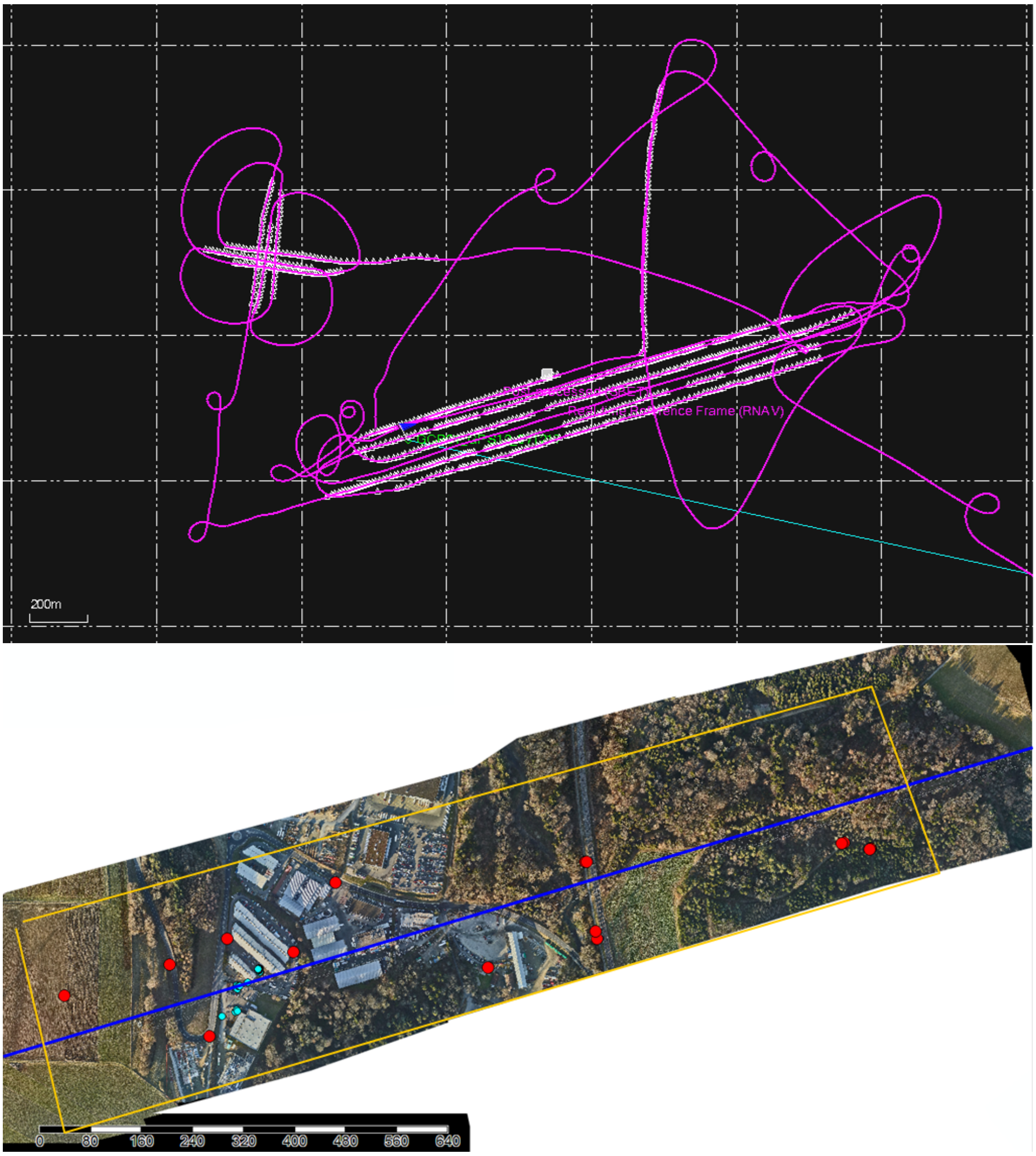
Post-processed (SBET)
Real-time Reference Frame (RNAV)
200m
0
80
160
240
320
400
480
560
640

Figure 9.2: Top: complete helicopter flight path (camera events represented as white triangles). Bottom: long strip area considered for the experiment (ground control points in red).

Table 9.1: Summary of the errors in the attitude from the navigation solution between our IMU with its different configurations and the reference AirINS.

Sensor	Error	roll [deg]	pitch [deg]	yaw [deg]
IMU	std	0.023	0.027	0.104
uncalibrated	max	0.080	0.129	0.248
IMU	std	0.022	0.027	0.087
precalibrated	max	0.064	0.106	0.181
SIMU	std	0.016	0.017	0.054
fused	max	0.047	0.063	0.116

9.2.2 Attitude Quality - Continuous Reference

Given the fact that the position-accuracy in nominal conditions is guided by the GNSS accuracy that is comparable between high-end receivers placed either on a helicopter or a drone (assuming comparable signal-to-noise ratio), the analysis focuses on the quality of the attitude determination.

The data from the base and airborne GNSS receivers are combined providing a solution at 1 Hz. Then, loosely coupled integration with different IMUs is performed in an Extended Kalman Filter. Four navigation solutions are considered, each one using the same GNSS position/velocity information but "different" inertial sensors. These are (i) the uncalibrated IMU, (ii) the calibrated IMU, and (iii) the fused SIMU. These are then compared to (iv) the reference solution provided by the fusion of GNSS and AirINS (see Figure 9.3).

The distribution and the amplitude of the errors in roll/pitch/yaw are quantified in Table 9.1. The 20% decrease of the yaw standard deviation is firstly due to the correct calibration, which was performed prior to the flight before the mission with the presented multi-position calibration scheme. Secondly, the fusion into one SIMU of our four individual IMUs of the sensor board allows decreasing the standard deviation (i.e., improve the accuracy) further by a factor of 2 between the uncalibrated and the fused version.

The maximum error (in the absolute sense) was reduced by about 20-30% by the calibration and again another 20-40% by the synthetic fusion. This can also be observed in Figure 9.3, where the amplitude of the yaw error is considerably decreased.

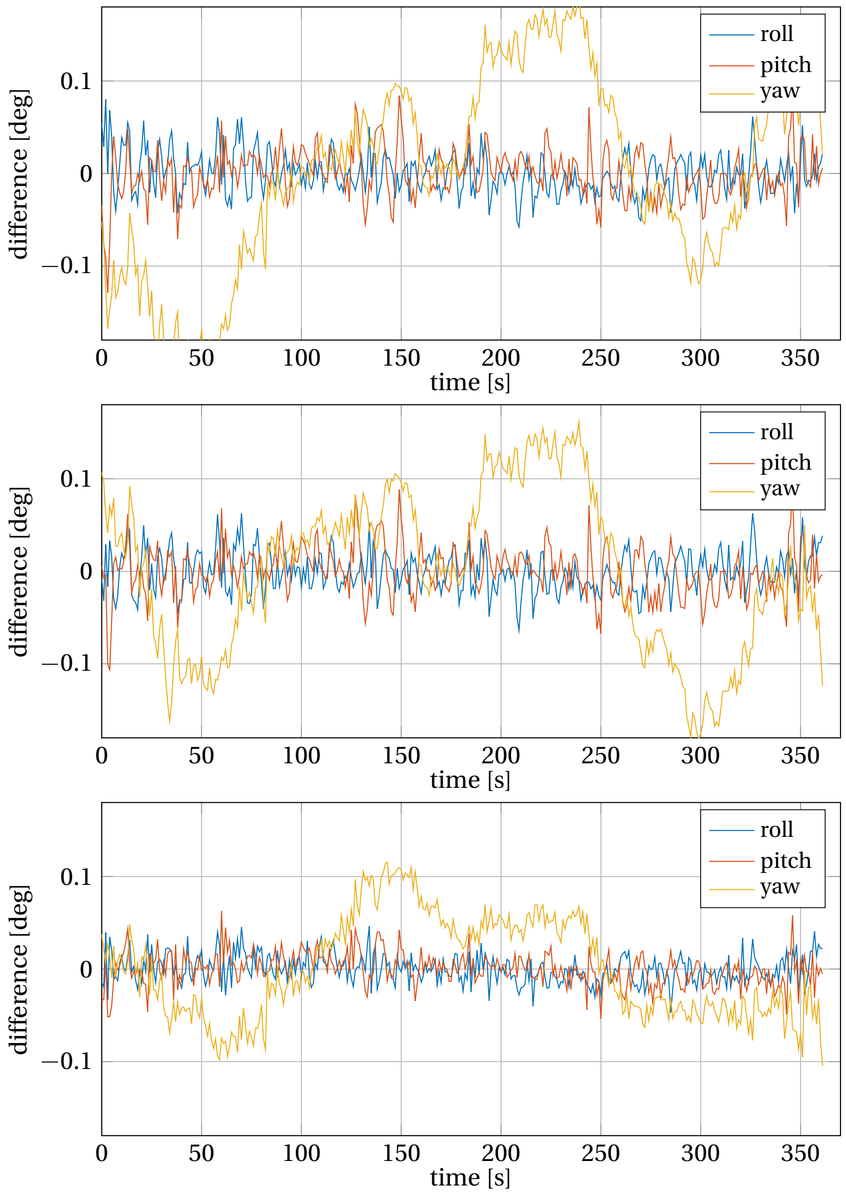

Figure 9.3: Differences to the AirINS in the attitude solution for the first flight line. Top: uncalibrated IMU. Middle: calibrated IMU. Bottom: fused SIMU.

Table 9.2: Summary of orientation differences between INS/GNSS derived trajectory and that resulting from the photogrammetric adjustment per photo and IMU.

Sensor	Error	ϕ [mdeg]	ω [mdeg]	κ [mdeg]
IMU uncalibrated	mean	3.8	-20.3	-87.1
	std	67.1	28.1	175.4
	max	146.9	100.7	362.4
IMU precalibrated	mean	13.0	-11.6	49.7
	std	49.2	23.21	170.5
	max	126.39	79.6	491.0
SIMU	mean	4.7	-12.7	-40.1
	std	23.4	18.4	79.9
	max	53.5	63.0	172.0
APX15	mean	-10.2	-4.0	14.7
	std	10.7	11.4	109.4
	max	35.5	33.8	235.5
AirINS	mean	-0.4	-0.1	-0.3
	std	1.0	1.0	4.9
	max	2.7	3.4	9.5

9.2.3 Attitude Quality - Photogrammetric Reference

Here the attitude reference is obtained by a photogrammetric block of roughly 350 images. The absolute orientation of the somewhat 90 photos (via ground control points) is then compared to the orientation of the different sensor systems. Figure 9.4 shows the evolution of the different residuals for each sensor system. The offset and dispersion by an uncalibrated IMU compared to a fully fused SIMU system is clearly visible on this plot, and it is quantified in Table 9.2, where the performances of our fused system are comparable if not even slightly better in heading than the commercially available sensor system APX15. This method also independently verifies the attitude quality of the AirINS that served for the continuous evaluation in the previous subsection. The agreement is at few mdeg.

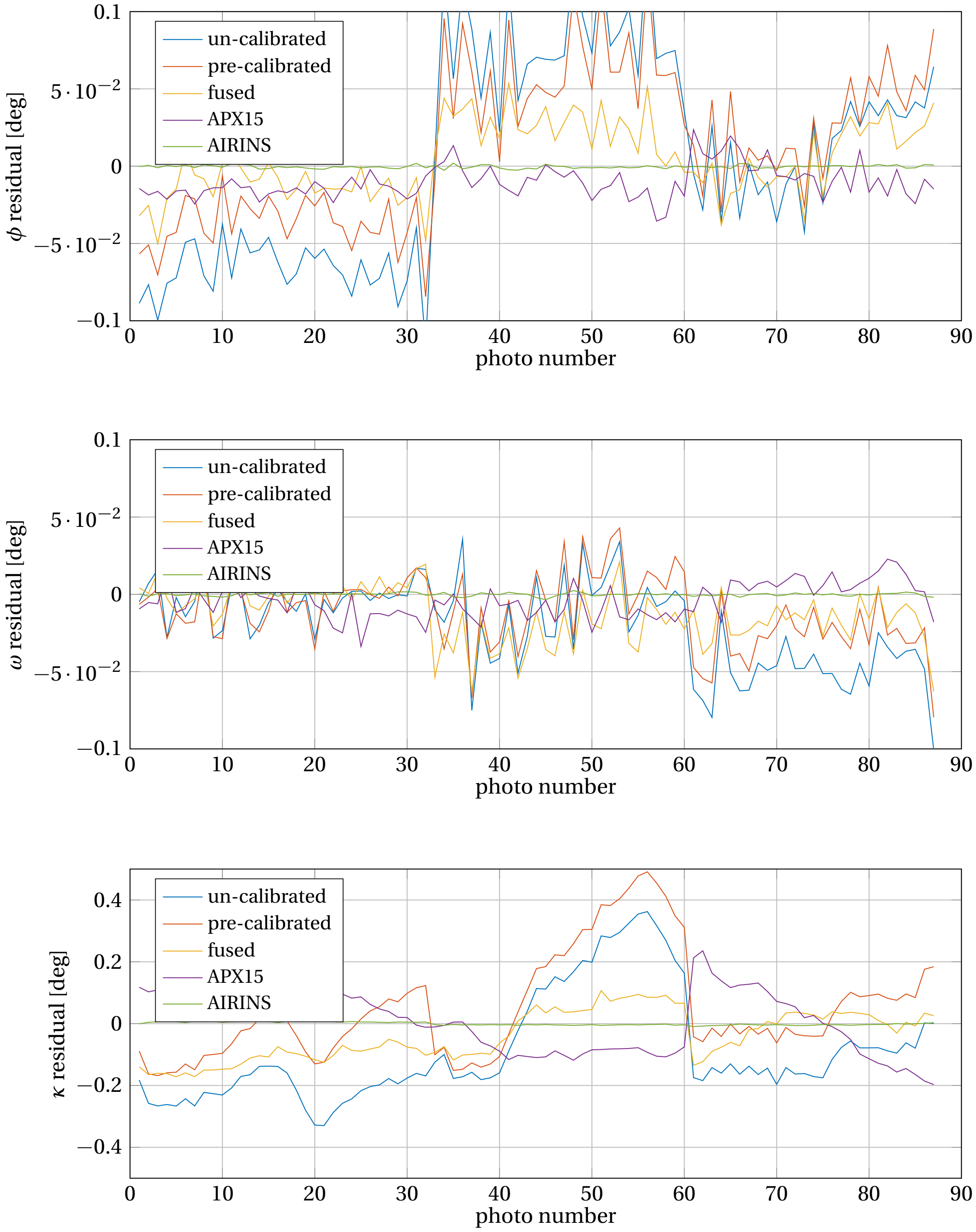

Figure 9.4: Orientation differences between INS/GNSS derived trajectory and that resulting from the photogrammetric adjustment per photo and IMU.

9.2.4 Attitude Quality - Direct Sensor Orientation

The AGL was 250 m during scanning. This is likely either at or above possible employment of laser scanner on micro-UAVs. Figure 9.6 shows an error in the derived surface height (reference produced by AirINS) and three specific MEMS IMU configurations. The first consists of using one IMU without any calibration. The second uses the configuration with a pre-calibrated IMU, whereas the third configuration was computed with the SIMU.

The impact of a well calibrated IMU and especially the SIMU is visible as a clear reduction of the amount of height-differences exceeding 15 cm (i.e., white colored patches). In the same plots, a general shift to a uniform green color can be seen, which makes the surface more close to the reference.

Figure 9.5 depicts a side view of two cross-sections of the same flight line. This shows just a small snippet of the whole dataset but allows to analyze the error on the surface height with relation to the slope of the terrain. Indirectly, this highlights systematic errors (if any) in the pitch. The different colors show the different IMU configurations again. It is clearly visible how the APX15 (cyan colored) is shifted, which is not the case with the data coming from our sensor board.

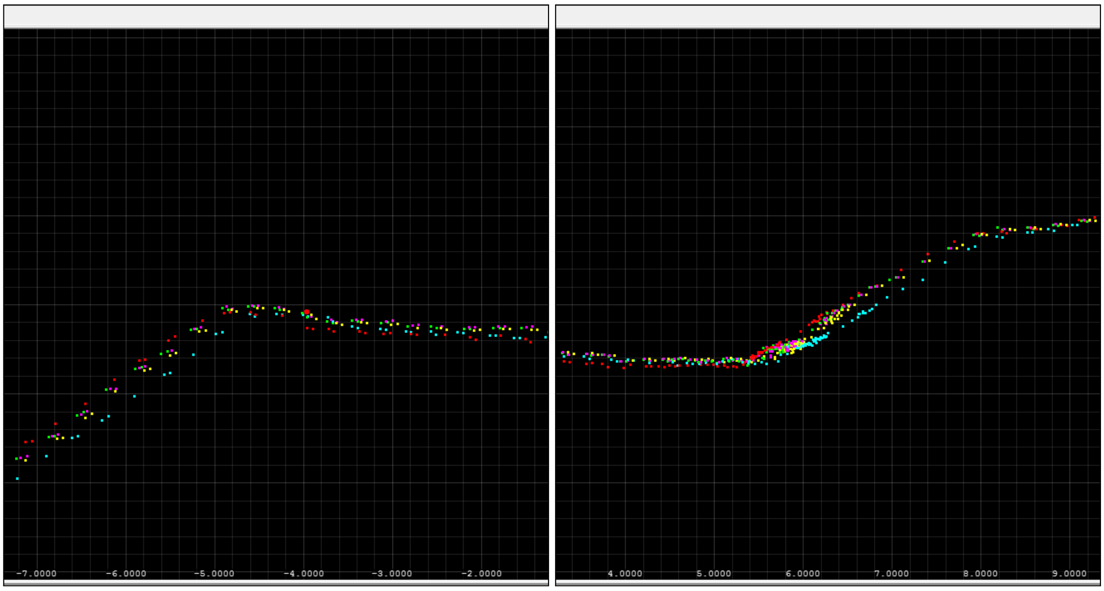

Figure 9.5: Side-view of height profile for two slopes for the different sensor configurations (pink: not-calibrated IMU; yellow: calibrated IMU; green: SIMU; cyan: APX15; red: AirINS).

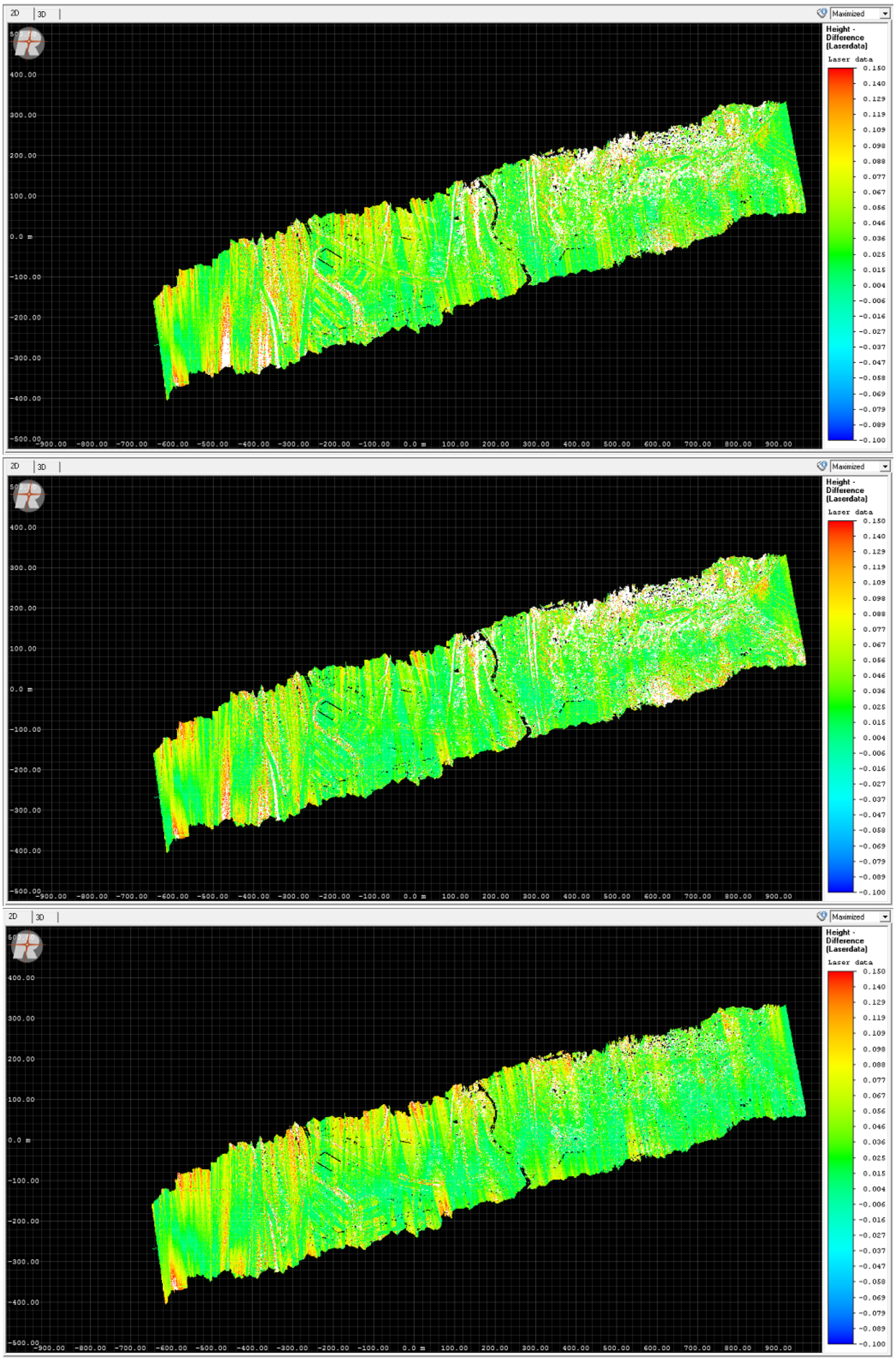
2D
3D
Maximized
Height - Difference (Laserdata)
Laser data
0.150
0.140
0.129
0.119
0.109
0.098
0.088
0.077
0.067
0.056
0.046
0.036
0.025
0.015
0.004
-0.006
-0.016
-0.027
-0.037
-0.047
-0.058
-0.069
-0.079
-0.089
-0.100
400.00
300.00
200.00
100.00
0.0 m
-100.00
-200.00
-300.00
-400.00
-500.00
-900.00
-800.00
-700.00
-600.00
-500.00
-400.00
-300.00
-200.00
-100.00
0.0 m
100.00
200.00
300.00
400.00
500.00
600.00
700.00
800.00
900.00

Figure 9.6: Height differences for the Laser data between the reference and specific sensor configurations. White patches indicate difference in height exceeding 15 cm. Top: IMU without calibration. Middle: pre-calibrated IMU. Bottom: SIMU.

9.3 Micro-UAV

We now study the impact of IMU calibration on the attitude determination on board of a microUAV. In contrary to the helicopter scenario described in the previous section, there will be, however, no navigation-grade INS as a reference. Instead, the fixed-wing UAV will be taking images for during about 40 min, orientation of which is derived by photogrammetry.

9.3.1 Platform

Our fixed-wing UAV with a take-of-weight of about 2.4 kg [Rehak and Skaloud, 2015] is fitted with a custom payload comprising our previously described IMU sensor board with the redundant IMUs and a camera developed by IGN [Martin et al., 2014]. The camera body utilizes a full-frame CMOS with 5120 x 3840 pixels and 6.4um x 6.4um pixel size. The images are panchromatic with 12bit resolution. Attached to the camera body via a Leica M-mount is the Zeiss Biogon f 2.8 / 35 mm lens. The IMU board and camera are connected rigidly by a carbon structure as shown in Figure 9.7 to preserve the relative orientation between both instruments.

While this offset is calibrated in flight (together with camera interior orientation), the spatial offset between the GNSS antenna and the camera-perspective centers are calibrated by tachymetric and photogrammetric means; setup of which is depicted in Figure 9.8. It shows the calibration field with the targets [Rehak and Skaloud, 2015]. The images are triggered by an open-source autopilot (PixHawk) according to the mission plan. The camera signals the time of each exposure via a pulse, the arrival of which is time-stamped by a dual frequency dual constellation GNSS receiver. A second static receiver is employed in the vicinity of the mission to provide a reference for the PPK, cm-level positioning that is used for INS-based filtering/smoothing.

9.3.2 Mission

A rural area north-west of Lausanne of 1 km $\times$ 0.7 km size and 30-40 m elevation changes is utilized as a test field. Several agriculture roads go through this zone and on their surface approximately 20 points of known coordinates are distributed and permanently signalized with 0.3 m $\times$ 0.3 m targets. Part of the zone is flown over at 180 m AGL, while the whole area is covered at 140 m AGL with 75% forward and 60% side overlap. Figure 9.9 shows the test-site with the implemented ground control points along the roads. The exposure time is 1/5000 s, so that the effect of smear on the ground sampling distance of 2.52 cm is negligible at 20 m/s. The IMU data are lab-calibrated for non-orthogonality and constant scale-factors, while the random offsets are calibrated in the field by the procedure described in Section 6.3. In less than one minute after static initialization the plane is thrown in the air where it stays for almost 45 min.

The derived orientation reference for each image is based on the combined adjustment of following observations: GNSS-observed coordinates of ground control points, INS/GNSS camera position/attitude, automatically observed image coordinates of signalized targets and

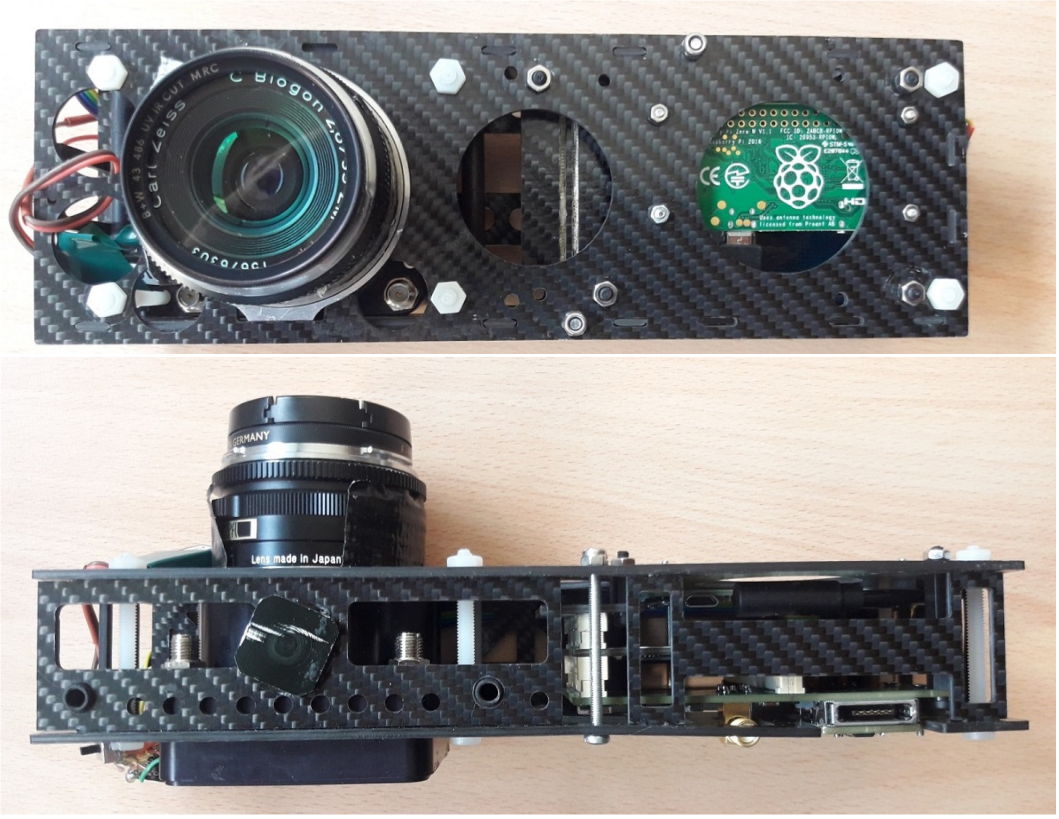

Figure 9.7: Bottom and side view of the IGN camera carbon mount (length of 23 cm) together with the IMU board and the embedded computer.

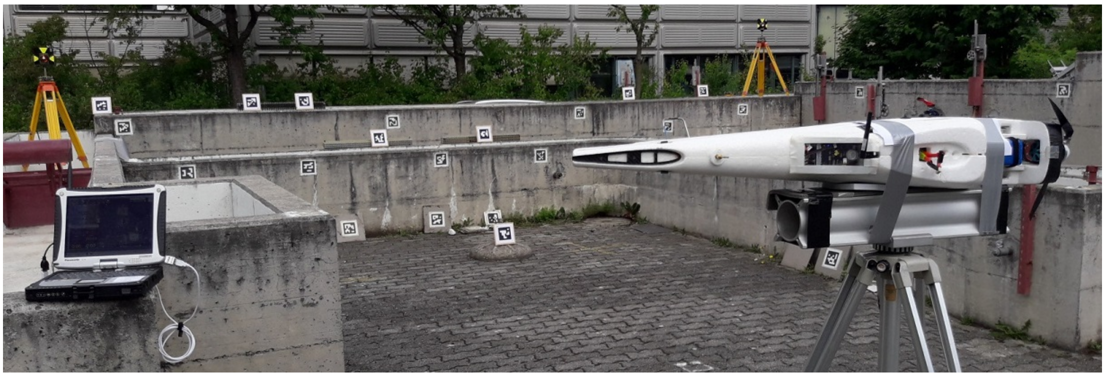

Figure 9.8: Calibration field with the targets and UAV fuselage.

homologous points.

9.3.3 Effect of Initialization

We consider two INS/GNSS trajectories both derived by optimal smoothing with PPK positions and velocities updates at 1 Hz. One utilizes the inertial observation without calibration, and the other applies the parameters of laboratory and pre-flight calibration procedure. Figure 9.10 plots the sequence of differences between the smoother predicted and updated roll values (units 1/60 deg) at 1 Hz. The considerably higher oscillations are apparent for the non-calibrated sensor as the filter/smoother tries to separate the observed discrepancies between INS-predicted and GNSS-observed position and velocities into many elements — error states — related to navigation and sensor biases. This is depicted on the left side of

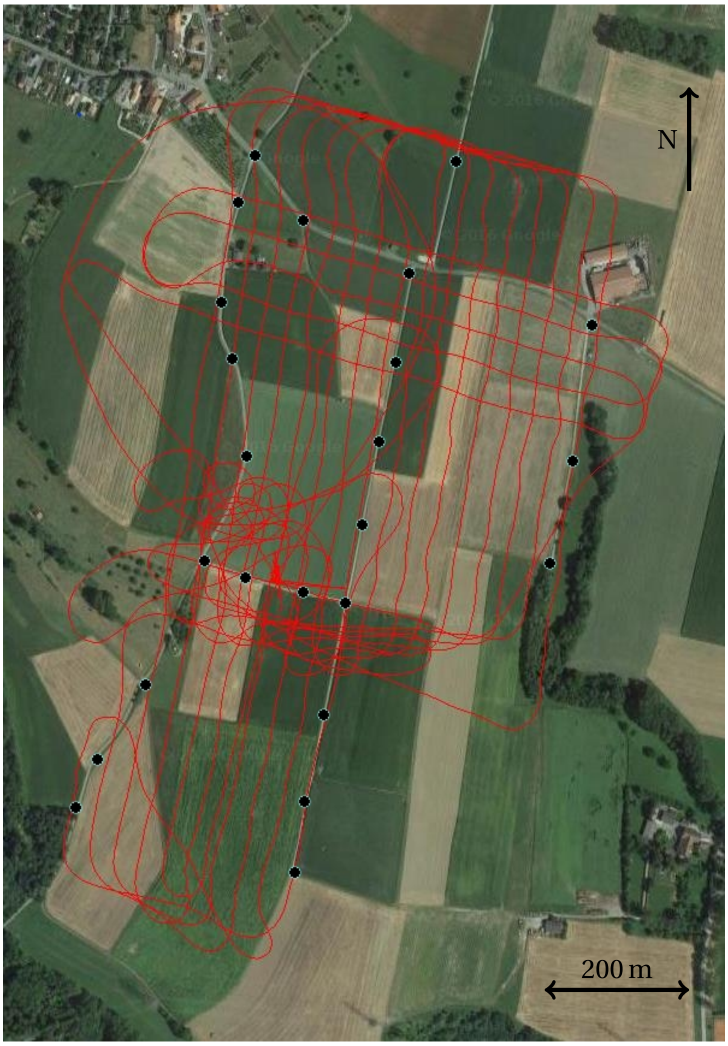

Figure 9.9: Test-site showing the flight path (in red) of the micro UAV with distribution of ground control points (black dots).

Figure 9.10. The oscillations take about 25 min to dampen, a time when many missions of small UAVs are already terminated.

The removal of sensor biases prior to the mission is represented in the filter by setting low variance of their respective states. In a combined consequence (less systematic errors and higher certitude) the oscillation magnitude of roll differences (on right side plot of Figure 9.10) is considerably lower than in the non-calibrated scenario. In other words, the derived attitude is exploitable for sensor orientation within a few minutes after the take-off.

9.3.4 Attitude Performance

Figure 9.11 compares the orientation differences between INS/GNSS derived trajectory to that resulting from the photogrammetric adjustment, again for non-calibrated and mission pre-calibrated IMU data. The differences of the former are considerably higher (> 2x for roll). The variance of the encountered deviations are summarized in Table 9.3.

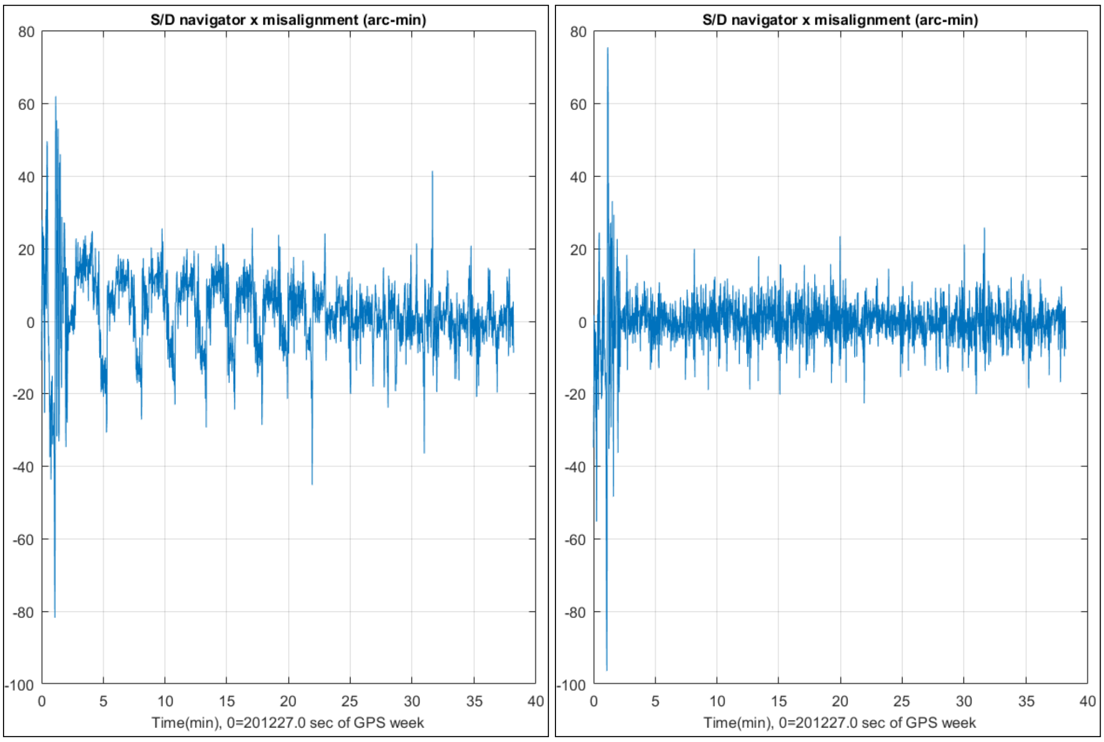

Figure 9.10: Differences between the predicted and updated roll values. Left: non-calibrated IMU exhibiting oscillations 25 min into the flight. Right: in-lab plus pre-mission calibrated IMU exploitable within minutes after take-off.

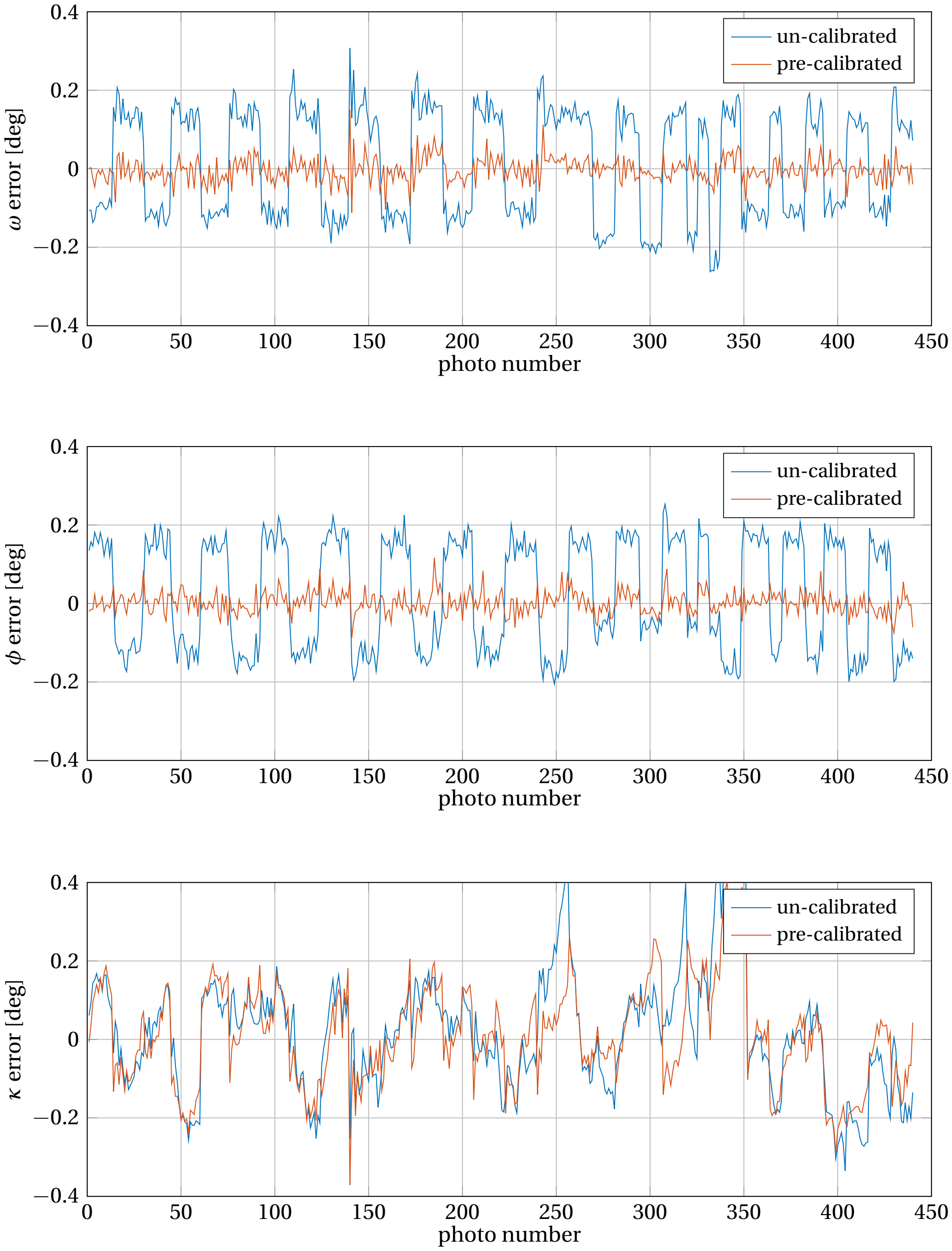

Figure 9.11: Orientation differences between INS/GNSS derived trajectory and that resulting from the photogrammetric adjustment for the IGN camera per photo and IMU.

Table 9.3: Summary of the orientation differences between INS/GNSS derived trajectory and that resulting from the photogrammetric adjustment for the IGN camera.

Sensor	Error	ω [mdeg]	ϕ [mdeg]	κ [mdeg]
IMU uncalibrated	mean	12.0	21.7	18.6
	std	139.8	143.1	154.5
	max	307.8	253.1	510.6
IMU precalibrated	mean	-3.7	2.2	9.7
	std	31.0	27.7	127.3
	max	150.1	116.6	400.0

10 Conclusion

10.1 Impact

This research aimed at developing the methodology to perform calibration of Micro-Electro-Mechanical System (MEMS) sensors used for autonomous navigation and/or sensor orientation both in deterministic as well as stochastic aspects. The main focus was on MEMS Inertial Measurement Unit (IMU), as their error structure is complicated and calibration is necessary. The developed theoretical concepts were presented with examples and their implementation shown in several fully functional software packages, that have practical and user-friendly interfaces. The presented experimental testing on the two platforms (Unmanned Aerial Vehicle (UAV) drone and Airborne Laser Scanning (ALS)) showed the impact of the developed techniques (e.g., un-calibrated, calibrated, fused) both on the quality of the navigation and direct orientation.

10.2 Summary of Contributions

The theoretical and engineering contributions of this research are summarized here.

10.2.1 Theoretical/Conceptual Contributions

Deterministic Error Calibration
A rigorous calibration scheme for deterministic errors is proposed, in which partial calibration from in-lab conditions is utilized alongside the calibration parameters specific to each mission. The procedure is especially adaptable to MEMS sensors mounted on a lightweight platform with short mission duration as it allows to improve the quality attitude initialization.

Stochastic Error Calibration

The parameters of complex stochastic processes as those present in MEMS IMU are best estimated within the Generalized Method of Wavelet Moments (GMWM) framework. However, up to now, these were considered as time invariant. An extension to this framework was presented, in which a covariate such as temperature or motion-dynamics influence the stochastic properties of the error signal. Such influence was presented on practical examples, a contribution to their estimation was formalized, and their impact was also quantified. While the theoretical proofs of the extended estimator were advanced in collaboration with leading statisticians, Samuel Orso from the University of Geneva and Prof. Stéphane Guerrier from the Pennsylvania State University, the implementation and the influence of such calibration on the estimated trajectory was investigated.

10.2.2 Engineering Contributions

Online stochastic calibration platform

A free to use online sensor calibration platform was created, that analyses the stochastic behavior of a given dataset. The basis for its implementation is the open-source "R" program with the updated GMWM framework package that is hosted either locally or on a server. The text-data format is accepted for the upload. The user does not need to learn "R" programming language, but it performs its analysis through the developed intuitive graphical user interface. This comfortable and fast usable platform is available online on a university web-server and can be freely downloaded from github[1]. The implementation allows to analyze several hours of data and to estimate model parameters together with their confidence levels with the combination of commonly used error models such as Quantization Noise (QN), White Noise (WN), Auto-Regressive model of order one (AR1), Random Walk (RW), and Drift (DR).

IMU board

The IMU board with multiple redundant sensors was developed and tested with external equipment such as different GNSS-receivers and barometers. The first protocol allows for accurate time stamping and storing of the data for treatment in post-processing. The second protocol provides real-time streaming of the incoming measurements directly to a computer at a rate of 1 Hz, which allows the user of this board to utilize the data in real-time navigation and for pre-calibration tasks. This software can also 're-play' old datasets, to re-visit the same conditions. Finally, this software allows to directly fuse the IMU data from the four redundant sensors into one Synthetic IMU (SIMU), which is presented in the same manner as a 'fifth' IMU. The sensor fusion is only possible after proper pre-calibration of the deterministic and stochastic properties.

---

[1] https://smac-group.github.io/gui4gmwm/

Sensor calibration software

This software allows calibrating the sensors such as magnetometer, gyroscope, and accelerometer for deterministic errors either in laboratory or in-field prior to missions. The μPC, connected to the IMU board, interprets the commands from the user via the ground control station on which runs a client program with a graphical user interface. This allows for real-time calibration of inertial and magnetic sensors with which the attitude initialization for the navigation is performed.

Embedded integrated navigation

The real-time strapdown inertial navigation/integration originally developed for PC-platforms [Skaloud et al., 2010] was adapted for the developed sensor board and embedded computer. This represented (i) the need for the estimation of adequate stochastic parameters per each IMU of the sensor board, (ii) communication of real-time calibrated values into initialization, (iii) code porting to different OS (Linux) and processor architecture, while supporting either multiple instances (up to 4 per IMU board) and/or the SIMU fusion for the estimation of the trajectory (position, velocity, and attitude) within an extended Kalman filter.

10.3 Main Scientific Publications

Peer-Reviewed

S. Orso, P. Clausen, S. Guerrier and J. Skaloud, "Estimation of Inertial Sensor Stochastic Characteristics under Varying Environmental Conditions," to be submitted in Spring 2019 to IEEE Transactions on Signal Processing.

P. Clausen, J. Skaloud, R. Molinari, J. Lee and S. Guerrier, "Use of a new online calibration platform with applications to inertial sensors," IEEE Aerospace and Electronic Systems Magazine, vol. 33, no. 8, pp. 30-36, August 2018.

P. Clausen, J. Skaloud, S. Orso and S. Guerrier, "Construction of dynamically-dependent stochastic error models," 2018 IEEE/ION Position, Location and Navigation Symposium (PLANS), Monterey, CA, 2018, pp. 1336-1341.

P. Clausen, P. Gilliéron, H. Perakis, V. Gikas and I. Spyropoulou, "Assessment of positioning accuracy of vehicle trajectories for different road applications," IET Intelligent Transport Systems, vol. 11, no. 3, pp. 113-125, 4 2017.

P. Clausen, J. Skaloud, P. Gilliéron, B. Merminod, H. Perakis, V. Gikas and I. Spyropoulou, Ioanna, "Position accuracy with redundant MEMS IMU for road applications," European Journal of Navigation, vol. 13, pp. 4-12, 2015.

Conference
J. Skaloud, P. Clausen, S. Guerrier and S. Orso, "Parameter determination of sensor stochastic models under covariate dependency," Presentation, European Geosciences Union (EGU) Conference, Vienna, Austria, April 2018.

P. Clausen, J. Skaloud, R. Molinari, J. Balamuta and S. Guerrier, "An overview of a new sensor calibration platform," 2017 IEEE International Workshop on Metrology for AeroSpace (MetroAeroSpace), Padua, 2017, pp. 364-368.

P. Clausen, M. Rehak, J. Skaloud, "UAV sensor orientation with pre-calibrated redundant IMU/GNSS observations: preliminary results", 36te Dreiländertagung Photogrammetrie and Fernerkundung der SGPF, DGPF und OVG, Bern, Switzerland, June 7-9, 2016.

Award
Best Demo Award, "A Computationally Efficient Framework for Automated Inertial Sensor Calibration", 4th IEEE International Workshop on Metrology for Aerospace 2017, Padua, Italy.

10.4 Perspective

Several new concepts and questions surfaced during this work, which would make further research and investigations justifiable.

Investigations on stochastic properties with multiple covariates
The influence of one covariate on the stochastic parameters was shown. Possible investigations could go in the direction of using multiple covariates and investigate their impact on error models and estimated quantities within integrated navigation.

Investigations on stochastic properties of fused sensors
Combining several IMUs with different/complementary stochastic properties within a SIMU could be another object of investigations. This would require deriving an adaptive or uneven weighing according to stationary or covariate-dependent error characteristics analyzed by the presented extension of the GMWM framework

Influence of stochastic calibration in an online tool
The developed web interface 'gui4gmwm' for stochastic characterization can estimate model parameters in a simple and user-friendly way, which has broad applications inside and outside the IMU-community. Nevertheless, the impact of employing stochastic models of higher complexity on navigation is not directly quantified inside the application. A simulated trajectory of different form and dynamic could be integrated inside the online version to demonstrate, in a simplified way, the advantages of using the correctly estimated model parameters through the GMWM framework.

Increase of Real-Time Update Frequency

The current system (IMU board with its software) allows for a real-time data transfer of a total of 4 IMUs sampled at 500 Hz at 1 Hz data packets. By increasing this rate to 10 Hz the continuity of the navigation solution can be dramatically improved. This is especially critical if the estimated trajectory is also used for platform control or guidance.

Appendix Part IV

A File Formats

A.1 Accepted GNSS Receiver Messages

The GECKO4NAV-board is connected to a GNSS receiver. The data is transmitted via a serial protocol at a baud rate of 9600 or 38400. The data can either be in a specific binary format or directly encoded as ASCII characters. The first format is used by the JPS-messages (see Subsection A.1.1), whereas the second format is used by the NMEA-messages (see Subsection A.1.2). The GECKO4NAV-board registers whatever is transmitted and is decoded accordingly.

A.1.1 JPS

The JPS-message is a binary standard for messages sent from a GNSS-receiver. All the different definitions and set-up options are discussed in [JAVAD, 2017]. The GECKO4NAV-board can decode the following messages:

- GT: time of week, GPS week number;
- PV: cartesian coordinates: x, y, z and velocities vx, vy, vz with corresponding position and velocity Spherical Error Probable (SEP), solution type;
- PG: geodetic coordinates: latitude, longitude, and ellipsoidal height with position SEP, solution type;
- VG: geodetic velocities: northing, easting, and height velocities with corresponding velocity SEP, solution type;
- DP: dilution of precision for east, horizontal, vertical, and time with solution type;
- PS: position statistics with the number of GPS satellites used in positioning.

A.1.2 NMEA

The NMEA-messages are ASCII-characters sent from a GNSS-receiver. All the different definitions and set-up options are discussed in [JAVAD, 2017]. The GECKO4NAV-board can decode the following messages:

- GPZDA: time expressed in UTC and date;
- GPGGA: time expressed in UTC, geodetic coordinates (latitude, longitude, and altitude above mean sea level), height of geoid above WGS84 ellipsoid, numbers of satellites tracked, horizontal dilution of precision, quality of fix;
- GPRMC: time expressed in UTC, geodetic coordinates (latitude, longitude), speed over ground, course with relation to geographic north;
- MCEXT: time expressed in UTC, up to 9 float-values separated by commas, special lab-intern NMEA-message-string.

B Geckoboard

B.1 Upload Specific Firmware

Once the firmware is loaded, it stays in the memory and is called automatically upon powering the system. There are different firmware available. Their difference lies in the acquisition frequency (100 Hz, 200 Hz, 250 Hz, 333 Hz, 500 Hz and 1000 Hz). They all require either 9600 bauds or 38400 bauds to communicate with the GNSS receiver via the serial connector and the 1 Hz PPS-signal either through the TTL or the RS232 protocol. The following lines give an example of how to upload the firmware to the GECKO4NAV-board through a Linux computer with the `usbtmc`-protocol:

1. connect the system to a computer running Linux
2. some LEDs will blink, don't bother
3. in terminal: 'sudo -s'
4. move to the repository where the firmware is stored
5. in terminal: 'echo "erase" > /dev/usbtmc0'
6. most right LED lights up for a few seconds
7. most right LED turns off
8. some LEDs will blink, don't bother
9. in terminal: 'cat firmware_autostart_250Hz_javad_9600baud.do > /dev/usbtmc0'
10. most right LED lights up for a few seconds
11. most right LED turns off

12. some LEDs will blink, don’t bother
13. done
14. power off the system

B.2 Download / Stream Data

This section explains how to transfer the data from the GECKO4NAV-board internal flash at the end of a mission to the computer running on a Linux system with the `usbtmc`-protocol. To be able to read out the measurement data with this method you first have to open a terminal. In the terminal you perform the command sequence listed below:

1. in terminal: ’sudo -s’
2. go to the repository where you want to save the data
3. in terminal: ’echo "fifo?" > /dev/usbtmc0’
4. most left LED on the GECKO4NAV-board blinks red
5. in terminal: ’cat /dev/usbtmc0 > measurements.dat’
6. wait until most left LED is static green (may take some time)
7. in terminal: ’chmod 777 measurements.dat’

After this sequence the file `measurements.dat` will contain the complete measurement data stream that can be converted by another program.

As explained in the previous chapter, after having transferred the data, the content of the flash is erased. This can take some time, and the power source shall not be unplugged until deleting is completed!

The same procedure can be executed in real-time during the acquisition. The difference here is that instead of the whole dataset, only one single packet with the data acquired during 1 s is transmitted to the host computer. The data is still kept in the flash memory of the GECKO4NAV-board board and is not erased.

C Datasheets

This chapter assembles the specifications and datasheets of the sensors used in this document.

C.1 IMAR: iIMU-FSAS

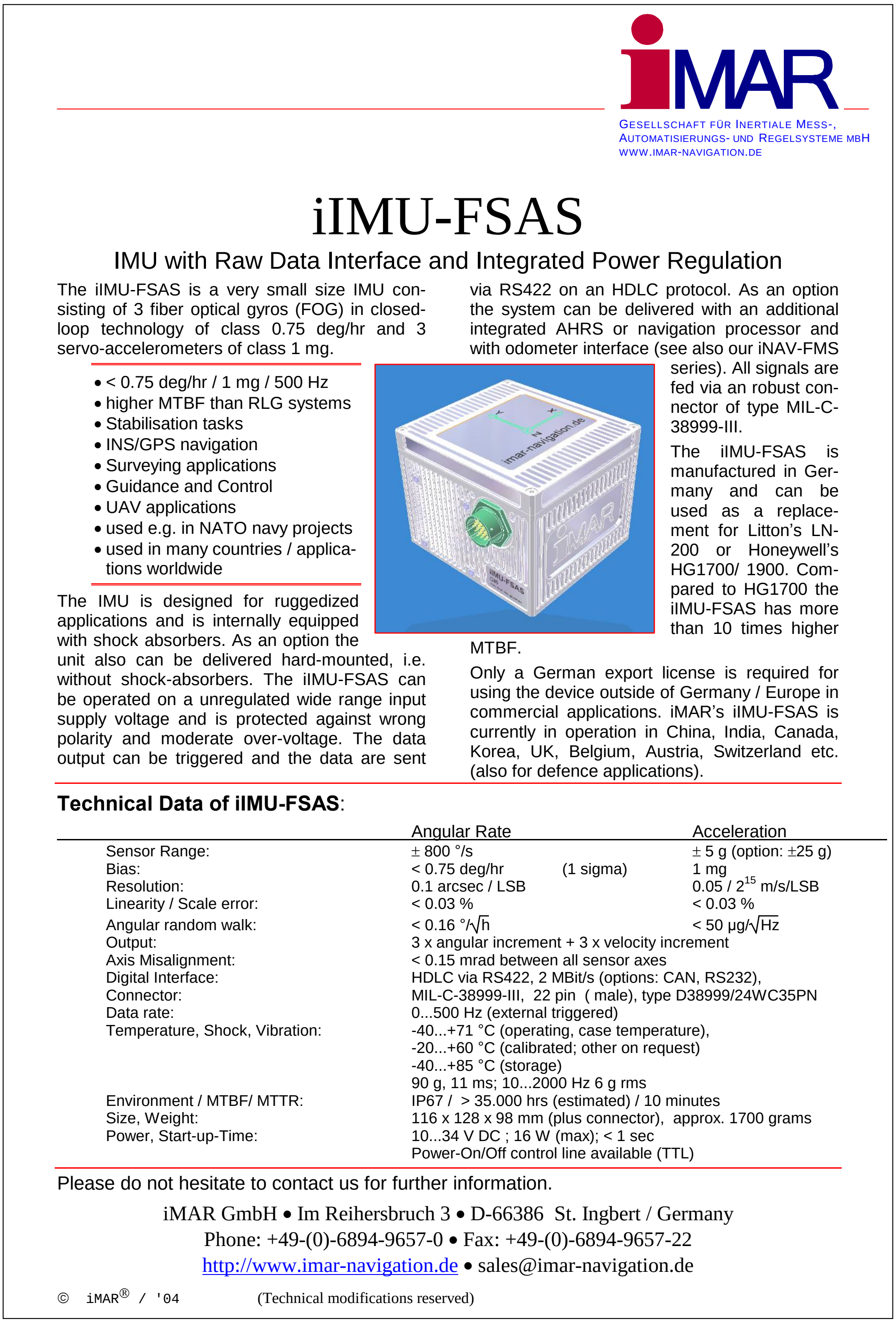

Gesellschaft für Inertiale Mess-,
Automatisierungs- und Regelsysteme mbH
www.imar-navigation.de

iIMU-FSAS

IMU with Raw Data Interface and Integrated Power Regulation

The iIMU-FSAS is a very small size IMU consisting of 3 fiber optical gyros (FOG) in closed-loop technology of class 0.75 deg/hr and 3 servo-accelerometers of class 1 mg.

- < 0.75 deg/hr / 1 mg / 500 Hz
- higher MTBF than RLG systems
- Stabilisation tasks
- INS/GPS navigation
- Surveying applications
- Guidance and Control
- UAV applications
- used e.g. in NATO navy projects
- used in many countries / applications worldwide

The IMU is designed for ruggedized applications and is internally equipped with shock absorbers. As an option the unit also can be delivered hard-mounted, i.e. without shock-absorbers. The iIMU-FSAS can be operated on a unregulated wide range input supply voltage and is protected against wrong polarity and moderate over-voltage. The data output can be triggered and the data are sent via RS422 on an HDLC protocol. As an option the system can be delivered with an additional integrated AHRS or navigation processor and with odometer interface (see also our iNAV-FMS series). All signals are fed via an robust connector of type MIL-C-38999-III.

The iIMU-FSAS is manufactured in Germany and can be used as a replacement for Litton's LN-200 or Honeywell's HG1700/ 1900. Compared to HG1700 the iIMU-FSAS has more than 10 times higher MTBF.

Only a German export license is required for using the device outside of Germany / Europe in commercial applications. iMAR's iIMU-FSAS is currently in operation in China, India, Canada, Korea, UK, Belgium, Austria, Switzerland etc. (also for defence applications).

Technical Data of iIMU-FSAS:

	Angular Rate		Acceleration
Sensor Range:	± 800 °/s		± 5 g (option: ±25 g)
Bias:	< 0.75 deg/hr	(1 sigma)	1 mg
Resolution:	0.1 arcsec / LSB		0.05 / 2^{15} m/s/LSB
Linearity / Scale error:	< 0.03 %		< 0.03 %
Angular random walk:	$< 0.16\ ^\circ/\sqrt{h}$		$< 50\ \mu g/\sqrt{Hz}$
Output:	3 x angular increment + 3 x velocity increment		
Axis Misalignment:	< 0.15 mrad between all sensor axes		
Digital Interface:	HDLC via RS422, 2 MBit/s (options: CAN, RS232),		
Connector:	MIL-C-38999-III, 22 pin (male), type D38999/24WC35PN		
Data rate:	0...500 Hz (external triggered)		
Temperature, Shock, Vibration:	-40...+71 °C (operating, case temperature), -20...+60 °C (calibrated; other on request) -40...+85 °C (storage) 90 g, 11 ms; 10...2000 Hz 6 g rms		
Environment / MTBF/ MTTR:	IP67 / > 35.000 hrs (estimated) / 10 minutes		
Size, Weight:	116 x 128 x 98 mm (plus connector), approx. 1700 grams		
Power, Start-up-Time:	10...34 V DC ; 16 W (max); < 1 sec Power-On/Off control line available (TTL)		

Please do not hesitate to contact us for further information.

iMAR GmbH • Im Reihersbruch 3 • D-66386 St. Ingbert / Germany
Phone: +49-(0)-6894-9657-0 • Fax: +49-(0)-6894-9657-22
http://www.imar-navigation.de • sales@imar-navigation.de

© iMAR® / '04 (Technical modifications reserved)

C.2 Northrop Grumman: LN200

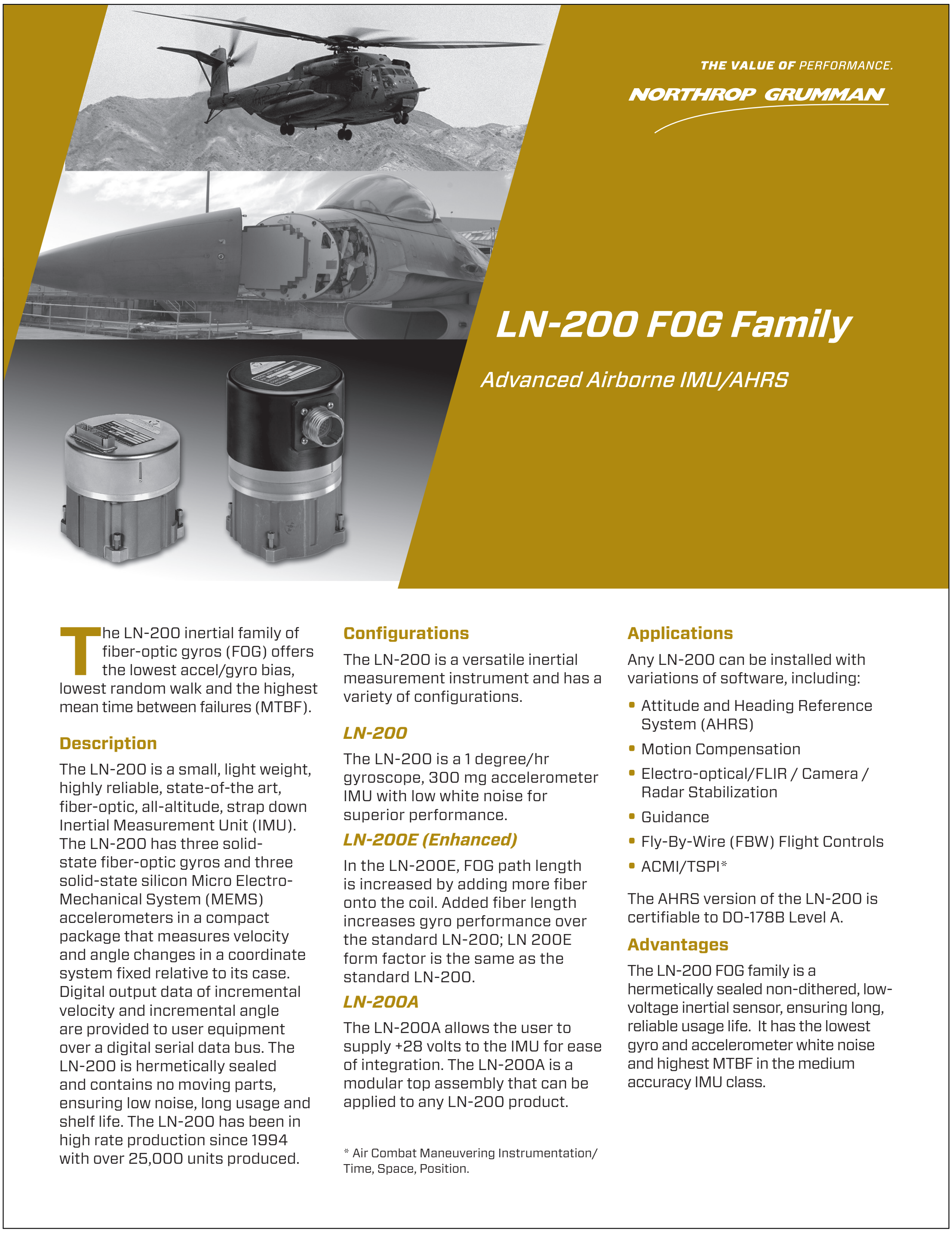

THE VALUE OF PERFORMANCE.

NORTHROP GRUMMAN

LN-200 FOG Family

Advanced Airborne IMU/AHRS

The LN-200 inertial family of fiber-optic gyros (FOG) offers the lowest accel/gyro bias, lowest random walk and the highest mean time between failures (MTBF).

Description

The LN-200 is a small, light weight, highly reliable, state-of-the-art, fiber-optic, all-altitude, strap down Inertial Measurement Unit (IMU). The LN-200 has three solid-state fiber-optic gyros and three solid-state silicon Micro Electro-Mechanical System (MEMS) accelerometers in a compact package that measures velocity and angle changes in a coordinate system fixed relative to its case. Digital output data of incremental velocity and incremental angle are provided to user equipment over a digital serial data bus. The LN-200 is hermetically sealed and contains no moving parts, ensuring low noise, long usage and shelf life. The LN-200 has been in high rate production since 1994 with over 25,000 units produced.

Configurations

The LN-200 is a versatile inertial measurement instrument and has a variety of configurations.

LN-200

The LN-200 is a 1 degree/hr gyroscope, 300 mg accelerometer IMU with low white noise for superior performance.

LN-200E (Enhanced)

In the LN-200E, FOG path length is increased by adding more fiber onto the coil. Added fiber length increases gyro performance over the standard LN-200; LN 200E form factor is the same as the standard LN-200.

LN-200A

The LN-200A allows the user to supply +28 volts to the IMU for ease of integration. The LN-200A is a modular top assembly that can be applied to any LN-200 product.

Applications

Any LN-200 can be installed with variations of software, including:

- Attitude and Heading Reference System (AHRS)
- Motion Compensation
- Electro-optical/FLIR / Camera / Radar Stabilization
- Guidance
- Fly-By-Wire (FBW) Flight Controls
- ACMI/TSPI[*]

The AHRS version of the LN-200 is certifiable to DO-178B Level A.

Advantages

The LN-200 FOG family is a hermetically sealed non-dithered, low-voltage inertial sensor, ensuring long, reliable usage life. It has the lowest gyro and accelerometer white noise and highest MTBF in the medium accuracy IMU class.

---

[*] Air Combat Maneuvering Instrumentation/Time, Space, Position.

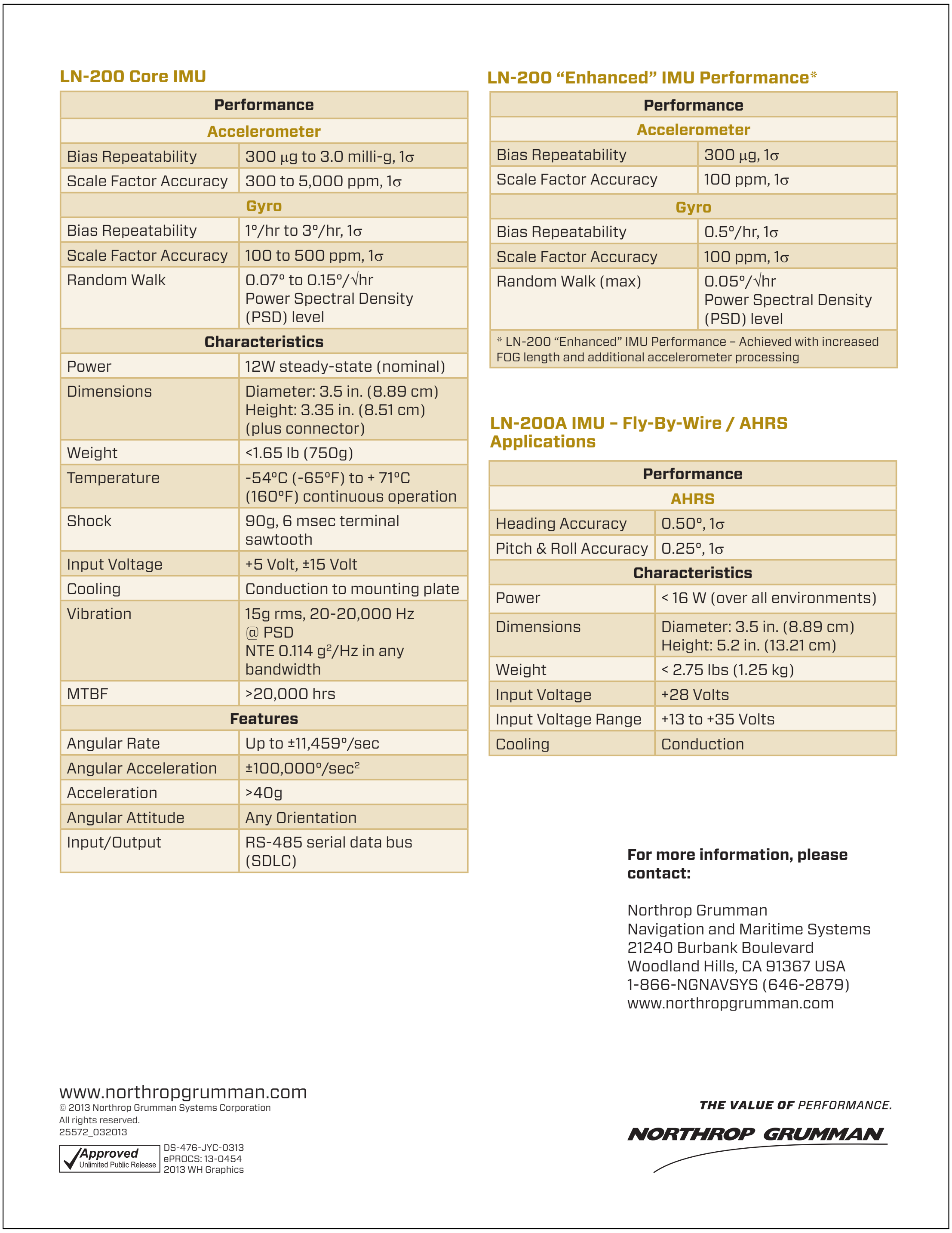

LN-200 Core IMU

Performance	
Accelerometer	
Bias Repeatability	300 µg to 3.0 milli-g, 1σ
Scale Factor Accuracy	300 to 5,000 ppm, 1σ
Gyro	
Bias Repeatability	1°/hr to 3°/hr, 1σ
Scale Factor Accuracy	100 to 500 ppm, 1σ
Random Walk	0.07° to 0.15°/√hr Power Spectral Density (PSD) level
Characteristics	
Power	12W steady-state (nominal)
Dimensions	Diameter: 3.5 in. (8.89 cm) Height: 3.35 in. (8.51 cm) (plus connector)
Weight	<1.65 lb (750g)
Temperature	-54°C (-65°F) to + 71°C (160°F) continuous operation
Shock	90g, 6 msec terminal sawtooth
Input Voltage	+5 Volt, ±15 Volt
Cooling	Conduction to mounting plate
Vibration	15g rms, 20-20,000 Hz @ PSD NTE 0.114 g^2/Hz in any bandwidth
MTBF	>20,000 hrs
Features	
Angular Rate	Up to ±11,459°/sec
Angular Acceleration	±100,000°/sec^2
Acceleration	>40g
Angular Attitude	Any Orientation
Input/Output	RS-485 serial data bus (SDLC)

LN-200 "Enhanced" IMU Performance*

Performance	
Accelerometer	
Bias Repeatability	300 µg, 1σ
Scale Factor Accuracy	100 ppm, 1σ
Gyro	
Bias Repeatability	0.5°/hr, 1σ
Scale Factor Accuracy	100 ppm, 1σ
Random Walk (max)	0.05°/√hr Power Spectral Density (PSD) level

* LN-200 "Enhanced" IMU Performance – Achieved with increased FOG length and additional accelerometer processing

LN-200A IMU – Fly-By-Wire / AHRS Applications

Performance	
AHRS	
Heading Accuracy	0.50°, 1σ
Pitch & Roll Accuracy	0.25°, 1σ
Characteristics	
Power	< 16 W (over all environments)
Dimensions	Diameter: 3.5 in. (8.89 cm) Height: 5.2 in. (13.21 cm)
Weight	< 2.75 lbs (1.25 kg)
Input Voltage	+28 Volts
Input Voltage Range	+13 to +35 Volts
Cooling	Conduction

For more information, please contact:

Northrop Grumman
Navigation and Maritime Systems
21240 Burbank Boulevard
Woodland Hills, CA 91367 USA
1-866-NGNAVSYS (646-2879)
www.northropgrumman.com

www.northropgrumman.com

© 2013 Northrop Grumman Systems Corporation
All rights reserved.
25572_032013

Approved
Unlimited Public Release

DS-476-JYC-0313
ePROCS: 13-0454
2013 WH Graphics

THE VALUE OF PERFORMANCE.

NORTHROP GRUMMAN

C.3 Intersense: Navchip

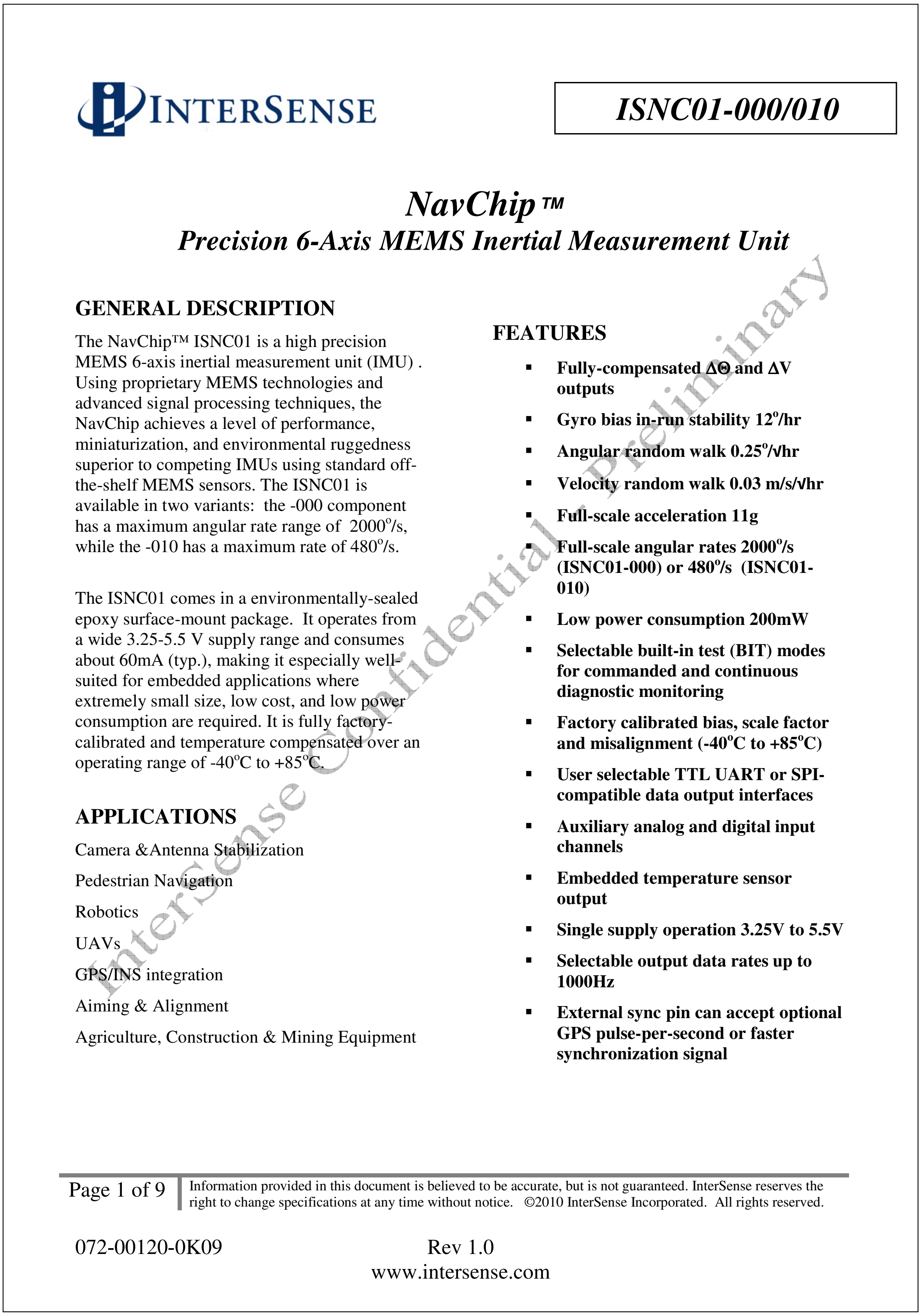

INTERSENSE

ISNC01-000/010

NavChip™

Precision 6-Axis MEMS Inertial Measurement Unit

GENERAL DESCRIPTION

The NavChip™ ISNC01 is a high precision MEMS 6-axis inertial measurement unit (IMU) . Using proprietary MEMS technologies and advanced signal processing techniques, the NavChip achieves a level of performance, miniaturization, and environmental ruggedness superior to competing IMUs using standard off-the-shelf MEMS sensors. The ISNC01 is available in two variants: the -000 component has a maximum angular rate range of 2000°/s, while the -010 has a maximum rate of 480°/s.

The ISNC01 comes in a environmentally-sealed epoxy surface-mount package. It operates from a wide 3.25-5.5 V supply range and consumes about 60mA (typ.), making it especially well-suited for embedded applications where extremely small size, low cost, and low power consumption are required. It is fully factory-calibrated and temperature compensated over an operating range of -40°C to +85°C.

APPLICATIONS

Camera &Antenna Stabilization

Pedestrian Navigation

Robotics

UAVs

GPS/INS integration

Aiming & Alignment

Agriculture, Construction & Mining Equipment

FEATURES

- **Fully-compensated $\Delta\Theta$ and ΔV outputs**
- **Gyro bias in-run stability 12°/hr**
- **Angular random walk 0.25°/√hr**
- **Velocity random walk 0.03 m/s/√hr**
- **Full-scale acceleration 11g**
- **Full-scale angular rates 2000°/s (ISNC01-000) or 480°/s (ISNC01-010)**
- **Low power consumption 200mW**
- **Selectable built-in test (BIT) modes for commanded and continuous diagnostic monitoring**
- **Factory calibrated bias, scale factor and misalignment (-40°C to +85°C)**
- **User selectable TTL UART or SPI-compatible data output interfaces**
- **Auxiliary analog and digital input channels**
- **Embedded temperature sensor output**
- **Single supply operation 3.25V to 5.5V**
- **Selectable output data rates up to 1000Hz**
- **External sync pin can accept optional GPS pulse-per-second or faster synchronization signal**

InterSense Confidential - Preliminary

Page 1 of 9

Information provided in this document is believed to be accurate, but is not guaranteed. InterSense reserves the right to change specifications at any time without notice. ©2010 InterSense Incorporated. All rights reserved.

072-00120-0K09 Rev 1.0
www.intersense.com

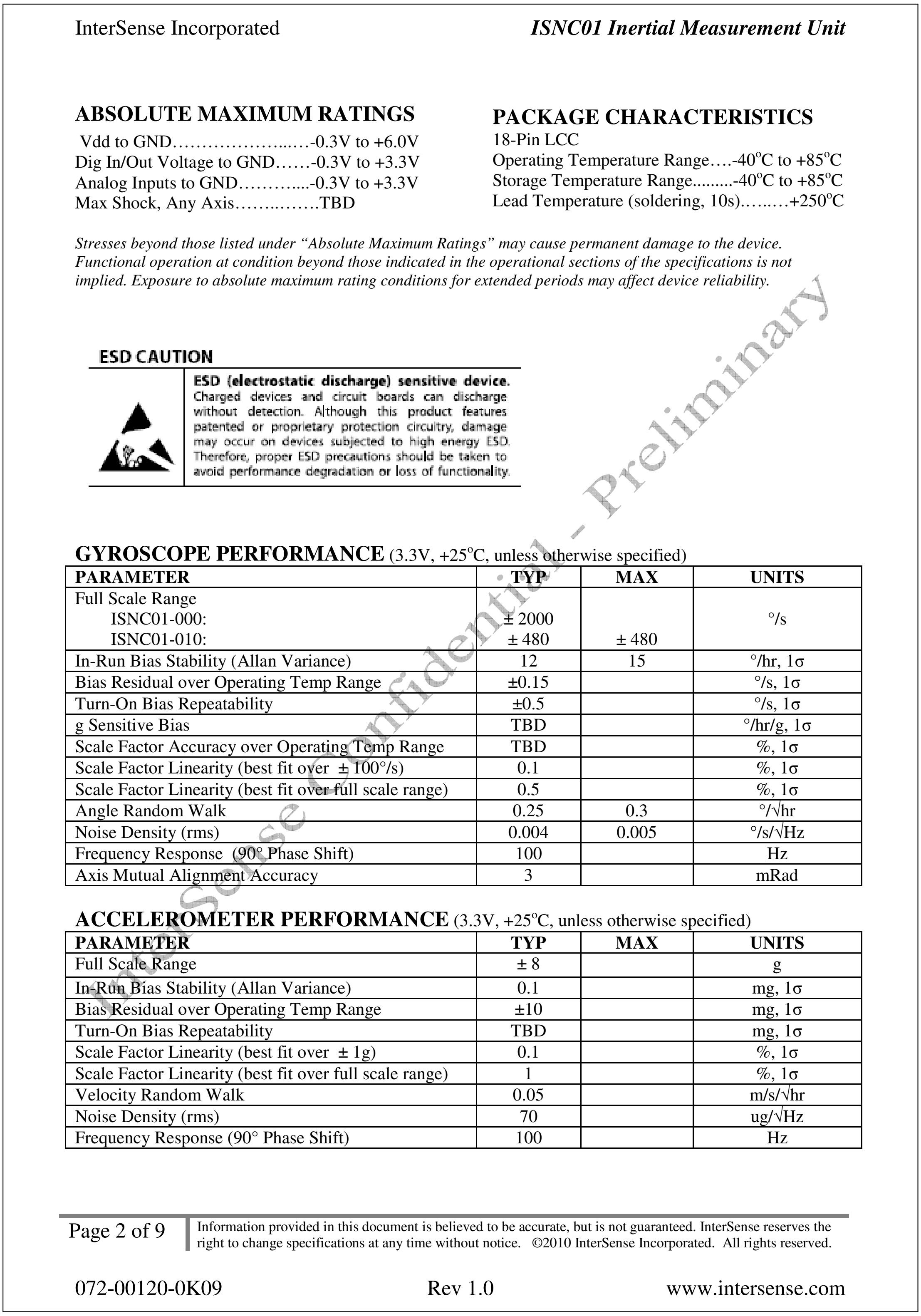

ABSOLUTE MAXIMUM RATINGS

Vdd to GND…………………..….-0.3V to +6.0V
Dig In/Out Voltage to GND……-0.3V to +3.3V
Analog Inputs to GND………....-0.3V to +3.3V
Max Shock, Any Axis……..…….TBD

PACKAGE CHARACTERISTICS

18-Pin LCC
Operating Temperature Range….-40°C to +85°C
Storage Temperature Range.........-40°C to +85°C
Lead Temperature (soldering, 10s)…..…+250°C

Stresses beyond those listed under "Absolute Maximum Ratings" may cause permanent damage to the device. Functional operation at condition beyond those indicated in the operational sections of the specifications is not implied. Exposure to absolute maximum rating conditions for extended periods may affect device reliability.

ESD CAUTION

ESD (electrostatic discharge) sensitive device. Charged devices and circuit boards can discharge without detection. Although this product features patented or proprietary protection circuitry, damage may occur on devices subjected to high energy ESD. Therefore, proper ESD precautions should be taken to avoid performance degradation or loss of functionality.

GYROSCOPE PERFORMANCE (3.3V, +25°C, unless otherwise specified)

PARAMETER	TYP	MAX	UNITS
Full Scale Range ISNC01-000: ISNC01-010:	 ± 2000 ± 480	 ± 480	°/s
In-Run Bias Stability (Allan Variance)	12	15	°/hr, 1σ
Bias Residual over Operating Temp Range	±0.15		°/s, 1σ
Turn-On Bias Repeatability	±0.5		°/s, 1σ
g Sensitive Bias	TBD		°/hr/g, 1σ
Scale Factor Accuracy over Operating Temp Range	TBD		%, 1σ
Scale Factor Linearity (best fit over ± 100°/s)	0.1		%, 1σ
Scale Factor Linearity (best fit over full scale range)	0.5		%, 1σ
Angle Random Walk	0.25	0.3	°/√hr
Noise Density (rms)	0.004	0.005	°/s/√Hz
Frequency Response (90° Phase Shift)	100		Hz
Axis Mutual Alignment Accuracy	3		mRad

ACCELEROMETER PERFORMANCE (3.3V, +25°C, unless otherwise specified)

PARAMETER	TYP	MAX	UNITS
Full Scale Range	± 8		g
In-Run Bias Stability (Allan Variance)	0.1		mg, 1σ
Bias Residual over Operating Temp Range	±10		mg, 1σ
Turn-On Bias Repeatability	TBD		mg, 1σ
Scale Factor Linearity (best fit over ± 1g)	0.1		%, 1σ
Scale Factor Linearity (best fit over full scale range)	1		%, 1σ
Velocity Random Walk	0.05		m/s/√hr
Noise Density (rms)	70		ug/√Hz
Frequency Response (90° Phase Shift)	100		Hz

InterSense Confidential - Preliminary

Information provided in this document is believed to be accurate, but is not guaranteed. InterSense reserves the right to change specifications at any time without notice. ©2010 InterSense Incorporated. All rights reserved.

C.4 XSENS: MTi-G

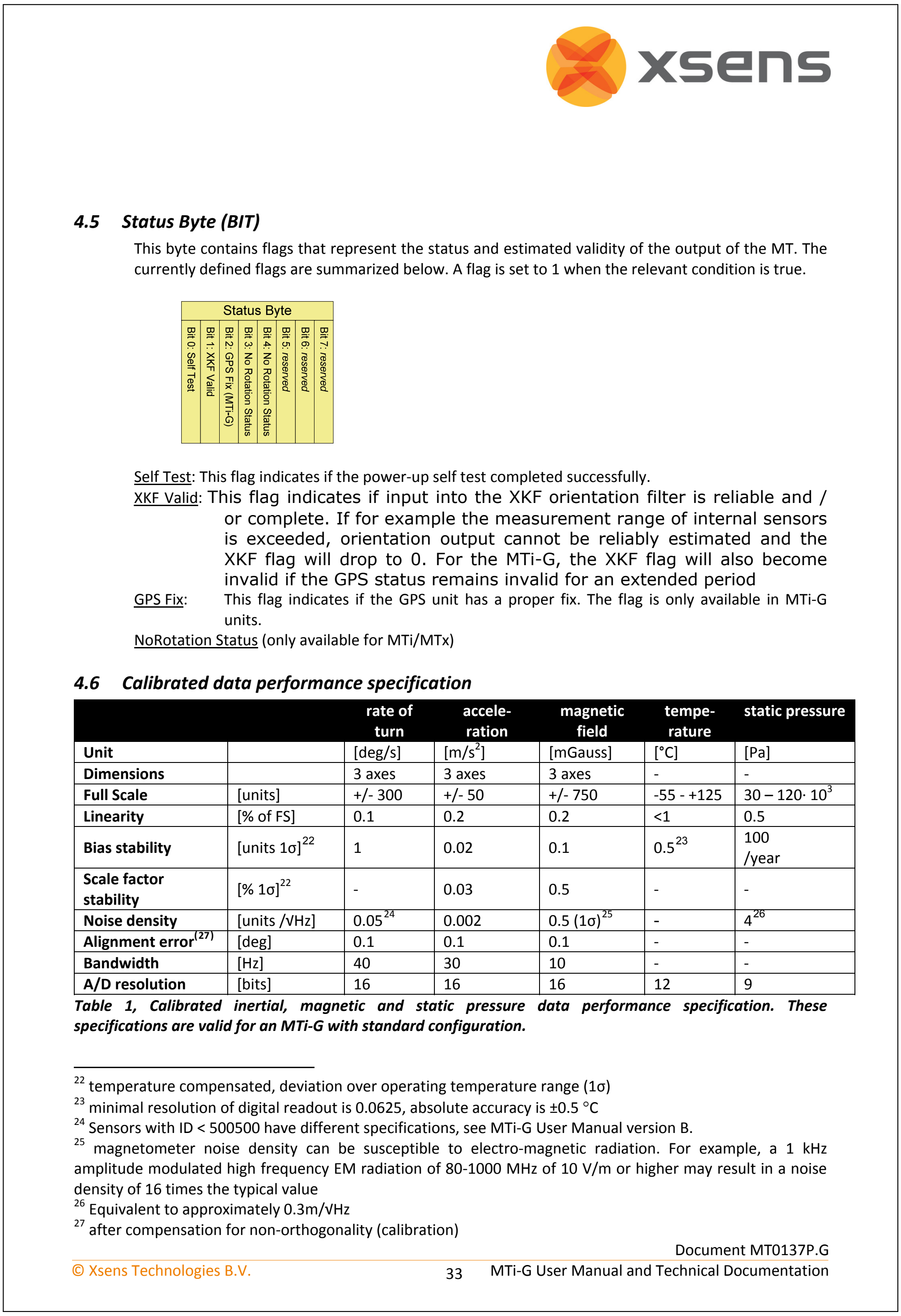

4.5 *Status Byte (BIT)*

This byte contains flags that represent the status and estimated validity of the output of the MT. The currently defined flags are summarized below. A flag is set to 1 when the relevant condition is true.

Status Byte							
Bit 0: Self Test	Bit 1: XKF Valid	Bit 2: GPS Fix (MTi-G)	Bit 3: No Rotation Status	Bit 4: No Rotation Status	Bit 5: *reserved*	Bit 6: *reserved*	Bit 7: *reserved*

Self Test: This flag indicates if the power-up self test completed successfully.

XKF Valid: This flag indicates if input into the XKF orientation filter is reliable and / or complete. If for example the measurement range of internal sensors is exceeded, orientation output cannot be reliably estimated and the XKF flag will drop to 0. For the MTi-G, the XKF flag will also become invalid if the GPS status remains invalid for an extended period

GPS Fix: This flag indicates if the GPS unit has a proper fix. The flag is only available in MTi-G units.

NoRotation Status (only available for MTi/MTx)

4.6 *Calibrated data performance specification*

		rate of turn	acceleration	magnetic field	temperature	static pressure
Unit		[deg/s]	[m/s^2]	[mGauss]	[°C]	[Pa]
Dimensions		3 axes	3 axes	3 axes	-	-
Full Scale	[units]	+/- 300	+/- 50	+/- 750	-55 - +125	30 – 120· 10^3
Linearity	[% of FS]	0.1	0.2	0.2	<1	0.5
Bias stability	[units 1σ][22]	1	0.02	0.1	0.5[23]	100 /year
Scale factor stability	[% 1σ][22]	-	0.03	0.5	-	-
Noise density	[units /√Hz]	0.05[24]	0.002	0.5 (1σ)[25]	-	4[26]
Alignment error(27)	[deg]	0.1	0.1	0.1	-	-
Bandwidth	[Hz]	40	30	10	-	-
A/D resolution	[bits]	16	16	16	12	9

Table 1, Calibrated inertial, magnetic and static pressure data performance specification. These specifications are valid for an MTi-G with standard configuration.

---

[22] temperature compensated, deviation over operating temperature range (1σ)

[23] minimal resolution of digital readout is 0.0625, absolute accuracy is ±0.5 °C

[24] Sensors with ID < 500500 have different specifications, see MTi-G User Manual version B.

[25] magnetometer noise density can be susceptible to electro-magnetic radiation. For example, a 1 kHz amplitude modulated high frequency EM radiation of 80-1000 MHz of 10 V/m or higher may result in a noise density of 16 times the typical value

[26] Equivalent to approximately 0.3m/√Hz

[27] after compensation for non-orthogonality (calibration)

C.5 TE Connectivity Measurement Specialties: MS5611-01BA03

MS5611-01BA03 Barometric Pressure Sensor, with stainless steel cap

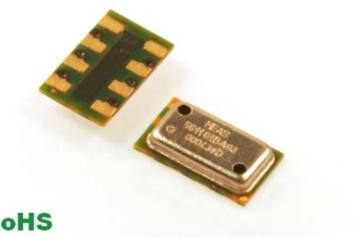

- **High resolution module, 10 cm**
- **Fast conversion down to 1 ms**
- **Low power, 1 µA (standby < 0.15 µA)**
- **QFN package 5.0 x 3.0 x 1.0 mm^3**
- **Supply voltage 1.8 to 3.6 V**
- **Integrated digital pressure sensor (24 bit ΔΣ ADC)**
- **Operating range: 10 to 1200 mbar, -40 to +85 °C**
- **I^{2}C and SPI interface up to 20 MHz**
- **No external components (Internal oscillator)**
- **Excellent long term stability**

DESCRIPTION

The MS5611-01BA is a new generation of high resolution altimeter sensors from MEAS Switzerland with SPI and I^{2}C bus interface. This barometric pressure sensor is optimized for altimeters and variometers with an altitude resolution of 10 cm. The sensor module includes a high linearity pressure sensor and an ultra low power 24 bit ΔΣ ADC with internal factory calibrated coefficients. It provides a precise digital 24 Bit pressure and temperature value and different operation modes that allow the user to optimize for conversion speed and current consumption. A high resolution temperature output allows the implementation of an altimeter/thermometer function without any additional sensor. The MS5611-01BA can be interfaced to virtually any microcontroller. The communication protocol is simple, without the need of programming internal registers in the device. Small dimensions of only 5.0 mm x 3.0 mm and a height of only 1.0 mm allow for integration in mobile devices. This new sensor module generation is based on leading MEMS technology and latest benefits from MEAS Switzerland proven experience and know-how in high volume manufacturing of altimeter modules, which have been widely used for over a decade. The sensing principle employed leads to very low hysteresis and high stability of both pressure and temperature signal.

FEATURES

FIELD OF APPLICATION

- Mobile altimeter / barometer systems
- Bike computers
- Variometers
- Height sensing for medical alarms
- Indoor navigation

FUNCTIONAL BLOCK DIAGRAM

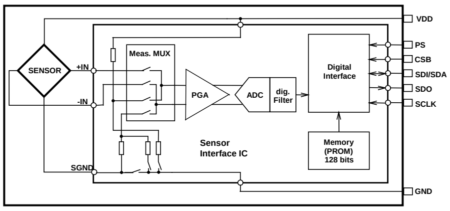

TECHNICAL DATA

Sensor Performances (V_{DD} = 3 V)				
Pressure	**Min**	**Typ**	**Max**	**Unit**
Range	10		1200	mbar
ADC		24		bit
Resolution (1)		0.065 / 0.042 / 0.027 / 0.018 / 0.012		mbar
Accuracy 25°C, 750 mbar	-1.5		+1.5	mbar
Error band, -20°C to +85°C 450 to 1100 mbar (2)	-2.5		+2.5	mbar
Response time (1)		0.5 / 1.1 / 2.1 / 4.1 / 8.22		ms
Long term stability		±1		mbar/yr
Temperature	**Min**	**Typ**	**Max**	**Unit**
Range	-40		+85	°C
Resolution		<0.01		°C
Accuracy	-0.8		+0.8	°C

Notes: (1) Oversampling Ratio: 256 / 512 / 1024 / 2048 / 4096
(2) With autozero at one pressure point

D GMWM Analysis

This chapter assembles the stochastic properties of the redundant sensor board called *ID2* with its four IMUs and their fusion as a synthetic IMU. The data with a sampling frequency of 500 Hz and the results are stored on the server under "\common\DATA\navchip\static\2018_01\id2".

This chapter assembles the stochastic properties of the redundant sensor board called *ID3* with its two IMUs. The data with a sampling frequency of 250 Hz and the results are stored on the server under "\common\DATA\navchip\static\2014_04\id_3_2014_04_08_5_hours".

This chapter assembles the stochastic properties of the redundant sensor board with the new Navchip V2. The data with a sampling frequency of 200 Hz and the results are stored on the server under "\common\DATA\navchip\static\2017_06\nc_v2_evalboard_on_id5\raw".

D.1 ID2 - NC0

Table D.1: Gyroscope X-axis

Process	R	mapping	conversion
QN	5.1596e-06	-	-
WN	1.0475e-06	-	σ_{WN}: 9.5 $\left[\frac{\text{deg}}{\text{h}\sqrt{\text{Hz}}}\right]$
AR1	9.9933e-01	β: 3.357e-01	$1/\beta$: 2.9 [s]
SIGMA2	7.7946e-12	σ^2_{GM}: 5.809e-09	σ_{GM}: 0.7 $\left[\frac{\text{deg}}{\text{h}\sqrt{\text{Hz}}}\right]$
AR1	9.9995e-01	β: 2.410e-02	$1/\beta$: 41.5 [s]
SIGMA2	1.1575e-12	σ^2_{GM}: 1.201e-08	σ_{GM}: 1.01 $\left[\frac{\text{deg}}{\text{h}\sqrt{\text{Hz}}}\right]$
RW	3.7396e-14	-	σ_{RW}: 0.00178 $\left[\frac{\text{deg}}{\text{h}\sqrt{\text{Hz}}}\right]$

Table D.2: Gyroscope Y-axis

Process	R	mapping	conversion
QN	9.0654e-06	-	-
WN	1.2232e-06	-	σ_{WN}: 10.3 $\left[\frac{\text{deg}}{\text{h}\sqrt{\text{Hz}}}\right]$
AR1	9.9792e-01	β: 1.04e+00	$1/\beta$: 0.96 [s]
SIGMA2	2.6735e-11	σ^2_{GM}: 6.433e-09	σ_{GM}: 0.74 $\left[\frac{\text{deg}}{\text{h}\sqrt{\text{Hz}}}\right]$
AR1	9.9992e-01	β: 3.85e-02	$1/\beta$: 25.97 [s]
SIGMA2	1.5122e-12	σ^2_{GM}: 9.820e-09	σ_{GM}: 0.92 $\left[\frac{\text{deg}}{\text{h}\sqrt{\text{Hz}}}\right]$
RW	6.5791e-13	-	σ_{RW}: 0.00748 $\left[\frac{\text{deg}}{\text{h}\sqrt{\text{Hz}}}\right]$

Table D.3: Gyroscope Z-axis

Process	R	mapping	conversion
QN	6.8458e-06	-	-
WN	1.0113e-06	-	σ_{WN}: 9.3 $\left[\frac{\text{deg}}{\text{h}\sqrt{\text{Hz}}}\right]$
AR1	9.9810e-01	β: 9.48e-01	$1/\beta$: 1.06 [s]
SIGMA2	3.5917e-11	σ^2_{GM}: 9.485e-09	σ_{GM}: 0.9 $\left[\frac{\text{deg}}{\text{h}\sqrt{\text{Hz}}}\right]$
AR1	9.9989e-01	β: 5.19e-02	$1/\beta$: 19.3 [s]
SIGMA2	1.0119e-12	σ^2_{GM}: 4.874e-09	σ_{GM}: 0.64 $\left[\frac{\text{deg}}{\text{h}\sqrt{\text{Hz}}}\right]$
RW	2.2446e-13	-	σ_{RW}: 0.00437 $\left[\frac{\text{deg}}{\text{h}\sqrt{\text{Hz}}}\right]$

Table D.4: Accelerometer X-axis

Process	R	mapping	conversion
QN	2.8247e-05	-	-
WN	1.1952e-04	-	σ_{WN}: 49 $\left[\frac{\mu\text{g}}{\sqrt{\text{Hz}}}\right]$
AR1	9.9775e-01	β: 1.12e-00	$1/\beta$: 0.89 [s]
SIGMA2	2.4884e-09	σ^2_{GM}: 5.545e-07	σ_{GM}: 3.35 $\left[\frac{\mu\text{g}}{\sqrt{\text{Hz}}}\right]$
AR1	9.9903e-01	β: 4.82e-01	$1/\beta$: 2.07 [s]
SIGMA2	7.1911e-10	σ^2_{GM}: 3.729e-07	σ_{GM}: 2.73 $\left[\frac{\mu\text{g}}{\sqrt{\text{Hz}}}\right]$
RW	7.4811e-12	-	σ_{RW}: 0.01223 $\left[\frac{\mu\text{g}}{\sqrt{\text{Hz}}}\right]$

Table D.5: Accelerometer Y-axis

Process	R	mapping	conversion
QN	5.4322e-05	-	-
WN	6.8811e-05	-	σ_{WN}: 38 $\left[\frac{\mu\text{g}}{\sqrt{\text{Hz}}}\right]$
AR1	9.5523e-01	β: 2.29e+01	$1/\beta$: 0.05 [s]
SIGMA2	5.7159e-07	σ^2_{GM}: 6.530e-06	σ_{GM}: 11.45 $\left[\frac{\mu\text{g}}{\sqrt{\text{Hz}}}\right]$
AR1	9.9938e-01	β: 3.09e-01	$1/\beta$: 3.23 [s]
SIGMA2	5.4619e-10	σ^2_{GM}: 4.416e-07	σ_{GM}: 2.97 $\left[\frac{\mu\text{g}}{\sqrt{\text{Hz}}}\right]$
RW	3.7165e-12	-	σ_{RW}: 0.00862 $\left[\frac{\mu\text{g}}{\sqrt{\text{Hz}}}\right]$

Table D.6: Accelerometer Z-axis

Process	R	mapping	conversion
QN	8.4058e-05	-	-
WN	6.3854e-05	-	σ_{WN}: 36 $\left[\frac{\mu\text{g}}{\sqrt{\text{Hz}}}\right]$
AR1	9.7292e-01	β: 1.37e+01	$1/\beta$: 0.08 [s]
SIGMA2	5.6116e-07	σ^2_{GM}: 1.050e-05	σ_{GM}: 14.53 $\left[\frac{\mu\text{g}}{\sqrt{\text{Hz}}}\right]$
AR1	9.9961e-01	β: 1.95e-01	$1/\beta$: 5.13 [s]
SIGMA2	1.4530e-09	σ^2_{GM}: 1.867e-06	σ_{GM}: 6.11 $\left[\frac{\mu\text{g}}{\sqrt{\text{Hz}}}\right]$
RW	3.6520e-12	-	σ_{RW}: 0.00854 $\left[\frac{\mu\text{g}}{\sqrt{\text{Hz}}}\right]$

D.2 ID2 - NC1

Table D.7: Gyroscope X-axis

Process	R	mapping	conversion
QN	7.8866e-06	-	-
WN	7.6081e-07	-	σ_{WN}: 8.1 $\left[\frac{\text{deg}}{\text{h}\sqrt{\text{Hz}}}\right]$
AR1	9.9869e-01	β: 6.575e-01	$1/\beta$: 1.52 [s]
SIGMA2	2.2740e-11	σ^2_{GM}: 8.657e-09	σ_{GM}: 0.9 $\left[\frac{\text{deg}}{\text{h}\sqrt{\text{Hz}}}\right]$
AR1	9.9995e-01	β: 2.605e-02	$1/\beta$: 38.39 [s]
SIGMA2	9.5718e-13	σ^2_{GM}: 9.186e-09	σ_{GM}: 0.88 $\left[\frac{\text{deg}}{\text{h}\sqrt{\text{Hz}}}\right]$
RW	3.7041e-14	-	σ_{RW}: 0.00178 $\left[\frac{\text{deg}}{\text{h}\sqrt{\text{Hz}}}\right]$

Table D.8: Gyroscope Y-axis

Process	R	mapping	conversion
QN	6.4882e-06	-	-
WN	2.2752e-06	-	σ_{WN}: 13.96 $\left[\frac{\text{deg}}{\text{h}\sqrt{\text{Hz}}}\right]$
AR1	9.9885e-01	β: 5.77e-01	$1/\beta$: 1.73 [s]
SIGMA2	2.1112e-11	σ^2_{GM}: 9.156e-09	σ_{GM}: 0.9 $\left[\frac{\text{deg}}{\text{h}\sqrt{\text{Hz}}}\right]$
AR1	9.9993e-01	β: 3.43e-02	$1/\beta$: 29.20 [s]
SIGMA2	2.0367e-12	σ^2_{GM}: 1.487e-08	σ_{GM}: 1.12 $\left[\frac{\text{deg}}{\text{h}\sqrt{\text{Hz}}}\right]$
RW	3.7955e-14	-	σ_{RW}: 0.00180 $\left[\frac{\text{deg}}{\text{h}\sqrt{\text{Hz}}}\right]$

Table D.9: Gyroscope Z-axis

Process	R	mapping	conversion
QN	9.0919e-06	-	-
WN	4.8246e-07	-	σ_{WN}: 6.44 $\left[\frac{\text{deg}}{\text{h}\sqrt{\text{Hz}}}\right]$
AR1	9.9692e-01	β: 1.54e-00	$1/\beta$: 0.64 [s]
SIGMA2	4.6474e-11	σ^2_{GM}: 7.549e-09	σ_{GM}: 0.8 $\left[\frac{\text{deg}}{\text{h}\sqrt{\text{Hz}}}\right]$
AR1	9.9992e-01	β: 4.15e-02	$1/\beta$: 24.12 [s]
SIGMA2	1.2381e-12	σ^2_{GM}: 7.467e-09	σ_{GM}: 0.8 $\left[\frac{\text{deg}}{\text{h}\sqrt{\text{Hz}}}\right]$
RW	2.6609e-13	-	σ_{RW}: 0.00476 $\left[\frac{\text{deg}}{\text{h}\sqrt{\text{Hz}}}\right]$

Table D.10: Accelerometer X-axis

Process	R	mapping	conversion
QN	3.7227e-05	-	-
WN	1.1306e-04	-	σ_{WN}: 48 $\left[\frac{\mu g}{\sqrt{Hz}}\right]$
AR1 SIGMA2	9.9330e-01 3.1118e-09	β: 3.36e+00 σ^2_{GM}: 2.331e-07	$1/\beta$: 0.30 [s] σ_{GM}: 2.16 $\left[\frac{\mu g}{\sqrt{Hz}}\right]$
AR1 SIGMA2	9.9959e-01 3.1520e-10	β: 2.04e-01 σ^2_{GM}: 3.859e-07	$1/\beta$: 4.89 [s] σ_{GM}: 2.8 $\left[\frac{\mu g}{\sqrt{Hz}}\right]$
RW	1.0720e-11	-	σ_{RW}: 0.01464 $\left[\frac{\mu g}{\sqrt{Hz}}\right]$

Table D.11: Accelerometer Y-axis

Process	R	mapping	conversion
QN	2.6752e-05	-	-
WN	8.7225e-05	-	σ_{WN}: 42 $\left[\frac{\mu g}{\sqrt{Hz}}\right]$
AR1 SIGMA2	8.0987e-01 2.1382e-06	β: 1.05e+02 σ^2_{GM}: 6.214e-06	$1/\beta$: 0.01 [s] σ_{GM}: 11.15 $\left[\frac{\mu g}{\sqrt{Hz}}\right]$
AR1 SIGMA2	9.9916e-01 8.7117e-10	β: 4.206e-01 σ^2_{GM}: 5.183e-07	$1/\beta$: 2.38 [s] σ_{GM}: 3.27 $\left[\frac{\mu g}{\sqrt{Hz}}\right]$
RW	3.7214e-12	-	σ_{RW}: 0.00863 $\left[\frac{\mu g}{\sqrt{Hz}}\right]$

Table D.12: Accelerometer Z-axis

Process	R	mapping	conversion
QN	3.4358e-04	-	-
WN	2.7640e-05	-	σ_{WN}: 24 $\left[\frac{\mu g}{\sqrt{Hz}}\right]$
AR1 SIGMA2	8.4422e-01 3.6514e-06	β: 8.47e+01 σ^2_{GM}: 1.271e-05	$1/\beta$: 0.01 [s] σ_{GM}: 15.94 $\left[\frac{\mu g}{\sqrt{Hz}}\right]$
AR1 SIGMA2	9.9922e-01 1.4349e-09	β: 3.91e-01 σ^2_{GM}: 9.175e-07	$1/\beta$: 2.56 [s] σ_{GM}: 4.3 $\left[\frac{\mu g}{\sqrt{Hz}}\right]$
RW	1.4280e-11	-	σ_{RW}: 0.01690 $\left[\frac{\mu g}{\sqrt{Hz}}\right]$

D.3 ID2 - NC2

Table D.13: Gyroscope X-axis

Process	R	mapping	conversion
QN	6.2269e-06	-	-
WN	9.7437e-07	-	σ_{WN}: 9.2 $\left[\frac{\text{deg}}{\text{h}\sqrt{\text{Hz}}}\right]$
AR1	9.9878e-01	β: 6.111e-01	$1/\beta$: 1.63 [s]
SIGMA2	2.5836e-11	σ^2_{GM}: 1.058e-08	σ_{GM}: 0.95 $\left[\frac{\text{deg}}{\text{h}\sqrt{\text{Hz}}}\right]$
AR1	9.9995e-01	β: 2.510e-02	$1/\beta$: 39.84 [s]
SIGMA2	1.0849e-12	σ^2_{GM}: 1.081e-08	σ_{GM}: 0.96 $\left[\frac{\text{deg}}{\text{h}\sqrt{\text{Hz}}}\right]$
RW	3.7244e-14	-	σ_{RW}: 0.00178 $\left[\frac{\text{deg}}{\text{h}\sqrt{\text{Hz}}}\right]$

Table D.14: Gyroscope Y-axis

Process	R	mapping	conversion
QN	7.3856e-06	-	-
WN	1.1724e-06	-	σ_{WN}: 10 $\left[\frac{\text{deg}}{\text{h}\sqrt{\text{Hz}}}\right]$
AR1	9.9788e-01	β: 1.06e+00	$1/\beta$: 0.94 [s]
SIGMA2	3.6630e-11	σ^2_{GM}: 8.661e-09	σ_{GM}: 0.85 $\left[\frac{\text{deg}}{\text{h}\sqrt{\text{Hz}}}\right]$
AR1	9.9993e-01	β: 3.72e-02	$1/\beta$: 26.88 [s]
SIGMA2	1.6165e-12	σ^2_{GM}: 1.086e-08	σ_{GM}: 0.96 $\left[\frac{\text{deg}}{\text{h}\sqrt{\text{Hz}}}\right]$
RW	3.7686e-14	-	σ_{RW}: 0.00179 $\left[\frac{\text{deg}}{\text{h}\sqrt{\text{Hz}}}\right]$

Table D.15: Gyroscope Z-axis

Process	R	mapping	conversion
QN	8.0358e-06	-	-
WN	8.1825e-07	-	σ_{WN}: 8.4 $\left[\frac{\text{deg}}{\text{h}\sqrt{\text{Hz}}}\right]$
AR1	9.9852e-01	β: 7.42e-01	$1/\beta$: 1.35 [s]
SIGMA2	2.8755e-11	σ^2_{GM}: 9.700e-09	σ_{GM}: 0.91 $\left[\frac{\text{deg}}{\text{h}\sqrt{\text{Hz}}}\right]$
AR1	9.9992e-01	β: 3.84e-02	$1/\beta$: 26.07 [s]
SIGMA2	1.4515e-12	σ^2_{GM}: 9.462e-09	σ_{GM}: 0.90 $\left[\frac{\text{deg}}{\text{h}\sqrt{\text{Hz}}}\right]$
RW	2.8391e-14	-	σ_{RW}: 0.00155 $\left[\frac{\text{deg}}{\text{h}\sqrt{\text{Hz}}}\right]$

Table D.16: Accelerometer X-axis

Process	R	mapping	conversion
QN	3.23497e-05	-	-
WN	1.1491e-04	-	σ_{WN}: 48 $\left[\frac{\mu g}{\sqrt{\mathrm{Hz}}}\right]$
AR1	9.9339e-01	β: 3.32e-00	$1/\beta$: 0.30 [s]
SIGMA2	2.6130e-09	σ^2_{GM}: 1.982e-07	σ_{GM}: 1.99 $\left[\frac{\mu g}{\sqrt{\mathrm{Hz}}}\right]$
AR1	9.9962e-01	β: 1.89e-01	$1/\beta$: 5.29 [s]
SIGMA2	3.4556e-10	σ^2_{GM}: 4.572e-07	σ_{GM}: 3.0 $\left[\frac{\mu g}{\sqrt{\mathrm{Hz}}}\right]$
RW	1.0974e-11	-	σ_{RW}: 0.0148 $\left[\frac{\mu g}{\sqrt{\mathrm{Hz}}}\right]$

Table D.17: Accelerometer Y-axis

Process	R	mapping	conversion
QN	2.5243e-05	-	-
WN	1.0336e-04	-	σ_{WN}: 46 $\left[\frac{\mu g}{\sqrt{\mathrm{Hz}}}\right]$
AR1	8.9644e-01	β: 5.47e+01	$1/\beta$: 0.02 [s]
SIGMA2	5.2592e-07	σ^2_{GM}: 2.6780e-06	σ_{GM}: 7.32 $\left[\frac{\mu g}{\sqrt{\mathrm{Hz}}}\right]$
AR1	9.9928e-01	β: 3.62e-01	$1/\beta$: 2.76 [s]
SIGMA2	1.5415e-09	σ^2_{GM}: 1.065e-06	σ_{GM}: 4.7 $\left[\frac{\mu g}{\sqrt{\mathrm{Hz}}}\right]$
RW	9.9368e-12	-	σ_{RW}: 0.0141 $\left[\frac{\mu g}{\sqrt{\mathrm{Hz}}}\right]$

Table D.18: Accelerometer Z-axis

Process	R	mapping	conversion
QN	3.7912e-04	-	-
WN	2.4267e-05	-	σ_{WN}: 22 $\left[\frac{\mu g}{\sqrt{\mathrm{Hz}}}\right]$
AR1	8.3578e-01	β: 8.997e+01	$1/\beta$: 0.01 [s]
SIGMA2	3.8079e-06	σ^2_{GM}: 1.263e-05	σ_{GM}: 15.89 $\left[\frac{\mu g}{\sqrt{\mathrm{Hz}}}\right]$
AR1	9.9907e-01	β: 4.66e-01	$1/\beta$: 2.14 [s]
SIGMA2	2.5970e-09	σ^2_{GM}: 1.393e-06	σ_{GM}: 5.3 $\left[\frac{\mu g}{\sqrt{\mathrm{Hz}}}\right]$
RW	3.4388e-11	-	σ_{RW}: 0.0262 $\left[\frac{\mu g}{\sqrt{\mathrm{Hz}}}\right]$

D.4 ID2 - NC3

Table D.19: Gyroscope X-axis

Process	R	mapping	conversion
QN	9.1311e-06	-	-
WN	7.4083e-07	-	σ_{WN}: 8.0 $\left[\frac{\text{deg}}{\text{h}\sqrt{\text{Hz}}}\right]$
AR1	9.9737e-01	β: 1.319e-00	$1/\beta$: 0.76 [s]
SIGMA2	5.7140e-11	σ^2_{GM}: 1.086e-08	σ_{GM}: 0.96 $\left[\frac{\text{deg}}{\text{h}\sqrt{\text{Hz}}}\right]$
AR1	9.9995e-01	β: 2.340e-02	$1/\beta$: 42.7 [s]
SIGMA2	1.1850e-12	σ^2_{GM}: 1.266e-08	σ_{GM}: 1.04 $\left[\frac{\text{deg}}{\text{h}\sqrt{\text{Hz}}}\right]$
RW	3.7556e-14	-	σ_{RW}: 0.00179 $\left[\frac{\text{deg}}{\text{h}\sqrt{\text{Hz}}}\right]$

Table D.20: Gyroscope Y-axis

Process	R	mapping	conversion
QN	7.1321e-06	-	-
WN	1.6898e-06	-	σ_{WN}: 12.0 $\left[\frac{\text{deg}}{\text{h}\sqrt{\text{Hz}}}\right]$
AR1	9.9787e-01	β: 1.07e+00	$1/\beta$: 0.93 [s]
SIGMA2	2.2571e-11	σ^2_{GM}: 5.294e-09	σ_{GM}: 0.67 $\left[\frac{\text{deg}}{\text{h}\sqrt{\text{Hz}}}\right]$
AR1	9.9992e-01	β: 3.84e-02	$1/\beta$: 26.04 [s]
SIGMA2	1.5102e-12	σ^2_{GM}: 9.832e-09	σ_{GM}: 0.92 $\left[\frac{\text{deg}}{\text{h}\sqrt{\text{Hz}}}\right]$
RW	3.7535e-14	-	σ_{RW}: 0.00179 $\left[\frac{\text{deg}}{\text{h}\sqrt{\text{Hz}}}\right]$

Table D.21: Gyroscope Z-axis

Process	R	mapping	conversion
QN	9.7948e-06	-	-
WN	5.2658e-07	-	σ_{WN}: 6.7 $\left[\frac{\text{deg}}{\text{h}\sqrt{\text{Hz}}}\right]$
AR1	9.9768e-01	β: 1.16e-00	$1/\beta$: 0.86 [s]
SIGMA2	3.7837e-11	σ^2_{GM}: 8.167e-09	σ_{GM}: 0.83 $\left[\frac{\text{deg}}{\text{h}\sqrt{\text{Hz}}}\right]$
AR1	9.9992e-01	β: 3.93e-02	$1/\beta$: 25.44 [s]
SIGMA2	1.3575e-12	σ^2_{GM}: 8.636e-09	σ_{GM}: 0.86 $\left[\frac{\text{deg}}{\text{h}\sqrt{\text{Hz}}}\right]$
RW	4.4930e-13	-	σ_{RW}: 0.00618 $\left[\frac{\text{deg}}{\text{h}\sqrt{\text{Hz}}}\right]$

Table D.22: Accelerometer X-axis

Process	R	mapping	conversion
QN	4.0584e-05	-	-
WN	1.1371e-04	-	σ_{WN}: 48 $\left[\frac{\mu\text{g}}{\sqrt{\text{Hz}}}\right]$
AR1	9.8959e-01	β: 5.23e-00	$1/\beta$: 0.19 [s]
SIGMA2	1.8179e-09	σ^2_{GM}: 8.781e-08	σ_{GM}: 1.325 $\left[\frac{\mu\text{g}}{\sqrt{\text{Hz}}}\right]$
AR1	9.9938e-01	β: 3.11e-01	$1/\beta$: 3.22 [s]
SIGMA2	1.7129e-10	σ^2_{GM}: 1.379e-07	σ_{GM}: 1.7 $\left[\frac{\mu\text{g}}{\sqrt{\text{Hz}}}\right]$
RW	4.7695e-12	-	σ_{RW}: 0.00977 $\left[\frac{\mu\text{g}}{\sqrt{\text{Hz}}}\right]$

Table D.23: Accelerometer Y-axis

Process	R	mapping	conversion
QN	5.2198e-05	-	-
WN	1.0144e-04	-	σ_{WN}: 46 $\left[\frac{\mu\text{g}}{\sqrt{\text{Hz}}}\right]$
AR1	8.8973e-01	β: 5.84e+01	$1/\beta$: 0.02 [s]
SIGMA2	2.5058e-07	σ^2_{GM}: 1.2025e-06	σ_{GM}: 4.9 $\left[\frac{\mu\text{g}}{\sqrt{\text{Hz}}}\right]$
AR1	9.9871e-01	β: 6.45e-01	$1/\beta$: 1.55 [s]
SIGMA2	6.4008e-10	σ^2_{GM}: 2.483e-07	σ_{GM}: 2.3 $\left[\frac{\mu\text{g}}{\sqrt{\text{Hz}}}\right]$
RW	5.6121e-12	-	σ_{RW}: 0.01059 $\left[\frac{\mu\text{g}}{\sqrt{\text{Hz}}}\right]$

Table D.24: Accelerometer Z-axis

Process	R	mapping	conversion
QN	1.6877e-04	-	-
WN	9.0674e-05	-	σ_{WN}: 43 $\left[\frac{\mu\text{g}}{\sqrt{\text{Hz}}}\right]$
AR1	9.7516e-01	β: 1.26e+01	$1/\beta$: 0.08 [s]
SIGMA2	1.5013e-07	σ^2_{GM}: 3.060e-06	σ_{GM}: 7.82 $\left[\frac{\mu\text{g}}{\sqrt{\text{Hz}}}\right]$
AR1	9.9938e-01	β: 3.12e-01	$1/\beta$: 3.21 [s]
SIGMA2	1.5961e-09	σ^2_{GM}: 1.281e-06	σ_{GM}: 5.1 $\left[\frac{\mu\text{g}}{\sqrt{\text{Hz}}}\right]$
RW	3.7749e-11	-	σ_{RW}: 0.02748 $\left[\frac{\mu\text{g}}{\sqrt{\text{Hz}}}\right]$

D.5 ID2 - Synthetic NC

Table D.25: Gyroscope X-axis

Process	R	mapping	conversion
QN	2.0352e-06	-	-
WN	1.9121e-07	-	σ_{WN}: 4.1 $\left[\frac{\text{deg}}{\text{h}\sqrt{\text{Hz}}}\right]$
AR1	9.9636e-01	β: 1.83e-00	$1/\beta$: 0.55 [s]
SIGMA2	1.5395e-11	σ^2_{GM}: 2.116e-09	σ_{GM}: 0.43 $\left[\frac{\text{deg}}{\text{h}\sqrt{\text{Hz}}}\right]$
AR1	9.9992e-01	β: 4.25e-02	$1/\beta$: 23.535 [s]
SIGMA2	5.2672e-13	σ^2_{GM}: 3.098e-09	σ_{GM}: 0.52 $\left[\frac{\text{deg}}{\text{h}\sqrt{\text{Hz}}}\right]$
RW	1.7501e-14	-	σ_{RW}: 0.00122 $\left[\frac{\text{deg}}{\text{h}\sqrt{\text{Hz}}}\right]$

Table D.26: Gyroscope Y-axis

Process	R	mapping	conversion
QN	2.0289e-06	-	-
WN	3.9185e-07	-	σ_{WN}: 5.8 $\left[\frac{\text{deg}}{\text{h}\sqrt{\text{Hz}}}\right]$
AR1	9.9809e-01	β: 9.54e-01	$1/\beta$: 1.05 [s]
SIGMA2	6.5234e-12	σ^2_{GM}: 1.713e-09	σ_{GM}: 0.39 $\left[\frac{\text{deg}}{\text{h}\sqrt{\text{Hz}}}\right]$
AR1	9.9984e-01	β: 8.15e-02	$1/\beta$: 12.27 [s]
SIGMA2	6.3292e-13	σ^2_{GM}: 1.942e-09	σ_{GM}: 0.41 $\left[\frac{\text{deg}}{\text{h}\sqrt{\text{Hz}}}\right]$
RW	6.3061e-13	-	σ_{RW}: 0.00232 $\left[\frac{\text{deg}}{\text{h}\sqrt{\text{Hz}}}\right]$

Table D.27: Gyroscope Z-axis

Process	R	mapping	conversion
QN	1.9570e-06	-	-
WN	2.3955e-07	-	σ_{WN}: 4.5 $\left[\frac{\text{deg}}{\text{h}\sqrt{\text{Hz}}}\right]$
AR1	9.9786e-01	β: 1.07e-00	$1/\beta$: 0.93 [s]
SIGMA2	6.7916e-12	σ^2_{GM}: 1.586e-09	σ_{GM}: 0.37 $\left[\frac{\text{deg}}{\text{h}\sqrt{\text{Hz}}}\right]$
AR1	9.9983e-01	β: 8.50e-02	$1/\beta$: 11.77 [s]
SIGMA2	5.8833e-13	σ^2_{GM}: 1.732e-09	σ_{GM}: 0.39 $\left[\frac{\text{deg}}{\text{h}\sqrt{\text{Hz}}}\right]$
RW	6.1979e-14	-	σ_{RW}: 0.00229 $\left[\frac{\text{deg}}{\text{h}\sqrt{\text{Hz}}}\right]$

Table D.28: Accelerometer X-axis

Process	R	mapping	conversion
QN	1.5216e-05	-	-
WN	3.0731e-05	-	σ_{WN}: 25 $\left[\frac{\mu\text{g}}{\sqrt{\text{Hz}}}\right]$
AR1	9.5515e-01	β: 2.29e+01	$1/\beta$: 0.04 [s]
SIGMA2	2.1667e-08	σ^2_{GM}: 2.471e-07	σ_{GM}: 2.23 $\left[\frac{\mu\text{g}}{\sqrt{\text{Hz}}}\right]$
AR1	9.9971e-01	β: 1.45e-01	$1/\beta$: 6.88 [s]
SIGMA2	5.9314e-11	σ^2_{GM}: 1.021e-07	σ_{GM}: 1.43 $\left[\frac{\mu\text{g}}{\sqrt{\text{Hz}}}\right]$
RW	2.3298e-12	-	σ_{RW}: 0.00683 $\left[\frac{\mu\text{g}}{\sqrt{\text{Hz}}}\right]$

Table D.29: Accelerometer Y-axis

Process	R	mapping	conversion
QN	6.3327e-06	-	-
WN	2.8606e-05	-	σ_{WN}: 24 $\left[\frac{\mu\text{g}}{\sqrt{\text{Hz}}}\right]$
AR1	9.5999e-01	β: 2.04e+01	$1/\beta$: 0.05 [s]
SIGMA2	4.3982e-08	σ^2_{GM}: 5.609e-07	σ_{GM}: 3.35 $\left[\frac{\mu\text{g}}{\sqrt{\text{Hz}}}\right]$
AR1	9.9972e-01	β: 1.41e-01	$1/\beta$: 7.1 [s]
SIGMA2	8.6745e-11	σ^2_{GM}: 1.541e-07	σ_{GM}: 1.76 $\left[\frac{\mu\text{g}}{\sqrt{\text{Hz}}}\right]$
RW	1.3699e-12	-	σ_{RW}: 0.00523 $\left[\frac{\mu\text{g}}{\sqrt{\text{Hz}}}\right]$

Table D.30: Accelerometer Z-axis

Process	R	mapping	conversion
QN	9.8402e-05	-	-
WN	3.1327e-05	-	σ_{WN}: 25 $\left[\frac{\mu\text{g}}{\sqrt{\text{Hz}}}\right]$
AR1	9.7541e-01	β: 1.25e+01	$1/\beta$: 0.08 [s]
SIGMA2	4.6037e-08	σ^2_{GM}: 9.478e-07	σ_{GM}: 4.36 $\left[\frac{\mu\text{g}}{\sqrt{\text{Hz}}}\right]$
AR1	9.9972e-01	β: 1.38e-01	$1/\beta$: 7.2 [s]
SIGMA2	2.0656e-10	σ^2_{GM}: 3.743e-07	σ_{GM}: 2.74 $\left[\frac{\mu\text{g}}{\sqrt{\text{Hz}}}\right]$
RW	6.1121e-12	-	σ_{RW}: 0.01106 $\left[\frac{\mu\text{g}}{\sqrt{\text{Hz}}}\right]$

D.6 ID3 - NC0

Table D.31: Gyroscope X-axis

Process	R	mapping	conversion
QN	1.9805e-06	-	-
WN	4.6464e-07	-	σ_{WN}: 8.89 $\left[\frac{\text{deg}}{\text{h}\sqrt{\text{Hz}}}\right]$
AR1	9.9683e-01	β: 7.95e-01	$1/\beta$: 1.26 [s]
SIGMA2	4.9769e-11	σ^2_{GM}: 7.852e-09	σ_{GM}: 1.16 $\left[\frac{\text{deg}}{\text{h}\sqrt{\text{Hz}}}\right]$
AR1	9.9997e-01	β: 8.60e-03	$1/\beta$: 116.28 [s]
SIGMA2	1.4152e-12	σ^2_{GM}: 2.0569e-08	σ_{GM}: 1.87 $\left[\frac{\text{deg}}{\text{h}\sqrt{\text{Hz}}}\right]$
RW	1.1787e-14	-	σ_{RW}: 0.001416 $\left[\frac{\text{deg}}{\text{h}\sqrt{\text{Hz}}}\right]$

Table D.32: Gyroscope Y-axis

Process	R	mapping	conversion
QN	2.9208e-06	-	-
WN	5.7064e-07	-	σ_{WN}: 9.85 $\left[\frac{\text{deg}}{\text{h}\sqrt{\text{Hz}}}\right]$
AR1	9.9634e-01	β: 9.18e-01	$1/\beta$: 1.09 [s]
SIGMA2	1.0002e-10	σ^2_{GM}: 1.367e-08	σ_{GM}: 1.53 $\left[\frac{\text{deg}}{\text{h}\sqrt{\text{Hz}}}\right]$
AR1	9.9996e-01	β: 1.03e-02	$1/\beta$: 97.56 [s]
SIGMA2	1.3414e-12	σ^2_{GM}: 1.636e-08	σ_{GM}: 1.67 $\left[\frac{\text{deg}}{\text{h}\sqrt{\text{Hz}}}\right]$
RW	4.8479e-15	-	σ_{RW}: 0.0009 $\left[\frac{\text{deg}}{\text{h}\sqrt{\text{Hz}}}\right]$

Table D.33: Gyroscope Z-axis

Process	R	mapping	conversion
QN	1.8793e-06	-	-
WN	5.5659e-07	-	σ_{WN}: 9.73 $\left[\frac{\text{deg}}{\text{h}\sqrt{\text{Hz}}}\right]$
AR1	9.9603e-01	β: 9.95e-01	$1/\beta$: 1.01 [s]
SIGMA2	9.9782e-11	σ^2_{GM}: 1.259e-08	σ_{GM}: 1.46 $\left[\frac{\text{deg}}{\text{h}\sqrt{\text{Hz}}}\right]$
AR1	9.9994e-01	β: 1.47e-02	$1/\beta$: 67.8 [s]
SIGMA2	3.2971e-12	σ^2_{GM}: 2.794e-08	σ_{GM}: 2.18 $\left[\frac{\text{deg}}{\text{h}\sqrt{\text{Hz}}}\right]$
RW	9.4035e-14	-	σ_{RW}: 0.004 $\left[\frac{\text{deg}}{\text{h}\sqrt{\text{Hz}}}\right]$

Table D.34: Accelerometer X-axis

Process	R	mapping	conversion
QN	1.5426e-05	-	-
WN	6.7604e-05	-	σ_{WN}: 52.0 $\left[\frac{\mu g}{\sqrt{Hz}}\right]$
RW	1.3993e-11	-	σ_{RW}: 0.023658 $\left[\frac{\mu g}{\sqrt{Hz}}\right]$

Table D.35: Accelerometer Y-axis

Process	R	mapping	conversion
QN	1.4833e-05	-	-
WN	6.0248e-05	-	σ_{WN}: 49.1 $\left[\frac{\mu g}{\sqrt{Hz}}\right]$
AR1 SIGMA2	9.9976e-01 2.9649e-11	β: 6.08e-02 σ^2_{GM}: 6.094e-08	$1/\beta$: 16.4 [s] σ_{GM}: 1.56 $\left[\frac{\mu g}{\sqrt{Hz}}\right]$
RW	1.6068e-12	-	σ_{RW}: 0.008017 $\left[\frac{\mu g}{\sqrt{Hz}}\right]$

Table D.36: Accelerometer Z-axis

Process	R	mapping	conversion
QN	5.2378e-05	-	-
WN	4.5997e-05	-	σ_{WN}: 42.89 $\left[\frac{\mu g}{\sqrt{Hz}}\right]$
AR1 SIGMA2	9.9987e-01 3.2081e-11	β: 2.82e-02 σ^2_{GM}: 1.423e-07	$1/\beta$: 35.49 [s] σ_{GM}: 2.39 $\left[\frac{\mu g}{\sqrt{Hz}}\right]$
RW	5.7022e-13	-	σ_{RW}: 0.0047758 $\left[\frac{\mu g}{\sqrt{Hz}}\right]$

D.7 ID3 - NC1

Table D.37: Gyroscope X-axis

Process	R	mapping	conversion
QN	2.4786e-06	-	-
WN	3.6449e-07	-	σ_{WN}: 7.88 $\left[\frac{\text{deg}}{\text{h}\sqrt{\text{Hz}}}\right]$
AR1	9.9134e-01	β: 2.18e-00	$1/\beta$: 0.46 [s]
SIGMA2	1.1276e-10	σ^2_{GM}: 6.518e-09	σ_{GM}: 1.05 $\left[\frac{\text{deg}}{\text{h}\sqrt{\text{Hz}}}\right]$
AR1	9.9975e-01	β: 6.21e-02	$1/\beta$: 16.09 [s]
SIGMA2	6.4216e-12	σ^2_{GM}: 1.292e-08	σ_{GM}: 1.48 $\left[\frac{\text{deg}}{\text{h}\sqrt{\text{Hz}}}\right]$
RW	8.4626e-14	-	σ_{RW}: 0.003794955 $\left[\frac{\text{deg}}{\text{h}\sqrt{\text{Hz}}}\right]$

Table D.38: Gyroscope Y-axis

Process	R	mapping	conversion
QN	2.9628e-06	-	-
WN	6.9192e-07	-	σ_{WN}: 10.85 $\left[\frac{\text{deg}}{\text{h}\sqrt{\text{Hz}}}\right]$
AR1	9.9848e-01	β: 3.79e-01	$1/\beta$: 2.63 [s]
SIGMA2	2.8083e-11	σ^2_{GM}: 9.255e-09	σ_{GM}: 1.26 $\left[\frac{\text{deg}}{\text{h}\sqrt{\text{Hz}}}\right]$
AR1	9.9998e-01	β: 4.85e-03	$1/\beta$: 206.2 [s]
SIGMA2	4.4839e-13	σ^2_{GM}: 1.156e-08	σ_{GM}: 1.4 $\left[\frac{\text{deg}}{\text{h}\sqrt{\text{Hz}}}\right]$
RW	3.3667e-15	-	σ_{RW}: 0.0007569348 $\left[\frac{\text{deg}}{\text{h}\sqrt{\text{Hz}}}\right]$

Table D.39: Gyroscope Z-axis

Process	R	mapping	conversion
QN	1.9714e-06	-	-
WN	3.4821e-07	-	σ_{WN}: 7.7 $\left[\frac{\text{deg}}{\text{h}\sqrt{\text{Hz}}}\right]$
AR1	9.9694e-01	β: 7.66e-01	$1/\beta$: 1.31 [s]
SIGMA2	4.4373e-11	σ^2_{GM}: 7.265e-09	σ_{GM}: 1.11 $\left[\frac{\text{deg}}{\text{h}\sqrt{\text{Hz}}}\right]$
AR1	9.9997e-01	β: 7.38e-03	$1/\beta$: 135.6 [s]
SIGMA2	1.8709e-12	σ^2_{GM}: 3.171e-08	σ_{GM}: 2.32 $\left[\frac{\text{deg}}{\text{h}\sqrt{\text{Hz}}}\right]$
RW	5.9291e-14	-	σ_{RW}: 0.0031765 $\left[\frac{\text{deg}}{\text{h}\sqrt{\text{Hz}}}\right]$

Table D.40: Accelerometer X-axis

Process	R	mapping	conversion
QN	3.2156e-05	-	-
WN	7.8737e-05	-	σ_{WN}: 56.12 $\left[\frac{\mu g}{\sqrt{Hz}}\right]$
AR1	9.9689e-01	β: 7.77e-01	$1/\beta$: 1.29 [s]
SIGMA2	3.6494e-09	σ_{GM}^2: 5.887e-07	σ_{GM}: 4.85 $\left[\frac{\mu g}{\sqrt{Hz}}\right]$
AR1	9.9989e-01	β: 2.72e-02	$1/\beta$: 36.79 [s]
SIGMA2	1.4032e-10	σ_{GM}^2: 6.455e-07	σ_{GM}: 5.08 $\left[\frac{\mu g}{\sqrt{Hz}}\right]$
RW	1.3122e-11	-	σ_{RW}: 0.02291 $\left[\frac{\mu g}{\sqrt{Hz}}\right]$

Table D.41: Accelerometer Y-axis

Process	R	mapping	conversion
QN	1.5673e-05	-	-
WN	7.7945e-05	-	σ_{WN}: 55.83 $\left[\frac{\mu g}{\sqrt{Hz}}\right]$
AR1	9.9990e-01	β: 2.48e-02	$1/\beta$: 40.36 [s]
SIGMA2	2.7476e-11	σ_{GM}^2: 1.386e-07	σ_{GM}: 2.35 $\left[\frac{\mu g}{\sqrt{Hz}}\right]$
RW	5.8441e-13	-	σ_{RW}: 0.004834895 $\left[\frac{\mu g}{\sqrt{Hz}}\right]$

Table D.42: Accelerometer Z-axis

Process	R	mapping	conversion
QN	9.9105e-05	-	-
WN	6.1972e-05	-	σ_{WN}: 49.8 $\left[\frac{\mu g}{\sqrt{Hz}}\right]$
AR1	9.9956e-01	β: 1.09e-01	$1/\beta$: 9.19 [s]
SIGMA2	1.0796e-10	σ_{GM}^2: 1.241e-07	σ_{GM}: 2.23 $\left[\frac{\mu g}{\sqrt{Hz}}\right]$
RW	3.9156e-12	-	σ_{RW}: 0.01251499 $\left[\frac{\mu g}{\sqrt{Hz}}\right]$

D.8 IDX - NCV2

Table D.43: Gyroscope X-axis

Process	R	mapping	conversion
QN	2.2936e-08	-	-
WN	6.1719e-07	-	σ_{WN}: 11.46 $\left[\frac{\text{deg}}{\text{h}\sqrt{\text{Hz}}}\right]$
AR1	9.9997e-01	β: 5.28e-03	$1/\beta$: 189.39 [s]
SIGMA2	1.1303e-13	σ^2_{GM}: 2.141e-09	σ_{GM}: 0.67 $\left[\frac{\text{deg}}{\text{h}\sqrt{\text{Hz}}}\right]$
RW	8.82178e-15	-	σ_{RW}: 0.00137 $\left[\frac{\text{deg}}{\text{h}\sqrt{\text{Hz}}}\right]$

Table D.44: Gyroscope Y-axis

Process	R	mapping	conversion
QN	1.3992e-08	-	-
WN	9.4623e-07	-	σ_{WN}: 14.19 $\left[\frac{\text{deg}}{\text{h}\sqrt{\text{Hz}}}\right]$
AR1	9.9996e-01	β: 8.46e-03	$1/\beta$: 118.2 [s]
SIGMA2	3.8311e-13	σ^2_{GM}: 4.529e-09	σ_{GM}: 0.98 $\left[\frac{\text{deg}}{\text{h}\sqrt{\text{Hz}}}\right]$
RW	3.8329e-15	-	σ_{RW}: 0.00090297 $\left[\frac{\text{deg}}{\text{h}\sqrt{\text{Hz}}}\right]$

Table D.45: Gyroscope Z-axis

Process	R	mapping	conversion
QN	2.0095e-08	-	-
WN	7.7029e-07	-	σ_{WN}: 12.8 $\left[\frac{\text{deg}}{\text{h}\sqrt{\text{Hz}}}\right]$
AR1	9.9920e-01	β: 1.59e-01	$1/\beta$: 6.27 [s]
SIGMA2	9.7967e-13	σ^2_{GM}: 6.146e-10	σ_{GM}: 0.36 $\left[\frac{\text{deg}}{\text{h}\sqrt{\text{Hz}}}\right]$
RW	2.0974e-14	-	σ_{RW}: 0.002112259 $\left[\frac{\text{deg}}{\text{h}\sqrt{\text{Hz}}}\right]$
DR	2.5244e-10	-	-

Table D.46: Accelerometer X-axis

Process	R	mapping	conversion
QN	5.1144e-07	-	-
WN	3.5949e-05	-	σ_{WN}: 42.4 $\left[\frac{\mu\text{g}}{\sqrt{\text{Hz}}}\right]$
AR1	9.9859e-01	β: 2.82e-01	$1/\beta$: 3.5[s]
SIGMA2	8.1477e-10	σ^2_{GM}: 2.89e-07	σ_{GM}: 3.8 $\left[\frac{\mu\text{g}}{\sqrt{\text{Hz}}}\right]$
RW	1.5873e-11	-	σ_{RW}: 0.02817155 $\left[\frac{\mu\text{g}}{\sqrt{\text{Hz}}}\right]$
DR	3.4126e-09	-	-

Table D.47: Accelerometer Y-axis

Process	R	mapping	conversion
QN	6.7442e-07	-	-
WN	3.5935e-05	-	σ_{WN}: 42.4 $\left[\frac{\mu\text{g}}{\sqrt{\text{Hz}}}\right]$
AR1	9.9309e-01	β: 1.39e+00	$1/\beta$: 0.7 [s]
SIGMA2	1.2313e-09	σ^2_{GM}: 8.947e-08	σ_{GM}: 2.11 $\left[\frac{\mu\text{g}}{\sqrt{\text{Hz}}}\right]$
RW	2.1135e-11	-	σ_{RW}: 0.03250745 $\left[\frac{\mu\text{g}}{\sqrt{\text{Hz}}}\right]$
DR	3.4103e-09	-	-

Table D.48: Accelerometer Z-axis

Process	R	mapping	conversion
QN	4.1645e-07	-	-
WN	2.8828e-05	-	σ_{WN}: 37.97 $\left[\frac{\mu\text{g}}{\sqrt{\text{Hz}}}\right]$
AR1	9.9769e-01	β: 4.63e-01	$1/\beta$: 2.16 [s]
SIGMA2	1.0514e-09	σ^2_{GM}: 2.274e-07	σ_{GM}: 3.37 $\left[\frac{\mu\text{g}}{\sqrt{\text{Hz}}}\right]$
AR1	9.9989e-01	β: 2.040e-02	$1/\beta$: 49.0 [s]
SIGMA2	1.0009e-10	σ^2_{GM}: 4.907e-07	σ_{GM}: 4.95 $\left[\frac{\mu\text{g}}{\sqrt{\text{Hz}}}\right]$
RW	1.3385e-12	-	σ_{RW}: 0.008180773 $\left[\frac{\mu\text{g}}{\sqrt{\text{Hz}}}\right]$

E Calibration Table

This chapter assembles the specifications and the calibration setup with its mount (Figure E.1) to interface the rotation table from Appendix F.

The rotation axes of this calibration table do no cross with the rotation axis of the rotation table. This is the case, as the gyroscope calibration procedure requires the precise rotation rate of the rotation table and compares it directly to the norm of the gyroscope measurements from the sensors mounted on this calibration table. Thus, information about orientation and alignment are not necessary.

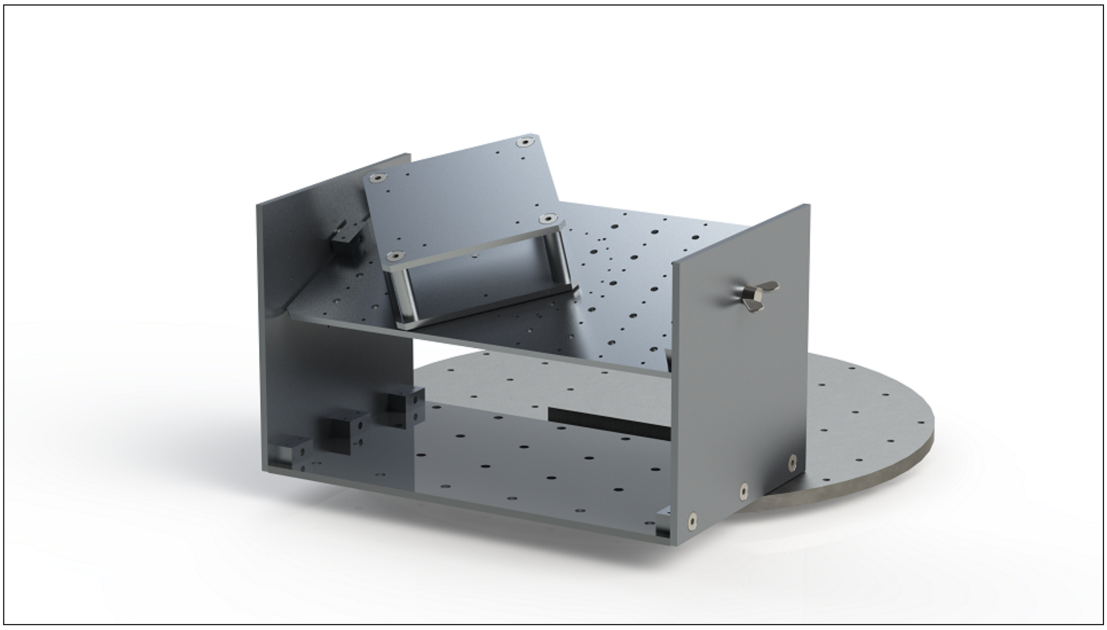

Figure E.1: Setup with 40 cm diameter base plate of the rotation table.

E.1 Base Plate

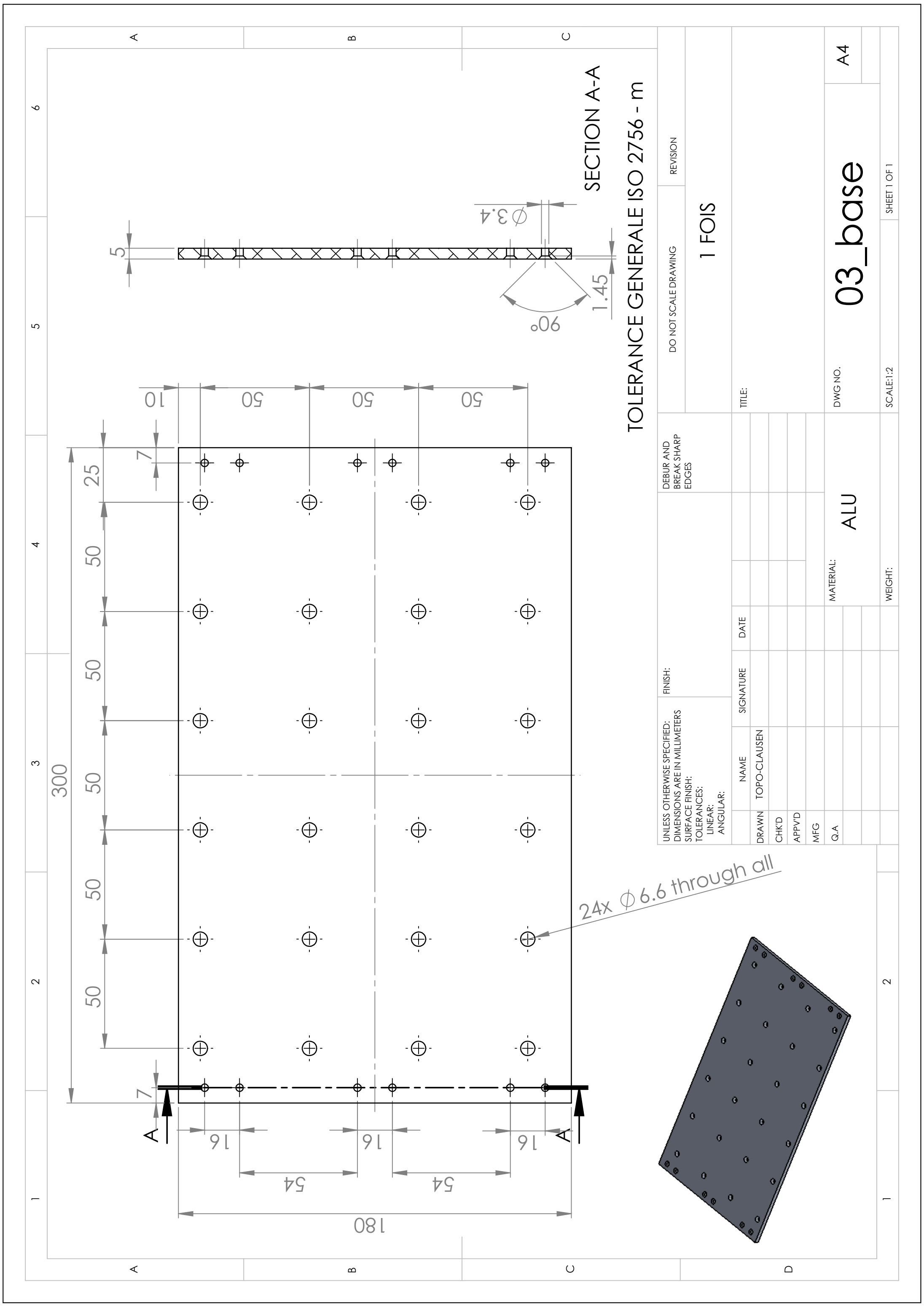
SECTION A-A
TOLERANCE GENERALE ISO 2756 - m
Ø3.4
5
1.45
90°
10
50
50
50
7
25
300
50
50
50
50
50
7
A
A
16
16
16
54
54
180
24x Ø6.6 through all
UNLESS OTHERWISE SPECIFIED:
DIMENSIONS ARE IN MILLIMETERS
SURFACE FINISH:
TOLERANCES:
LINEAR:
ANGULAR:
FINISH:
DEBUR AND BREAK SHARP EDGES
DO NOT SCALE DRAWING
REVISION
1 FOIS
NAME
SIGNATURE
DATE
DRAWN
TOPO-CLAUSEN
CHK'D
APPV'D
MFG
Q.A
TITLE:
MATERIAL:
ALU
DWG NO.
03_base
A4
WEIGHT:
SCALE:1:2
SHEET 1 OF 1
A
B
C
D
1
2
3
4
5
6

E.2 Base Wall

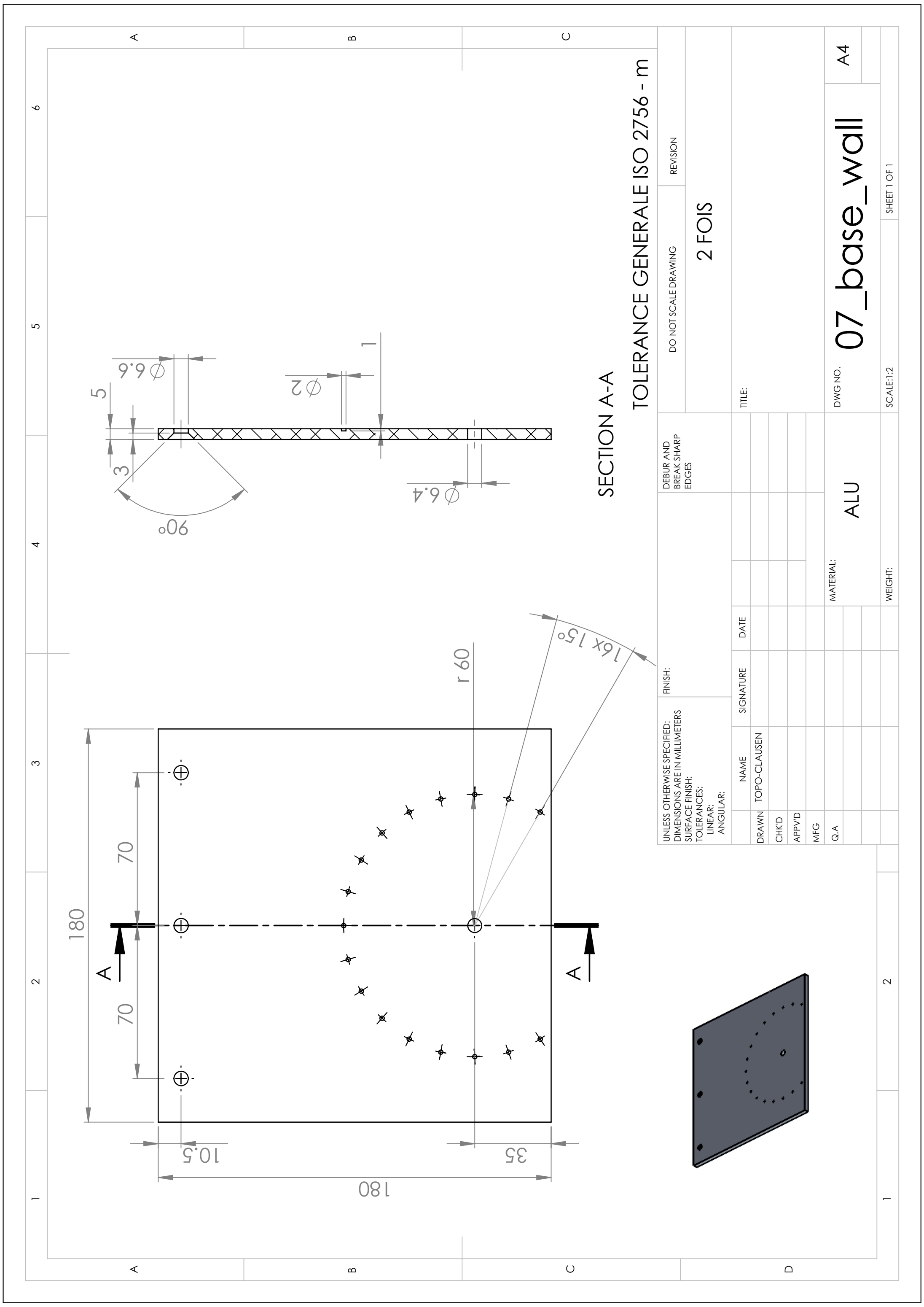
SECTION A-A
TOLERANCE GENERALE ISO 2756 - m
A
A
180
70
70
180
10.5
35
r 60
16x 15°
⌀6.6
5
3
90°
⌀2
1
⌀6.4
UNLESS OTHERWISE SPECIFIED:
DIMENSIONS ARE IN MILLIMETERS
SURFACE FINISH:
TOLERANCES:
LINEAR:
ANGULAR:
FINISH:
DEBUR AND BREAK SHARP EDGES
DO NOT SCALE DRAWING
REVISION
2 FOIS
NAME
SIGNATURE
DATE
DRAWN
TOPO-CLAUSEN
CHK'D
APPV'D
MFG
Q.A
TITLE:
MATERIAL:
ALU
DWG NO.
07_base_wall
A4
WEIGHT:
SCALE:1:2
SHEET 1 OF 1

E.3 Transversal

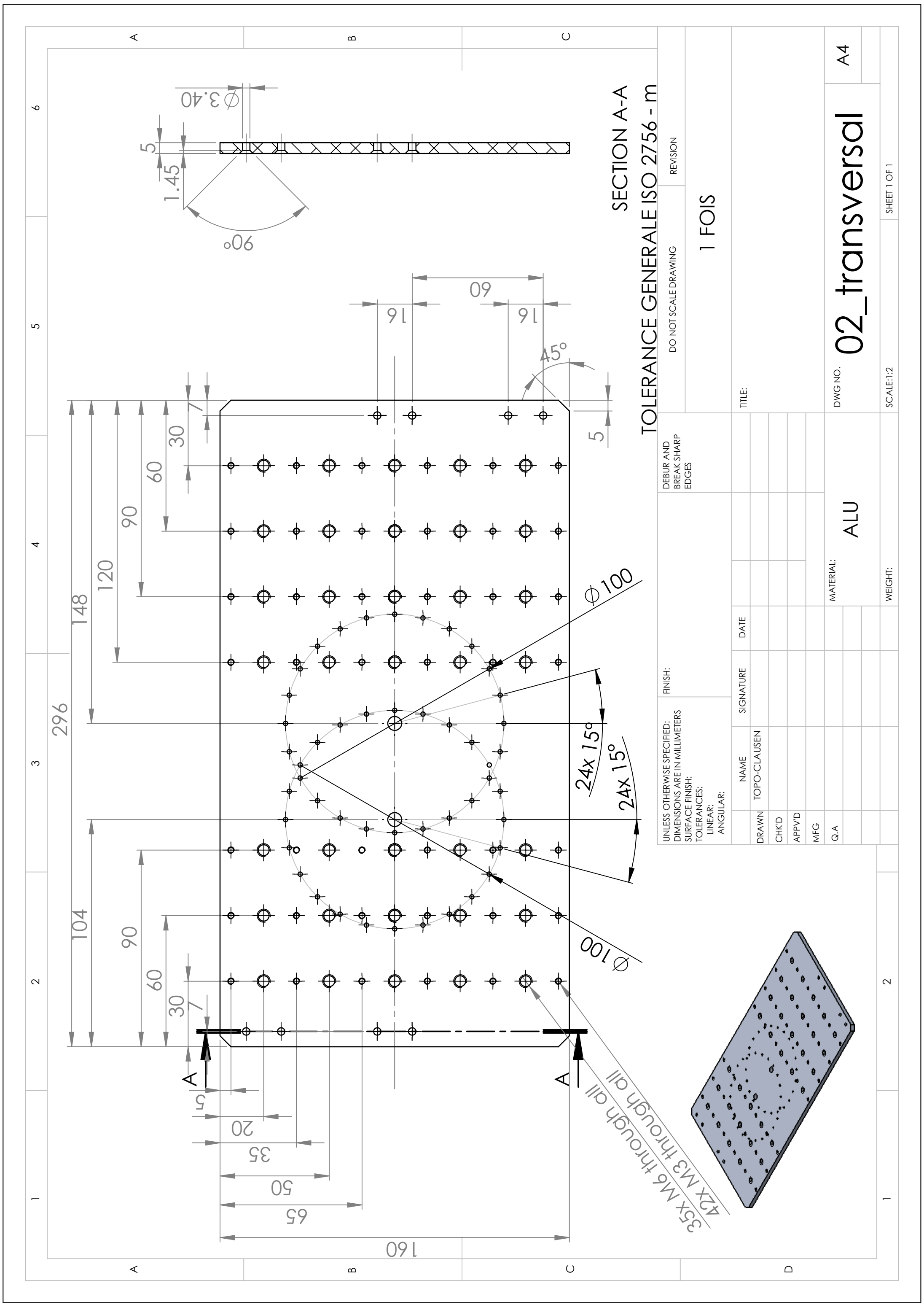
SECTION A-A
TOLERANCE GENERALE ISO 2756 - m
∅3.40
5
1.45
90°
60
16
16
45°
5
7
30
60
90
120
148
296
∅100
24x 15°
24x 15°
104
90
60
30
7
∅100
A
A
5
20
35
50
65
160
35x M6 through all
42x M3 through all
UNLESS OTHERWISE SPECIFIED:
DIMENSIONS ARE IN MILLIMETERS
SURFACE FINISH:
TOLERANCES:
LINEAR:
ANGULAR:
FINISH:
DEBUR AND BREAK SHARP EDGES
DO NOT SCALE DRAWING
REVISION
1 FOIS
NAME
SIGNATURE
DATE
TITLE:
DRAWN
TOPO-CLAUSEN
CHK'D
APPV'D
MFG
Q.A
MATERIAL:
ALU
DWG NO.
02_transversal
A4
WEIGHT:
SCALE:1:2
SHEET 1 OF 1
A
B
C
D
1
2
3
4
5
6

E.4 Case Holder

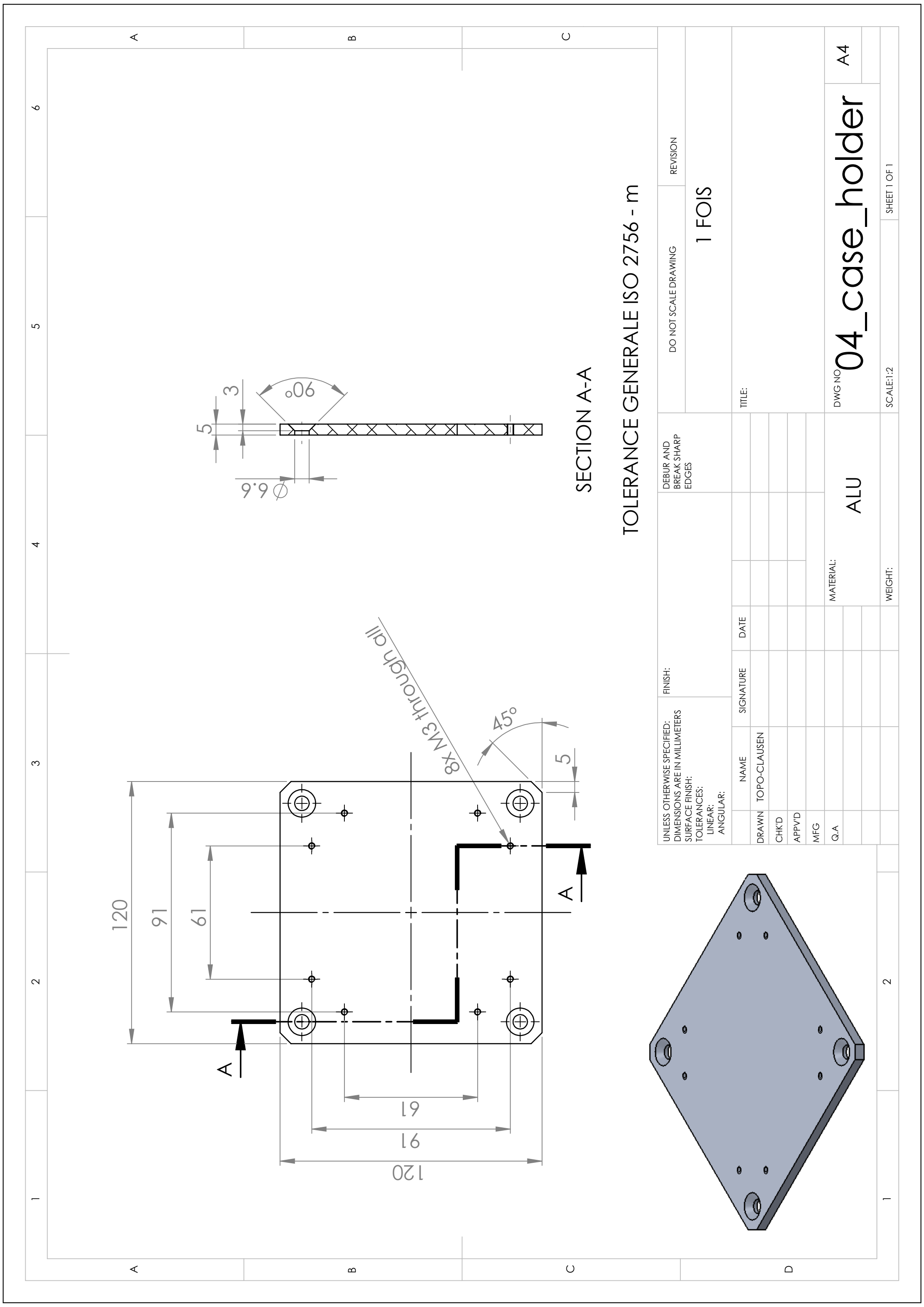
A
B
C
D
1
2
3
4
5
6
120
91
61
A
8x M3 through all
45°
5
3
5
90°
⌀6.6
SECTION A-A
TOLERANCE GENERALE ISO 2756 - m
UNLESS OTHERWISE SPECIFIED:
DIMENSIONS ARE IN MILLIMETERS
SURFACE FINISH:
TOLERANCES:
LINEAR:
ANGULAR:
FINISH:
DEBUR AND BREAK SHARP EDGES
DO NOT SCALE DRAWING
REVISION
1 FOIS
NAME
SIGNATURE
DATE
DRAWN
TOPO-CLAUSEN
CHK'D
APPV'D
MFG
Q.A
TITLE:
MATERIAL:
ALU
DWG NO.
04_case_holder
A4
WEIGHT:
SCALE:1:2
SHEET 1 OF 1

F Rotation Table

This chapter shows the specifications for the rotation table (see Figure F.1) installed at the EPFL facilities.

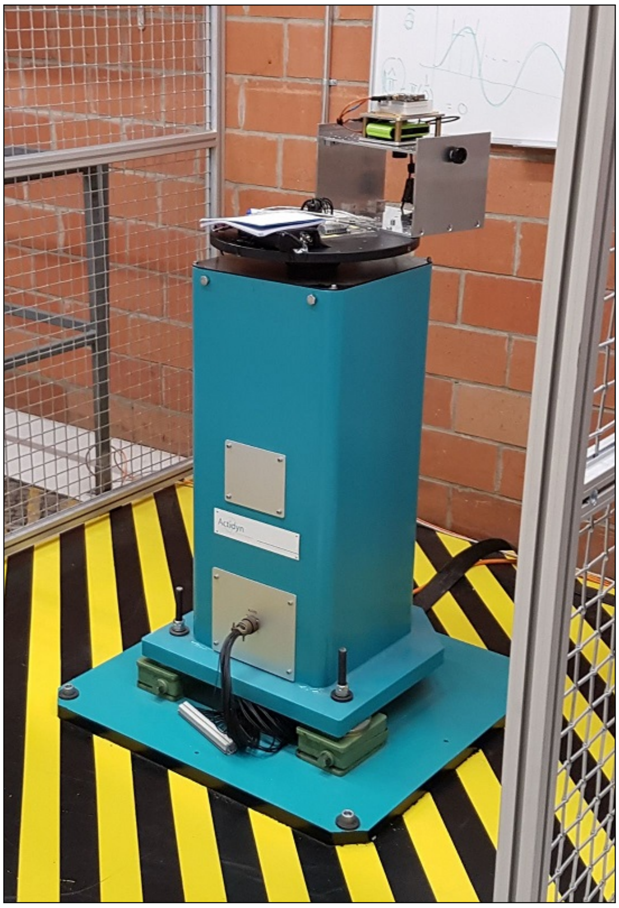

Figure F.1: Rotation table with 40 cm diameter base plate.

F.1 Specifications

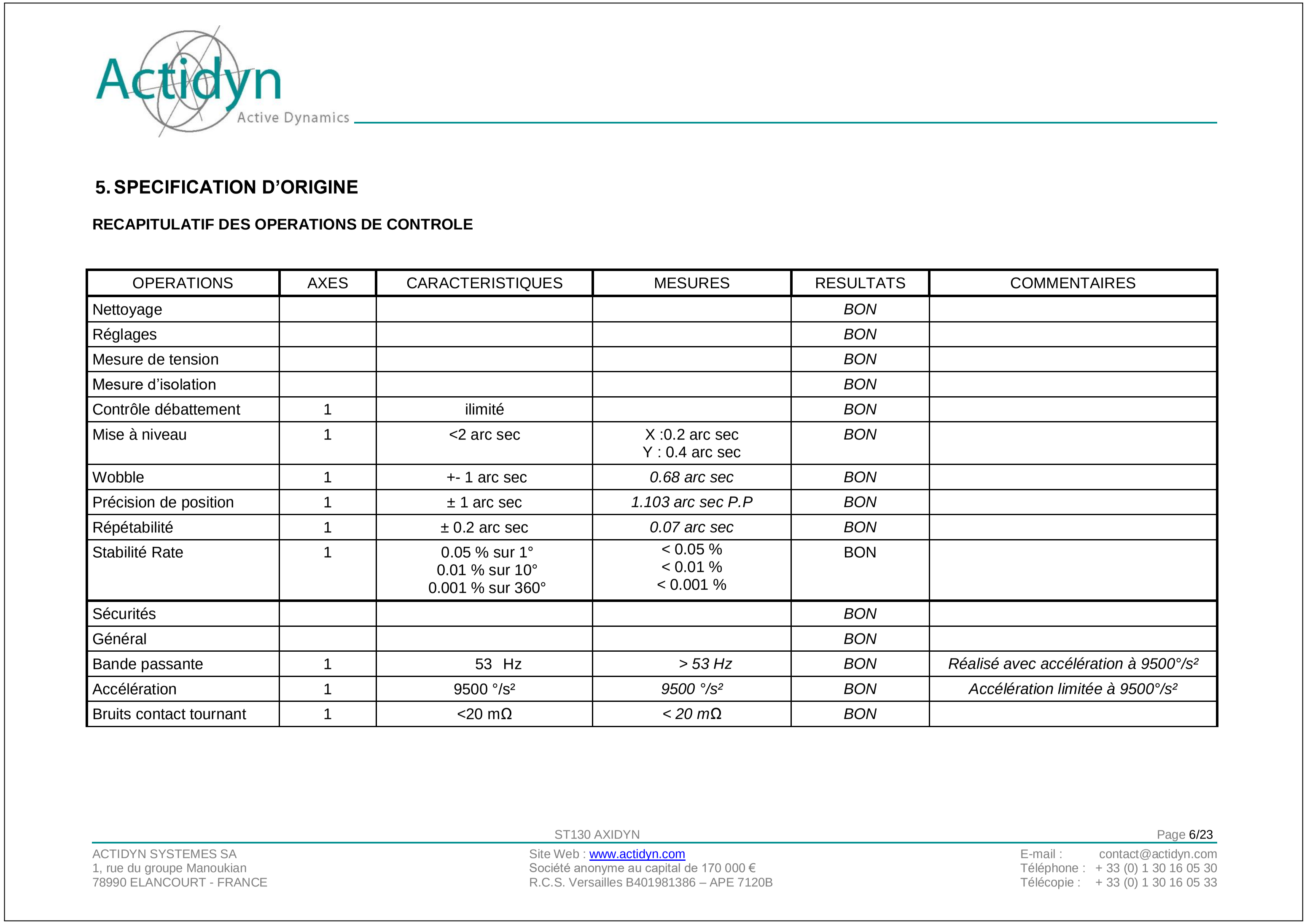

Actidyn
Active Dynamics

5. SPECIFICATION D'ORIGINE

RECAPITULATIF DES OPERATIONS DE CONTROLE

OPERATIONS	AXES	CARACTERISTIQUES	MESURES	RESULTATS	COMMENTAIRES
Nettoyage				*BON*	
Réglages				*BON*	
Mesure de tension				*BON*	
Mesure d'isolation				*BON*	
Contrôle débattement	1	ilimité		*BON*	
Mise à niveau	1	<2 arc sec	X :0.2 arc sec Y : 0.4 arc sec	*BON*	
Wobble	1	+- 1 arc sec	*0.68 arc sec*	*BON*	
Précision de position	1	± 1 arc sec	*1.103 arc sec P.P*	*BON*	
Répétabilité	1	± 0.2 arc sec	*0.07 arc sec*	*BON*	
Stabilité Rate	1	0.05 % sur 1° 0.01 % sur 10° 0.001 % sur 360°	< 0.05 % < 0.01 % < 0.001 %	BON	
Sécurités				*BON*	
Général				*BON*	
Bande passante	1	53 Hz	*> 53 Hz*	*BON*	*Réalisé avec accélération à 9500°/s²*
Accélération	1	9500 °/s²	*9500 °/s²*	*BON*	*Accélération limitée à 9500°/s²*
Bruits contact tournant	1	<20 mΩ	*< 20 mΩ*	*BON*	

ST130 AXIDYN
Page 6/23

ACTIDYN SYSTEMES SA
1, rue du groupe Manoukian
78990 ELANCOURT - FRANCE

Site Web : www.actidyn.com
Société anonyme au capital de 170 000 €
R.C.S. Versailles B401981386 – APE 7120B

E-mail : contact@actidyn.com
Téléphone : + 33 (0) 1 30 16 05 30
Télécopie : + 33 (0) 1 30 16 05 33

F.2 Measurements

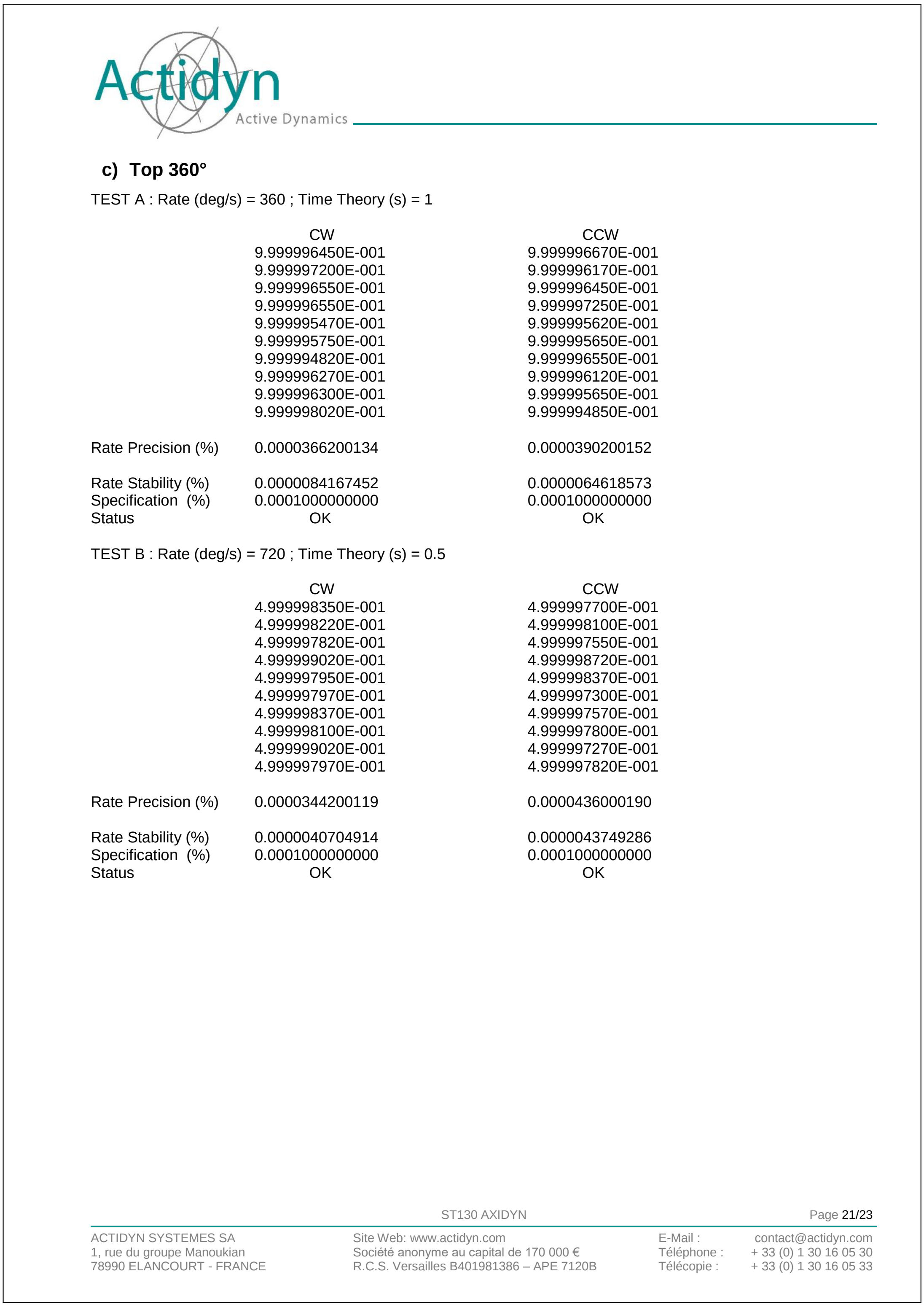

Actidyn
Active Dynamics

c) Top 360°

TEST A : Rate (deg/s) = 360 ; Time Theory (s) = 1

	CW	CCW
	9.999996450E-001	9.999996670E-001
	9.999997200E-001	9.999996170E-001
	9.999996550E-001	9.999996450E-001
	9.999996550E-001	9.999997250E-001
	9.999995470E-001	9.999995620E-001
	9.999995750E-001	9.999995650E-001
	9.999994820E-001	9.999996550E-001
	9.999996270E-001	9.999996120E-001
	9.999996300E-001	9.999995650E-001
	9.999998020E-001	9.999994850E-001
Rate Precision (%)	0.0000366200134	0.0000390200152
Rate Stability (%)	0.0000084167452	0.0000064618573
Specification (%)	0.0001000000000	0.0001000000000
Status	OK	OK

TEST B : Rate (deg/s) = 720 ; Time Theory (s) = 0.5

	CW	CCW
	4.999998350E-001	4.999997700E-001
	4.999998220E-001	4.999998100E-001
	4.999997820E-001	4.999997550E-001
	4.999999020E-001	4.999998720E-001
	4.999997950E-001	4.999998370E-001
	4.999997970E-001	4.999997300E-001
	4.999998370E-001	4.999997570E-001
	4.999998100E-001	4.999997800E-001
	4.999999020E-001	4.999997270E-001
	4.999997970E-001	4.999997820E-001
Rate Precision (%)	0.0000344200119	0.0000436000190
Rate Stability (%)	0.0000040704914	0.0000043749286
Specification (%)	0.0001000000000	0.0001000000000
Status	OK	OK

G Gyroscope Calibration Result

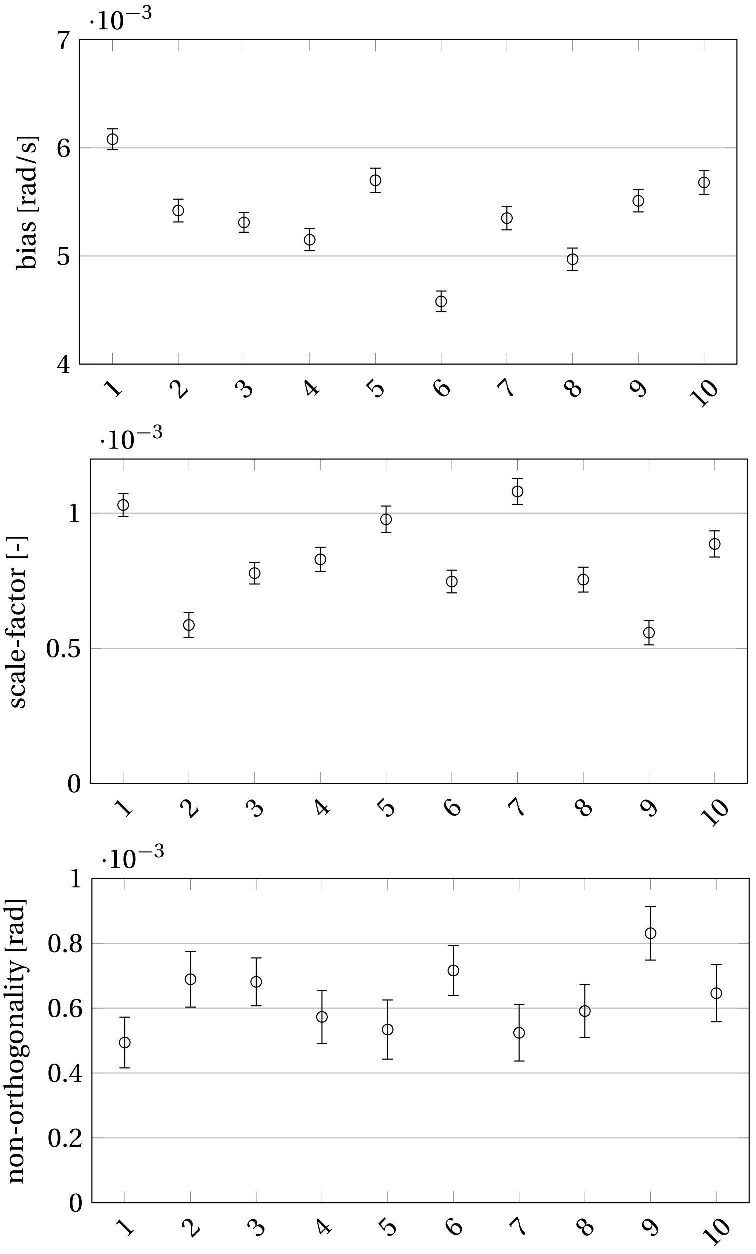

Figure G.1: Variations of 10 independent gyroscope calibration results with a 2σ bound for a typical Navchip z axis. The bias changes between 1000 °/h and 1300 °/h. The scale-factor changes between 500 ppm and 1000 ppm. The non-orthogonality changes between 0.5 mrad and 0.8 mrad.

Bibliography

P. Aggarwal, Z. Syed, X. Niu, and N. El-Sheimy. A Standard Testing and Calibration Procedure for Low Cost MEMS Inertial Sensors and Units. *Journal of Navigation*, 61:323 – 336, 04 2008.

D. W. Allan. Statistics of Atomic Frequency Standards. *Proceedings of the IEEE*, 54(2):221–230, Feb 1966. ISSN 0018-9219. doi: 10.1109/PROC.1966.4634.

D. W. Allan. Time and frequency (time-domain) characterization, estimation, and prediction of precision clocks and oscillators. *IEEE Transactions on Ultrasonics, Ferroelectrics, and Frequency Control*, 34(6):647–654, Nov 1987. ISSN 0885-3010. doi: 10.1109/T-UFFC.1987.26997.

D. W. Allan and J. A. Barnes. A modified "allan variance" with increased oscillator characterization ability. In *Thirty Fifth Annual Frequency Control Symposium*, pages 470–475, May 1981. doi: 10.1109/FREQ.1981.200514.

J. J. Allen, R. D. Kinney, J. Sarsfield, M. R. Daily, J. R. Ellis, J. H. Smith, S. Montague, R. T. Howe, B. E. Boser, R. Horowitz, A. P. Pisano, M. A. Lemkin, W. A. Clark, and T. Juneau. Integrated Micro-Electro-Mechanical Sensor Development for Inertial Applications. *IEEE Aerospace and Electronic Systems Magazine*, 13(11):36–40, Nov 1998. ISSN 0885-8985. doi: 10.1109/62.730622.

R. Alonso and M. Shuster. Complete Linear Attitude-Independent Magnetometer Calibration. *The Journal of the Astronautical Sciences*, 50:477–490, 10 2003.

S. L. Altmann. *Rotations, Quaternions, and Double Groups.* Clarendon Press, Oxford, 1986. ISBN 0-19-855372-2.

Analog Devices. ADIS16465 Datasheet. https://www.analog.com/media/en/technical-documentation/data-sheets/adis16465.pdf, 2018a. (Accessed on 12/2018).

Analog Devices. ADIS16488A Datasheet. https://www.analog.com/media/en/technical-documentation/data-sheets/ADIS16488A.pdf, 2018b. (Accessed on 12/2018).

Atmosphere. *U.S. Standard Atmosphere, 1962: ICAO Standard Atmosphere to 20 kilometers; Proposed ICAO Extension to 32 kilometers; Tables and Data to 700 kilometers.* United States Committee on Extension to the Standard, U.S. Govt. Print. Off., [Washington], 1962.

J. Balamuta, S. Guerrier, R. Molinari, and W. Yang. gmwm: Generalized Method of Wavelet Moments. R package (version 3.0.0.1000), 2016a. URL https://cran.r-project.org/package=gmwm. GitHub repository: https://github.com/SMAC-Group/GMWM.

J. Balamuta, R. Molinari, S. Guerrier, and W. Yang. The gmwm R Package: A Comprehensive Tool for Time Series Analysis from State-Space Models to Robustness. *arXiv*, 07 2016b.

E. P. Baltsavias. Airborne Laser Scanning: Existing Systems and Firms and Other Resources. *ISPRS Journal of Photogrammetry and Remote Sensing*, 54(2):164 – 198, 1999. ISSN 0924-2716. doi: https://doi.org/10.1016/S0924-2716(99)00016-7. URL http://www.sciencedirect.com/science/article/pii/S0924271699000167.

M. Baumker and F. Heimes. New Calibration and Computing Method for Direct Georeferencing of Image and Scanner Data Using the Position and Angular Data of an Hybrid Inertial Navigation System. In *Workshop, Integrated sensor orientation, test report and workshop proceedings*, volume 43, pages 197–212, Hannover, Germany, 2002. Bundesamt fur Kartographie und Geodasie.

M. Bevermeier, O. Walter, S. Peschke, and R. Haeb-Umbach. Barometric Height Estimation Combined with Map-Matching in a Loosely-Coupled Kalman-filter. In *2010 7th Workshop on Positioning, Navigation and Communication*, pages 128–134, March 2010. doi: 10.1109/WPNC.2010.5650745.

N. .-. Bowditch. *American Practical Navigator: an Epitome of Navigation.* 1984 ed. [Washington, D.C.?] : Defense Mapping Agency Hydrographic/Topographic Center : For sale by authorized Sales Agents of the Defense Mapping Agency, Office of Distribution Services, 1984-, 1984. URL https://search.library.wisc.edu/catalog/999654731602121. Includes bibliographical references and index.

R. G. Brown and P. Y. Hwang. *Introduction to Random Signals and Applied Kalman Filtering: with MATLAB Exercises.* Wiley, Hoboken, N.J, 4th ed. edition, 2011. ISBN 978-0-470-60969-9.

W. Chang, J. Cheng, J. Allaire, Y. Xie, and J. McPherson. *shiny: Web Application Framework for R*, 2017. URL https://CRAN.R-project.org/package=shiny. R package version 1.0.3.

D. Choukroun, I. Y. Bar-Itzhack, and Y. Oshman. Optimal-REQUEST Algorithm for Attitude Determination. *Journal of Guidance, Control, and Dynamics*, 27(3):418–425, May 2004. ISSN 0731-5090. doi: 10.2514/1.10337. URL https://doi.org/10.2514/1.10337.

A. Chulliat, W. Brown, P. Alken, S. Macmillan, M. Nair, C. Beggan, A. Woods, B. Hamilton, B. Meyer, and R. Redmon. Out-of-Cycle Update of the US/UK World Magnetic Model for 2015-2020: Technical Note. Technical report, National Centers for Environmental Information, NOAA, 2015a. URL https://www.ngdc.noaa.gov/geomag/WMM/soft.shtml.

A. Chulliat, S. Macmillan, P. Alken, C. Beggan, M. Nair, B. Hamilton, A. Woods, V. Ridley, S. Maus, and A. Thomson. The US/UK World Magnetic Model for 2015-2020: Technical Report. Technical report, National Geophysical Data Center, NOAA, 01 2015b.

P. Clausen, S. Guerrier, J. Lee, and R. Molinari. gui4gmwm Overview, Graphical User Interface for the Inertial Sensors Calibration. https://smac-group.github.io/gui4gmwm, October 2018a. (Accessed on 10/2018).

P. Clausen, J. Skaloud, R. Molinari, J. Lee, and S. Guerrier. Use of a New Online Calibration Platform with Applications to Inertial Sensors. *IEEE Aerospace and Electronic Systems Magazine*, 33(8):30–36, August 2018b. ISSN 0885-8985. doi: 10.1109/MAES.2018.170153.

Colibry. MS1010 Datasheet. https://www.colibrys.com/product/ms1000-mems-accelerometer/, 2018. (Accessed on 12/2018).

N. El-Sheimy, H. Hou, and X. Niu. Analysis and Modeling of Inertial Sensors Using Allan Variance. *IEEE Transactions on Instrumentation and Measurement*, 57(1):140–149, Jan 2008. ISSN 0018-9456. doi: 10.1109/TIM.2007.908635.

J. A. Farrell and M. Barth. *The Global Positioning System & Inertial Navigation.* McGraw-Hill, New York, 1999. ISBN 0-07-022045-X.

J. L. Farrell. Carrier Phase Processing Without Integers. *Proceedings of the 57th Annual Meeting of the Institute of Navigation*, pages 423–428, June 2001.

D. Gebre-Egziabher, G. H. Elkaim, J. Powell, and B. W. Parkinson. Calibration of Strapdown Magnetometers in Magnetic Field Domain. *Journal of Aerospace Engineering - J AEROSP ENG*, 19, 04 2006.

A. Gelb and A. S. Corporation. *Applied Optimal Estimation.* The M.I.T. Press, Cambridge, Massachusetts, [thirteenth printing 1994] edition, 1994. ISBN 0-262-57048-3.

C. A. Greenhall. Recipes for degrees of freedom of frequency stability estimators. *IEEE Transactions on Instrumentation and Measurement*, 40(6):994–999, Dec 1991. ISSN 0018-9456. doi: 10.1109/19.119780.

R. L. Greenspan. Inertial Navigation Technology from 1970–1995. *Journal of the Institute of Navigation*, 42(1):165–185, Spring 1995. doi: 10.1002/j.2161-4296.1995.tb02334.x. URL https://onlinelibrary.wiley.com/doi/abs/10.1002/j.2161-4296.1995.tb02334.x.

S. Guerrier. Improving accuracy with multiple sensors: Study of redundant mems-imu/gps configurations. *22nd International Technical Meeting of the Satellite Division of the Institute of Navigation 2009, ION GNSS 2009*, 5, 09 2009.

S. Guerrier and R. Molinari. Wavelet Variance for Random Fields: an M-Estimation Framework. *ArXiv e-prints*, July 2016. URL http://adsabs.harvard.edu/abs/2016arXiv160705858G. Provided by the SAO/NASA Astrophysics Data System.

S. Guerrier, J. Skaloud, Y. Stebler, and M.-P. Victoria-Feser. Wavelet-Variance-Based Estimation for Composite Stochastic Processes. *Journal of the American Statistical Association*, 108 (503):1021–1030, 2013a. doi: 10.1080/01621459.2013.799920. URL ttps://doi.org/10.1080/01621459.2013.799920. PMID: 24174689.

S. Guerrier, Y. Stebler, J. Skalud, and M.-P. Victoria-Feser. Limits of the Allan Variance and Optimal Tuning of Wavelet Variance based Estimators. *Open Archives University Geneva*, 2013b. URL https://archive-ouverte.unige.ch/unige:29034. ID: unige:29034; IEEE Transactions on Signal Processing, revision invited.

S. Guerrier, R. Molinari, and J. Skaloud. Automatic Identification and Calibration of Stochastic Parameters in Inertial Sensors. *NAVIGATION, Journal of The Institute of Navigation*, 62(4): 265–272, Winter 2015.

S. Guerrier, R. Molinari, and Y. Stebler. Theoretical Limitations of Allan Variance-Based Regression for Time Series Model Estimation. *IEEE Signal Processing Letters*, 23(5):597–601, May 2016. ISSN 1070-9908. doi: 10.1109/LSP.2016.2541867.

H. Haiying. Modeling inertial sensors errors using allan variance. *Master Thesis, University of Calgary, Department of Geomatics Engineering*, 09 2004.

J. D. Hamilton. *Time Series Analysis.* Princeton University Press, Princeton, N.J, 1994. ISBN 0-691-04289-6.

S. Han and J. Wang. Quantization and Colored Noises Error Modeling for Inertial Sensors for GPS/INS Integration. *IEEE Sensors Journal*, 11(6):1493–1503, June 2011. ISSN 1530-437X. doi: 10.1109/JSEN.2010.2093878.

T. Hastie and R. Tibshirani. *Generalized Additive Models*, volume 43. CRC Press, 1990.

Helimap System SA. *Helimap System*, 2018. URL http://www.helimap.ch/en_index.html. 2008 - 2018.

IEEE. IEEE standard specification format guide and test procedure for single-axis interferometric fiber optic gyros. *IEEE Std 952-1997*, pages 1–84, Feb 1998. doi: 10.1109/IEEESTD.1998.86153.

IEEE. IEEE Standard Specification Format Guide and Test Procedure for Linear, Single-Axis, Non-Gyroscopic Accelerometers. *IEEE Std 1293-1998 (R2008)*, pages 1–249, July 2011. doi: 10.1109/IEEESTD.2011.5960745.

Intersense. Navchip V2 Datasheet. http://www.intersense.com/pages/16/246/, 2018. (Accessed on 12/2018).

Ixblue. Airins Datasheet. https://www.ixblue.com/sites/default/files/downloads/ixblue-br-airins-2015-03-15.pdf, March 2015. (Accessed on 12/2018).

JAVAD. GREIS - GNSS Receiver External Interface Specification. https://www.javad.com/downloads/javadgnss/manuals/GREIS/GREIS_Reference_Guide.pdf, August 2017. (Accessed on 09/2017).

K. Jonghyuk and S. Sukkarieh. A Baro-Altimeter Augmented INS/GPS Navigation System for an Uninhabited Aerial Vehicle. Presented at SatNav 2003, The 6th International Symposium on Satellite Navigation Technology Including Mobile Positioning & Location Services, Melbourbe, Australia, 07 2003.

T. Kluter. GECKO4NAV Technical Reference Manual Revision 1.0. *Internal Document*, 2012.

M. Kok, J. D. Hol, T. B. Schön, F. Gustafsson, and H. Luinge. Calibration of a magnetometer in combination with inertial sensors. In *2012 15th International Conference on Information Fusion*, pages 787–793, July 2012.

M. Kraft, C. Lewis, T. Hesketh, and S. Szymkowiak. Closed Loop Digital Accelerometer Employing Oversampling Conversion. *Sensors and Actuators*, A68:466–473, 1997.

P. Lesage and C. Audoin. Characterization of frequency stability: Uncertainty due to the finite number of measurements. *IEEE Transactions on Instrumentation and Measurement*, 22(2): 157–161, June 1973. ISSN 0018-9456. doi: 10.1109/TIM.1973.4314128.

F. L. Markley. Attitude Determination Using Two Vector Measurements. Technical report, Spacecraft Design, Testing and Performance, NASA Goddard Space Flight Center; Greenbelt, MD United States, January 1998.

O. Martin, C. Meynard, M. Pierrot-Deseilligny, J.-P. Souchon, and C. Thom. Réalisation d'une caméra photogrammétrique ultralégère et de haute résolution. *Proceedings of the colloque drones et moyens légers aéroportés d'observation*, IGN, Montpellier, France, June 2014.

B. Merminod. *Méthodes d'estimation*. EPFl, Faculté de l'Environnement Naturel Architectural et Construit, Institut d'Ingénierie de l'Environnement, Géomatique - Topométrie, Septembre, 2018. Nouvelle édition.

P. Molina, I. Colomina, T. Vitoria, P. F. Silva, Y. Stebler, J. Skaloud, W. Kornus, and R. Prades. Egnos-Based Multi-Sensor Accurate and Reliable Navigation in Search-And Missions with UAVs. *ISPRS - International Archives of the Photogrammetry, Remote Sensing and Spatial Information Sciences*, 3822:87–93, Sept. 2011. doi: 10.5194/isprsarchives-XXXVIII-1-C22-87-2011.

R. Molinari, J. Balamuta, S. Guerrier, and J. Skaloud. Automatic and Computationally Efficient Method for Model Selection in Inertial Sensor Calibration. In *ION GNSS+*, September 2015.

R. C. Molinari. Robust inference for random fields and latent models. *PhD Thesis*, 08/26 2016. URL https://nbn-resolving.org/urn:nbn:ch:unige-868996. ID: unige:86899.

J. Nikolic, P. Furgale, A. Melzer, and R. Siegwart. Maximum Likelihood Identification of Inertial Sensor Noise Model Parameters. *IEEE Sensors Journal*, 16(1):163–176, 2016. ISSN 1530-437X. doi: 10.1109/JSEN.2015.2476668.

J. Parviainen, J. Hautamäki, J. Collin, and J. Takala. Barometer-Aided Road Grade Estimation. *Journal*, 01 2011.

D. B. Percival. On Estimation of the Wavelet Variance. *Biometrika*, 82(3):619–631, 1995.

D. B. Percival and P. Guttorp. Long-Memory Processes, the Allan Variance and Wavelets. In E. Foufoula-Georgiou and P. Kumar, editors, *Wavelets in Geophysics*, volume 4 of *Wavelet Analysis and Its Applications*, pages 325 – 344. Academic Press, 1994. doi: https://doi.org/10.1016/B978-0-08-052087-2.50018-9. URL http://www.sciencedirect.com/science/article/pii/B9780080520872500189.

D. B. Percival and A. T. Walden. *Wavelet methods for time series analysis*, volume 4 of *Cambridge series in statistical and probabilistic mathematics*. Cambridge University Press, Cambridge, 2000. ISBN 0-521-64068-7.

PhaseOne. Phase One Aerial Adds iXA-R Camera Platform. https://industrial.phaseone.com/documents/Phase_One_PR_New_Products.pdf, September 2014. (Accessed on 12/2018).

Pix4D. *Pix4D Homepage*, 2018. URL https://pix4d.com/. (Accessed on 09/2018).

Pixhawk. Pixhawk Homepage. http://pixhawk.org/, December 2018. (Accessed on 12/2018).

R Core Team. *R: A Language and Environment for Statistical Computing*. R Foundation for Statistical Computing, Vienna, Austria, 2016. URL https://www.R-project.org/.

Raspberry Pi. Raspberry Pi Zero Homepage. https://www.raspberrypi.org/products/raspberry-pi-zero/, December 2018. (Accessed on 12/2018).

M. Rehak and J. Skaloud. Fixed-Wing Micro Aerial Vehicle for Accurate Corridor Mapping. *ISPRS Annals of the Photogrammetry, Remote Sensing and Spatial Information Sciences*, XL-1/W4:23–31, 2015. doi: 10.5194/isprsannals-II-1-W1-23-2015. URL http://infoscience.epfl.ch/record/211104.

V. Renaudin, M. H. Afzal, and G. Lachapelle. Complete Triaxis Magnetometer Calibration in the Magnetic Domain. *Journal of Sensors*, 2010:967245:1–967245:10, 2010.

Riegl. VQ-48-U. http://www.riegl.com/uploads/tx_pxpriegldownloads/DataSheet_VQ-480-U_2015-03-24.pdf, March 2015. (Accessed on 12/2018).

RStudio Inc. Shiny, from RStudio. https://shiny.rstudio.com/, 2017. (Accessed on 11/2018).

P. Schär. In-Flight Quality Assessment and Data Processing for Airborne Laser Scanning. *EPFL PhD Thesis*, 2010. doi: 10.5075/epfl-thesis-4590. URL http://infoscience.epfl.ch/record/142389.

Sensonor. STIM300 Datasheet. https://www.sensonor.com/media/1308/ts1524r24-datasheet-stim300.pdf, 8 2017. (Accessed on 12/2018).

D. K. Shaeffer. MEMS Inertial Sensors: A Tutorial Overview. *IEEE Communications Magazine*, 51(4):100–109, April 2013. ISSN 0163-6804. doi: 10.1109/MCOM.2013.6495768.

J. Skaloud, P. Schaer, Y. Stebler, and P. Tomé. Real-Time Registration of Airborne Laser Data with Sub-Decimeter Accuracy. *ISPRS Journal of Photogrammetry and Remote Sensing*, 2010. doi: 10.1016/j.isprsjprs.2009.12.003. URL http://infoscience.epfl.ch/record/144130.

Sony. ilce 6000 body kit. https://www.sony.com/electronics/interchangeable-lens-cameras/ilce-6000-body-kit, 2018. (Accessed on 12/2018).

Y. Stebler. Modeling and Processing Approaches for Integrated Inertial Navigation. *EPFL PhD Thesis*, 2013. doi: 10.5075/epfl-thesis-5601. URL http://infoscience.epfl.ch/record/183073.

Y. Stebler, S. Guerrier, J. Skaloud, and M.-P. Victoria-Feser. Constrained Expectation-Maximization Algorithm for Stochastic Inertial Error Modeling: Study of Feasibility. *Measurement Science and Technology*, 22(8):1–12, 2011.

Y. Stebler, S. Guerrier, J. Skaloud, and M. Victoria-Feser. Generalized method of wavelet moments for inertial navigation filter design. *IEEE Transactions on Aerospace and Electronic Systems*, 50(3):2269–2283, July 2014. ISSN 0018-9251. doi: 10.1109/TAES.2014.120751.

K. M. S. J. W. Strus, Joseph M. Development of a high accuracy pointing system for maneuvering platforms. *Proceedings of the 20th International Technical Meeting of the Satellite Division of The Institute of Navigation (ION GNSS 2007),Fort Worth, TX,*, 5:2541–2549, September 2007.

Z. F. Syed, P. Aggarwal, C. Goodall, X. Niu, and N. El-Sheimy. A New Multi-Position Calibration Method for MEMS Inertial Navigation Systems. *Measurement Science and Technology*, 18(7): 1897, 2007. URL http://stacks.iop.org/0957-0233/18/i=7/a=016.

D. H. Titterton and J. L. Weston. *Strapdown Inertial Navigation Technology*, volume 17 of *IEE Radar, Sonar, Navigation and Avionics Series*. Institution of Electrical Engineers, Stevenage, 2nd ed edition, 2004. ISBN 0-86341-358-7.

Trimble. APX-15 Datasheet. https://www.applanix.com/downloads/products/specs/APX15_DS_NEW_0408_YW.pdf, March 2016. (Accessed on 12/2018).

UP board. UP board 4GB RAM+ 32 GB eMMC (Cooler). https://up-shop.org/up-boards/62-up-board-4b-32-gb-emmc-memory.html, December 2018. (Accessed on 12/2018).

R. J. Vaccaro and A. S. Zaki. Statistical Modeling of Rate Gyros. *IEEE Transactions on Instrumentation and Measurement*, 61(3):673–684, 2012.

J. F. Vasconcelos, G. Elkaim, C. Silvestre, P. Oliveira, and B. Cardeira. Geometric Approach to Strapdown Magnetometer Calibration in Sensor Frame. *IEEE Transactions on Aerospace and Electronic Systems*, 47(2):1293–1306, April 2011. ISSN 0018-9251. doi: 10.1109/TAES.2011.5751259.

Velodyne Lidar. Puck LITE. https://velodynelidar.com/vlp-16-lite.html, 2018. (Accessed on 12/2018).

D. W. Allan. Historicity, Strengths, and Weaknesses of Allan Variances and Their General Applications. *Gyroscopy and Navigation*, 7:1–17, 01 2016. doi: 10.1134/S2075108716010028.

A. Waegli, S. Guerrier, and J. Skaloud. Redundant mems-imu integrated with gps for performance assessment in sports. *Proceedings of IEEE/ION PLANS 2008*, pages 1260–1268, 2008. doi: 10.1109/PLANS.2008.4570079. URL http://infoscience.epfl.ch/record/124735.

G. Wahba. Problem 65-1: A Least Squares Estimate of Satellite Attitude. *SIAM Review*, 7(3): 409–409, 1965. ISSN 00361445. URL http://www.jstor.org/stable/2027852.

Y. Wu and W. Shi. On Calibration of Three-Axis Magnetometer. *IEEE Sensors Journal*, 15(11): 6424–6431, Nov 2015. ISSN 1530-437X. doi: 10.1109/JSEN.2015.2459767.

A. Wägli. Trajectory Determination and Analysis in Sports by Satellite and Inertial Navigation. *EPFL PhD Thesis*, 2009.

A. Wägli, J. Skaloud, S. Guerrier, M. E. Parés, and I. Colomina. Noise Reduction and Estimation in Multiple Micro-Electro-Mechanical Inertial Systems. *Measurement Science and Technology*, 21:065201 (11 p.), 2010. doi: 10.1088/0957-0233/21/6/065201. URL http://infoscience.epfl.ch/record/148574.

Z. Xing and D. Gebre-Egziabher. Modeling and bounding low cost inertial sensor errors. In *2008 IEEE/ION Position, Location and Navigation Symposium*, pages 1122–1132, May 2008. doi: 10.1109/PLANS.2008.4569999.

L. Xue, C. Jiang, L. Wang, J. Liu, and W. Yuan. Noise Reduction of MEMS Gyroscope Based on Direct Modeling for an Angular Rate Signal. *Micromachines*, 6(2):266–280, 2015.

I. Y. Bar-Itzhack. REQUEST - A Recursive QUEST Algorithm for Sequential Attitude Determination. *Journal of Guidance Control Dynamics*, 19:1034–1038, Sept. 1996. doi: 10.2514/3.21742.

D. Yuan, X. Ma, Y. Liu, Z. Shang, and S. Yan. Statistical modeling of random walk errors for triaxial rate gyros. *IEEE Transactions on Instrumentation and Measurement*, 65(2):286–296, Feb 2016. ISSN 0018-9456. doi: 10.1109/TIM.2015.2450358.

J. Zhang, E. Edwan, J. Zhou, W. Chai, and O. Loffeld. Performance Investigation of Barometer Aided GPS/MEMS-IMU Integration. In *Proceedings of the 2012 IEEE/ION Position, Location and Navigation Symposium*, pages 598–604, April 2012. doi: 10.1109/PLANS.2012.6236933.

N. F. Zhang. Allan Variance of Time Series Models for Measurement Data. *Metrologia*, 45: 549–561, 2008.

S. Zhang, S. Yu, C. Liu, X. Yuan, and S. Liu. A Dual-Linear Kalman Filter for Real-Time Orientation Determination System Using Low-Cost MEMS Sensors. *Sensors*, 16(2):264, 2016.

Y. Zhao, M. Horemuz, and L. E. Sjöberg. Stochastic Modelling and Analysis of IMU Sensor Errors. *Archives of Photogrammetry, Cartography and Remote Sensing*, 22:437–449, 2011.